

Spring 2000

Improvements of X-band and Q-band EPR
/ENDOR spectrometers Studies of ferritin iron
nitrosyl and copper cis,
cis-1,3,5-triaminocyclohexane chloride complexes,
and the application of Q-band EPR to the dating of
fossil teeth

Junlong Shao

University of New Hampshire, Durham

Follow this and additional works at: <https://scholars.unh.edu/dissertation>

Recommended Citation

Shao, Junlong, "Improvements of X-band and Q-band EPR /ENDOR spectrometers Studies of ferritin iron nitrosyl and copper cis, cis-1,3,5-triaminocyclohexane chloride complexes, and the application of Q-band EPR to the dating of fossil teeth" (2000). *Doctoral Dissertations*. 2128.

<https://scholars.unh.edu/dissertation/2128>

This Dissertation is brought to you for free and open access by the Student Scholarship at University of New Hampshire Scholars' Repository. It has been accepted for inclusion in Doctoral Dissertations by an authorized administrator of University of New Hampshire Scholars' Repository. For more information, please contact nicole.hentz@unh.edu.

INFORMATION TO USERS

This manuscript has been reproduced from the microfilm master. UMI films the text directly from the original or copy submitted. Thus, some thesis and dissertation copies are in typewriter face, while others may be from any type of computer printer.

The quality of this reproduction is dependent upon the quality of the copy submitted. Broken or indistinct print, colored or poor quality illustrations and photographs, print bleedthrough, substandard margins, and improper alignment can adversely affect reproduction.

In the unlikely event that the author did not send UMI a complete manuscript and there are missing pages, these will be noted. Also, if unauthorized copyright material had to be removed, a note will indicate the deletion.

Oversize materials (e.g., maps, drawings, charts) are reproduced by sectioning the original, beginning at the upper left-hand corner and continuing from left to right in equal sections with small overlaps.

Photographs included in the original manuscript have been reproduced xerographically in this copy. Higher quality 6" x 9" black and white photographic prints are available for any photographs or illustrations appearing in this copy for an additional charge. Contact UMI directly to order.

**Bell & Howell Information and Learning
300 North Zeeb Road, Ann Arbor, MI 48106-1346 USA
800-521-0600**

UMI[®]

Improvements of X-band and Q-band EPR/ENDOR Spectrometers. Studies of Ferritin Iron Nitrosyl and Copper *cis,cis*-1,3,5-Triaminocyclohexane Chloride Complexes, and the Application of Q-band EPR to the Dating of Fossil Teeth

by

Junlong Shao

B. S. Shadong University, 1985

M. S. Dalian Institute of Chemical Physics, Chinese Academy of Science, 1988

A DISSERTATION

**Submitted to the University of New Hampshire
in Partial Fulfillment of
the Requirements for the Degree of**

**Doctor of Philosophy
in
Chemistry**

May, 2000

UMI Number: 9969213

UMI[®]

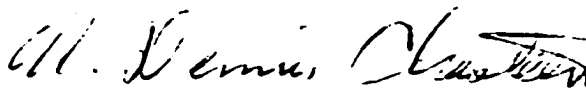
UMI Microform 9969213

Copyright 2000 by Bell & Howell Information and Learning Company.


All rights reserved. This microform edition is protected against
unauthorized copying under Title 17, United States Code.

Bell & Howell Information and Learning Company
300 North Zeeb Road
P.O. Box 1346
Ann Arbor, MI 48106-1346

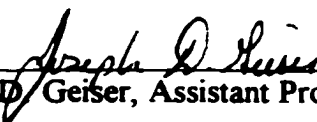
This dissertation has been examined and approved.



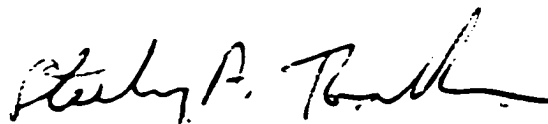
Dissertation Director, N. Dennis Chasteen
Professor of Chemistry



Olof E. Eicht, Professor of Physics



Joseph D. Geiser, Assistant Professor of Chemistry



Sterling A. Tomellini, Associate Professor of Chemistry



Roy P. Planalp, Associate Professor of Chemistry

1/24/00

Date

DEDICATION

This dissertation is dedicated to my wife, Linge Li and my son Andrew Y. Shao.

ACKNOWLEDGMENTS

I would like to give my heartfelt gratitude to my research advisor, Dr. N. Dennis Chasteen, for his professional guidance, creative ideas, continuous encourage, unlimited patience, as well as for his great assistance in my dissertation writing. My thanks to John Grady for his support in instrument operation and valuable advice, to Dr. Planalp and G. Park for providing the copper tach complexes and much of the optical measurements, to Dr. Brechbiel for tach ligand synthesis, and to Dr. Skinner for providing the fossil tooth samples. I am grateful to Xiaoke Yang and Wenge Wang for their timely help in my research work, as well as for my living in Durham through all these years. My thanks also goes to the group members, Lisa Budzinski, Rebecca Wagers, Roshi Pakdaman, Chris Janus-Chandler, Chun Liang and Pam Proulx-Curry for their support and help, which left a special part in my memory.

Furthermore, I wish to express my acknowledgment to the Department of Chemistry Faculty and Staff for sharing their knowledge and providing their professional support, to the technicians in the Space Center Machine shop for their excellent job on the parts of our spectrometers, to Dr. Chifuru Noda for his help in getting me accepted to the Graduate School at UNH, and to NIH for the research grants which have supported me for all these years.

Finally, I feel deeply indebted to my wife, Linge Li and my parents, Baozhong

Shao and Qiling Xiao for their vigorous support and warm care. Their sacrifice made it possible for me to pursue my career in science.

TABLE OF CONTENTS

DEDICATION.....	iii
ACKNOWLEDGMENTS.....	iv
LIST OF FIGURES.....	x
LIST OF TABLES.....	xv
LIST OF SYMBOLS.....	xvii
ABBREVIATIONS.....	xix
ABSTRACT.....	xx

	Page
CHAPTER 1. INTRODUCTION.....	1
EPR and ENDOR Theories.....	1
EPR/ENDOR Instrument.....	10
Applications of EPR/ENDOR Spectroscopy to Metal Complexes and Radicals.....	13
CHAPTER 2. MODIFICATION OF Q-BAND MICROWAVE BRIDGE.....	15
Installation of the Microwave Amplifier.....	15
Installation of the Microwave Frequency Counter.....	23
Replacement of the Magnetized RF Coaxial Cable.....	29
Installation of Line Conditioner.....	31

Installation of an Oscilloscope near the Microwave Bridge.....	31
Innovation of a New Robust Coupler.....	32
Comparisons of Performance before and after the Modifications.....	37
The EPR Spectra of Standard Samples in Absorption Mode and Dispersion Mode.....	39
 CHAPTER 3. CONSTRUCTION OF X-BAND ENDOR SPECTROMETER.....	42
Introduction.....	42
Design and Making of the ENDOR Coil.....	44
Spacer for the ENDOR Coil Connection.....	48
Assembly of the ENDOR Coil.....	52
Test of the Various ENDOR Coils.....	53
Sample Tube Change from 4 mm to 5 mm Outer Diameter.....	54
Modifications of the Helium Cooling System.....	54
Background Noise of the ENDOR Spectrometer.....	55
Test of the ENDOR Spectrometer.....	60
 CHAPTER 4. ENDOR STUDIES OF APOHOSF-Fe-NO AND MODEL IRON NITROSYL COMPLEXES.....	68
Introduction.....	68
Experimental.....	70
Results.....	74
A. EPR Spectra of ApoHoSF-Fe-NO and Model Complexes.....	74
B. Proton ENDOR Spectra of ApoHoSF-Fe-NO.....	74
C. ENDOR Spectra of Model Complexes.....	81
D. Molecular Modeling of Iron Nitrosyl Complexes.....	87

E. Distances from Fe to the Surrounding Protons.....	98
Discussion.....	106
A. EPR Studies of the Model Complexes.....	106
B. Molecular Modeling Calculations.....	111
C. Proton ENDOR Results.....	112
D. Comparison with the Proton Results in the Literature.....	113
Conclusions.....	115
 CHAPTER 5. EPR AND ENDOR STUDIES OF COPPER TACH COMPLEXES...	116
Introduction.....	116
Experimental.....	118
Results.....	121
A. g- and A-values of the Copper Tach Complexes.....	121
B. Optical Transitions of Copper Tach Complexes.....	134
C. Orbital Bonding Coefficients of Copper Tach Complexes.....	138
D. ENDOR Studies of the [Cu(N-Me) ₃ tachCl ₂] Complex.....	142
Discussion.....	148
A. The Structure of Copper Tach Complexes.....	148
B. The Orbital Bonding Coefficients of Copper Tach Complexes.....	151
Conclusions.....	152
 CHAPTER 6. APPLICATIONS OF Q-BAND EPR TO THE DATING OF FOSSIL TEETH.....	153
Introduction.....	153
Experimental.....	156
Results and Discussion.....	156
Conclusions.....	163

REFERENCES.....	165
APPENDIX A. OPERATION OF LIQUID HELIUM COOLING SYSTEM AT 2 K IN X-BAND ENDOR SYSTEM.....	171
APPENDIX B. OPERATION OF THE Q-BAND EPR/ENDOR SYSTEM.....	173
APPENDIX C. OPERATION OF THE X-BAND EPR/ENDOR SYSTEM.....	179
APPENDIX D. PROCEDURES FOR MAKING THE ENDOR COIL.....	183
APPENDIX E. CALCULATION OF ISOTROPIC G-VALUES AND ISOTROPIC HYPERFINE COUPLINGS.....	187
APPENDIX F. BONDING PARAMETER CALCULATIONS.....	199
APPENDIX G. MEASUREMENT OF FREQUENCY MODULATION DEPTH.....	206
APPENDIX H. THE DETERMINATION OF THE ANGLES BETWEEN THE PSEUDO SYMMETRY AXIS AND THE VECTOR OF METAL ION CENTER TO THE SURROUNDING PROTONS.....	211
APPENDIX I. MOLECULAR MODELING CALCULATIONS FOR THE PREVIOUS PROTON ENDOR SPECTRA OF CYSTEINE AND PENICILLAMINE IRON NITROSYL COMPLEXES.....	215

LIST OF FIGURES

Figure	Page
1.1 The schematic diagram of the electron spin energy levels for a $S = \frac{1}{2}$, $I = \frac{1}{2}$ spin system.....	5
1.2 The schematic diagram of a typical X-band EPR spectrometer.....	9
2.1 The schematic diagram of the Varian Q-band E110 microwave bridge.....	16
2.2 The schematic diagram of modified Q-band microwave bridge by J. S. Hyde.....	18
2.3 The schematic diagram of the Q-band microwave bridge after the modification.....	19
2.4 The schematic diagram of the specific microwave bend.....	21
2.5 The photo of the Varian Q-band microwave bridge after the modification.....	22
2.6 The EPR signal and the background spectra of the weak pitch standard sample before and after the modifications.....	24
2.7 The S/N ratio of weak pitch sample versus the attenuation before and after the modification.....	26
2.8 The circuit of the low gain amplifier.....	30
2.9 The schematic diagram for the second oscilloscope wiring.....	32
2.10 The diagram of the newly designed Q-band cavity coupler.....	33
2.11a The mechanical drawing of the coupler base.....	34
2.11b The mechanical drawing of the coupler holder.....	35
2.11c The mechanical drawing of the coupler finger.....	36
2.12 The EPR spectra of standard samples in both absorption and dispersion modes....	40

3.1 The schematic diagrams of our ENDOR coils.....	43
3.2a The drawing of the designed front side ENDOR coil.....	45
3.2b The drawing of the designed back side ENDOR coil.....	46
3.3 The photograph of the ENDOR coil.....	49
3.4 The drawing of the assembled coil and spacer with electrical connections.....	50
3.5 The mechanical drawing of the spacer for the ENDOR coil.....	51
3.6 The EPR signal amplitudes of sucrose standard sample versus the three different coils.....	56
3.7 The ENDOR signal amplitudes of sucrose standard sample versus the three different coils.....	58
3.8 The partial drawing of the X-band EPR/ENDOR cooling system.....	61
3.9 The EPR spectrum of sucrose standard sample from the present TE104 cavity.....	62
3.10 The sucrose ENDOR signals from two different spectrometers.....	63
3.11 The EPR/ENDOR signals for BDPA samples in 4 mm and 5 mm tubes.....	64
4.1 The schematic diagram of the apparatus for the preparation of the ferritin iron nitrosyl complex.....	71
4.2 The EPR spectra of HoSF-Fe-NO and model complexes.....	75
4.3 The proton ENDOR spectra of HoSF-Fe-NO complexes at parallel position.....	78
4.4 The molecular weight assay of ferritin samples by Gel electrophoresis.....	79
4.5 The proton ENDOR spectra of HoSF-Fe-NO complexes at perpendicular position..	80
4.6 The temperature dependence of ENDOR signal amplitude of Cys-Fe-NO complex..	82
4.7 The ^1H ENDOR spectra of Pen-Fe-NO at parallel position.....	83
4.8 The ^1H ENDOR spectra of Pen-Fe-NO at perpendicular position.....	84

4.9 The ^1H ENDOR spectra of Cys-Fe-NO at the parallel field position.....	85
4.10 The ^1H ENDOR spectra of Cys-Fe-NO complexes at the perpendicular field position.....	86
4.11 The model of Cys-Fe-NO complex.....	90
4.12 The model of Pen-Fe-NO complex.....	91
4.13 The visual local structure of HoSF-Fe-NO in ferritin 3-fold channel generated with ChemSite molecular modeling.....	92
4.14 The enlarged view of the complex structure of ferritin iron nitrosyl complex.....	93
4.15 The schematic diagram for the vector operation on penicillamine iron nitrosyl complex.....	94
4.16 The graph of the angle function of $3\cos^2\phi-1$	103
4.17 The schematic diagram of the iron nitrosyl complex.....	104
5.1 The X-ray crystallography of $[\text{Cu}(\text{N-Et})_3\text{tachCl}_x\text{Br}_{2-x}]$ complex.....	117
5.2 The schematic diagram of the d orbital energy levels under a series of symmetric crystal fields.....	119
5.3 The Q-band powder EPR spectra of copper tach chloride complexes.....	123
5.4 The X-band EPR spectra of copper tach chloride complexes at 77 K.....	125
5.5 The Q-band EPR spectra of copper tach chloride complexes at 100 K.....	129
5.6 The room temperature X-band EPR spectra of copper tach chloride complexes....	131
5.7 The optical spectra of copper tach chloride complexes prepared in methanol.....	135
5.8 The optical spectra of copper tach chloride complexes prepared in methanol.....	136
5.9 The experimental and simulated optical spectrum of $[\text{Cu}(\text{N-Et})_3\text{tachCl}_2]$ prepared in methanol.....	137
5.10 The ^1H ENDOR spectra at parallel field position of $M_I = -1/2$ for the copper complex in H_2O and D_2O	144

5.11 The ^1H ENDOR spectra at perpendicular position for the copper complex in H_2O and D_2O	145
5.12 The ^{14}N ENDOR spectra of $[\text{Cu}(\text{N-Et})_3\text{tachCl}_2]$ complex in H_2O	147
6.1 The trapping scheme of electrons in minerals.....	154
6.2 The X-band EPR spectrum of the fossil tooth enamel sample.....	157
6.3 The Q-band EPR spectrum of the fossil tooth enamel sample.....	158
6.4 The EPR amplitudes of the dating peak and the interfering peak versus the irradiated doses.....	159
6.5 The EPR signal amplitude versus the artificially irradiated dose for the fossil teeth samples.....	160
6.6 The EPR signal amplitude versus the artificially accumulated dose for the fossil teeth samples.....	161
6.7 The microwave power saturation characteristics of the fossil tooth enamel sample.....	164
A.1 The schematic diagram of the Q-band liquid nitrogen flow system.....	172
B.1 The complete liquid helium system in the X-band EPR/ENDOR spectrometer.....	178
C.1 The schematic diagram of the channel selector wiring.....	181
C.2 The wiring of the RF circuit in the X-band ENDOR spectrometer.....	182
D.1 The schematic diagram of one piece of the copper coil.....	185
D.2 The schematic diagram of the exposure process.....	186
E.1 The flow chart for the second-order calculation of isotropic g_0 and isotropic A_0	198
G.1 The wiring for the modulation depth measurement.....	207
G.2 The diagram of the modulated signal displayed on the oscilloscope.....	208
G.3 The measured modulated frequency depth versus the modulation signal amplitude.....	209

H.1 The schematic diagram for the determination of ϕ_0	213
I.1 The proton ENDOR spectrum of Cys-Fe-NO along with the modeling calculation results at the parallel field position.....	217
I.2 The proton ENDOR spectrum of Cys-Fe-NO along with the modeling calculation results at the perpendicular field position.....	218
I.3 The proton ENDOR spectrum of Pen-Fe-NO along with the modeling calculation results at the parallel field position.....	219
I.4 The proton ENDOR spectrum of Pen-Fe-NO along with the modeling calculation results at the perpendicular field position.....	220

LIST OF TABLES

Table	Page
2.1 Comparison of the improvements after the modifications.....	38
2.2 Summary of the modifications made on the Q-band spectrometer.....	39
3.1 The comparison of our two X-band ENDOR systems.....	67
4.1 The $g_{ }$ and g_{\perp} values for the studied complexes.....	76
4.2 The ^1H ENDOR couplings of HoSF-Fe-NO and model complexes.....	77
4.3 The bond lengths chosen for the model complex modeling.....	88
4.4 The calculated ϕ_0 and proton hyperfine couplings with a tilted pseudo symmetry axis.....	100
4.4a The bond lengths and angles for the first coordination sphere ligand atoms of the iron nitrosyl complexes.....	102
4.5 The calculated distance for the protons to the iron center from the ENDOR data..	107
4.6 The g-values and hyperfine couplings for the model complexes from previous work.....	108
5.1 The complete list of the experiments carried out on the copper tach chloride complexes.....	122
5.2 The g-values and hyperfine couplings for the copper tach chloride complexes.....	133
5.3 The transition assignments for the optical spectra of the copper tach chloride complexes.....	139
5.3a The oscillator strength for the copper tach complexes.....	140
5.4 The calculated bonding parameters of the $[\text{Cu}(\text{N-Et})_3\text{tachCl}_2]$ complex in HEPES	

buffer.....	143
5.5 The ^1H hyperfine couplings and ^{14}N peak positions of aqueous $[\text{Cu}(\text{N-Me})_3\text{tachCl}_2]$ sample.....	146
B.1 The status of all the valves in Figure B.1 at the beginning and the end of an ENDOR experiment.....	174
F.1 The arrangement of all the data used and resolved in the bonding parameter calculations.....	203
G.1 The frequency modulation depth at 14 MHz versus the modulation voltage for 10 kHz modulation on Varian console set at 5 G.....	210
H.1 The measured bond lengths and the calculated ϕ_0 and proton hyperfine couplings..	214

LIST OF SYMBOLS

a	hyperfine splitting
A	electron nuclear hyperfine tensor
c	the speed of the light
β	Bohr magneton
β_N	Nuclear magneton
g	electron g tensor
g_{\perp}	perpendicular g factor
g_{\parallel}	parallel g factor
g_N	the nuclear g factor
\mathcal{H}	spin Hamiltonian
B	applied magnetic field
h	Planck's constant
I	nuclear spin angular momentum
κ	Fermi-contact term
λ	wavelength
m_s	magnetic spin quantum number of the electron
m_I	magnetic spin quantum number of the nucleus
ν_n	nuclear Larmor frequency
ν_0	resonance frequency of the cavity

\mathbf{Q}	the quadrupole tensor
Q	cavity quality factor
\mathbf{r}	radial vector from m_c to m_N
\mathbf{S}	spin angular momentum operator
T_1	spin-lattice (longitudinal) relaxation time
T_2	spin-spin (transverse) relaxation time

ABBREVIATIONS

AET	Aminoethanethiol
BDPA	α, γ -bisdiphenylene- β -phenylallyl
CAPS	3-cyclohexylamino-1-propanesulfonic acid
Cys	cysteine
DPPH	2,2-di(4- <i>tert</i> -octylphenyl)-1-picrylhydrazyl
ENDOR	electron-nuclear double resonance
EPR	electron paramagnetic resonance
ETH	Ethanethiol
Hepes	4-(2-hydroxyethyl)-1-piperazineethanesulfonic acid
HoSF	horse spleen ferritin
MER	Mercaptoethanol
MES	4-morpholineethanesulfonic acid
MOPS	4-morpholinepropanesulfonic acid
Pen	Penicillamine
rHF	recombinant human H-chain apoferritin
S5	rHF variant with Cys90 replaced by glutamate and Cys102 and Cys130 replaced by alanine
tach	<i>cis, cis</i> -1,3,5-triaminocyclohexane
(N-R) ₃ tach	<i>N, N', N''</i> -trialkylated derivatives of <i>cis, cis</i> -1,3,5-triaminocyclohexane

ABSTRACT

Improvements of X-band and Q-band EPR/ENDOR Spectrometers. Studies of Ferritin Iron Nitrosyl and Copper *cis,cis*-1,3,5-Triaminocyclohexane Chloride Complexes, and the Application of Q-band EPR to the Dating of Fossil Teeth

by

Junlong Shao

University of New Hampshire, May, 2000

Several modifications were made on a Varian Q-band EPR/ENDOR spectrometer, including the installation of a microwave amplifier in the E110 bridge, design and assembly of a new cavity coupler, addition of frequency counting capability, as well as other useful minor changes. The performance of the spectrometer was improved in signal-to-noise ratio, convenience of tuning and operation and accuracy of g-value and hyperfine coupling measurements. The signal-to-noise ratio was increased by a factor of six.

Improvements were also achieved with our X-band EPR/ENDOR spectrometer by design and assembly of a new printed ENDOR coil for use in a TE104 rectangular cavity. The Dewar and sample holder were changed to accommodate EPR tubes of 5 mm o.d.. The ENDOR signal-to-noise ratio of a sucrose standard sample was increased by a factor of three by these changes.

¹H ENDOR studies of ferritin iron nitrosyl complexes and other model complexes were carried out with the new ENDOR system. The proton ENDOR signals of ferritin iron nitrosyl complexes were first observed in this laboratory. Molecular modeling

xx

calculations and the equations derived for the iron nitrosyl complexes enable one to undertake a complete ENDOR data analysis. The ENDOR studies suggested that the local structure of the iron site in the ferritin iron nitrosyl complex was identical to that of a model complex of penicillamine with the iron atom coordinated to a sulphur atom of a cysteine residue, a nitrogen atom in the protein backbone and two nitric oxide radicals.

EPR/ENDOR studies of copper *cis,cis*-1,3,5-triaminocyclohexane have shown the complexes to have a rhombic magnetic symmetry in powders, but axial symmetry in aqueous solution. When the complex was prepared in methanol, it retained its molecular configuration as in the crystal. However, when prepared in aqueous solution, two water molecules might replace one or two of the chloride ions in the equatorial plane of the complex. The sample in aqueous solution had covalent in-plane sigma bonding. The out-plane pi bonds and the in-plane pi bond were ionic for the aqueous sample.

Finally, Q-band EPR studies of fossil tooth enamel demonstrated that X-band EPR could be used for routine dating of fossil teeth samples by slightly over modulating the overlapping signals of the dating and interfering radical centers. The interfering peak in some of the fossil tooth enamel samples appears to arise from a slight structural deformation of the radical center in hydroxyapatite. The age of the measured fossil teeth sample was determined to be about 1400 years old.

CHAPTER 1

INTRODUCTION

EPR and ENDOR Theories

Radicals and paramagnetic transition metal complexes widely exist in nature.^[1,2]

One common characteristic of them is that there is one or more unpaired electrons in each molecule. Thus, there is a net electron spin angular momentum. In a strong magnetic field, the degenerate energy levels of the electron spin are separated. When a sample is irradiated with electromagnetic radiation of appropriate energy (RF, microwave or IR) and the incident energy matches the difference in spin energy levels, a transition occurs between the spin states of the electron. Electron paramagnetic resonance (EPR) spectroscopy is based on this principle. It is an irreplaceable method for studying radicals and transition metal complexes.

EPR spectroscopy measures the spin energy transitions of samples in a magnetic field. EPR spectra reflect the interactions of the unpaired electron with the host atom as well as the surrounding atoms, and provide structural information about the spin center in molecules. When a sample is in a magnetic field, there exist various interactions, including electron spin-magnetic field, nuclear spin-magnetic field, electron spin-nuclear spin and nuclear quadrupole moment ($I > 1/2$)-gradient of the electric field. The corresponding Hamiltonian operator is as follows.^[3]

$$\mathcal{H} = \beta \mathbf{B} \cdot \mathbf{g} \cdot \mathbf{S} - g_N \beta_N \mathbf{B} \cdot \mathbf{I} + h \mathbf{S} \cdot \mathbf{A} \cdot \mathbf{I} + h \mathbf{I} \cdot \mathbf{Q} \cdot \mathbf{I} \quad 1.1$$

where β and β_N are the Bohr magneton and nuclear Bohr magneton, respectively, and \mathbf{B} is the applied magnetic field, \mathbf{g} a symmetric electron g-tensor, \mathbf{S} the electron spin angular momentum, g_N the nuclear g-tensor, \mathbf{I} the nuclear spin angular momentum, \mathbf{A} the hyperfine tensor, h Planck's constant, and \mathbf{Q} the quadrupole tensor.

The first term $\beta \mathbf{B} \cdot \mathbf{g} \cdot \mathbf{S}$ is the operator for the electron Zeeman energy. For isotropic samples and samples in liquid solutions where the anisotropy is averaged out by fast molecular rotation, \mathbf{g} becomes a scalar quantity. Thus, the first term reduces to $g\beta \mathbf{B} \cdot \mathbf{S}$. When there is only one unpaired electron in the molecule, $S = 1/2$, and in the absence of other interactions, the electron spin orientates along the applied magnetic field. The energy associated with the first term becomes $\pm 1/2 g\beta B$.

The second term $g_N \beta_N \mathbf{B} \cdot \mathbf{I}$ is the operator for the nuclear Zeeman energy. This term is analogous to the electron Zeeman energy except for the negative sign due to the positive charge of the nucleus. This term does not affect the EPR transition energies. It is usually omitted from the Hamiltonian equation for EPR.

$h \mathbf{S} \cdot \mathbf{A} \cdot \mathbf{I}$, the third term, is the operator for the interaction energy between the electron spin and the nuclear spin. \mathbf{A} can be rewritten as a sum of two terms, $\mathbf{A} = A_0 \mathbf{1} + \mathbf{T}$, where A_0 is the isotropic hyperfine coupling, and $\mathbf{1}$, the unit tensor. The isotropic hyperfine coupling arises from the interaction of the nuclear moment with the magnetic field generated at the nucleus by the electron spin. The isotropic hyperfine coupling constant is,^[3]

$$A_0 = \frac{8\pi}{3} g\beta g_N \beta_N |\psi(0)|^2 \quad 1.2$$

where $\psi(0)$ represents the wave function of the unpaired electron evaluated at the nucleus. \mathbf{T} is the tensor for the anisotropic interactions, which comes from the dipolar coupling between the magnetic moments of the electron and the nucleus. The Hamiltonian for the dipolar interaction $\mathcal{H}_D = \hbar \mathbf{S} \cdot \mathbf{T} \cdot \mathbf{I}$ in expanded form is given by

$$\mathcal{H}_D = g \beta g_N \beta_N \left[\frac{\mathbf{S} \cdot \mathbf{I}}{r^3} - \frac{3(\mathbf{S} \cdot \mathbf{r})(\mathbf{I} \cdot \mathbf{r})}{r^5} \right] \quad 1.3$$

where r and \mathbf{r} are the distance and vector joining the unpaired electron and nucleus, respectively.

For the most commonly encountered case, where $B \ll B_{hf}$ (B is the applied magnetic field and B_{hf} is the magnetic field generated at the nucleus due to the unpaired electron orbital distribution), the hyperfine coupling Hamiltonian for an electron in a p orbital centered on the interacting nucleus is $-g_N \beta_N [B_{//} I_z + B_{\perp} I_x]$.

$$B_{//} = \frac{-\hbar m_S}{g_N \beta_N} \left[A_0 + B(3 \cos^2 \theta - 1) \right] \quad 1.4$$

$$B_{\perp} = \frac{-\hbar m_S}{g_N \beta_N} 3B \sin \theta \cos \theta \quad 1.5$$

where θ is the angle between \mathbf{r} and \mathbf{B} , and m_s is the spin quantum number of the unpaired

electron. B is given by

$$B = \frac{g\beta g_N \beta_N}{h} \left\langle \frac{3 \cos^2 \alpha - 1}{2r^3} \right\rangle \quad 1.6$$

where α is the angle between r and the axis of the p orbital.

The last term in Equation 1.1 is the quadrupole interaction energy, which needs to be taken into consideration when $I > 1/2$. The quadrupole interaction is the product of the nuclear quadrupole moment and the gradient of the electric field due to all surrounding electrons and nuclei. If there is a charge distribution in the bond between two atoms (e.g. a transition metal atom and a ligand atom), the gradient is nonzero. The magnitude of the quadrupole coupling is a measure of the electron distribution in the bond.

For a specific case, where $S = 1/2$ and $I = 1/2$, and both the g and the hyperfine coupling are isotropic, the Hamiltonian (eq. 1.1) reduces to

$$\mathcal{H} = g\beta \mathbf{B} \cdot \mathbf{S} - g_N \beta_N \mathbf{B} \cdot \mathbf{I} + hA_0 \mathbf{S} \cdot \mathbf{I} \quad 1.7$$

When the magnetic field is in the z -axis direction, $\mathbf{B} = B_z \mathbf{z} = B \mathbf{z}$, and with $S_+, S_- = S_x \pm iS_y$, $I_+, I_- = I_x \pm iI_y$, then Equation 1.7 can be rewritten as

$$\mathcal{H} = g\beta B S_z - g_N \beta_N B I_z + hA_0 S_z I_z + 1/2 hA_0 (S_+ I_- + S_- I_+) \quad 1.8$$

When the hyperfine coupling is small compared to the electron Zeeman interaction, the term $1/2 hA_0 (S_+ I_- + S_- I_+)$ can be treated as perturbation. The eigenvalues for the splitting

levels in the magnetic field to second order are given by Equation 1.9.

$$E(m_S, m_I) = g\beta B m_S - g_N \beta_N B m_I + h A_0 m_S m_I + \left| \frac{m_S - m_I}{m_S} \right| \frac{m_S h A_0^2}{4 g \beta B} (I(I+1) - m_I^2) \quad 1.9$$

The second order term can be omitted at high magnetic field, such as in Q-band spectroscopy or when A_0 is small. The energy level diagram (to first order) from Equation 1.9 is displayed in Figure 1.1.^[4]

There are six possible transitions in the four-level system, but only two EPR transitions are allowed by the selection rule $\Delta M_S = \pm 1$, $\Delta M_I = 0$, (1 \rightarrow 3, 2 \rightarrow 4), and only two NMR transitions are permitted by the selection rule $\Delta M_I = \pm 1$, $\Delta M_S = 0$, (1 \rightarrow 2, 3 \rightarrow 4). If the incident microwave frequency is constant and the magnetic field is scanned, we see two peaks in the cw-EPR spectrum. One occurs at B_1 in the equation

$$h\nu = g\beta B_1 - \frac{1}{2} h A_0 - \frac{h A_0^2}{4 g \beta B_1} \quad 1.10$$

The other is at B_2 in the equation

$$h\nu = g\beta B_2 + \frac{1}{2} h A_0 - \frac{h A_0^2}{4 g \beta B_2} \quad 1.11$$

When A_0 is small, the term $h A_0^2 / 4 g \beta H$ can be neglected, and we combine Equations 1.10 and 1.11 to obtain

$$h\nu = 1/2 g\beta (B_1 + B_2) \quad 1.12$$

By measuring the microwave frequency and the two resonant magnetic fields, we can calculate the g value of the sample. Even if we cannot ignore the second-order term, the g value can be calculated by the computer program in Appendix E. In the same way, the hyperfine coupling constant A_0 can be obtained from the expression

$$g\beta(B_1 - B_2) = hA_0 + \frac{hA_0^2}{4g\beta} \left(\frac{1}{B_1} - \frac{1}{B_2} \right) \quad 1.13$$

When A_0 is small or B is large, A_0 is given by:

$$A_0 = g\beta(B_1 - B_2)/h \quad 1.14$$

Otherwise, we need to use the computer program which corrects for second order effects to determine A_0 .

EPR spectroscopy provides useful information about the paramagnetic center. Nevertheless, in most complexes, such as ferritin iron nitrosyl and copper *cis,cis*-1,3,5-triaminocyclohexane chloride, the hyperfine splittings from the interactions between the electron spin and the neighboring nuclei (proton or nitrogen nuclei) are not distinguishable. This lack of resolution is due to the broad width of the EPR lines and the relatively weak interaction of the electron with the nucleus. We can overcome this obstacle either by scanning the samples at lower frequencies to narrow the EPR peak width, such as at S-band (2-4 GHz) or L-band (1-2 GHz), or by running ENDOR

(electron nuclear double resonance) on the samples.

Usually, ENDOR is required to resolve hyperfine lines and thus obtain hyperfine couplings, to identify the interacting nucleus from its nuclear g_N factor, or to measure the quadrupole couplings in systems with $I \geq 1$. ENDOR detects the NMR transitions via the intensity change of a simultaneously measured EPR transition. In practice, we set the magnetic field at an EPR line of interest where the microwave energy is absorbed. The absorbed microwave energy is released through the spin-spin and spin-lattice relaxation channels. This system eventually reaches equilibrium. By irradiating the sample with a scanning radio frequency, we can introduce NMR transitions. These NMR transitions interrupt the equilibrium state mentioned above, and cause an intensity variation in the EPR transition. This variation in the EPR signal versus the radio frequency constitutes an ENDOR spectrum. To first order, when the Larmor frequency of the nucleus is less than one half of the hyperfine coupling, the ENDOR signals appear at

$$\nu_{n1} = \left| \frac{A}{2} - \frac{g_N \beta_N B}{h} \right| = \left| \frac{A}{2} - \nu_0 \right|$$

and

$$\nu_{n2} = \left| \frac{A}{2} + \frac{g_N \beta_N B}{h} \right| = \left| \frac{A}{2} + \nu_0 \right|$$

where $\nu_0 = g_N \beta_N B/h$. When $A/2 < \nu_0$, $A = \nu_{n1} - \nu_{n2}$, and $\nu_0 = \frac{1}{2} (\nu_{n1} + \nu_{n2})$. Otherwise, when $A/2 > \nu_0$, $A = \nu_{n1} + \nu_{n2}$, and $\nu_0 = \frac{1}{2} (\nu_{n1} - \nu_{n2})$. Thus, by measuring the ENDOR lines,

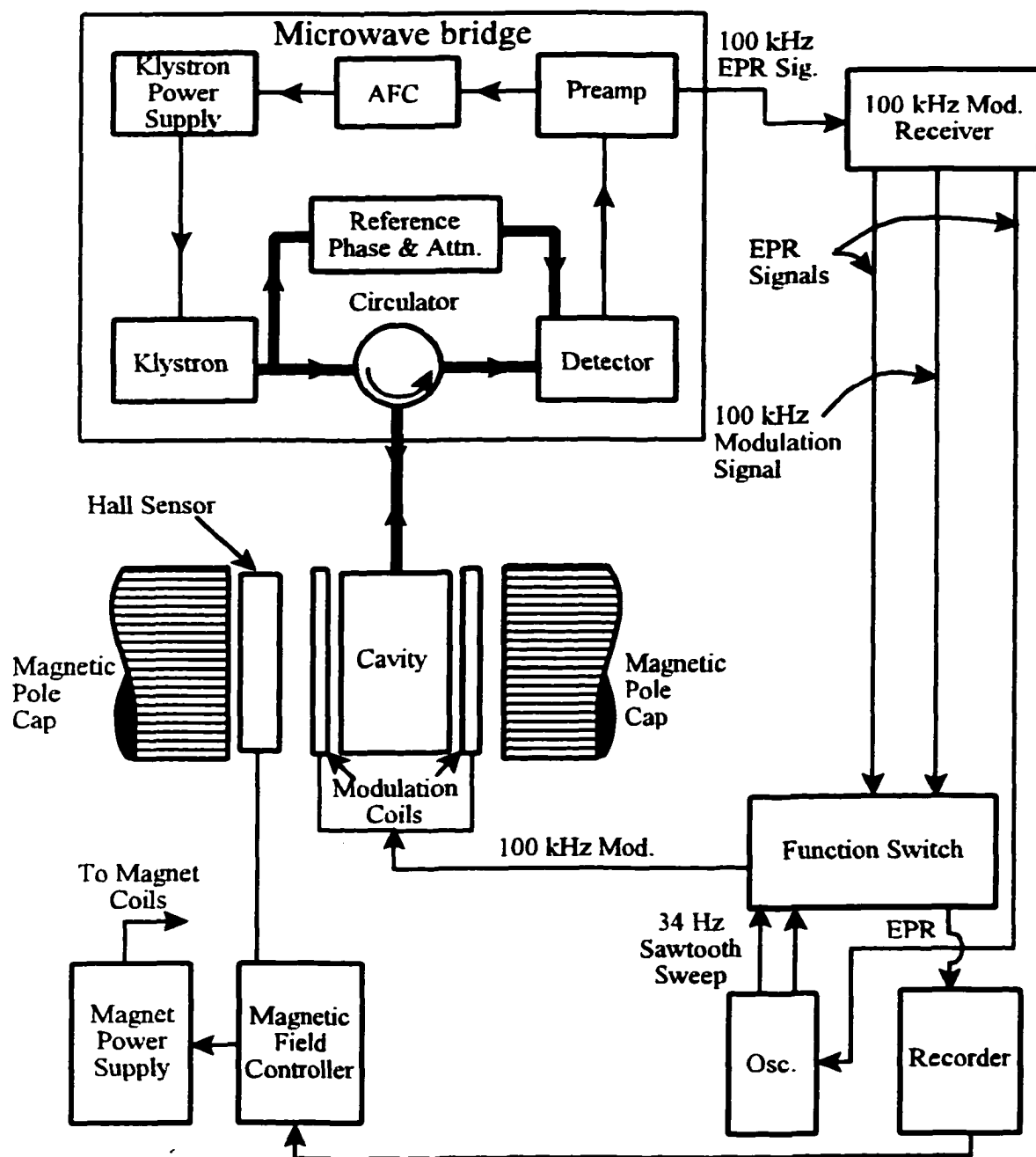


Figure 1.2 The schematic diagram of a typical X-band EPR spectrometer.

we can calculate both the nuclear g_N -values and the hyperfine coupling constants.

The optimum value of the microwave magnetic field B_{1e} for the steady-state ENDOR experiment is^[5]

$$\gamma_e^2 B_{1e}^2 T_1 T_2 \geq 1$$

Here γ_e is the magnetogyric ratio of the electron, B_{1e} is the amplitude of the microwave magnetic field, T_1 is the electron spin-lattice relaxation time, and T_2 is the electron spin-spin relaxation time.

EPR and ENDOR Instrumentation

The EPR signal derives from the reflected microwave radiation from the probe or cavity, in which the sample undergoes the resonant absorption during a sweep of the static magnetic field. Normally, an EPR spectrometer has four parts: the microwave source pumping energy to the sample, the circuit generating the static magnetic field, the cavity holding the sample and storing the microwave energy and the detection system collecting the EPR signal. Figure 1.2 is the block diagram of a typical X-band EPR spectrometer.^[6]

The microwave radiation generated from the klystron goes through an isolator protecting the klystron from reflected microwave energy, an attenuator controlling the microwave power irradiating the sample, a circulator directing the microwaves in one direction of the circuit loop, and finally the cavity. The reflected microwave energy from the cavity reaches the detector through the circulator. The microwave source is modulated by a 70 kHz oscillator circuit, so that the detected 70 kHz electrical signal from the detector is used to lock the spectrometer at the resonant frequency of the cavity. This

function is the auto-frequency-control (AFC).

The static magnetic field is generated electrically by a magnet power supply and electromagnets, and controlled by the field scan drive. This system provides a stable, uniform, reproducible and linearly varied magnetic field over the sample volume. The magnetic field is modulated at 100 kHz by a Helmholtz coil. This modulation is essential for the first derivative EPR signal detection.

The rectangular cavity for X-band usually operates in the TE_{102} mode for single cavity or TE_{104} mode for dual cavity. The cylindrical Q-band cavity is usually in the TE_{110} mode. The mode of the cavity permits a high-energy density, allows the placement of the sample at the maximum magnetic field of the standing microwave energy, and has the microwave magnetic component perpendicular to the static magnetic field. The microwave power is coupled into the cavity by the coupler. The merit of cavity is represented by the Q value, which is defined as^[7]

$$Q = \frac{2\pi \text{ (maximum microwave energy stored in the cavity)}}{\text{energy dissipated per cycle}}$$

The Q value is also defined as

$$Q = \frac{\nu_r}{\Delta \nu}$$

where ν_r is the resonant frequency of the cavity and, $\Delta \nu$, the width of the frequency (the difference of the frequency values at the half-power point). The higher the Q value, the

more sensitive the EPR spectrometer. When putting a quartz sample tube in the cavity, the resonant wavelength tends to increase. This is due to the quartz material, which has a refractive index of 1.46, hence a longer traveling length for the microwave transmission.

The detection system consists of a diode detector, preamplifier, 100 kHz amplifier, phase detection circuit and recorder. The first-derivative of the absorption signal is obtained by properly modulating the magnetic field. A personal computer is used to collect data.

For an ENDOR spectrometer, the third magnetic component, which is generated from the RF coil and powered by the radio frequency source, is perpendicular to both the static magnetic field and the microwave magnetic component. Insertion of a coil into the cavity deteriorates the cavity Q value. Generally speaking, an ENDOR spectrometer is less sensitive than an EPR spectrometer. In practice, the ENDOR spectrum is acquired by setting the magnetic field at an EPR resonant position, and the microwave energy is set high enough to partially or fully saturate the EPR signal. Then the radio frequency is scanned and the change in resonant absorption of the EPR signal measured. The ENDOR signal is also collected by the computer.

ENDOR signals can be more readily obtained at low temperature (liquid nitrogen and liquid helium) than at room temperature. The samples tested in my experiments were usually obtained at liquid helium temperature (about 2.5 K). The cryostat system for the X-band ENDOR spectrometer was made by Cryo Industries of America, Inc.. The operation and schematic diagram of the liquid helium system are given in Appendix B.

Applications of EPR/ENDOR Spectrometers to Transition Metal Complexes and Radicals

EPR/ENDOR spectroscopy is a powerful tool for studying chemical systems with unpaired electrons.^[8-12] The g -values of a paramagnetic system reflect the spin-orbit interaction and the symmetry of the system. For example, a system with two g -values, g_{\parallel} and g_{\perp} , has axial symmetry. But one with three different g -values, g_x , g_y and g_z , has a rhombic symmetry. The hyperfine splitting patterns, on the other hand, is determined by the nuclei around the central metal ion. Detailed structural information can be obtained from ENDOR spectroscopy. Proton and nitrogen ENDOR spectra are normally collected to distinguish the different proton and nitrogen atoms in a transition metal complex and to estimate the distances between the central metal ion and the surrounding proton and nitrogen atoms.

By monitoring the EPR signal amplitude, we can study the kinetics of a reaction system, so as to deduce the mechanism of that system. In conjunction with UV-Vis spectroscopy, the bonding parameters (molecular orbital coefficients) for the metal complexes can be determined.

Another application of EPR spectroscopy is the dating of fossil teeth. The radicals in a fossil are generated by γ -ray irradiation. By artificially irradiating the fossil tooth sample with a controlled dose and recording the EPR signal amplitude growth, one can extrapolate back in time to estimate the date of the fossil tooth.

The modification of the Q-band spectrometer and the improvement of the X-band ENDOR spectrometer are presented in Chapter 2 and Chapter 3, respectively. Studies of ferritin iron nitrosyl and model complexes are given in Chapter 4 including the proton

ENDOR spectra analysis and the complex modeling. Chapter 5 focuses on the structural characteristics of copper *cis,cis*-1,3,5-triaminocyclohexane chloride complexes investigated by EPR, ENDOR and optical spectroscopies. Q-band EPR studies of the fossil teeth samples are presented in the last chapter. The ultimate goal of this research project is to deepen our insight into the structure of transition metal complexes with improved EPR/ENDOR spectrometers.

CHAPTER 2

MODIFICATION OF Q-BAND MICROWAVE BRIDGE

The Q-band (35 GHz) spectrometer in our laboratory was constructed with a Varian E110 microwave bridge, a Varian E-line console, a Harvey-Wells magnet, a Magnion power supply and a home-made cylindrical TE 011 cavity. This spectrometer worked fine on most of chemical samples. However, the signal/noise ratio of the Varian E110 microwave bridge was often too low for biological sample studies due to the relatively high noise level of the klystron. In addition, the microwave bridge does not have a microwave outlet for a frequency counter which is essential for accurate g-value measurements. Finally, critical coupling of the cavity at low temperature was a problem because the original Varian coupler frequently broke when it was adjusted at low temperature. Therefore, several modifications were made to improve the performance of our Q-band spectrometer.

Installation of the Microwave Amplifier

Hyde and colleagues significantly improved the signal/noise ratio of their Varian Q-band microwave bridge by adding a low-noise GaAs field effect transistor microwave amplifier, a balanced mixer and a Gunn diode oscillator as the microwave source.^[13] In order to fully understand the modification they made, a schematic diagram of the original Varian Q-band microwave bridge is shown in Figure 2.1.

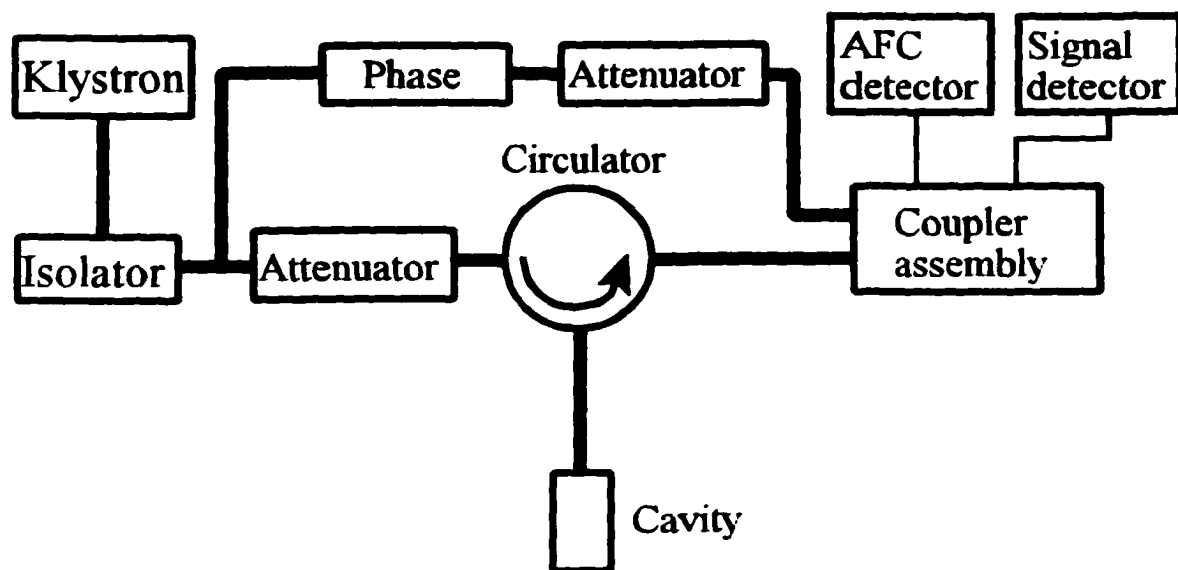


Figure 2.1 The schematic diagram of the Varian Q-band E110 microwave bridge.^[13]

The Q-band microwave bridge consists of the following major microwave components: klystron, isolator, directional coupler, attenuator, phase shifter, circulator, coupler assembly, AFC detector and signal detector. The microwave signal from the klystron transfers through an isolator and then splits into two signals when passing across the directional coupler. The major part of the split signal transfers through an attenuator, then across a three port circulator and finally into the sample cavity. The microwave containing the EPR signal from the sample is reflected out of the cavity, transfers through the circulator and enters the coupler assembly. The minor split signal from the directional coupler propagates through the reference arm phase shifter and an attenuator, then enters the coupler assembly where they are mixed. The mixed microwave signals are eventually rectified by two diode detectors.

Hyde and colleagues used a Gunn diode oscillator as a microwave source due to its lower noise level compared to a klystron. On the other hand, based on the fact that a microwave amplifier multiplies the microwave signal amplitude by a factor of 18 (25 db), but amplifies the noise by only a factor of 1.5 (3.5 db), they installed a microwave amplifier in their Q-band bridge. They also employed a balanced mixer to cut the phase noise from the reference arm. Figure 2.2 is the schematic diagram of Hyde's Q-band bridge after the modification. The dash line marked components in Figure 2.2 that were modified parts. As a consequence, a signal/noise improvement of 24.6 db or seventeen-fold was achieved.

In Hyde's modification, the major improvement of the signal/noise ratio arises from the insertion of the microwave amplifier. It is also the simplest modification that one

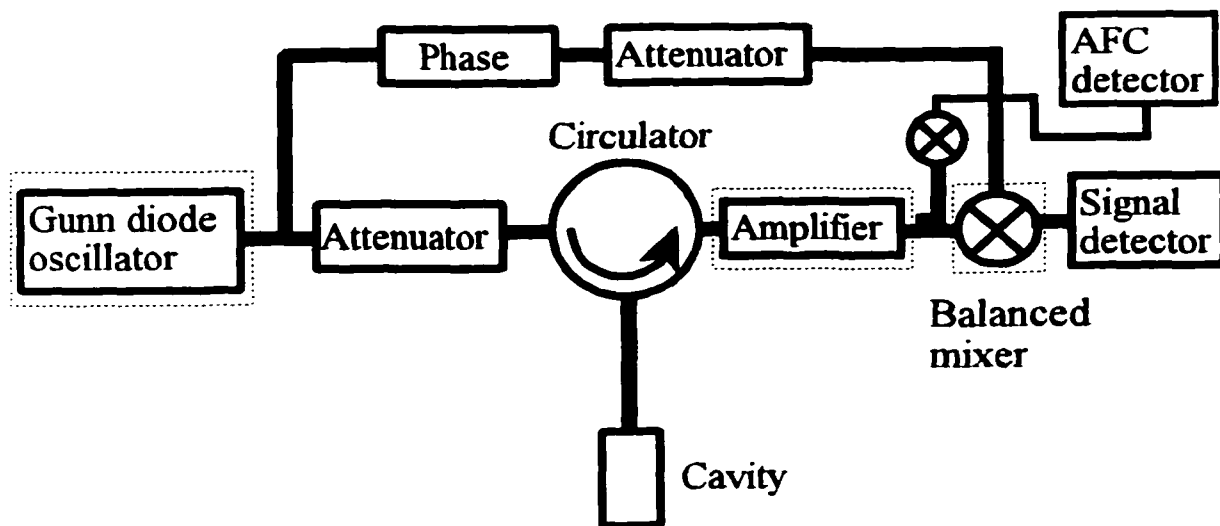


Fig. 2.2 The schematic diagram of modified Q-band microwave bridge by J. S. Hyde.^[13]
Altered or added components are highlighted by dashes lines.

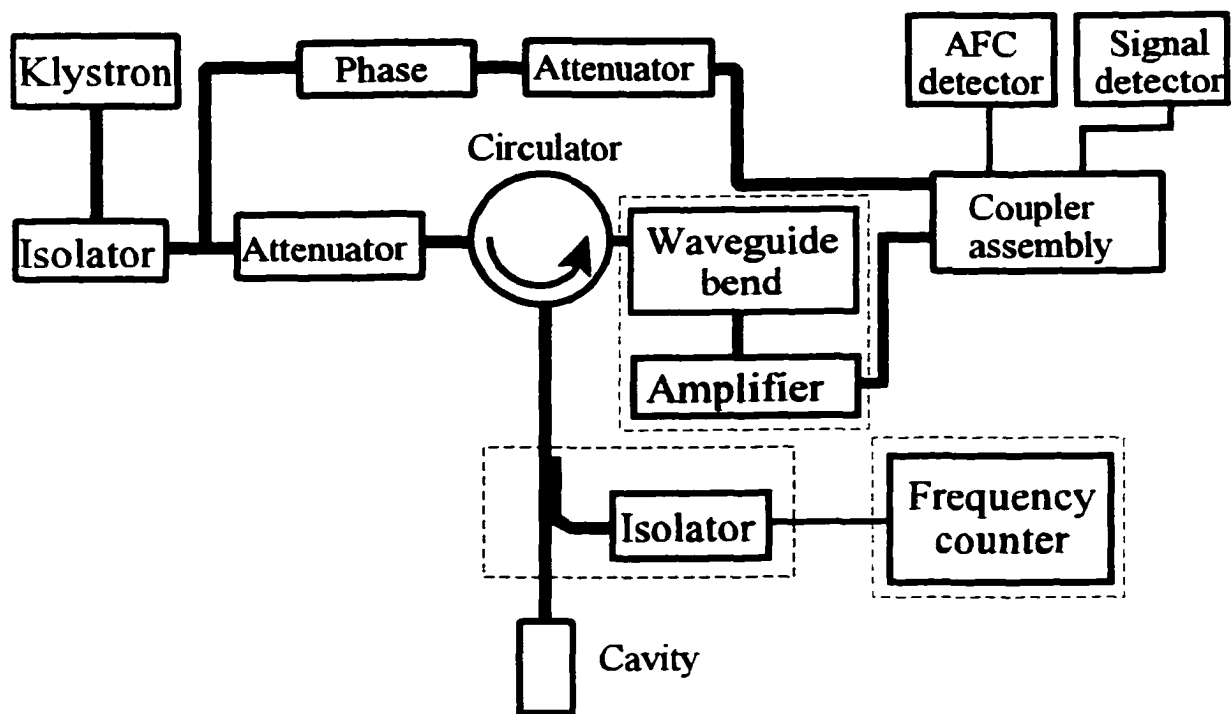


Fig. 2.3 The schematic diagram of the Varian E110 Q-band microwave bridge in the Chasteen laboratory after the modification. Added components are highlighted by dashed lines.

can make to the Varian E110 microwave bridge without major rearrangement of the components in the already crowded housing. Rationally, insertion of a microwave amplifier was an effective way for us to improve the signal /noise ratio of our Q-band spectrometer. Figure 2.3 shows the schematic diagram of our Varian E110 Q-band bridge after the modification. The practical problem was that there was limited space in the bridge. A waveguide bend was needed to fit everything in place. So, a special microwave bend was designed and machined to serve this purpose as shown in Figure 2.4. All the waveguide components used in this bend were made of unfinished copper alloy, and were purchased from Microwave Development Laboratories, Inc. (Needham Heights, MA), including two H-bends (28BH11), two E-bends (28BE11), two flanges (F28BBC) and several pieces of waveguide tubing (WR28). The waveguide tubing was cut into five pieces of different lengths: 23.9, 8.4, 34.4, 8.4 and 41.9 mm, respectively. All these components were soldered together at the Space Center machine shop of the University of New Hampshire. The assembled waveguide bend is shown in Figure 2.4.

The microwave amplifier (QLN-3635-AA) was purchased from Quinstar Technology, Inc. (Torrance, CA), which has a maximum of 3.5 dB noise gain and 25 dB signal gain. The amplifier required +15 V DC power which was generated by the +20 V power source (pin L on J1202) in the bridge (see Varian Technical Manual E110 Microwave Bridge circuit) and a voltage regulator UA7815UC (from Texas Instruments, Dallas, TX). The voltage regulator was installed by the previous technician, Dick Sweet.

When the amplifier was installed, the bend-assembly was first fixed onto the input port of the microwave amplifier. Then the coupler assembly (see Figure 2.1) was taken

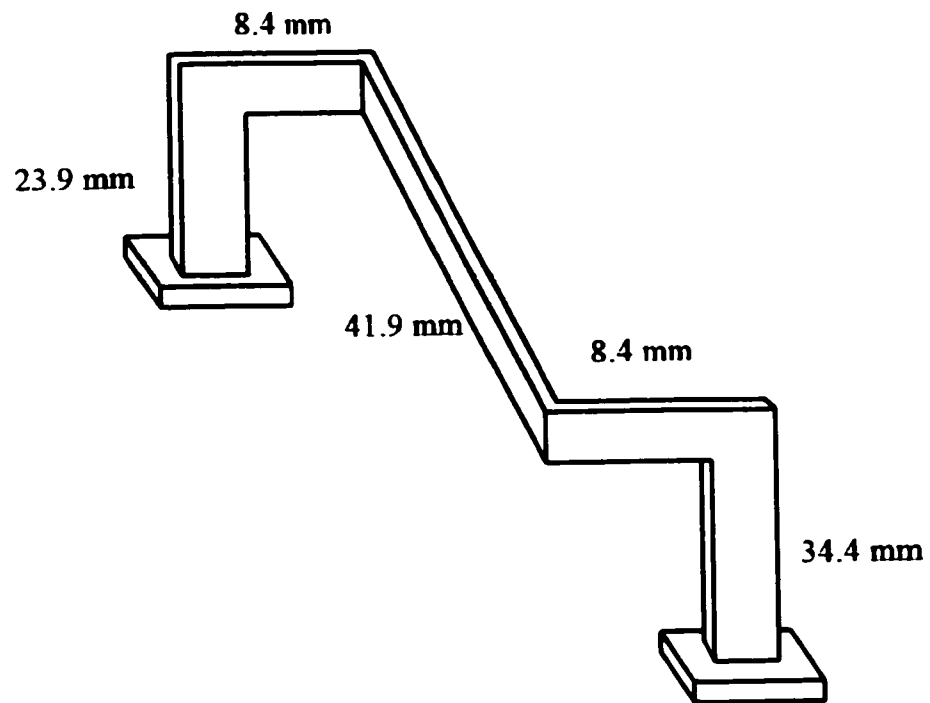


Figure 2.4 The schematic diagram of the specific microwave bend.

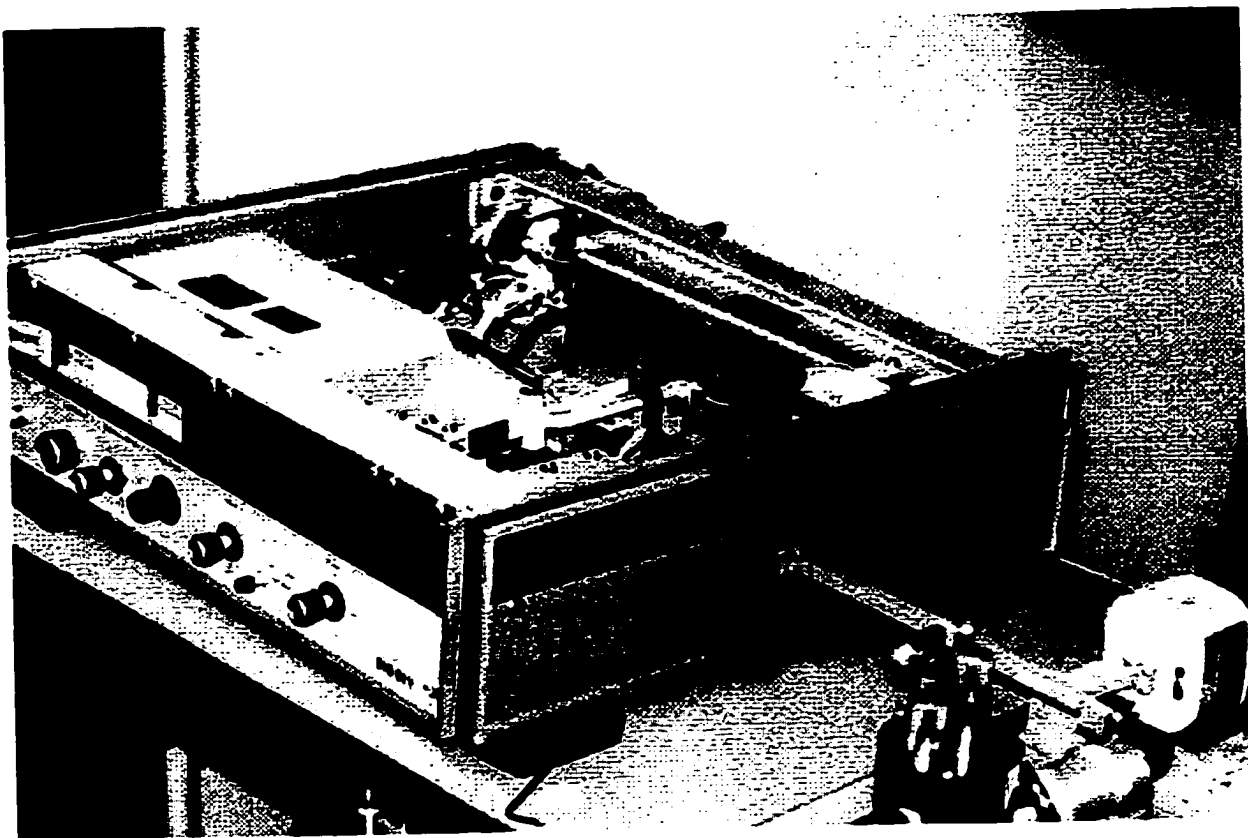


Figure 2.5 The photo of the Varian Q-band microwave bridge after the modifications.

off the circulator and tightened to the outlet of the microwave amplifier. Finally, the second flange of the bend-assembly was fixed to the circulator port. All the components nest snugly in the bridge case. Figure 2.5 shows the Q-band microwave bridge after the installation of the microwave amplifier.

The signal-to-noise ratio was calculated by Equation 2.1 using a 1 s time constant for the measurement.^[14]

$$S/N \cong 2.5 \times \frac{\text{peak-to-peak value of signal voltage}}{\text{peak-to-peak value of noise voltage}} \quad 2.1$$

The S/N of the weak pitch samples was significantly improved after installation of the microwave amplifier. Figure 2.6 displays the EPR signal and the noise spectra of the weak pitch standard sample before and after the modifications. Without the amplifier, the S/N increases and then decreases with decreasing attenuation (see Figure 2.7A, curve A). The maximum S/N was 10.0/1 at 10 db attenuation. After installing the microwave amplifier, the S/N achieved a maximum of 65/1 at 13 db (see curve B in Figure 2.7A) or an improvement of 6.5-fold.

Installation of the Microwave Frequency Counter

The frequency displayed on the frequency dial of the microwave bridge is only approximate. A Q-band frequency counter was therefore needed. Unfortunately, there is no microwave output port on the bridge for connecting a counter. One way to solve this problem is to put a directional coupler between the circulator and the cavity. A 20 db coupler (R752D) was purchased from Lectronic Research Labs. Inc., Camden, NJ.

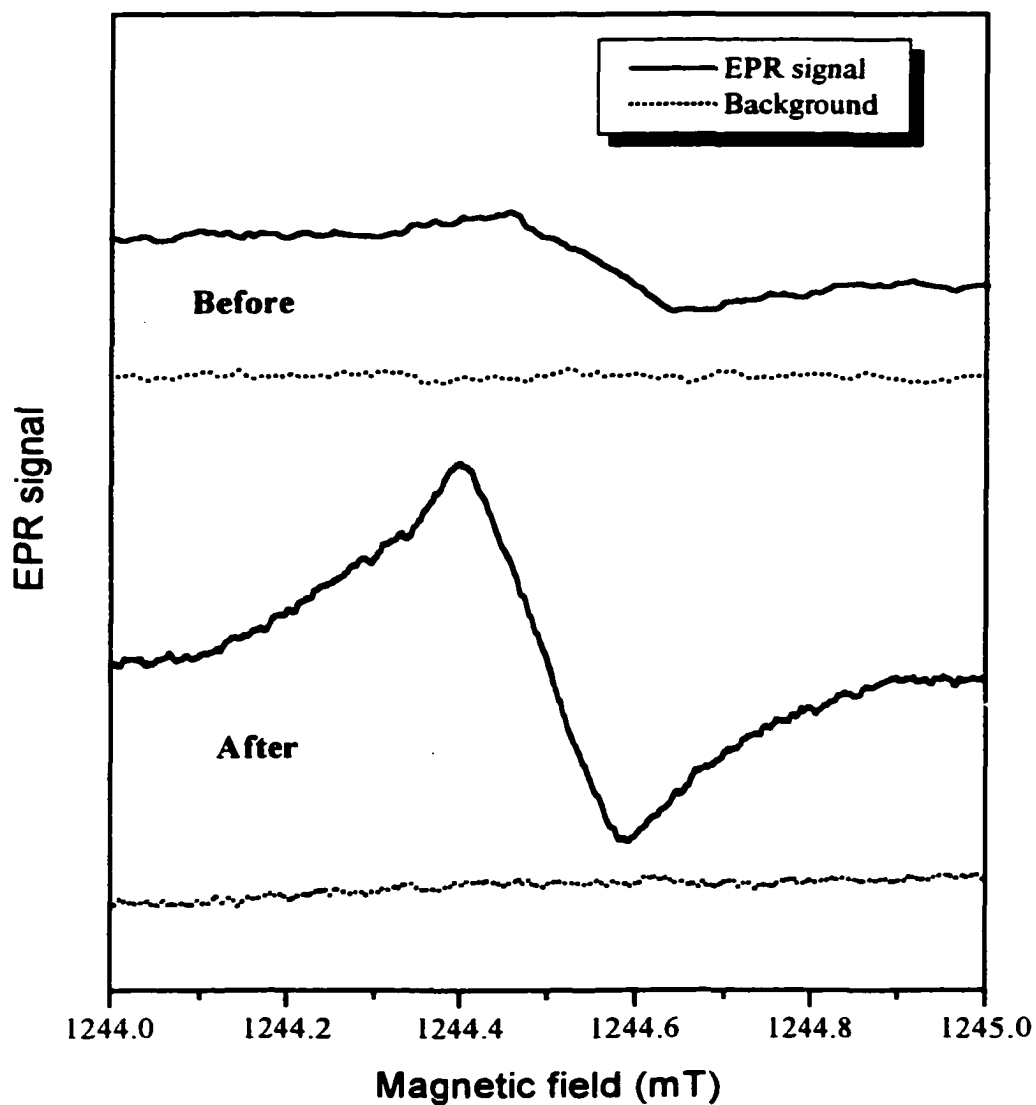


Figure 2.6 The EPR signal and the background spectra of the weak pitch standard sample before and after the modifications (without the directional coupler).

Before the modifications, Experimental Conditions: Signal, Field Set, 1244.6 mT; Scan Range, 1 mT; Modulation Frequency, 100 kHz; Modulation Amplitude, 0.4 mT; Microwave

(continued)

power, 12 dB, 3.8 mW; Microwave frequency, 34.82 GHz; Receiver Gain, 5000; Time Constant, 1 s; Scan Time, 4 minutes; Temperature, 298 K; Spectrometer, Q-band EPR/ENDOR; File Name, 97040727.fl; background, Field Set, 1234.6 mT; Scan Range, 0 mT; Modulation Frequency, 100 kHz; Modulation Amplitude, 0.4 mT; Microwave power, 12 dB, 3.8 mW; Microwave frequency, 34.82 GHz; Receiver Gain, 5000; Time Constant, 1 s; Scan Time, 4 minutes; Temperature, 298 K; Spectrometer, Q-band EPR/ENDOR; File Name, 97040728.fl.

After the modifications (without the directional coupler), Experimental Conditions: Signal, Field Set, 1242.9 mT; Scan Range, 1 mT; Modulation Frequency, 100 kHz; Modulation Amplitude, 0.4 mT; Microwave power, 12 dB, 3.8 mW; Microwave frequency, 34.819 GHz; Receiver Gain, 5000; Time Constant, 1 s; Scan Time, 4 minutes; Temperature, 298 K; Spectrometer, Q-band EPR/ENDOR; File Name, 99101901.fl; background, Field Set, 1232.9 mT; Scan Range, 0 mT; Modulation Frequency, 100 kHz; Modulation Amplitude, 0.4 mT; Microwave power, 12 dB, 3.8 mW; Microwave frequency, 34.819; Receiver Gain, 5000; Time Constant, 1 s; Scan Time, 4 minutes; Temperature, 298 K; Spectrometer, Q-band EPR/ENDOR; File Name, 99101902.fl.

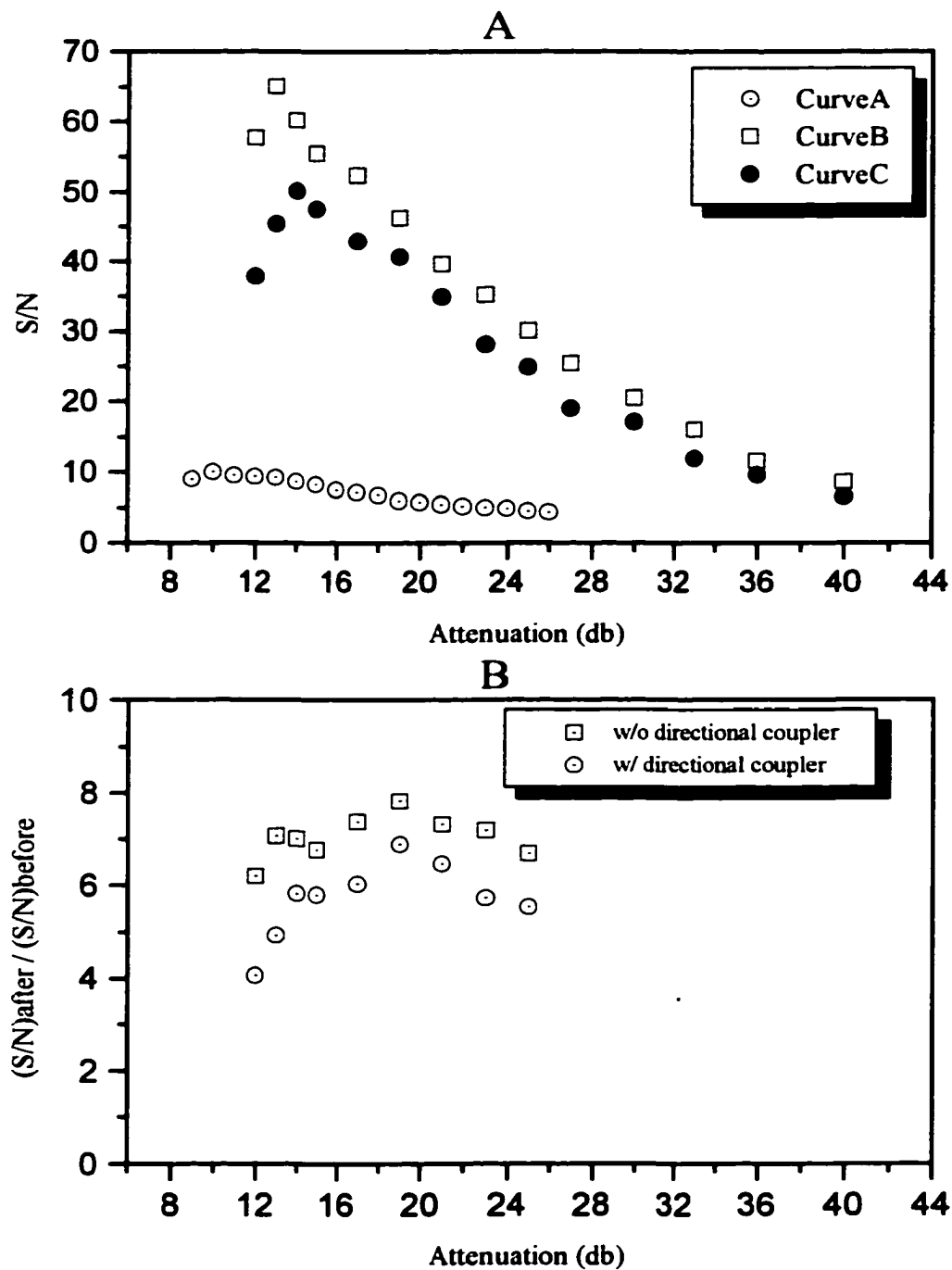


Figure 2.7 The S/N ratio of weak pitch sample versus the attenuation before and after the

(continued)

modification. CurveA: without any modifications; File Name, 97040723.flx ~ 97040746.flx, 97041001.flx ~ 97041016.flx; CurveB: after insertion of the amplifier; File Name, 99101901.flx ~ 99101928.flx; CurveC: after insertion of the amplifier and the directional coupler. File Name, 99101801.flx ~ 99701828.flx;

Before the modifications, Experimental Conditions: Signal, Field Set, 1244.6 mT; Scan Range, 4 mT; Modulation Frequency, 100 kHz; Modulation Amplitude, 4 mT; Microwave frequency, 34.82 GHz; Receiver Gain, 5000; Time Constant, 1 s; Scan Time, 4 minutes; Temperature, 298 K; Spectrometer, Q-band EPR/ENDOR; background, Field Set, 1234.6 mT; Scan Range, 0 mT; Modulation Frequency, 100 kHz; Modulation Amplitude, 0.4 mT; Microwave frequency, 34.82; Receiver Gain, 5000; Time Constant, 1 s; Scan Time, 4 minutes; Temperature, 298 K; Spectrometer, Q-band EPR/ENDOR.

After the modifications (without the directional coupler), Experimental Conditions: Signal, Field Set, 1242.9 mT; Scan Range, 4 mT; Modulation Frequency, 100 kHz; Modulation Amplitude, 0.4 mT; Microwave frequency, 34.819 GHz; Receiver Gain, 500; Time Constant, 1 s; Scan Time, 4 minutes; Temperature, 298 K; Spectrometer, Q-band EPR/ENDOR; background, Field Set, 1232.9 mT; Scan Range, 0 mT; Modulation Frequency, 100 kHz; Modulation Amplitude, 0.4 mT; Microwave frequency, 34.819; Receiver Gain, 500; Time Constant, 1 s; Scan Time, 4 minutes; Temperature, 298 K; Spectrometer, Q-band EPR/ENDOR.

After the modifications (with the directional coupler), Experimental Conditions: Signal, Field Set, 1242.9 mT; Scan Range, 4 mT; Modulation Frequency, 100 kHz; Modulation Amplitude, 0.4 mT; Microwave frequency, 34.819 GHz; Receiver Gain, 500; Time Constant, 1 s; Scan Time, 4 minutes; Temperature, 298 K; Spectrometer, Q-band EPR/ENDOR; Background, Field Set, 1232.9 mT; Scan Range, 0 mT; Modulation Frequency, 100 kHz; Modulation Amplitude, 0.4 mT; Microwave frequency, 34.819; Receiver Gain, 500; Time Constant, 1 s; Scan Time, 4 minutes; Temperature, 298 K; Spectrometer, Q-band EPR/ENDOR;
(S_TO_N WITH AMP&COUNTER.OPJ)

However, it was discovered that the purchased Q-band frequency counter EIP model 548A (from EIP Microwave, Inc., San Jose, CA) sent out microwave signal which passed back through the directional coupler and was picked up by the EPR signal detector. As a consequence, a 27 db isolator KA-13-11 (Cascade Research Division of Huggins Labs., Inc., Sunnyvale, CA) had to be connected to the coupled port on the directional coupler. The output of the isolator is hooked up to a diode which rectifies the microwave signal. The rectified signal is finally sent to the frequency counter. Due to the low signal intensity at the branch port of the installed directional coupler, the microwave counter only works when the microwave bridge is set below 30 db attenuation during the spectral scan. The frequency counter can be left on while scanning a spectrum providing the microwave power is higher than 0.06 mW (or lower than 30 dB attenuation). If the spectrometer works at 0.06 mW or lower power, the power should be raised above 0.06 mW until the frequency counter is triggered. After recording the frequency, the counter should be powered off and the spectrometer power should be returned to the operating power. The counter displays the frequency automatically after turning on the power of the counter and pushing the buttons of "band", "4" and "1" sequentially.

After the installation of the directional coupler (see Figure 2.3), the S/N deteriorates by 18.3% compared to that without the directional coupler. The S/N versus microwave power is also presented in Figure 2.7A (curve C). It has a maximum of 50.0 at 14 db. The overall S/N after all of the above bridge modifications is increased by a factor of 4.9 at 13 db.

Figure 2.7B shows the S/N improvements after the insertion of the amplifier and

the directional coupler. The circle marked data were from $(S/N)_{\text{after}} / (S/N)_{\text{before}}$ with only the amplifier installed. The $(S/N)_{\text{after}} / (S/N)_{\text{before}}$ with both amplifier and directional coupler installed are marked with squares. Excluding the data at higher microwave power (lower attenuation) where the improvements after these modifications were poor, we averaged the rest data over the ranges of 13db~25db and 14db~25db for the two sets of data in Figure 2.7B. The results showed that after the installation of the amplifier, the S/N was improved by a factor of 7.1 in our test attenuation range. Whereas, in the presence of the directional coupler for the frequency counter, the S/N was improved by a factor of 6.0.

Replacement of the Magnetized RF Coaxial Cables

The Q-band spectrometer had a large noise source which was believed not to come from the microwave bridge itself. Attention was drawn to the sample cavity and the stability of the long waveguide (about one meter in length), which connects the cavity to the bridge circulator. After the Dewar and the modulation coil were disassembled, the cavity was visible between the magnet pole caps. When the magnetic field was increased, the cavity was seen to pull to one side of the magnet poles, indicating that something on the waveguide or cavity was magnetized. The torque generated by the scanning magnetic field produced the observed noise.

A compass was used to locate the magnetized part. It was found that the two RF cables running along the waveguide had become magnetized. Further investigation confirmed that the inner wires of the RF cables were magnetized, being made of silver plated steel wire. In order to eliminate the magnetization, semirigid RF cable assemblies

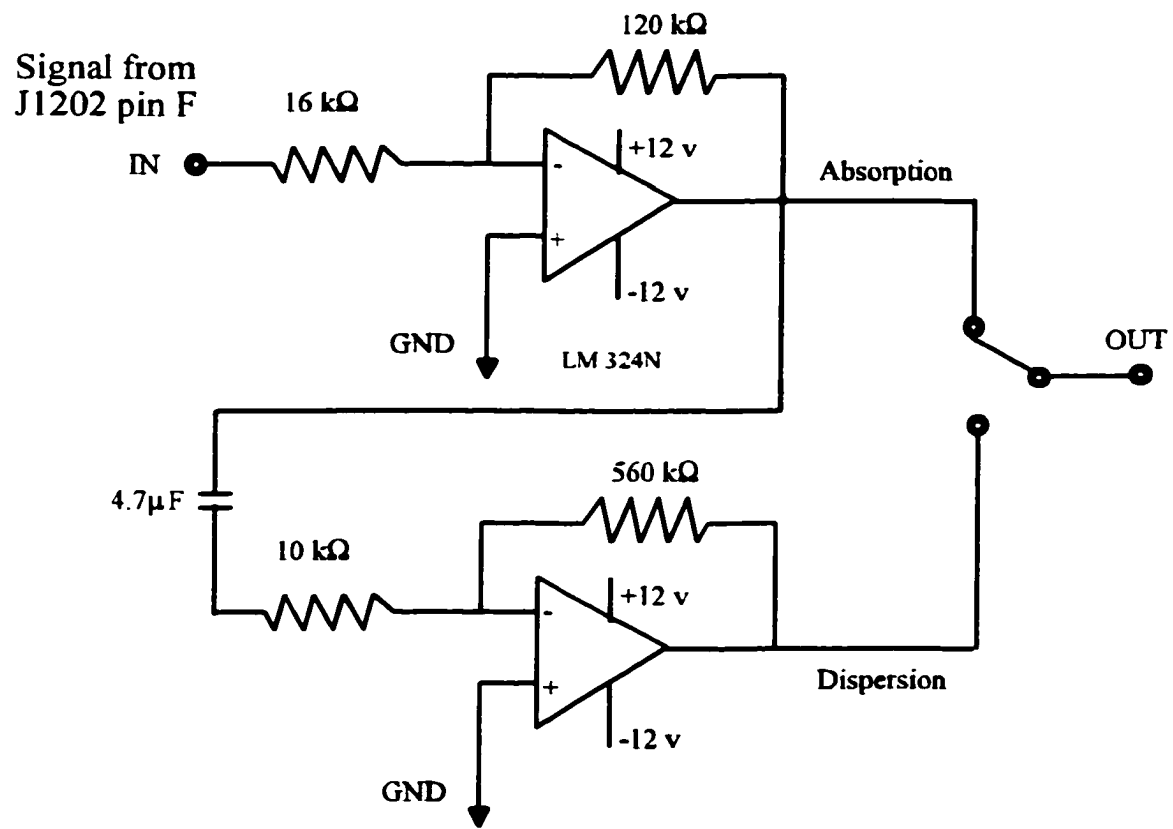


Figure 2.8 The circuit of the low gain amplifier used in Figure 2.9.

with copper inner wire (part # 145-01-45.6) were ordered from SSI Cable Corporation (Shelton, WA) and the original ones replaced, eliminating the noise.

Installation of the Line Conditioner

Increased noise was observed in the spectrometer plotter pen whenever the centrifuge in the adjacent lab was turned on and off. A line conditioner (SD180, Sola Electric Inc., NJ) was then installed. The line conditioner completely eliminated the interference from the centrifuge. However, no improvement in S/N was generally observed, suggesting that the house lines are not a significant source of noise for the spectrometer.

Installation of an Oscilloscope near the Microwave Bridge

As the E-line console was used to control both the X-band EPR/ENDOR and Q-band EPR/ENDOR spectrometers, the Q-band microwave bridge has to be relatively far away from the console. This physical arrangement made the tuning of the Q-band spectrometer an inconvenient two-person job. A second oscilloscope was therefore installed near the Q-band microwave bridge. A Hewlett-Packard oscilloscope module 1340A was used due to its large screen and single function. The X-axis scanning saw-tooth signal was taken from the console oscilloscope module (J201 pin F, GND and pin E, SWP), and the Y-axis signal was taken from the microwave bridge after the pre-amplifier (J1201 pin F, MOD SWP and pin E, GND. J1202 pin F and pin E were wired to J1201 pin F and pin E, respectively). In order to match the Y-signal from the preamp to the Y-

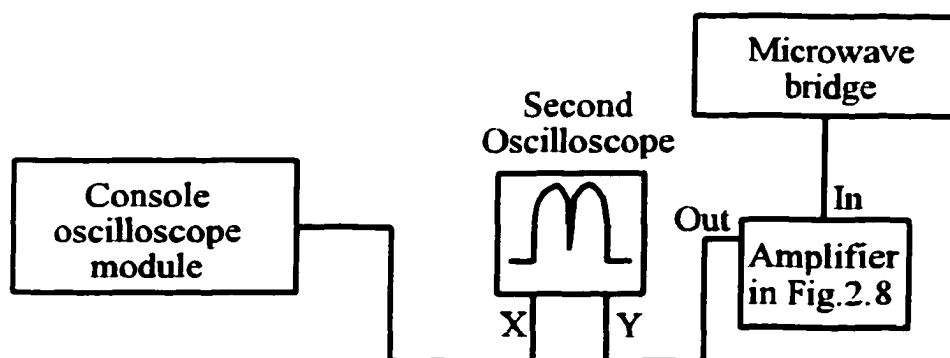


Figure 2.9 The schematic diagram for the second oscilloscope wiring

axis range of the oscilloscope, a simple low-gain amplifier (see circuit in Figure 2.8) was built.^[15] The schematic diagram of the wiring is displayed in Figure 2.9. After the set up of the second oscilloscope, the Q-band EPR/ENDOR spectrometer could be operated by one person only.

Innovation of a New Robust Coupler

The Varian E-110 microwave bridge and the cylindrical TE_{011} cavity are still widely used in Q-band cw-EPR and ENDOR spectroscopy. A robust yet sensitive ribbon-wound TE_{011} cylindrical cavity for Q-band EPR/ENDOR spectroscopy, capable of repeated temperature cycling down to 2 K, was developed by Wang and Chasteen.^[16] However, critical coupling of the cavity at low temperature has been a problem because the original Varian coupler frequently breaks when adjusted at low temperature. The difference in the thermal coefficients of expansion of Rexolite and stainless steel causes the

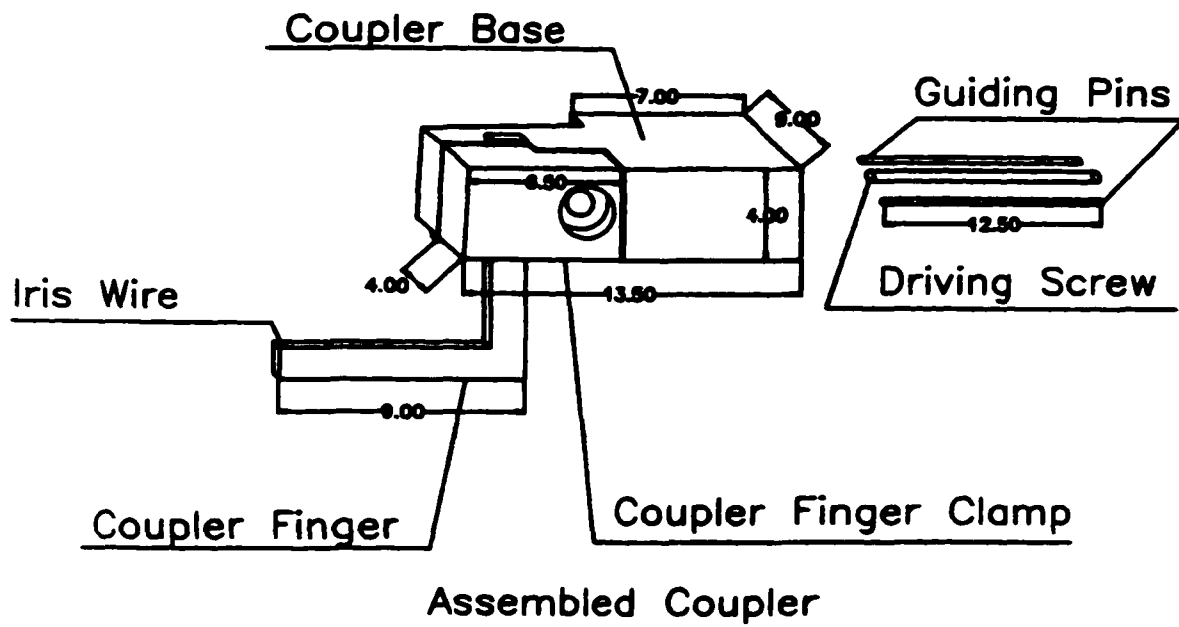
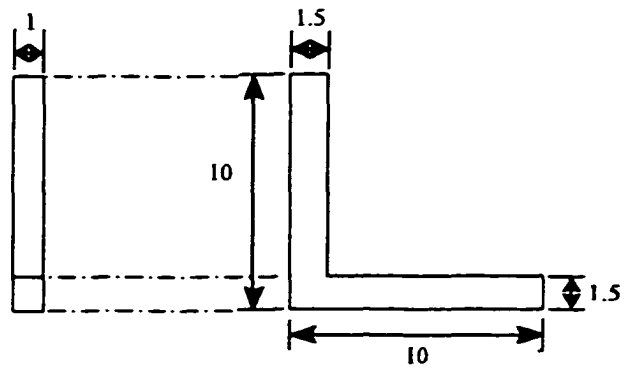


Figure 2.10 The diagram of the newly designed Q-band cavity coupler (units in mm).



The coupler finger

Material: Rexolite

Unit: mm

6/18/98

Figure 2.11c The mechanical drawing of the coupler finger.

threaded Rexolite coupler to grip the steel driving screw at low temperature. When adjusted, the fragile coupler finger tends to rotate laterally against the waveguide and snaps.

We have therefore designed a new coupler which is easy to machine, assemble and adjust (see Figure 2.10). The mechanical drawings of the coupler parts are shown in Figure 2.11a to Figure 2.11c. It consists of three parts: a coupler base, coupler finger clamp and coupler finger. The coupler base and coupler finger clamp are made of alloy 360 standard free-cutting brass which is free of magnetization. The coupler finger is made of Rexolite. The small protrusion on the bottom of the coupler base is designed to insert into the slot in the waveguide and guides the precise movement of the coupler base move back and forth. The Rexolite finger, if broken, is easily replaced.

The coupler is installed by first prying slightly the two guiding pins on the Varian waveguide and sliding the coupler base onto them. Then the coupler base is pushed slightly to one side and the coupler finger is inserted into the waveguide slot. The coupler base is released and the finger is inserted in the coupler base. Next, the coupler base is pushed toward the cavity. After adjusting the height of the finger so that its tip is centered in the opening at the top of the cavity, the finger is tightened in place by the screw. The positions of the guiding pins differ for some Varian waveguides, so the appropriate dimensions need to be checked before machining the coupler base.^[17]

Comparison of Performance Before and After the Modifications

Table 2.1 presents the improvements of our Q-band spectrometer after the

modifications. Hyde's results are also included in this table. After the installation of the microwave amplifier, the S/N improved by a factor of 7.1, which is almost as good as Hyde's 7.8 where he replaced his noisy klystron with a Gunn diode oscillator. When a directional coupler was used in the spectrometer (see Figure 2.3), the S/N reduced to 6.0. However, the benefit of the insertion of the directional coupler was obvious in that it enabled us to measure the exact cavity resonant frequency. This is crucial for measuring accurate g-values.

The further improvement Hyde attained by installing a balanced mixer was 2.2. This modification brought the total S/N improvement to 17.2-fold on his spectrometer. Accordingly, we can further improve the S/N of our Q-band spectrometer in the future by installing a balanced mixer.

A summary of the Q-band microwave bridge modifications, costs and sources is presented in Table 2.2.

Table 2.1 Comparison of the improvements after the modifications

Modifications	$(S/N)_{\text{after}} / (S/N)_{\text{before}}$	Reference
Amplifier alone	7.1 ¹	This work
Amplifier & directional coupler	6.0 ²	This work
amplifier & Gunn diode oscillator	7.8	Hyde's work
above & mixer	17.2	Hyde's work

1. Average among data in figure 2.6B except the point at 12 db.

2. Average among data in figure 2.6B except the point at 12 and 13 db.

Table 2.2 Summary of the modifications made on the Q-band spectrometer.

Device	Model number	Manufacturers	Cost
Microwave amplifier	QLN-3635-AA	Quinstar Technology, Inc., Torrance, CA	3,470.00
Directional coupler	R752D	Lectronic Research Labs, Camden, NJ	200.00
Coaxial RF cables	JS50141	Precision Tube Co. Inc., Salisbury, MD	150.00
Oscilloscope	HP 1340A	J. L. Stevenson Equipment Co., Hamilton, NJ	160.00
Waveguide bend	28BH11, 28E11, F28BBC, WR28	parts from MDL inc., Needham Heights, MA. Assembling at the Space Center machine shop of University of New Hampshire.	160.00
Frequency counter	548A	EIP Microwave Inc., San Jose, CA	4700.00
Isolator	KA-13-11	Huggins Labs., Inc., Sunnyvale, CA	800.00
Total			9,640.00

The EPR Spectra of Standard Samples in Absorption Mode and Dispersion Mode

One essential function for our Q-band EPR/ENDOR spectrometer is to operate in dispersion mode for the ENDOR experiment. After modification of the Q-band bridge, the spectrometer still works well in dispersion mode. Figure 2.12 shows the Q-band EPR spectra for two standard samples, Mn^{2+}/CaO and BDPA (α, γ -bisdiphenylene- β -phenylallyl), in both absorption and dispersion modes. The tuning of the Q-band spectrometer is the same as the unmodified spectrometer. The operation of the Q-band spectrometer at 100 K is described in Appendix A.

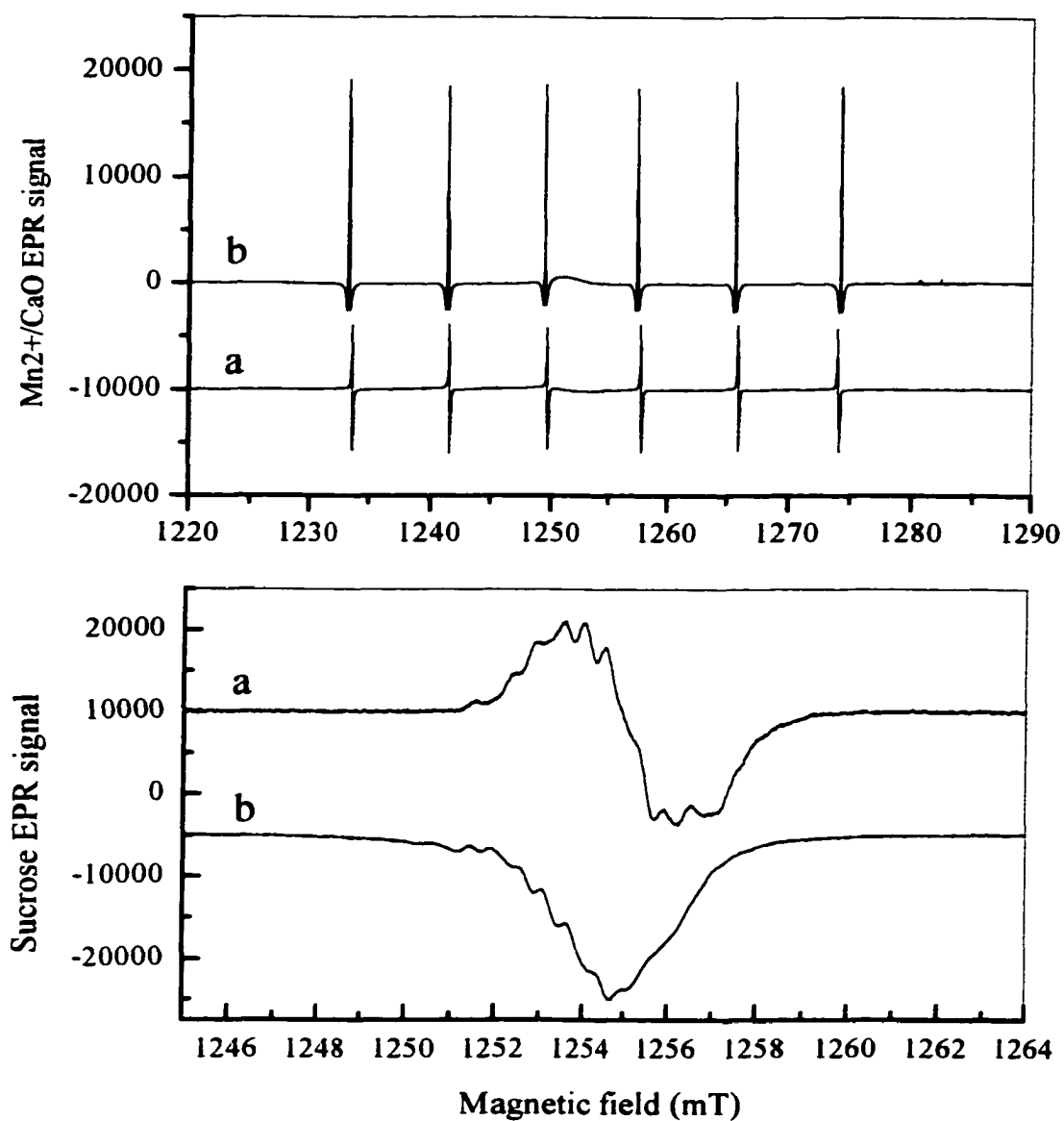


Figure 2.12 The EPR spectra of standard samples in both absorption (a) and dispersion (b) modes. Spectrometer settings: $\text{Mn}^{2+}/\text{CaO}$, Absorption Mode, Field Set, 1255 mT; Scan Range, 100 mT; Modulation Frequency, 100 kHz; Modulation Amplitude, 0.01 mT; Microwave power, 0.02 mW; Microwave Frequency, 34.901 GHz; Receiver Gain, 10; Time Constant, 1 s; Scan Time, 16 minutes; Temperature, 298 K; Spectrometer, Q-band

(continued)

EPR/ENDOR; File Name, 97080209.fl; Dispersion Mode, Field Set, 1255 mT; Scan Range, 100 mT; Modulation Frequency, 100 kHz; Modulation Amplitude, 0.05 mT; Microwave power, 0.06 mW; Microwave Frequency, 34.779 GHz, Receiver Gain, 4; Time Constant, 1 s; Scan Time, 30 minutes; Temperature, 298 K; Spectrometer, Q-band EPR/ENDOR; File Name, 97080207.fl;

Sucrose, Absorption Mode, Field Set, 1255 mT; Scan Range, 20 mT; Modulation Frequency, 100 kHz; Modulation Amplitude, 0.1 mT; Microwave power, 0.02 mW; Microwave Frequency, 34.600 GHz, Receiver Gain, 100; Time Constant, 1 s; Scan Time, 4 minutes; Temperature, 298 K; Spectrometer, Q-band EPR/ENDOR; File Name, 97080201.fl; Dispersion Mode, Field Set, 1255 mT; Scan Range, 20 mT; Modulation Frequency, 100 kHz; Modulation Amplitude, 0.1 mT; Microwave power, 0.2 mW; Microwave Frequency, 34.680 GHz, Receiver Gain, 100; Time Constant, 1 s; Scan Time, 4 minutes; Temperature, 298 K; Spectrometer, Q-band EPR/ENDOR; File Name, 97080202.fl; (dispers.opj)

CHAPTER 3

IMPROVEMENTS IN THE X-BAND ENDOR SPECTROMETER

Introduction

The EPR spectra of proteins and model complexes measured in our laboratory often have incompletely resolved hyperfine lines. The hyperfine splittings usually are less than the EPR line widths. Hyperfine coupling constants are used to obtain the structural information about the coordination environments of metal ions having unpaired electrons. In order to measure small hyperfine interactions, an X-band ENDOR spectrometer was previously built in this laboratory.

The first ENDOR spectrometer in our laboratory used a coil design developed by Hüttermann and coworkers (Figure 3.1 A), which had a printed coil inserted coaxially inside the Dewar finger and a sample inserted inside the coil.^[18] The coil and Dewar were placed in a TE104 dual cavity. The disadvantage of this ENDOR device was its lack of reproducibility. When a sample tube was put in the cavity, the coil tended to shift, and the cavity Q-value was destroyed. Also at low temperature, ENDOR signals were observed from the printed coil itself in addition to those from the sample.

Subsequently, a home-made cylindrical TM110 cavity was built which had a fixed coupling device, and a spiral copper RF coil inserted coaxially in the cavity and outside the Dewar finger (see Figure 3.1 B).^[19] This ENDOR cavity had a low Q-value (about 2500 without RF coil and 1200 with the RF coil) and poor penetration by the 10 kHz

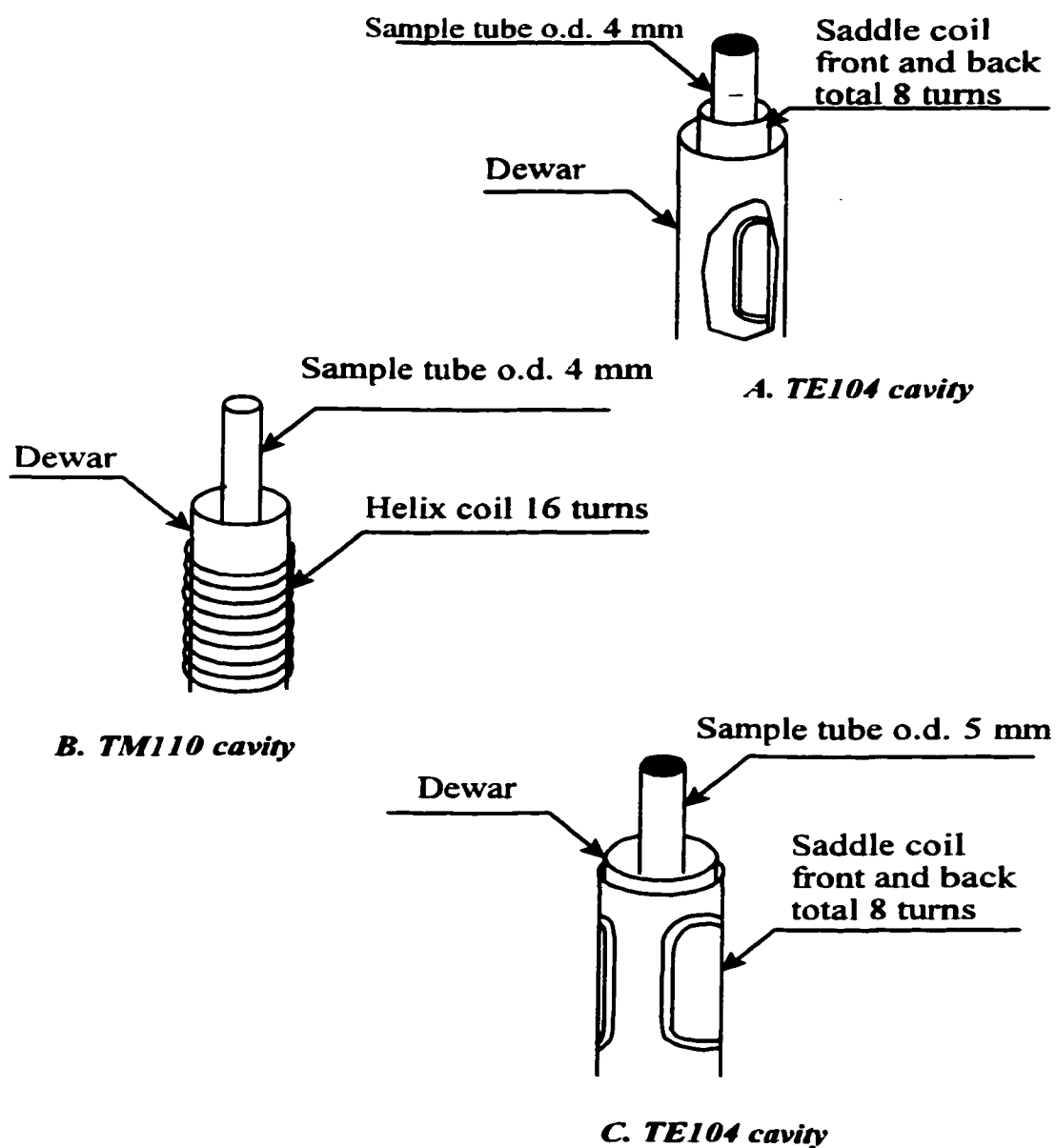


Figure 3.1 Schematic diagrams of our ENDOR coils. (3.1.wpd)

modulation field due to the thickness of the aluminum walls. Therefore EPR signals obtained with this spectrometer tended to be extremely weak. A new stepping spiral coil made of copper wire (24 gauge) was also fabricated according to Lubitz's design,^[20] but no improvement in cavity Q-value was obtained.

After several years of research work on our ENDOR spectrometer, we decided once again to employ a printed coil in the Varian dual TE104 cavity. But this time, the coil was placed outside the Dewar finger (see Figure 3.1 C). The following sections describe how to make and assemble the RF coil, and describe the performance of the improved ENDOR spectrometer.

The Design and fabrication of the ENDOR Coil

A series of steps are required in making the printed coil. The steps are as follows:

1. designing coils on the computer and printing out an image of the circuits; 2. making negative films; 3. drilling the alignment holes in the negative films; 4. processing photo resist in the dark room; 5. etching the copper foils; 6. soldering up both sides of the circuits; 7. cutting off the substrate; and 8. rolling up and gluing the coil.

Wordperfect Coreldraw was used to design the RF coils. The designed circuits for both sides of a RF coil were twice the size of the real ones (see Figure 3.2 A and B). The crucial points in designing the coils were that the shorter the vertical wire length, the better the RF coil, and that no horizontal wires, which serve as RF chokes, stayed in the active region of the cavity. In order to get a high Q-value of the ENDOR cavity, the width of the wire should be as thin as possible. The width of the designed coil was 0.5

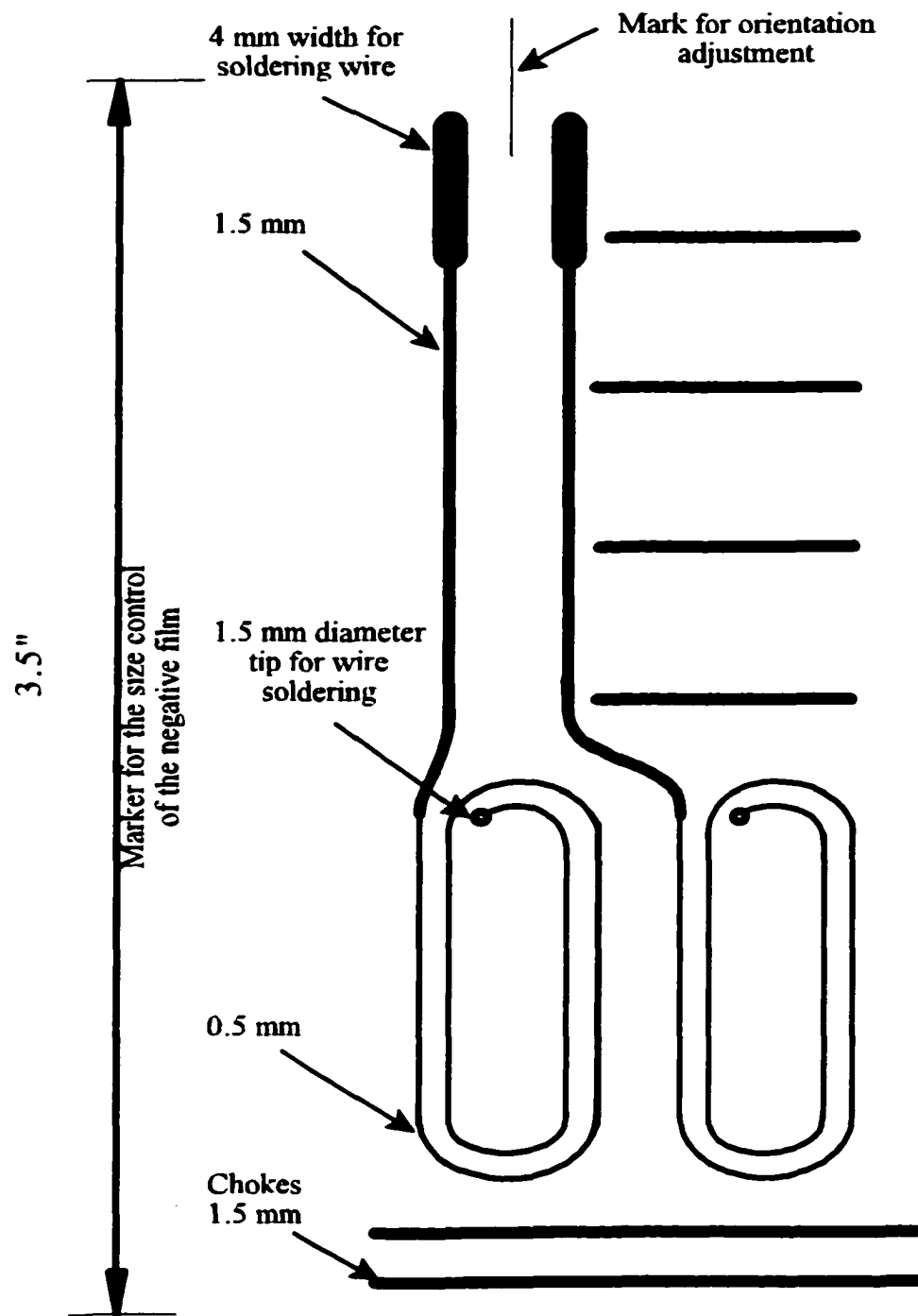


Figure 3.2a The drawing of the designed front side ENDOR coil. The negative film would be $\frac{1}{2}$ this size. (3.2.wpd)

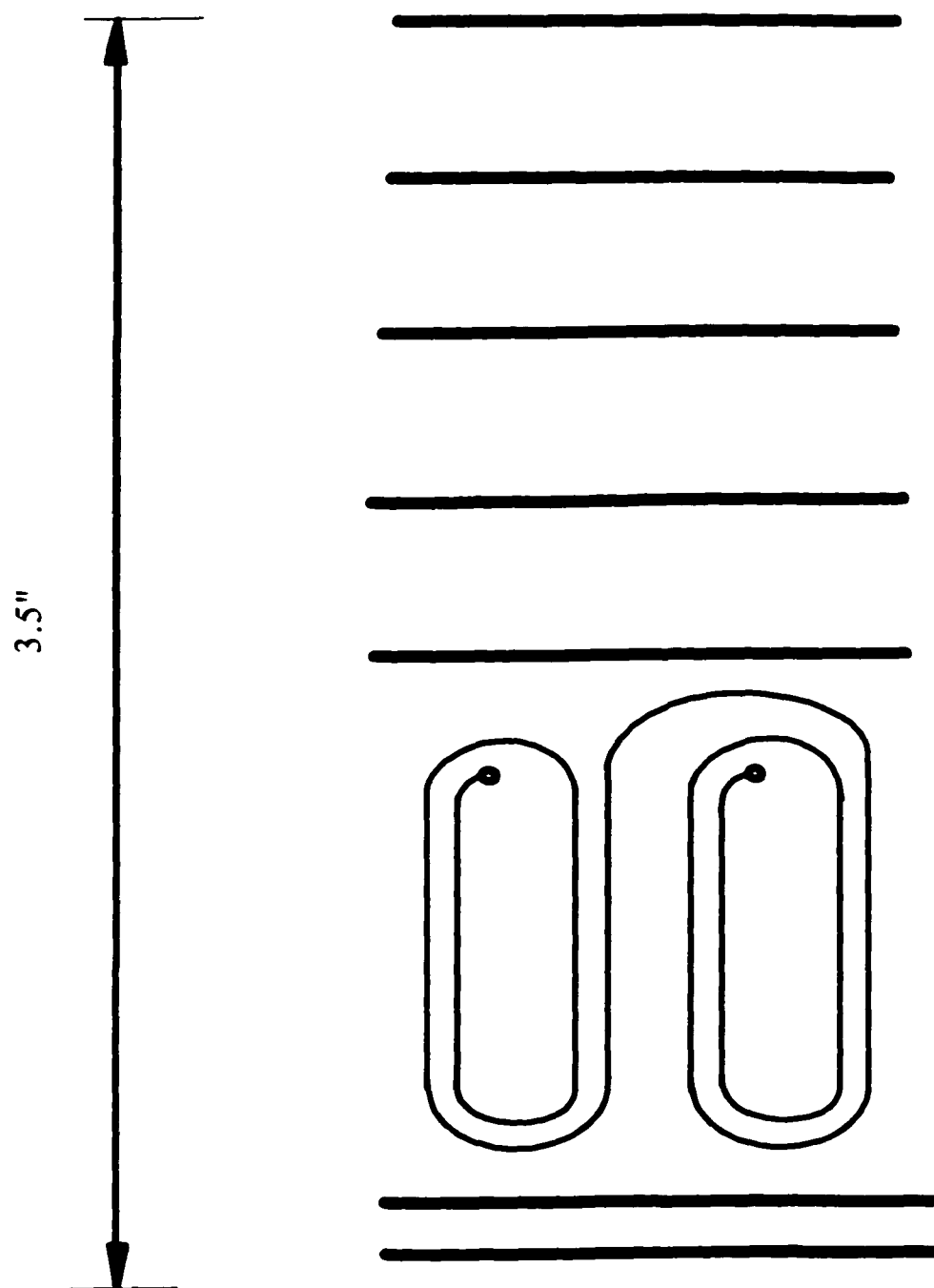


Figure 3.2b The drawing of the designed back side ENDOR coil. The negative film would be $\frac{1}{2}$ this size. (3.2.wpd)

mm on the printed papers (or 0.25 mm for the negative films). An even thinner wire could be made, but it would make the wire less durable, hard to make and carry less current. The circuits for both sides of a RF coil were designed to exactly match with one another when overlaid. Scale lines were drawn in the blue-prints (see Figure 3.2 A and B), which were labeled 3.5 inches to make the negative-film-making easier. On each blue-print, there are two groups of two-turn coil. Thus, each side of the coil has four turns. The total number of turns for a finished coil is eight. The test coils had 4, 8, 12 and 16 turns, respectively.

The negative films were made in the Photo Service Center of UNH. Dark negative films were required in order to get decent development of the photo resist on the dual side flexible copper sheet. The two negative films of both sides of the coil circuits were overlaid together. The front and back coil circuits were then adjusted to match up exactly. Afterwards, an aluminum plate mold, which had two alignment holes, was put onto the films. Then two alignment holes were drilled through the mold into the negative films. One was at the top and the other was at the bottom of the negative films. There are two ways to overlay the negative films. The correct overlay was only possible when the current in the coils was flowing in the same direction on both sides of the printed coil. The photo-print-processing in the dark room was carried out according to the standard photo-fabrication methods (see appendix D).

After the coils on the dual-sided foils were developed, they were washed and dried in an oven at 80 °C for five minutes. Then, the residues of unwanted photo resist around the circuits were scraped off with a razor under a magnifying glass, whereas the broken

wires were connected by a resist ink pen.

The copper foils were then suspended in a container having concentrated FeCl_3 (about 2 M) with a stir bar at the bottom. The etching process took about one hour depending upon the concentration and temperature of the etching solution. Frequent checking of the foils was needed to avoid over etching which resulted in a thinner or even broken circuit. The coils were then rinsed with distilled water and dried.

The following steps were followed to punch connecting-holes (about 0.25 mm, see Figure 3.2) with a sewing needle, to place thin wires (AWG 36) through the holes, and finally to solder the wires on both sides of the coil. The soldering points were flattened with pliers. Two threads of Scotchflex flat cable wires (28 AWG, 7 x 36 or 7 x 0.127 mm) connected to the BNC connector were soldered onto the coils. Then, all the substrate inside the cavity area of the printed coil was cut off. Next, coils were wrapped onto a spare Dewar finger (o.d. 10 mm), and fastened up by a few pieces of laboratory labeling tape. Figure 3.3 shows the photograph of a finished ENDOR coil.

The Spacer for the ENDOR Coil Connection

Touch connections were used in the previous ENDOR coil of the cylindrical cavity (see Figure 3.1 B). This kind of connection could not be applied in the present ENDOR coil due to the utilization of the Varian dual TE104 cavity. Therefore, a spacer was designed to make the connection (see Figure 3.4).

The spacer was made of brass which had a good conductivity for the RF circuit. The height of the spacer was 16 mm. Two BNC connector threads were made on the

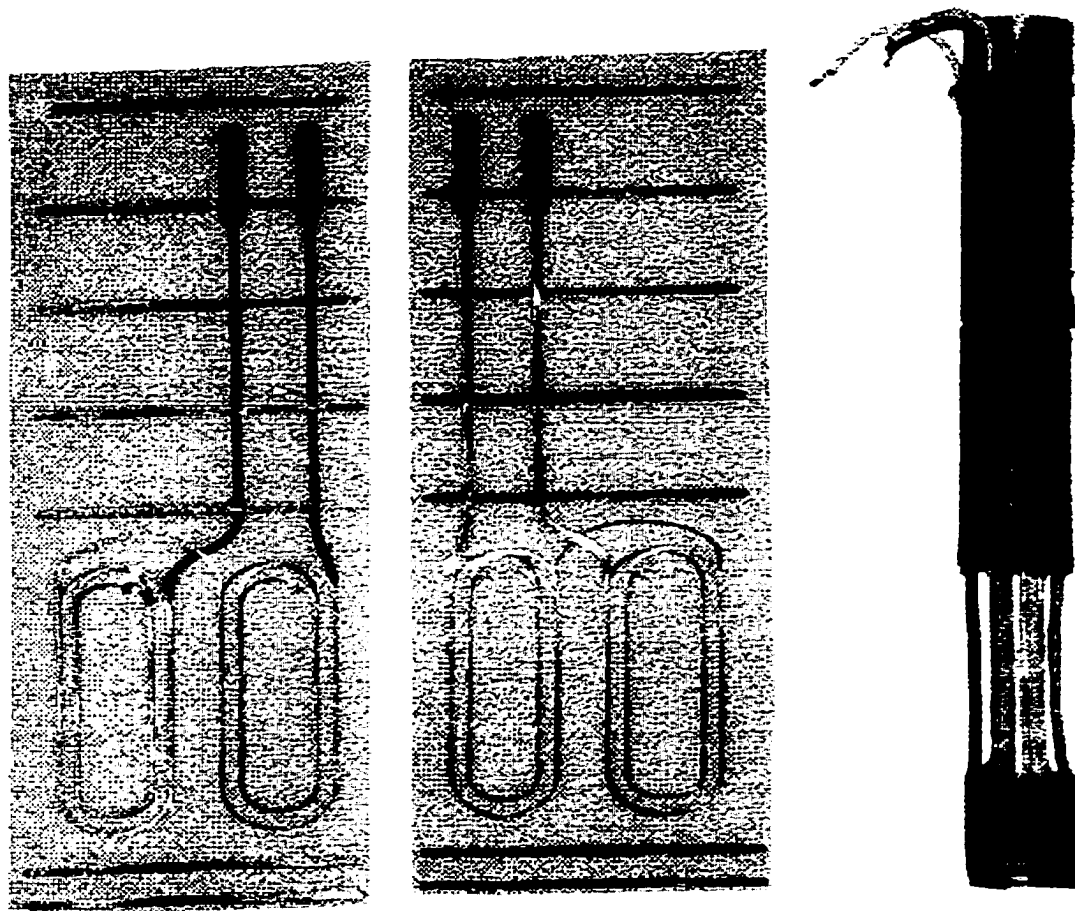


Figure 3.3 The photograph of the ENDOR coil.

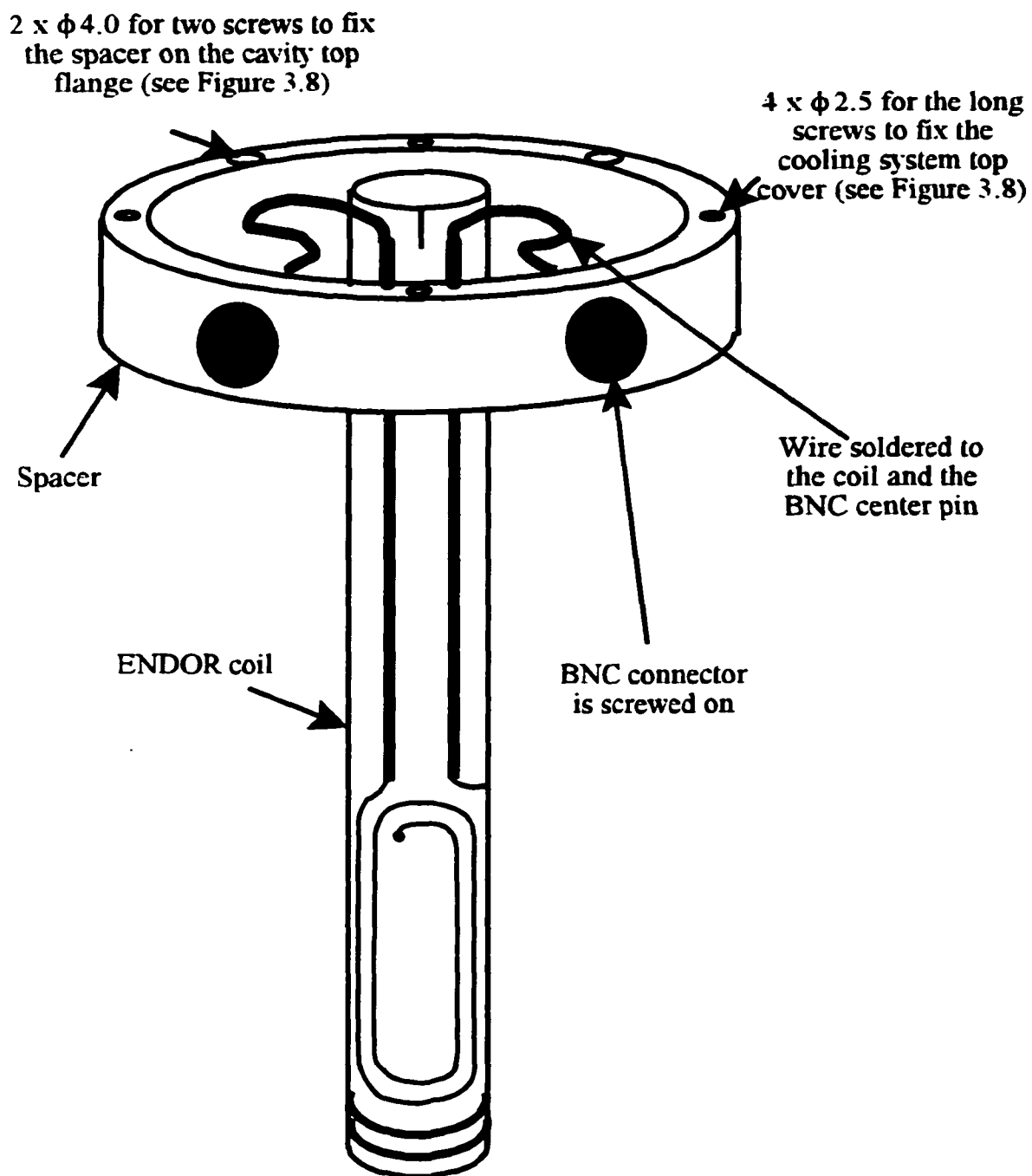
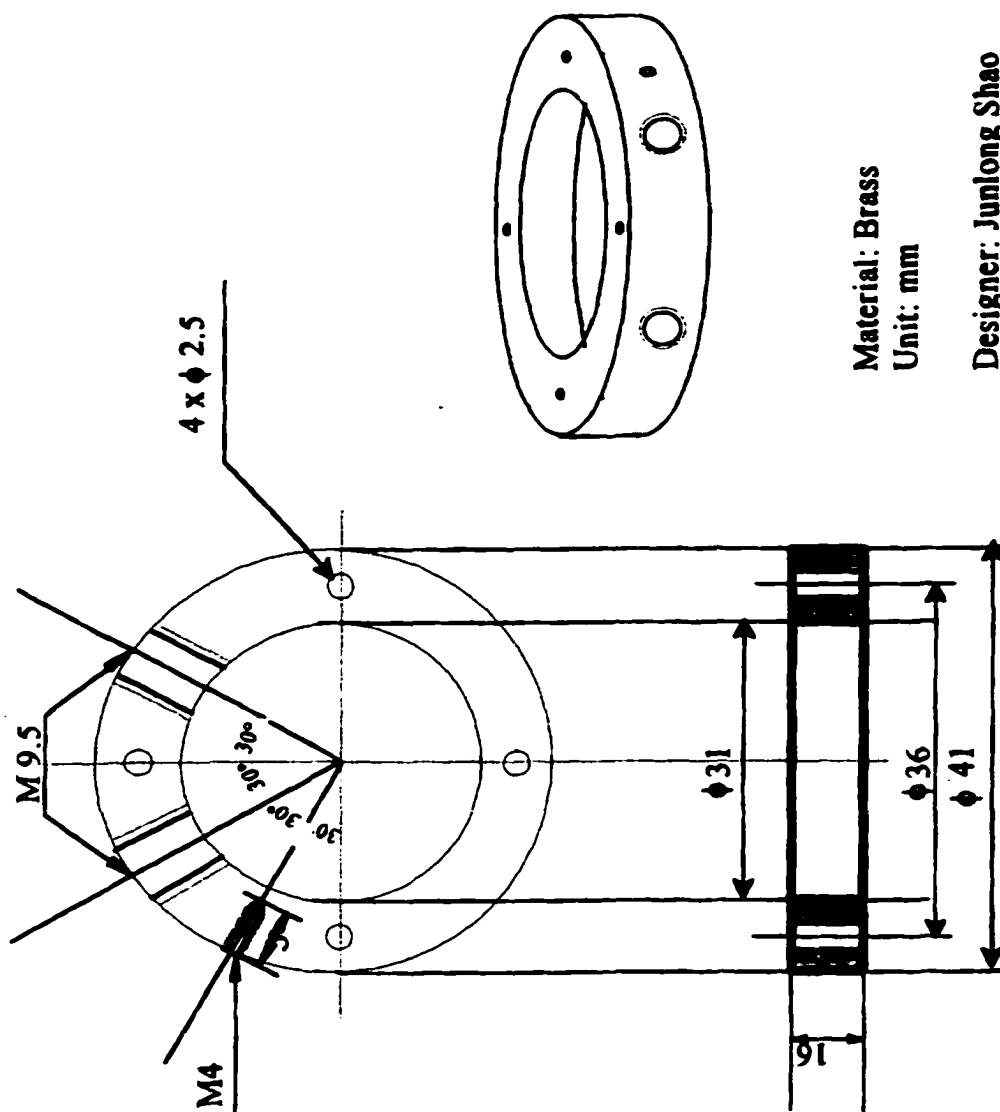


Figure 3.4 The drawing of the assembled coil and spacer with electrical connections.
(3.4.wpd)



Material: Brass
Unit: mm

Designer: Junlong Shao
Chemistry Chasteen's group
Tel: 2-1354

Figure 3.5 The mechanical drawing of the spacer for the ENDOR coil. (3.5.wpd)

front side of the spacer. The outer diameter of the spacer was 41 mm, which was about the same size as the cavity top flange. The inner diameter was 36 mm, being wide enough for ENDOR coil adjustment by fingers. The four 2.0 mm holes were drilled evenly through the spacer with the exact positions shown in Figure 3.5. Two other 2.0 mm holes were made on the spacer later. They were evenly located among the other three holes (see Figure 3.4). One M4 thread was made on the front side of the spacer for the electrical connection in the RF circuit.

The dual cavity was used due to its excellent tolerance to the inserted ENDOR coil without major reduction in cavity Q. As the thread on the cryostat top piece and the thread on the cavity bottom were not aligned coaxially, the dual cavity was not tightened onto the cryostat. However, when the waveguide was connected to both the cavity and the bridge, the cavity was held in place firmly. The exact position of the dual cavity was adjusted carefully by moving the microwave bridge around so that the cavity was coaxially aligned with the Dewar finger.

Assembly of the ENDOR Coil

When assembling the ENDOR coil, the two BNC connectors were tightened on the spacer first. Then the two wires from the coil were soldered onto each center pin of the two BNC connector. Afterwards, the spacer was held firmly and the coil was inserted into a spare Dewar finger with an O. D. of 10 mm. The coil was shaped so that the middle of the coil was a little bit wider than the ends. The next step was to insert the coil into the cavity by lowering the spacer using extreme caution not to alter the coil shape. When the

spacer was placed on the cavity top flange, it was tightened by two screws. With the spectrometer operating in tune, the tune mode was watched while carefully rotating and moving the ENDOR coil up and down. When the sharpest mode was found, the ENDOR coil was left untouched. If no satisfactory mode was found, the coil had to be taken out of the cavity and shaped again. The top cover of the cooling system was finally put onto the spacer and tightened up using four long screws. The ENDOR coil was finally connected to the RF amplifier with a heavy-duty cable and to the dummy load (or a BNC connector having its two pins connected together). No difference in performance of the ENDOR spectrometer was observed with the two configurations. The latter configuration was used throughout for the ENDOR experiments reported here.

Test of Various ENDOR Coils

A series of ENDOR coils with different turns, shapes and wire widths were made in an attempt to obtain the best design. They were tested by both EPR and ENDOR spectra of the sucrose sample (see Figures 3.6 and 3.7, respectively). It was found that in comparison to circuit wires of 0.75 and 0.5 mm width, the wire of 0.25 mm width had a better tune mode, as well as bigger EPR and ENDOR signal amplitudes (data not shown). A thinner width wire was not tried due to the reasons mentioned above. Coils with 4 to 16 total turns were made. As no ENDOR signals were obtained for both 4- and 16- turn coils, no points for them were drawn on Figures 3.6 and 3.7. The EPR signal amplitudes in Figure 3.6 show that with the same shape, fewer turns resulted in bigger EPR signals (see Coil A, 8-turn and Coil B, 12-turn). However, the shape of the coil could be crucial

to the cavity quality as well. The cavity had a larger EPR amplitude with Coil B (12-turn coil) than with Coil C (8-turn coil). In addition, the 8-turn coils (Coil A and Coil C) had the bigger ENDOR signal amplitudes than the 12-turn coil (Coil B) in Figure 3.7. The weak ENDOR signal for the 12-turn coil might arise from the resistance mismatch in the RF circuit. No RF power saturation was found for any of the ENDOR coils. The sucrose ENDOR signal obtained for each coil continued to grow up to the limit of the amplifier. As Coil C gave the strongest ENDOR signal, it was taken as the best ENDOR coil for further use in our X-band ENDOR spectrometer.

Sample Tube Change from 4 mm to 5 mm Outer Diameter

The sample tubes for ENDOR measurements were switched from 4 mm o.d., 3 mm i.d. to 5 mm o.d., 4 mm i.d.. The sample volume increased by a factor of $(4/3)^2 = 1.78$. The sample holder center hole on the top of the cooling system cover (see Figure 3.8) was widened to fit the bigger sample tube. A spare sample holder was made for quickly switching from sample to sample. The EPR and ENDOR spectra of a BDPA sample measured with the two sample tubes are presented in the following section.

The Modifications of the Helium Cooling System

The complete cooling system for the X-band ENDOR spectrometer is displayed in Appendix B, Figure B.1. Figure 3.8 shows a partial diagram of the cooling system. Originally the cooling system was operated by pumping mainly from the back outlet of the cryostat system. Since a bigger diameter sample tubing (O. D. changed from 4 mm to 5

mm) was used, the helium flow over the sample became restricted. As a result, the temperature around the sample could no longer reach 2 K. When a thermosensor within a 5 mm O. D. sample tube was put in the cavity, the temperature around the sample tube was measured to be about 6 K.

The flow rate of helium gas was the dominant factor for the lowest temperature achieved. In the previous helium flow system, helium gas passed from the opening of the capillary tubing, through a piece of collar tubing (made of either quartz tubing or a Jumbo brand plastic straw), then passed downwards through the outside of the collar tubing and out the back outlet. As the 5 mm O. D. sample tube was used in the new ENDOR spectrometer, the gap between the sample tube and the collar tubing became much smaller. The helium flow rate was thus greatly reduced.

The collar tubing was eventually removed. The back outlet could no longer be used and was stoppered. A brass manifold with 0.5" O. D. was made and fixed at the rear of the magnet. The cooling system top cover (see Figure 3.8) was rotated 135 ° toward the back of the magnets in order to minimize kinking of the vacuum tubing and connected to the vacuum tubing ending to the brass manifold (see Figure B.1 of Appendix B). In this way helium gas was pumped over the sample tube and out of the top of the Dewar. After all these modifications, the lowest temperature reached was 2.3 K.

Background Noise of the ENDOR Spectrometer

A significant problem in operation of the ENDOR spectrometer is background noise and spurious baseline signals. The source of the noise was found to come mainly

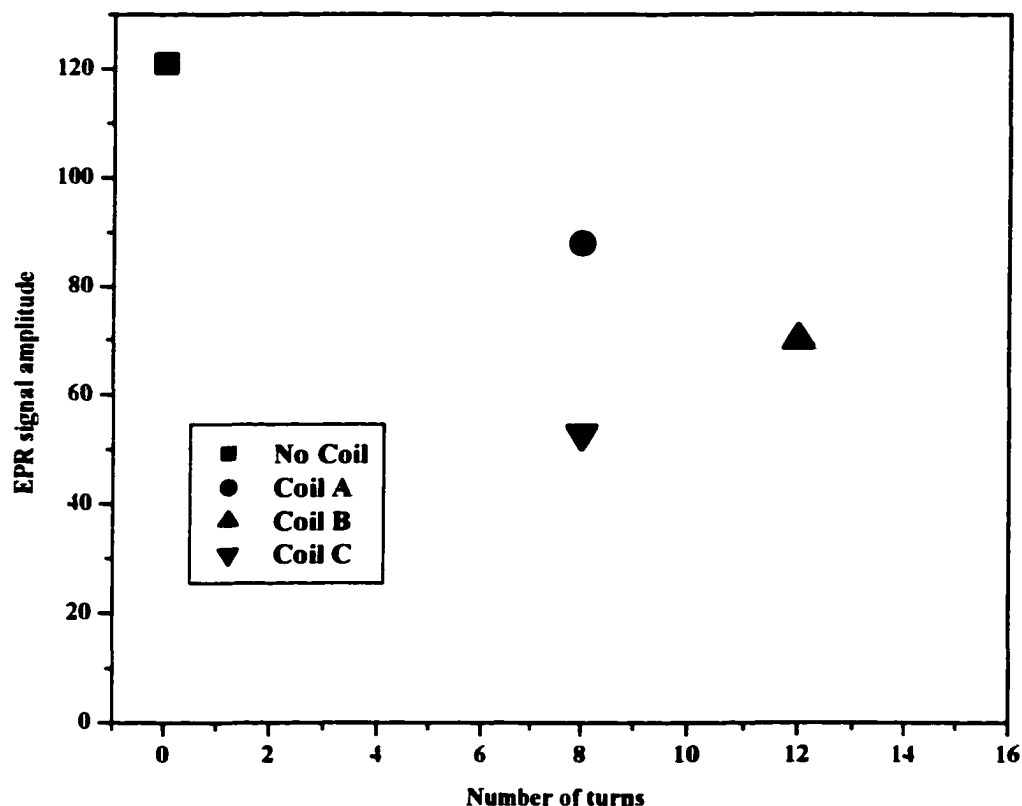


Figure 3.6 The EPR signal amplitudes of sucrose standard sample versus the three different coils.

Coil A •: total 8 turns; wire thickness, 0.25 mm; gap between wires, 0.5 mm; label 2d.

Coil B ▲: total 12 turns; wire thickness, 0.25 mm; gap between wires, 0.5 mm; label 3d.

Coil C ▼: total 8 turns; wire thickness, 0.25 mm; gap between wires, 1.5 mm; label 2a.

Experimental Conditions:

Coil A •, Microwave Power, 6 mW; Magnetic Field, 336 mT; Scan Range, 100G; Modulation Amplitude, 0.1 mT; Microwave Frequency, 9.452 GHz; Time Constant, 0.01s; Receiver Gain, 500; Modulation Frequency, 100 kHz; Scan Time, 4 minutes; File Name, 971002 (on EPR sheet).

Coil B ▲, Microwave Power, 6 mW; Magnetic Field, 3360 mT; Scan Range, 100G; Modulation Amplitude, 0.1 mT; Microwave Frequency, 9.451 GHz; Time

(continued)

Constant, 0.01s; Receiver Gain, 500; Modulation Frequency, 100 kHz; Scan Time, 4 minutes; File Name, 971002 (on EPR sheet).

Coil C ▲, Microwave Power, 6 mW; Magnetic Field, 336 mT; Scan Range, 100G; Modulation Amplitude, 0.1 mT; Microwave Frequency, 9.448 GHz; Time Constant, 0.01s; Receiver Gain, 500; Modulation Frequency, 100 kHz; Scan Time, 4 minutes; File Name, 971002 (on EPR sheet). (3.6.wpd).

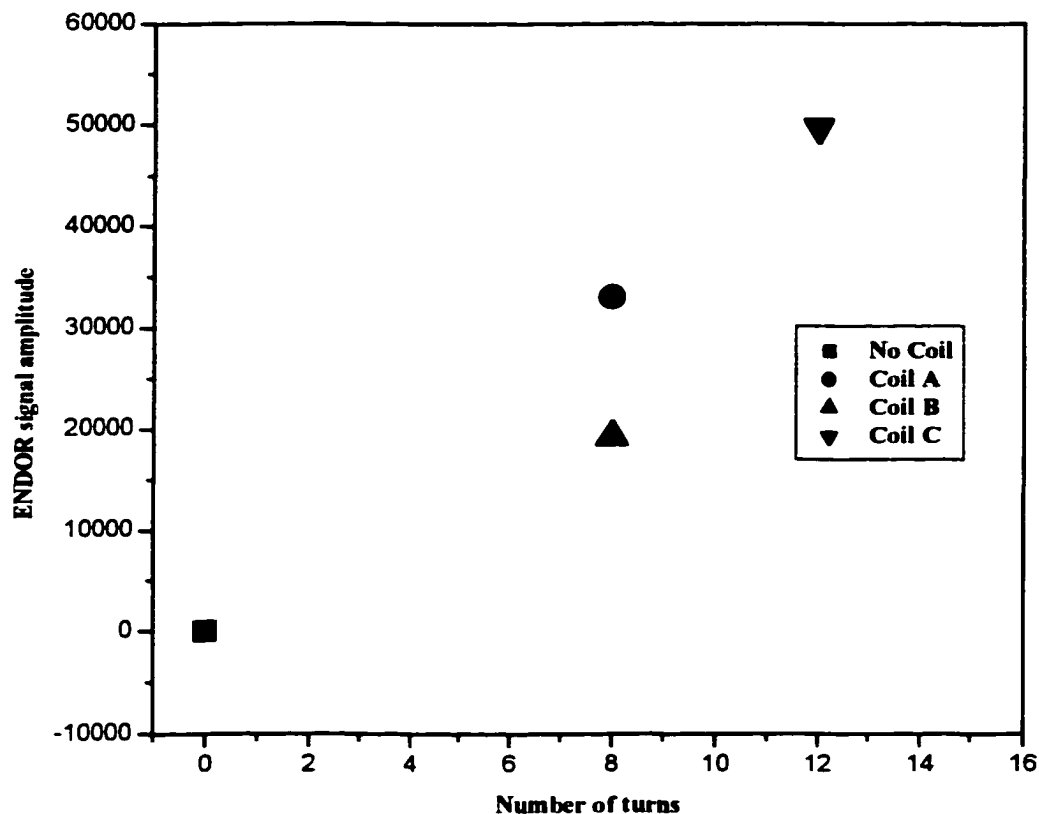


Figure 3.7 The ENDOR signal amplitudes of sucrose standard sample versus the three different coils.

Coil A ●: total 8 turns; wire thickness, 0.25 mm; gap between wires, 0.5 mm; label 2d.

Coil B ▲: total 12 turns; wire thickness, 0.25 mm; gap between wires, 0.5 mm; label 3d.

Coil C ▼: total 8 turns; wire thickness, 0.25 mm; gap between wires, 1.5 mm; label 2a.

Experimental Conditions:

Coil A ●, Microwave Power, 1 mW; Radio Frequency Power, 100 W; Modulation Amplitude, 2.0 V; Microwave Frequency, 9.452 GHz; Time Constant, 0.03s; Receiver Gain, 16000; Modulation Frequency, 10 kHz; Scan Rate, 0.5 MHz/s; Scan Range, 9~19 MHz; File Name, 97100201.

Coil B ▲, Microwave Power, 1 mW; Radio Frequency Power, 100 W; Modulation Amplitude, 2.0 V; Microwave Frequency, 9.451 GHz; Time Constant, 0.03s; Receiver Gain, 16000; Modulation Frequency, 10 kHz; Scan Rate, 0.5 MHz/s; Scan Range, 9~19

(continued)

MHz; File Name, 97100202.

Coil C ▼, Microwave Power, 1 mW; Radio Frequency Power, 100 W; Modulation Amplitude, 2.0 V; Microwave Frequency, 9.448 GHz; Time Constant, 0.03s; Receiver Gain, 16000; Modulation Frequency, 10 kHz; Scan Rate, 0.5 MHz/s; Scan Range, 9~19 MHz; File Name, 97100203. (3.7.wpd)

from induction of the radio frequency energy in the waveguide which connects the microwave bridge to the ENDOR cavity. Noise is also picked up by the modulation coil and magnetic field probe. Both are close to the NMR coil. The 10 kHz modulation cable is another noise source. Several procedures were undertaken to get rid of these sources of noise. The waveguide connections were insulated by pieces of well-trimmed teflon sheet to minimize the induced noise. Then the waveguide was grounded with four wires to the water pipe and the three legs of the EPR/ENDOR spectrometer bench upon which the bridge sits. The 10 kHz frequency modulation cable was also put as far as possible from the cavity to minimize the background signal. No dummy load was used through all the ENDOR experiments. A heavy duty coaxial cable (about four feet in length) was used to connect the ENI amplifier to the ENDOR coil.

Test of the ENDOR Spectrometer

The sucrose sample, which is exactly the same one as we used before, was tested on our new X-band ENDOR spectrometer. Figure 3.9 shows the EPR spectrum of the sucrose standard sample obtained on the present ENDOR spectrometer. The sucrose ENDOR signals were measured on our previous and present ENDOR spectrometers (Figure 3.10). According to the Equation 2.1, the S/N was measured to be 58 with the present system compared to 35 previously or improved by a factor of 1.66. We also tested the influence of the sample volume increase (sample tube i.d. increased from 3 mm to 4 mm) on the EPR and ENDOR signals. The results are presented in Figure 3.11. As the volume increased by a factor of 1.78, so did the EPR and ENDOR signal amplitudes

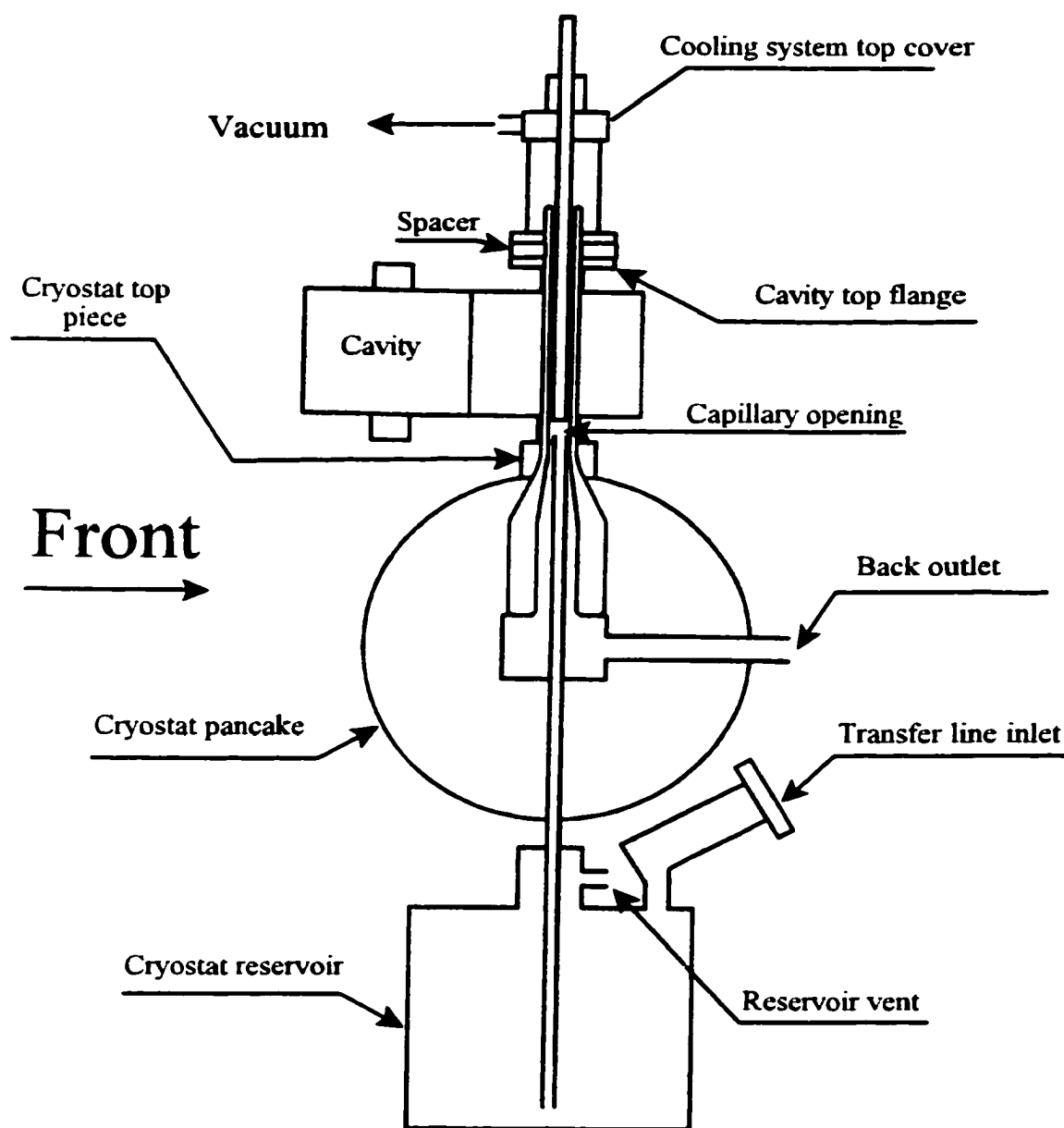


Figure 3.8 The partial drawing of the X-band EPR/ENDOR cooling system. (3.8.wpd).

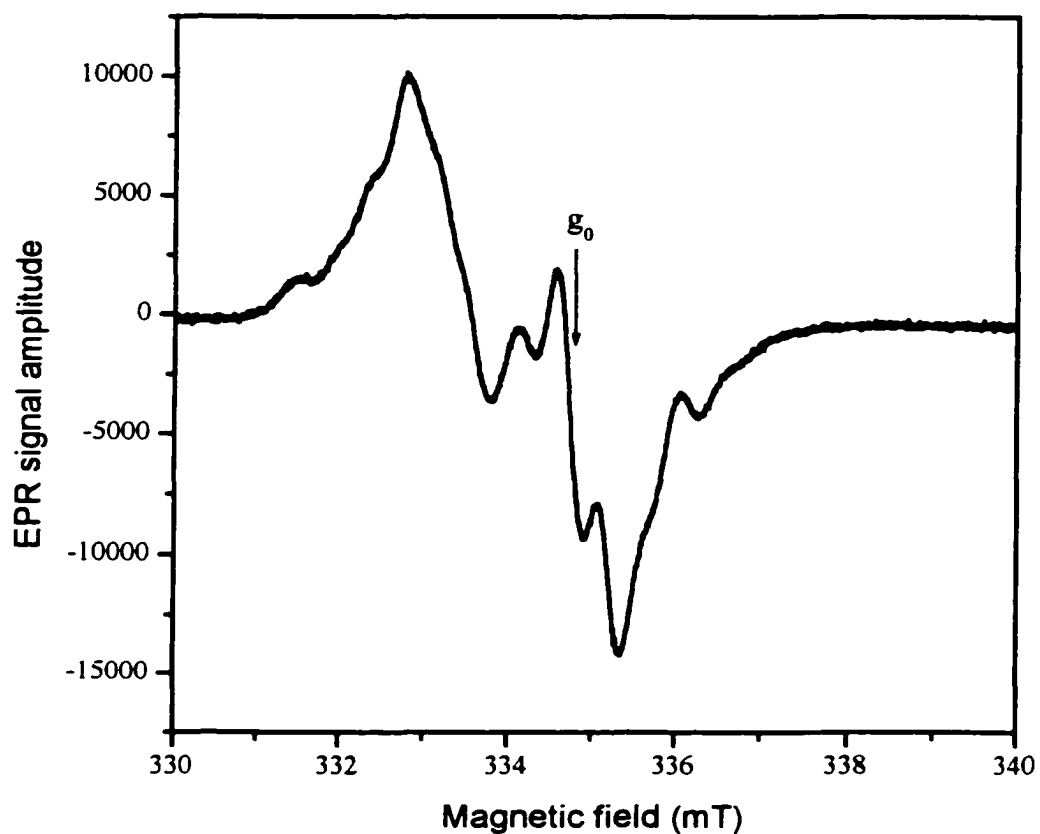
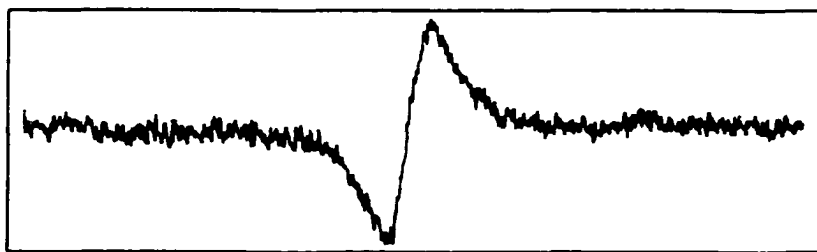
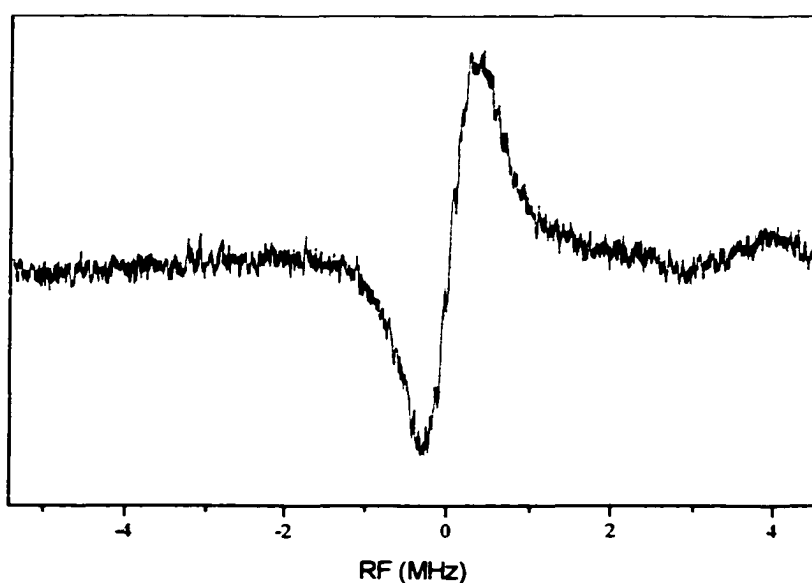


Figure 3.9 The EPR spectrum of sucrose standard sample from the present TE104 cavity. Experimental conditions: Magnetic Field, 335 mT; Scan Range, 10 mT; Microwave Power, 4 mW; Modulation Amplitude, 0.05 mT; Modulation Frequency, 100 kHz; Temperature, 298 K; Time Constant, 1 s; Receiver Gain, 100; Microwave Frequency, 9.432 GHz; Scan time, 4 minutes; File Name, 98021701.flr; (3.9.wpd).



A. The ENDOR signal from the previous TM110 cavity (see Figure 3.1 B).



B. The ENDOR signal from the present TE104 cavity (see Figure 3.1 C).

Figure 3.10 The Sucrose ENDOR signals from two different spectrometers.

Experimental Conditions: A, Microwave Power, 10 mW; Radio Frequency Power, 0.4v PTS; Modulation Amplitude, 2.5 V (280 kHz); Time Constant, 0.03s; Receiver Gain, 10000; Modulation Frequency, 10 kHz; Scan Rate, 0.2 MHz/s; Scan Range, 9~19 MHz; number of scans, 1; File Name, 19apr95a.flc. B, Field set, 334.74 mT; Microwave Power, 4 mW; Radio Frequency Power, 120 W; Modulation Amplitude, 6.0 V, 660 kHz; Time constant, 0.03s; Receiver Gain, 16000; Modulation Frequency, 10 kHz; Scan Rate, 0.5 MHz/s; Scan range, 9~19 MHz; number of scans, 1; File Name, 98021603.flc (3.10.wpd).

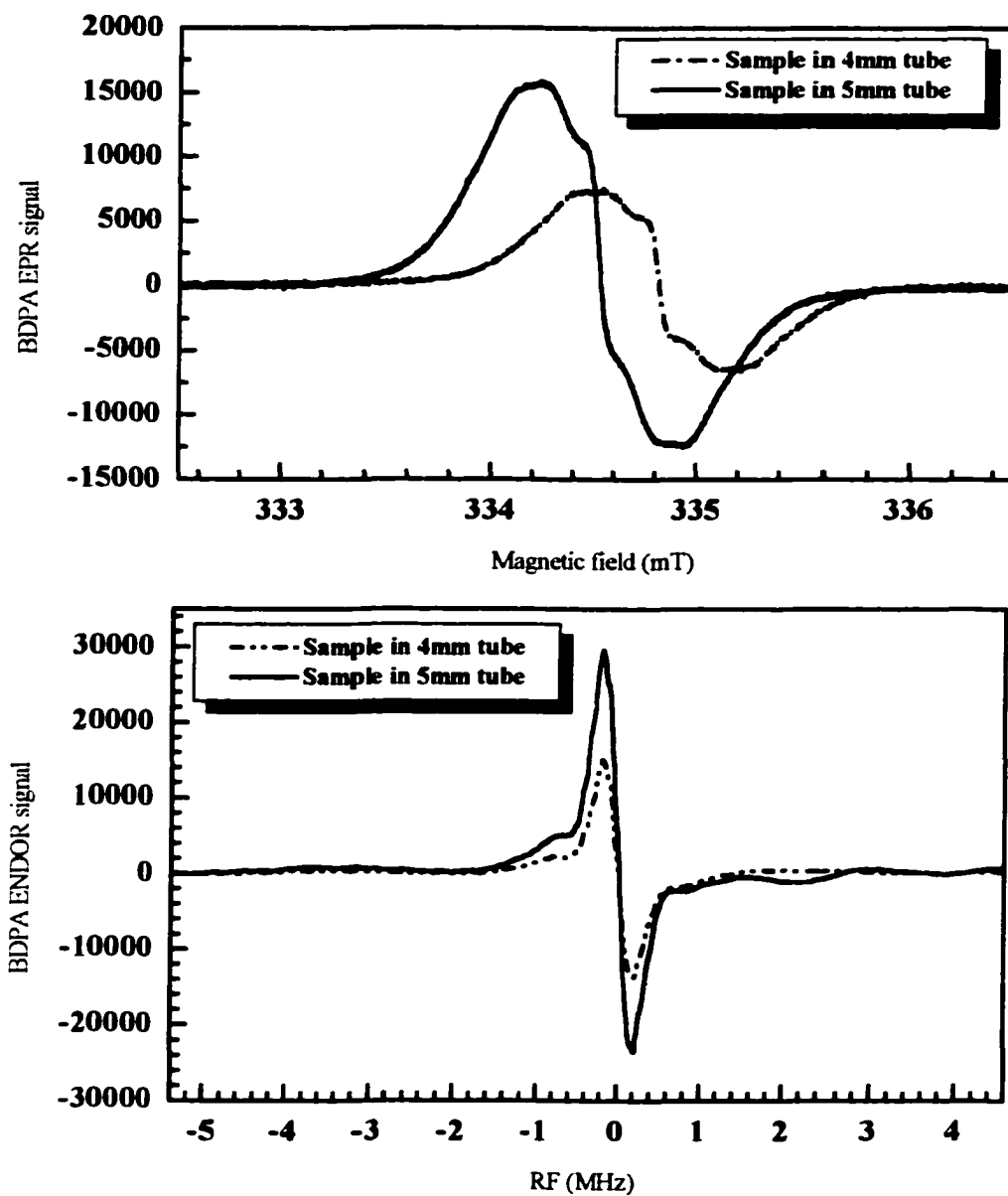


Figure 3.11 The EPR/ENDOR signals for BDPA samples in 4 mm and 5 mm tubes. Experimental Conditions: EPR, Magnetic Field, 334.5 mT; Scan Range, 4 mT; Microwave Power, 0.05 mW; Modulation Amplitude, 0.05 mT; Modulation Frequency, 100 kHz;

(continued)

Temperature, 298 K; Time Constant, 1 s; Receiver Gain, 1000; Microwave Frequency, 4 mm tube, 9.409 GHz; 5 mm tube, 9.391 GHz; File Name, 4 mm tube, 98030419; 5 mm tube, 98030417; ENDOR, Field position, 5 mm tube, 3345.36, 4 mm tube, 3348.14; Microwave Power, 1 mW; Radio Frequency Power, 100 W; Receiver Gain, 3200; Modulation Frequency, 10 kHz; Modulation Amplitude, 2.0 V (220 kHz); Time Constant, 0.1 s; Temperature, 298 K; Scan Rate, 0.5 MHz/s; Scan Range, 9 ~ 19 MHz; Number of scans, 1; File Name, 4 mm tube, 98030420; 5 mm tube, 98030418; (2.11.wpd).

by about the same factor. Table 3.1 lists the tested results for our new EPR/ENDOR spectrometer and the ones from Dr. Proulx-Curry. The overall S/N of our new EPR/ENDOR spectrometer is a factor of 3.0 better than our previous one. This gives a reduction of acquisition time of $1/9 = (1/3)^2$ for the same S/N, enabling spectra of weak signals to be observed. As a consequence, the ENDOR spectrum of the ferritin iron nitrosyl complex, which was not possible to observe on the previous spectrometer, was obtained with the improved ENDOR spectrometer. The performance of our new ENDOR spectrometer significantly exceeds the previous one regarding stability of operation, modulation field penetration, tuning and sensitivity.

Table 3.1 The comparison of our two X-band ENDOR systems

	Previous ENDOR system	Present ENDOR system		
Cavity	TM110 home-made	TE104 Varian		
Cavity Q-value w/o RF coil	2,500	5,000		
Cavity Q-value w/ RF coil	1,200	2,050		
RF coil	helix 16 turns	saddle 8 turns		
Sample tube	i. d. 3 mm; o. d. 4 mm	i. d. 3 mm; o. d. 4 mm	i. d. 3 mm; o. d. 4 mm	i. d. 4 mm; o. d. 5 mm
Test sample	Sucrose	Sucrose	BDPA	BDPA
Microwave power	10 mW	4 mW	1 mW	1 mW
RF power	0.4 PTS	0.24 V, 120 W	0.24v, 100 W	0.24v, 100 W
RF modulation amplitude	2.5 V, 280 kHz	6.0 V, 660 kHz	2.0 V, 220 kHz	2.0 V, 220 kHz
Sweep rate	0.2 MHz/s	0.5 MHz/s	0.5 MHz/s	0.5 MHz/s
Time constant	0.03 s	0.03 s	0.03 s	0.03 s
S/N	35	58	p-to-p, 27807	p-to-p, 49431
Total S/N	35	103 ^a		

a. The total S/N for present ENDOR system is $58 \times 49431/27807 = 103$.

CHAPTER 4

ENDOR STUDIES OF FERRITIN IRON NITROSYL COMPLEXES

Introduction

Ferritin, the iron storage protein, has been studied extensively.^[21-23] Ferritin has twenty four subunits which assemble into a highly symmetric structure of space group F432.^[24, 25] The protein stores iron in its central cavity in the form of ferric hydroxy phosphate mineral phase.^[26] Ferrous iron diffuses into and out of the ferritin cavity through the three-fold hydrophilic channels of the protein shell.^[27] However, the mechanism of iron deposition in the protein *in vivo* is still unclear. One possible mechanism for iron deposition in ferritin may involve the formation of ferritin iron nitrosyl complexes.^[28]

Nitric oxide (NO) is an important small radical in living cells.^[29-32] It plays vital roles in many physiological functions such as digestion, blood pressure regulation, neurotransmission and antimicrobial defense.^[33-36] It may serve as a cytotoxic effector, neurotransmitter, immune regulator, and endothelium-derived relaxing factor.^[34,37-40] In both normal and tumor cells, iron nitrosyl complexes have been found by EPR spectroscopy.^[41-43] The EPR spectra of ferritin in the presence of NO is similar to those of liver cells.^[44] This similarity suggests a possible presence of ferritin iron nitrosyl complexes in liver cells. Other studies have suggested that the nitric oxide could play a role in iron release from the ferritin cavity.^[33]

The general structure of dinitrosyl iron complexes has been described as tetrahedral.^[45] The total electron spin is $S = 1/2$.^[45a] Thus, the g-values of the complexes are near the free electron value. The EPR spectra of such complexes generally consist of a resonance at $g = 2.032$,^[46] but their structures in protein molecules are generally unknown.

Studies of ferritin iron nitrosyl complexes of site-directed mutant proteins were previously carried out in our group.^[28] Rhombic and axial EPR signals of the complexes were found to come from the iron nitrosyl complexes coordinated at His128 and Cys130 residues, respectively, in the vicinity of the three-fold hydrophilic channels.^[28] However, the EPR spectra showed no resolved ^{14}N or ^1H coupling in frozen solution, so no further information about the structures of the complexes was obtained. Therefore, ENDOR spectroscopy was used to obtain the proton hyperfine splittings for the complexes. Unfortunately, due to the weak ENDOR signals of ferritin iron nitrosyl complexes, and the relatively low sensitivity of our previous ENDOR spectrometer toward dilute biological samples, ENDOR spectra from ferritin iron nitrosyl complexes were not obtained. However, ENDOR spectra of model complexes were obtained, which provided indirect insight into the possible local configuration of the iron nitrosyl complexes in ferritin itself.^[47]

After improvement of our ENDOR spectrometer, the ENDOR spectra of ferritin iron nitrosyl complexes were again investigated and successfully observed in this laboratory. Two model complexes were also studied by ENDOR spectroscopy, namely the cysteine iron nitrosyl and penicillamine iron nitrosyl complexes. The distances from the iron to the surrounding protons were estimated for the protein and model complexes

using the point dipole approximation.^[47] The possible structures of the model complexes were generated by ChemSite, a computer molecular modeling program. The local structure of ferritin iron nitrosyl complex is inferred from the data on the protein and model complexes.

Experimental

The X-band ENDOR spectrometer was operated according to the description in Appendix C. Most of the experiments were carried out at 2.3 K. All the proton ENDOR spectra presented here have the off resonance background subtracted from the spectra.

All the materials were reagent grade and used without further purification unless otherwise indicated. Horse spleen apoferritin, 2,2'-dipyridyl, sodium chloride and ascorbic acid were purchased from Sigma Chemical Co., St. Louis, MO. Trace metal ions in ferritin were removed by the standard procedures.^[48] MOPS, MES and HEPES buffers were from Research Organics, Inc., Cleveland, OH. Sodium hydrosulfite, sodium hydroxide, sodium nitrite and penicillamine was obtained from Aldrich Chemical Co., Inc., Milwaukee, WI. Sulfuric acid and hydrochloric acid were from J. T. Baker Inc., Phillipsburg, NJ. Deuterium chloride, D₂O and sodium deuterioxide were from Cambridge Isotope Laboratories, Inc., Andover, MA. Ferrous sulfate heptahydrate was from Fisher Chemical Inc., Fair Lawn, NJ. Cysteine was from Fluka Chemical Co., Ronkonkoma, NY.

MOPS buffer (0.1 M MOPS, 0.15 M NaCl) was made for all the protein samples in H₂O and D₂O. The pH and pD of the protein solution was adjusted to 7.0 for samples

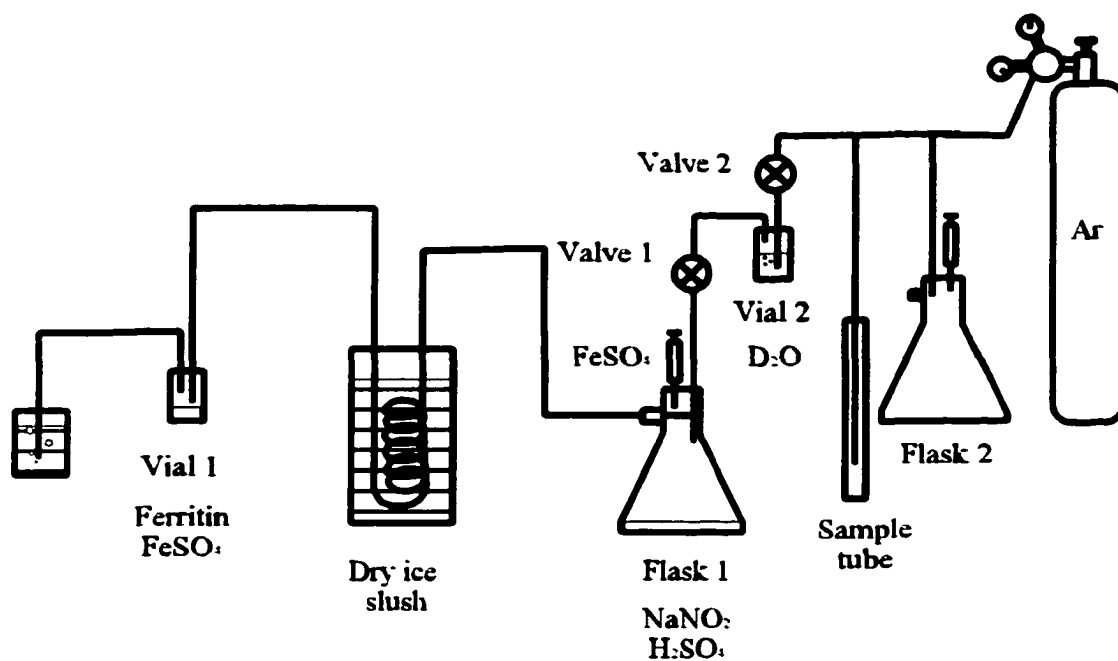


Figure 4.1 The schematic diagram of the apparatus for the preparation of the ferritin iron nitrosyl complex. (4.1.wpd)

in H_2O and in D_2O where $\text{pD} = \text{pH} - 0.4$. Here, pH is the meter reading for D_2O samples while the meter is calibrated with pH buffers. The pD adjustment of samples in D_2O was protected by argon gas. Similarly, the pH and pD values for the model complexes in H_2O and in D_2O were 6.0.

Ferritin was concentrated with a 3 ml ultrafiltration cell and a PM 30 membrane (Molecular weight cut-off 30,000, Amicon, Inc., Beverly, MA). The operating pressure was 20 psi. The concentration of horse spleen apoferritin was determined by its absorbance at 280 nm, with the molar absorptivity $\epsilon = 1.95 \times 10^4 \text{ cm}^{-1} \text{ M}^{-1}$ per subunit.^[49]

The ferritin iron nitrosyl complexes were prepared by passing freshly generated NO gas over the top surface of the ferritin solution, which consisted of about 2 mM subunit concentration of horse spleen ferritin and eight ferrous iron ions per protein. Figure 4.1 shows a schematic diagram for the preparation of the ferritin iron nitrosyl complexes. Usually, 700 μl of solution with 0.08 mM ferritin 24 mer, 0.15 M MOPS and 0.1 M NaCl, at $\text{pH} = 7.0$ was put in Vial 1 (see Figure 4.1). Then, 0.345 g of NaNO_2 was weighed and put in Flask 1. The preparation system was flushed with Ar gas for one hour. Vial 2 contains H_2O (or D_2O) to moisturize the Ar gas. Before generating NO gas, a dry ice slush trap (mixture of propanol and dry ice pellets) was set up to trap any acidic moisture and some N_2O gas. Next, 5 ml of H_2O flushed with Ar gas was put in Flask 1 to make a 1 M NaNO_2 solution.

Then 4.5 μl 0.1 M FeSO_4 in H_2SO_4 , $\text{pH} 2.0$, was added anaerobically to Vial 1 (containing ferritin). The Ar gas flow was stopped by Valve 1. Finally, the 1 M FeSO_4 solution in 1 M H_2SO_4 was dripped into Flask 1 (containing 1 M NaNO_2). After five

minutes, the solution in Vial 1 was taken immediately with a 1 ml syringe (which was purged with Ar gas) and transferred to an Ar gas flushed standard sample tube (o.d. 5 mm and i.d. 4 mm). The sample tube was then covered with a non-pierced septa and the sample was frozen in liquid nitrogen.

Samples of ferritin in D₂O were prepared in two ways, multi-step ultrafiltration and multi-step dialysis. In multi-step ultrafiltration, a 3 ml cell attached with a YM 30 membrane was used and 1 ml ferritin solution with 2.0 mM subunit concentration was placed in the cell. Then, 2 ml MOPS buffer prepared in D₂O was added. The operating pressure was 20 psi. It took about one and half hours to squeeze out 2 ml of solution. After 1 ml ferritin solution remained in the cell, another 2 ml MOPS buffer in D₂O was added to the cell. A total of three refills was done, giving a final 1 ml solution of 96.3% D₂O in the solvent.

In multi-step dialysis, a Spectra/Por 3 dialysis bag with a molecular weight cut-off of 3,500 was used to contain 1 ml apoferritin solution with 2.0 mM subunit concentration. The dialysis bag was put in a 12 ml glass bottle filled with 3 ml MOPS buffer (pD = 7.0, 0.1 M MOPS and 0.15 M NaCl) in D₂O. The small bottle was then tightened on a shaker and put in the 4° C refrigerator. The shaker was operated continuously in order to facilitate the dialysis process. It took two days for each change and two changes was performed for the ferritin sample giving D₂O composition of 93.7% by volume in the solvent.

The model complexes (cysteine nitrosyl complex and penicillamine nitrosyl complex) were prepared following the procedures described by Wang.^[47] The solutions of

model complexes have 10 mM iron and 200 mM ligand concentrations.

Results

A. EPR Spectra of ApoHoSF-Fe-NO and Model Complexes

Ferritin iron nitrosyl and model complexes were previously investigated by our group.^[28, 47] Although no effort was put into the EPR studies of these complexes in the present research, all the complexes studied herein were scanned on our EPR spectrometer equipped with a Bruker microwave bridge.^[50] The EPR spectra are displayed in Figure 4.2. All of these EPR spectra have similar axial features. The g_{\parallel} and g_{\perp} values for each of the complexes were calculated and are tabulated in Table 4.1. The g_{\parallel} and g_{\perp} values are the same for all these complexes within experimental error.

B. Proton ENDOR of Ferritin Iron Nitrosyl Complexes

The ^1H ENDOR spectra of the HoSF-Fe-NO complex at the parallel position in both H_2O and D_2O are presented in Figure 4.3. The paired bars correspond to the measured hyperfine couplings. Both samples have four hyperfine couplings, which were measured and are presented in Table 4.2. The 0.82 MHz hyperfine coupling (a) in Figure 4.3 was partially resolved from the 1.41 MHz (b) coupling in the H_2O sample. A bump (out of the range) around -3.12 MHz was not eliminated completely by subtracting the ENDOR signal with the off-resonance background having the same number of scans. As it was not mirrored about the free proton Larmor frequency (14.90 MHz at 3500 G), it should not be from the electron spin and proton hyperfine interaction.^[4] The source of the

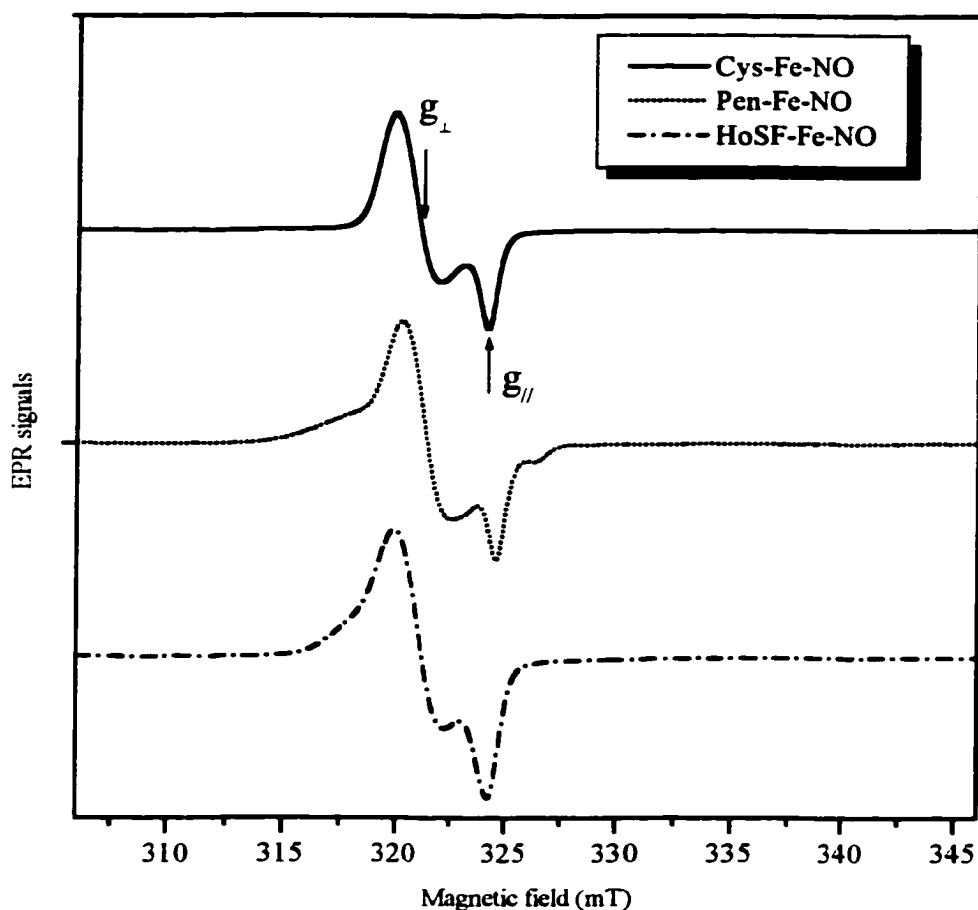


Figure 4.2 The EPR spectra of HoSF-Fe-NO and model complexes. Common Experimental conditions: Field Set, 326 mT; Scan Range, 40 mT; Microwave power, 5 mW; Modulation Frequency, 100 kHz; Modulation Amplitude, 0.1 mT; Time Constant, 0.3 s; Scan Time, 500 s; Temperature, 77 K; Spectrometer, Bruker; Individual Experimental Conditions: Cys-Fe-NO, Concentration, 10 mM; pH, 6.0; Microwave Frequency, 9.1365 GHz; Receiver Gain, 0.3 V; File Name, 98120802.fl; Pen-Fe-NO, Concentration, 10 mM; pH, 6.0; Microwave Frequency, 9.1371 GHz; Receiver Gain, 0.3 V; File Name, 98092402.fl; HoSF-Fe-NO, Concentration, 2.0 mM, pH, 7.0; Buffer, 0.1 M MOPS, 0.15 M NaCl; Microwave Frequency, 9.1358 GHz; Receiver Gain, 0.1 V; File Name, 98120501.fl; (4.2.opj)

Table 4.1 The $g_{//}$ and g_{\perp} values for the studied complexes*

	apoHoSF-Fe-NO	Cys-Fe-NO	Pen-Fe-NO
$g_{//}$	2.015 ± 0.001	2.015 ± 0.001	2.014 ± 0.001
g_{\perp}	2.033 ± 0.001	2.034 ± 0.001	2.033 ± 0.001

* The EPR spectra were measured at 77 K.

signal is unknown. The ENDOR signal amplitude of the $A = 0.82$ MHz hyperfine coupling decreased but was not eliminated for the sample prepared in D_2O (dotted lines), indicating that this hyperfine coupling arises from an exchangeable proton. The coupling d for the complex prepared in H_2O has a noise signal superimposed with itself. The coupling c for the samples prepared in both H_2O and D_2O was partially resolved from the coupling d. The stick ENDOR spectra at the bottom of Figures 4.3, 4.5 and 4.7 - 4.10 indicate the expected ENDOR resonance frequencies from molecular modeling calculations, as detailed later in this Chapter.

The sample in D_2O was prepared by incubating ferritin in D_2O MOPS buffer (0.1 M MOPS, 0.1 M NaCl, pD = 7.0) for two days. However, the ENDOR results indicated that a longer time is needed for a complete proton exchange in ferritin. Horse spleen apoferritin incubated in D_2O buffer for seven to fourteen days gave no ferritin iron nitrosyl EPR signal, suggesting that deuteration of the protein caused a structural change or possible damage to it. In order to minimize possible damage to the protein, two methods were tried in the deuteration of the ferritin samples. One method used a series of ultra-filtration steps. The other one used multi-dialysis changes against the buffer in D_2O . No

Table 4.2 The ^1H ENDOR couplings (MHz) of HoSF-Fe-NO and model complexes. ^{a b}

	at parallel position, //					at perpendicular position, \perp				
	a	b	c	d	e	a'	b'	c'	d'	e'
$\begin{array}{c} \text{SH} \\ \\ \text{CH}_2 \\ \\ \text{HO}_2\text{C}-\text{C}-\text{NH}_2 \\ \\ \text{H} \end{array}$ l-Cysteine	(-)<u>0.60</u>	1.48	2.90	—	—	2.78	3.70	—	—	—
$\begin{array}{c} \text{SH} \\ \\ \text{H}_3\text{C}-\text{C}-\text{CH}_3 \\ \quad \\ \text{HO}_2\text{C}-\text{C}-\text{NH}_2 \\ \\ \text{H} \end{array}$ l-Penicillamine	0.35	<u>1.18</u>	(-)1.69	1.87	2.83	<u>0.42</u>	(-)1.17	(-)2.59	3.88	—
HoSF	a	b	c	d	e	a'	b'	c'	d'	e'
	<u>0.82</u>	1.41	2.32	3.06	—	(-)0.79	(-)1.36	(-)1.75	<u>3.34</u>	(-)4.30

a. Bold numbers from exchangeable protons. Error is ± 0.05 MHz. Signs of coupling constants in parentheses are inferred from the dipole calculation.

b. The underlined couplings of the complexes are from the same proton, and are both positive at the parallel and the perpendicular field positions.

EPR signals were observed for samples prepared by either method. As the apoHoSF protein shell is less stable, holoHoSF was used to prepare the HoSF-Fe-NO in D_2O as well. Still no EPR signal was obtained. All the samples in D_2O were then tested by gel electrophoresis, which gave no indication of molecular breakup (see Figure 4.4). The top lighter bands are from dimers in the protein samples.

Figure 4.5 shows the ENDOR spectra of ferritin iron nitrosyl complexes in H_2O and D_2O taken at the EPR perpendicular position. These spectra had stronger ENDOR signals than those at the parallel position. There are five apparent hyperfine couplings.

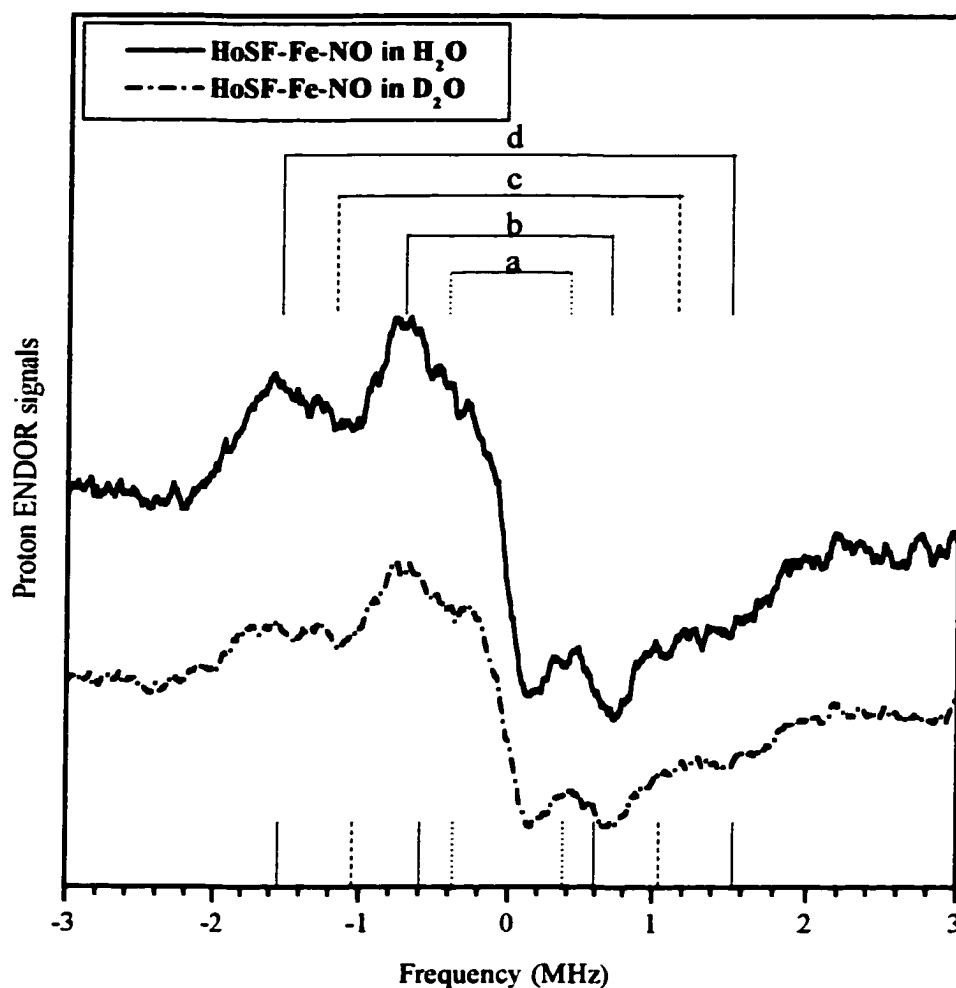


Figure 4.3 The proton ENDOR spectra of HoSF-Fe-NO complexes at parallel position. Common Experimental Conditions: Ferritin Subunit Concentration, 2.0 mM; Iron Concentration, 0.67 mM; Buffer, 0.1 M MOPS; Microwave Power, 2 mW; Radio Frequency Power, 100 W; Modulation Depth, 2.0 V (220 kHz); Time Constant, 0.1 s; Scan Rate, 0.5 MHz/s; Temperature, 2.4 K; Scan Range, 10 MHz; Number of Scans, 150; Individual Experimental Conditions: HoSF-Fe-NO in H₂O, Receiver gain, 50,000; File Name, 98102302.flis; HoSF-Fe-NO in D₂O, Receiver gain, 32,000; File Name, 98102301.flis; The dotted lines are couplings from the exchangeable protons; The dash lines are from α protons; The solid lines are from methylene protons; (4.3.opj).

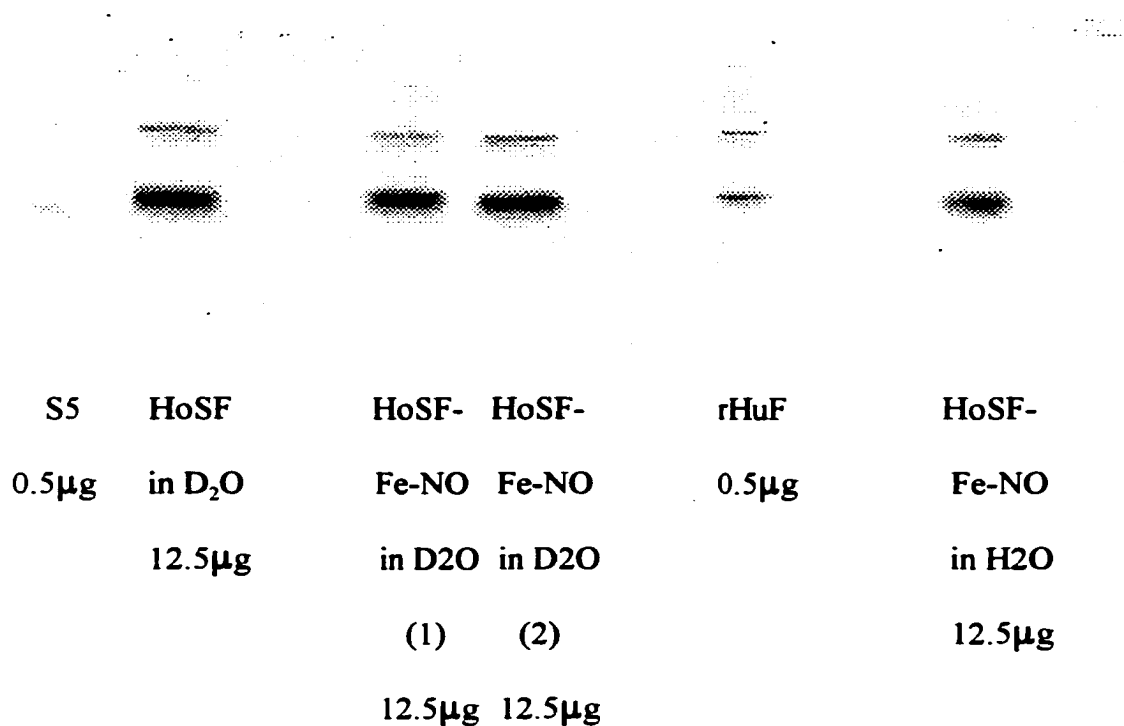


Figure 4.4 The molecular weight assay of ferritin samples by Gel Electrophoresis. Experimental conditions: Buffer, 10 mM MOPS for 0.5 μ g samples, 0.4 mM MOPS for 12.5 μ g samples; pH, 7.0 for samples in H_2O , 7.4 for samples in D_2O ; Voltage, 125 V; Current Set, 400 μ A; Time, 1.5 hours; Gel, native, 8% Tris-Glycine Gel from NOVEX.

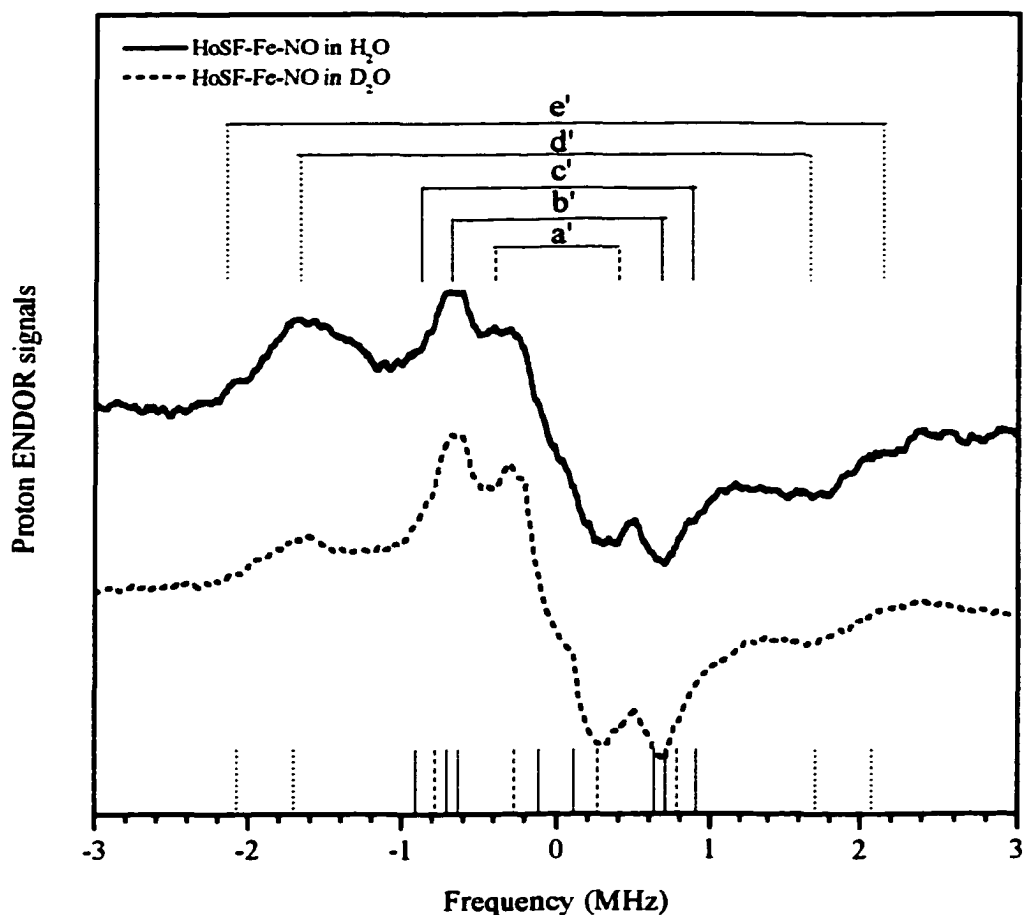


Figure 4.5 The proton ENDOR spectra of HoSF-Fe-NO complexes at perpendicular position. Common Experimental Conditions: Ferritin Subunit Concentration, 2.0 mM; Iron Concentration, 0.67 mM; Buffer, 0.1 M MOPS; Microwave Power, 2 mW; Radio Frequency Power, 100 W; Modulation Depth, 2.0 V (220 kHz); Time Constant, 0.1 s; Scan Rate, 0.5 MHz/s; Temperature, 2.4 K; Scan Range, 10 MHz; Number of Scans, 150; Individual Experimental Conditions: HoSF-Fe-NO in H₂O, Receiver gain, 50,000; File Name, 98102302.flis; HoSF-Fe-NO in D₂O, Receiver gain, 32,000; File Name, 98102301.flis; The dotted lines are from exchangeable protons; (4.5.opj).

The measured couplings are listed in Table 4.2. The $A = 1.36$ MHz coupling (b') consists of three overlapped couplings (see the following section). The largest hyperfine couplings of $A = 4.30$ and 3.34 MHz show a smaller amplitude for the D_2O sample (Figure 4.5). Therefore, these hyperfine coupling signals come from an exchangeable proton as well. A bump at -2.92 MHz out of the spectral range of Figure 4.5 is from the same source as that in Figure 4.3.

C. ENDOR Spectra of Model Complexes

The temperature dependence of the 1H ENDOR spectral intensity of Cys-Fe-NO complex was measured. It was found that in the range of $10 - 30$ K, the ENDOR signals were strong. Above 70 K and below 5 K, the signal was very weak or there was no ENDOR signal. Figure 4.6 shows the temperature dependence of the Cys-Fe-NO complex ENDOR signal. ^{14}N ENDOR peaks were sought under the same conditions as that used to obtain 1H ENDOR, but were not observed. As the model complexes have at least six and nine protons for Cys-Fe-NO and Pen-Fe-NO, respectively, some hyperfine couplings were not resolved in the spectra. The following are the tentative assignments of the hyperfine couplings. A complete explanation of the 1H ENDOR spectra of the model complexes is an ongoing project.

The ENDOR spectra of Pen-Fe-NO in H_2O and D_2O at the parallel position are presented in Figure 4.7. The sample in H_2O has five hyperfine couplings. The measured hyperfine splittings are given in Table 4.2. The decrease in intensity of the hyperfine splittings of 2.83 (coupling e) and 0.35 (coupling a) MHz indicates that these couplings

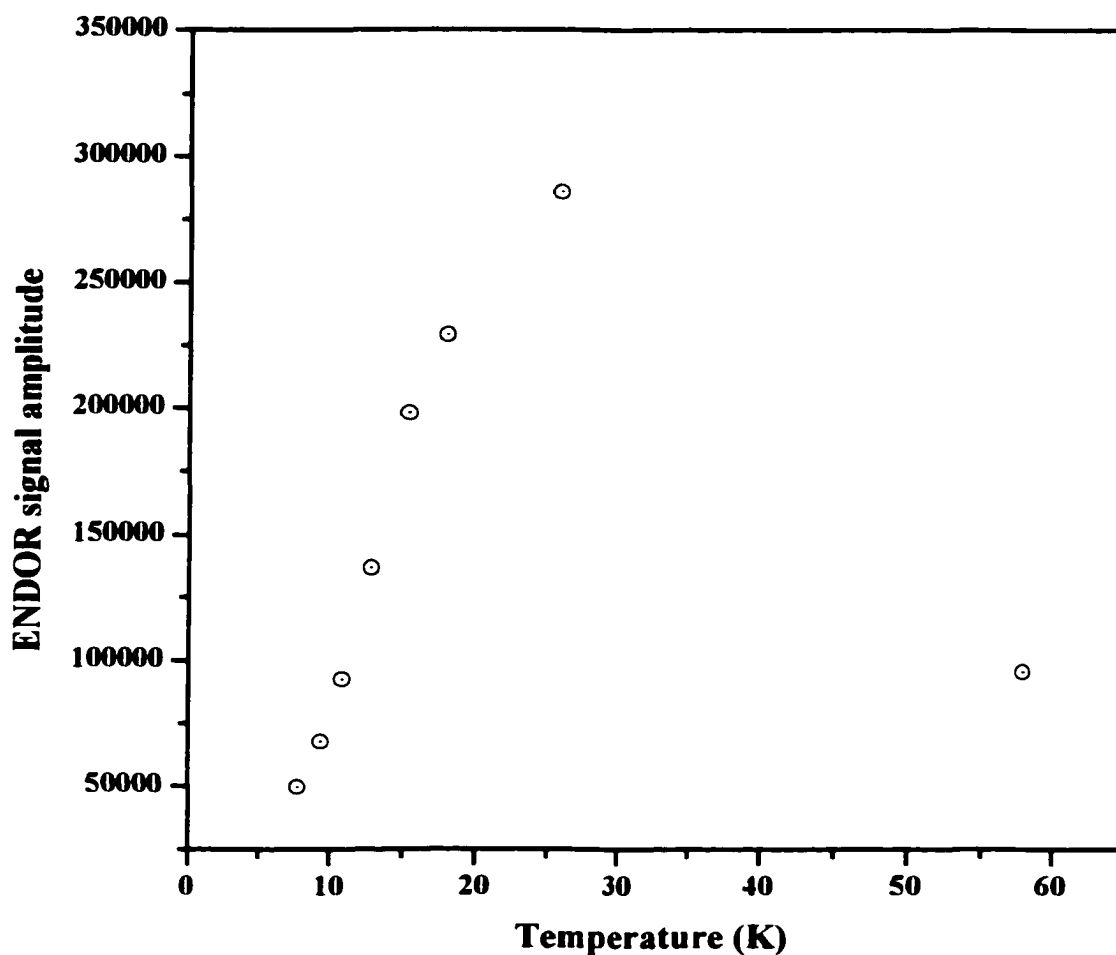


Figure 4.6 Temperature dependence of ENDOR signal amplitude of Cys-Fe-NO complex. Experimental conditions: Buffer, None; pH, 6.0; Concentration of Complex, 10 mM; Radio Frequency Power, 100 W; Modulation Depth, 1.0 V (110 kHz); Time Constant, 0.1 s; Scan Rate, 0.5 MHz/s; Temperature, Various; Scan Range, 10 MHz; Microwave Power, 2 mW; Receiver gain, Various; Number of Scans, 20; File Name, 99112420 - 99112427.flis; (4.6.opj).

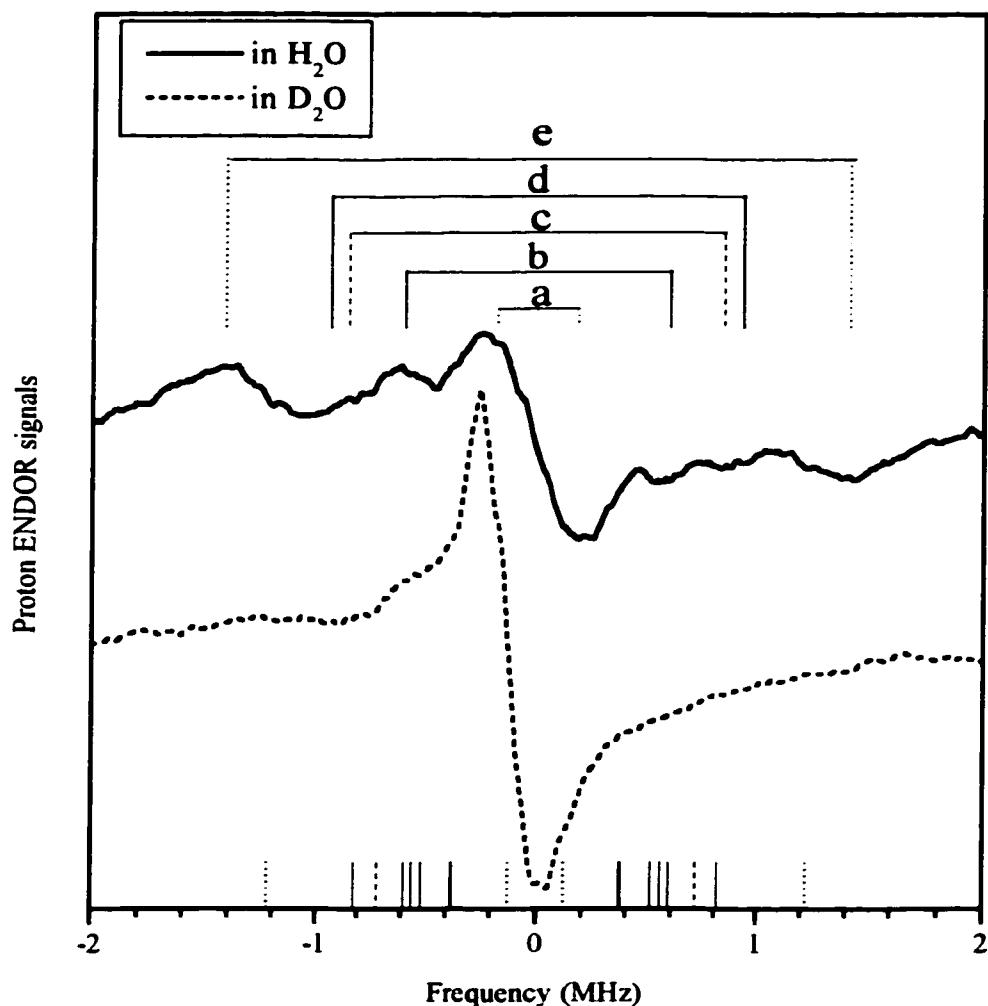


Figure 4.7 The ^1H ENDOR spectra of Pen-Fe-NO at parallel position. Common Experimental Conditions: Buffer, None; pH, 6.0; Concentration of Complex, 10 mM; Radio Frequency Power, 100 W; Modulation Depth, 2.0 V (220 kHz); Time Constant, 0.1 s; Scan Rate, 0.5 MHz/s; Temperature, 2.35 K; Scan Range, 10 MHz; Individual Experimental Conditions: Pen-Fe-NO in H_2O , Microwave Power, 1 mW; Receiver gain, 50,000; Number of Scans, 50; File Name, 98102303.fl; Pen-Fe-NO in D_2O , Microwave Power, 10 mW; Receiver gain, 32,000; Number of Scans, 10; File Name, 98101907.fl; The stick ENDOR spectrum at the bottom of the graph was obtained from the model calculations with the axis tilt of -9° . The dotted lines represents the couplings from the exchangeable protons, dashed lines from the α protons and solid lines from the methyl protons (4.7.opj).

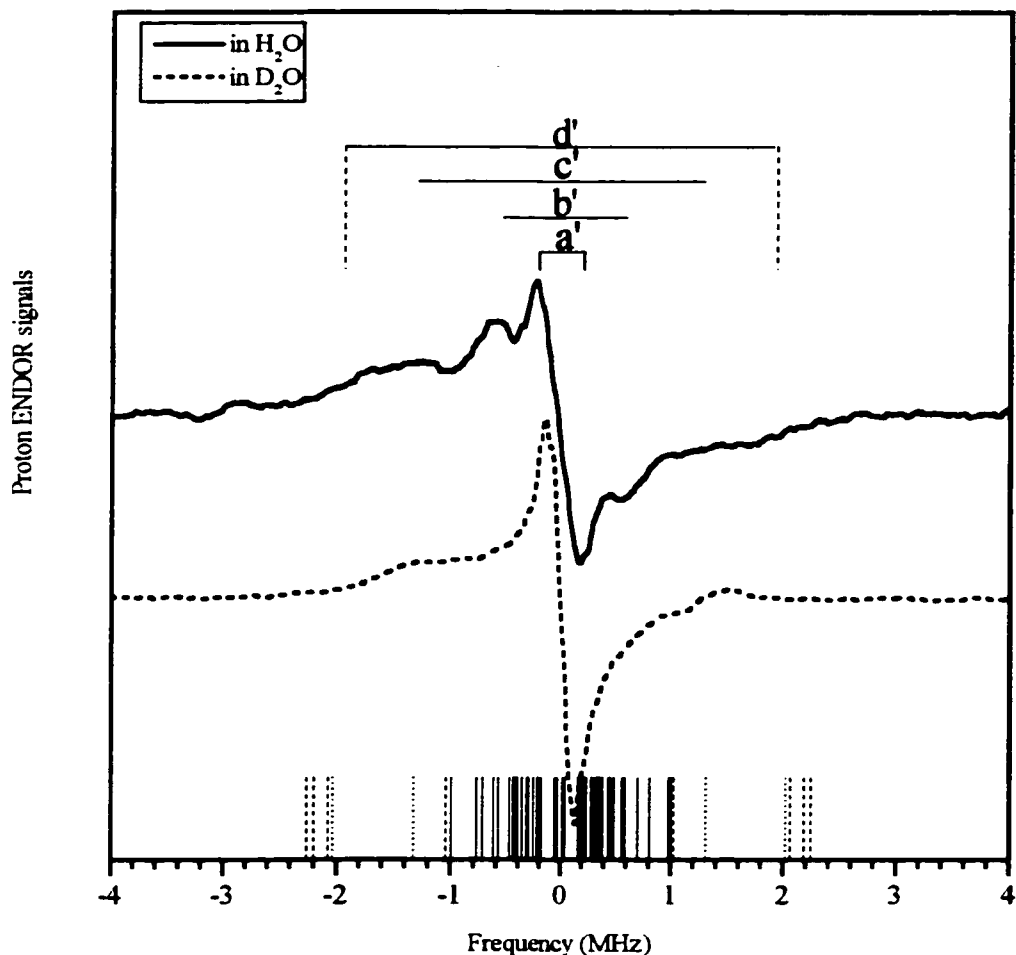


Figure 4.8 The ^1H ENDOR spectra of Pen-Fe-NO at perpendicular position. Common Experimental Conditions: Concentration of complex, 10 mM; Buffer, None; pH, 6.0 for complex in H_2O , 6.4 for complex in D_2O ; Radio Frequency Power, 100 W; Modulation Depth, 2.0 V; Time Constant, 0.1 s; Scan Rate, 0.5 MHz/s; Scan Range, 10 MHz; Individual Experimental Conditions: Pen-Fe-NO in H_2O , Microwave Power, 1 mW; Receiver gain, 50,000; Number of Scans, 50; File Name, Temperature, 2.31 K; 98102305.flx; Pen-Fe-NO in D_2O , Microwave Power, 10 mW; Receiver gain, 32,000; Number of Scans, 10; File Name, 98101908.flx; The line types are the same as in Figure 4.7 (4.8.opj).

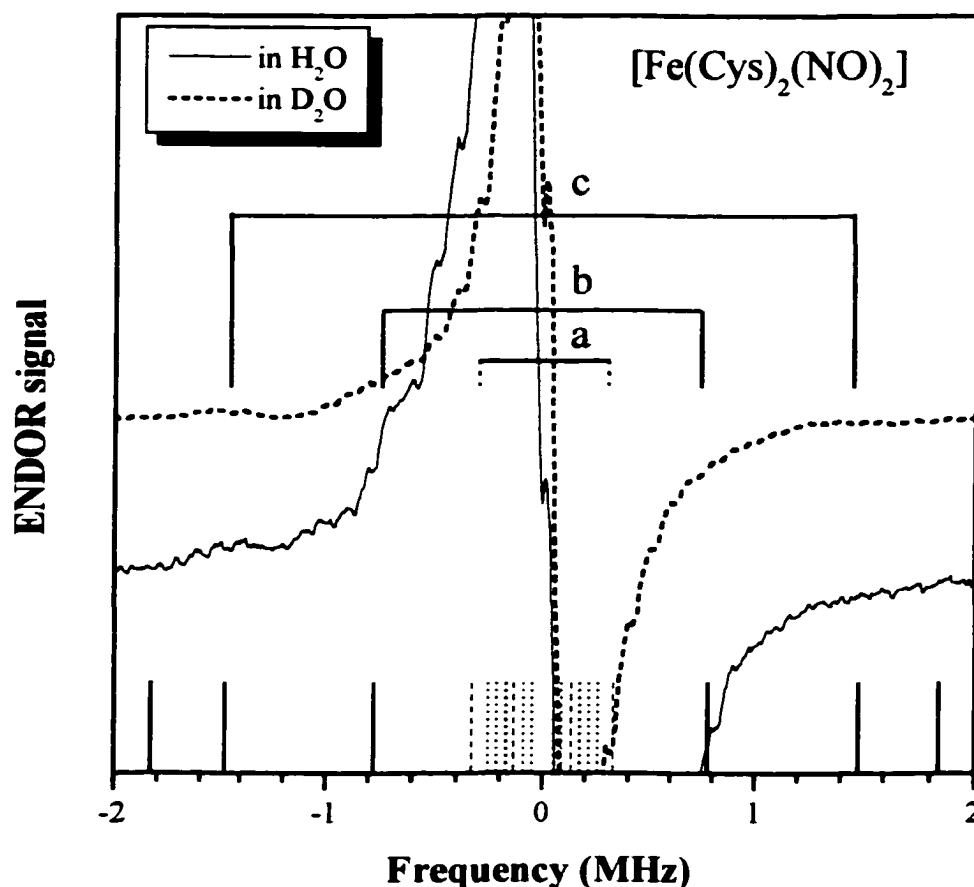


Figure 4.9 The proton ENDOR spectra of Cys-Fe-NO complexes at the parallel field position. The EPR spectra were the same for the samples in H₂O and D₂O. The steps on the curve could be the artifacts due to the ENDOR circuit of the spectrometer. Common experimental conditions: Complex concentration, 10.0 mM; Buffer, none; pH, 6.0; Microwave power, 2 mW; Radio frequency power, 100 W; Modulation depth, 1.0 V (110 kHz); Time constant, 0.03 s; Scan rate, 0.5 MHz/s; Temperature, 24.0 K; Scan range, 10 MHz; Number of scans, 200; Individual experimental conditions: In H₂O, Receiver gain, 25,000; File name, 99112431.fl; In D₂O, Receiver gain, 8,000; File name, 99112430.fl; The inset graph shows the full scale ENDOR signals for both samples at the parallel field position. The line types are the same as in Figure 4.7. (4.9.opj).

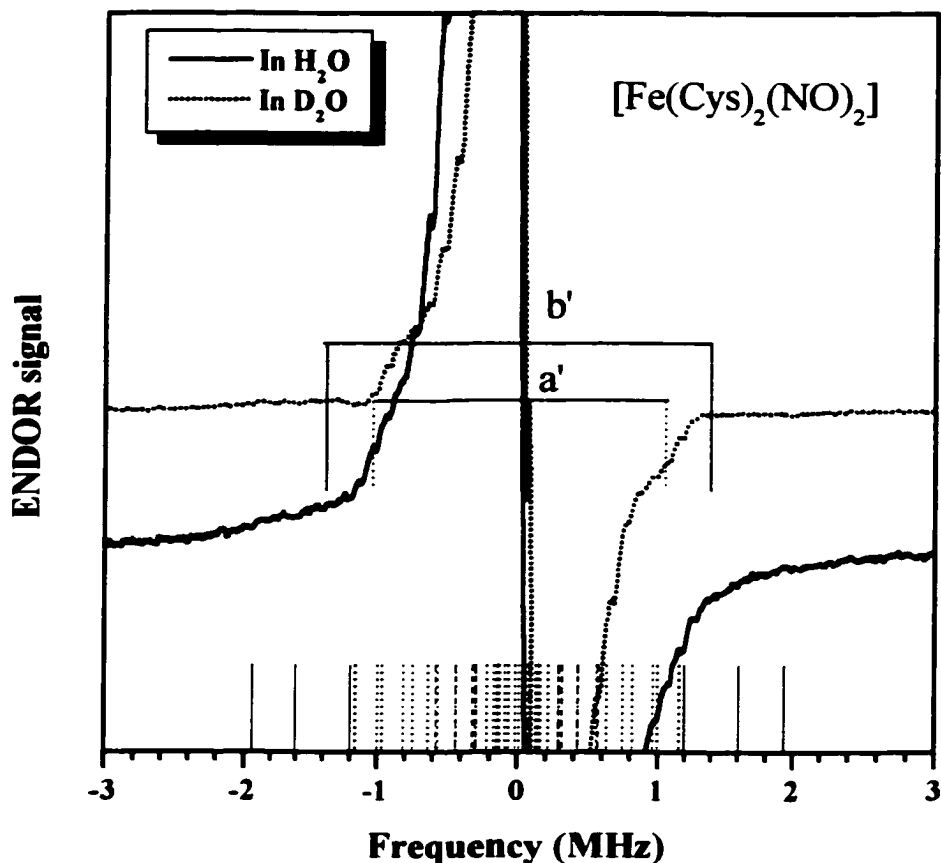


Figure 4.10 The proton ENDOR spectra of Cys-Fe-NO complexes at perpendicular position. The steps on the curve could be the artifacts due to the ENDOR circuit of the spectrometer. Common experimental conditions: Complex concentration, 10.0 mM; Buffer, none; pH, 6.0; Microwave power, 2 mW; Radio frequency power, 100 W; Modulation depth, 1.0 V (110 kHz); Time constant, 0.03 s; Scan rate, 0.5 MHz/s; Temperature, 24.0 K; Scan range, 10 MHz; Number of scans, 50; Individual experimental conditions: In H_2O , Receiver gain, 4,000; File name, 99112428.flc; In D_2O , Receiver gain, 1,600; File name, 99112429.flc; The inset graph shows the full scale ENDOR signals for both samples at perpendicular position. The line types are the same as in Figure 4.7 (4.10.opj).

arise from exchangeable protons (dotted lines). The 1.18 MHz peak (coupling b) is from the summation of five closely distributed peaks (see below).

Figure 4.8 displays the ENDOR spectra of Pen-Fe-NO in H₂O and D₂O at the perpendicular position in the spectrum of Figure 4.2. Four hyperfine couplings were observed (Table 4.2). The exchangeable proton responsible for the 1.17 and 2.59 MHz couplings b' and c' were present in the H₂O sample and absent or partially absent in the D₂O sample. The center peak a' of 0.42 MHz represents many overlapped hyperfine couplings. The exchangeable proton splittings at the parallel position were different from that at the perpendicular position, 0.35 and 2.83 (a and e in Figure 4.7) vs. 1.17 and 2.59 MHz (b' and c' in Figure 4.8), respectively.

Similarly, ENDOR spectra were obtained for Cys-Fe-NO complexes. The parallel and perpendicular ENDOR spectra of samples in both H₂O and D₂O are displayed in Figure 4.9 and Figure 4.10, respectively. The three hyperfine splittings at the parallel field position and two hyperfine couplings at the perpendicular field positions were measured (Table 4.2). The center a' peak represents unresolved couplings.

D. Molecular Modeling of Iron Nitrosyl Complexes

In order to make correct assignments of the peaks in the ENDOR spectra, molecular modeling calculations were carried out for all the complexes. Bond lengths were taken from the CRC Handbook of Chemistry and Physics 79 ed. and the literature,^[57] and are presented in Table 4.3. The models of the complexes were made and energetically minimized with ChemSite software using quenched molecular dynamics and are displayed

Table 4.3 The bond lengths chosen for the model complex modeling.

Bond type ^a	r (Å)	Reference
Csp ³ - Csp ³	1.53	100
Csp ³ - Csp ²	1.51	100
Csp ³ - H(methylene)	1.09	100
C sp ³ - H(methyl)	1.06	100
C sp ³ - N(4)	1.48	100
C sp ³ - S(2)	1.82	100
C sp ² = O(2)	1.21	100
Csp ² - O(2)	1.31	100
N(4) - H	1.03	100
O(2) - H	1.02	100
N(4) - Fe(4)	2.18	57
S(2) - Fe(4)	2.34	57
ON - Fe(4)	1.68	57
N ≡ O	1.15	57

a. Specification of elements in the bond, with coordination number given in parentheses, and bond type (single, double, etc.). For carbon, the hybridization state is given.

in Figure 4.11 and 4.12 for Cys-Fe-NO (monodentate ligation through sulfur and a water molecule H-bonded with the two sulfur atoms) and Pen-Fe-NO (bidentate ligation through sulfur and the amine nitrogen), respectively. The distance between each proton to the iron center was determined from the program.

The ChemSite Molecular Modeling program was also used to envision the local structure of the HoSF-Fe-NO complex (bidentate ligation). Only the three fold channel part of the protein structure was regenerated and manipulated here.

First, the protein file `pdbl1ier.pdb`^[58] of the tetragonal crystal structure of native horse spleen ferritin was abbreviated by deleting unwanted structural data from the original file, leaving only the three subunits surrounding the three-fold channel, and saved in `hrs3fold.ent`. Then, `hrs3fold.ent` was loaded in the ChemSite program. Later, an iron atom was added and bonded to both S and N on the Cys130 residue. Then, two NO molecules were added and bound with the iron atom. Finally, three protons were introduced into the complexes, one on the α carbon and the other two on the methylene carbon of Cys130. Afterwards, the S, N, Fe, two NO and the three proton atoms or molecules were selected as moveable atoms or molecules. Then, an energy minimization (quenched molecular dynamics) was performed on these groups of atoms holding the bond lengths fixed but varying the bond angles. The structure of the HoSF-Fe-NO complex near the ferritin three fold channel is shown in Figure 4.13. The enlarged view of the complex structure is in Figure 4.14.

The angle ϕ_0 between the iron-proton vector and the pseudo symmetry axis which approximately bisects the ON-Fe-NO angle (see Figure 4.17) could not be determined

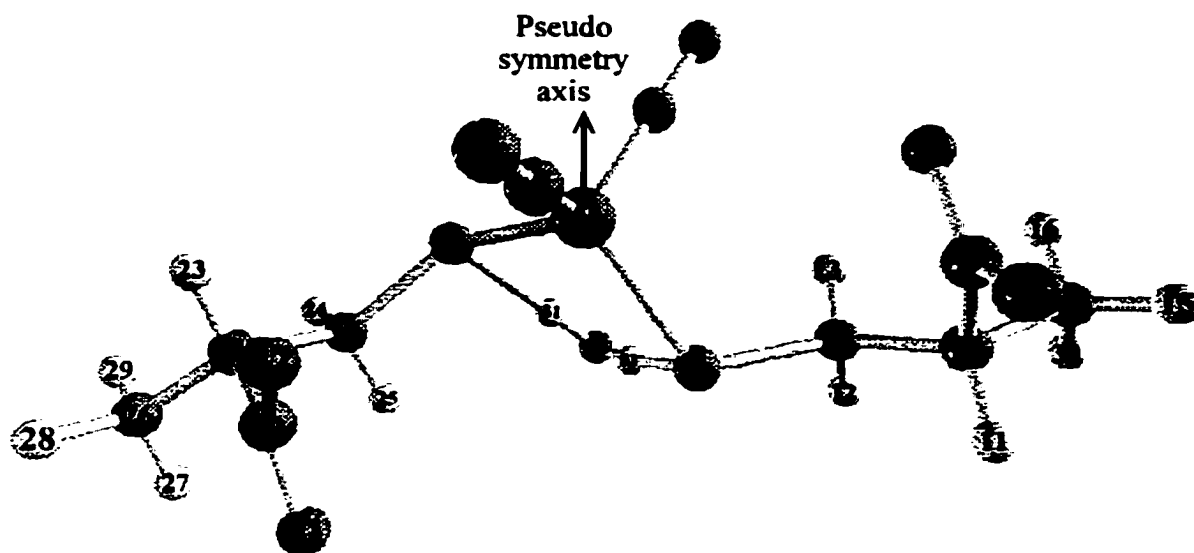


Figure 4.11 The model of Cys-Fe-NO complex. 0 is Fe; 3,5,14 and 26 N; 4, 6, 9, 10, 21 and 22 are O; 2, 7, 8, 18, 19 and 20 C; 1 and 17 S; 11, 12, 13, 15, 16, 23, 24, 25, 27, 28, 29, 30, 31 and 33 H. File name, 4.11.wpd.

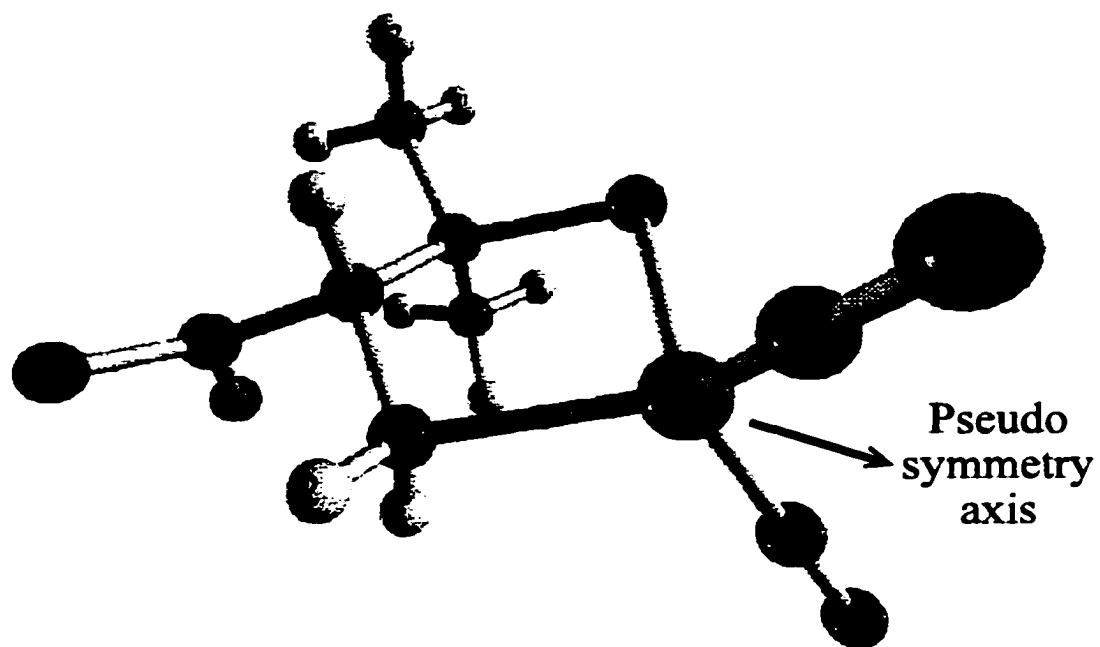


Figure 4.12 The model of Pen-Fe-NO complex. 0 is Fe; 1, 6 and 8 N; 7, 9, 12 and 13 are O; 5, 10, 11 and 19 C; 4 S; 2, 3, 14, 16, 17, 18, 20, 21 and 22 H. File name, 4.12.wpd.

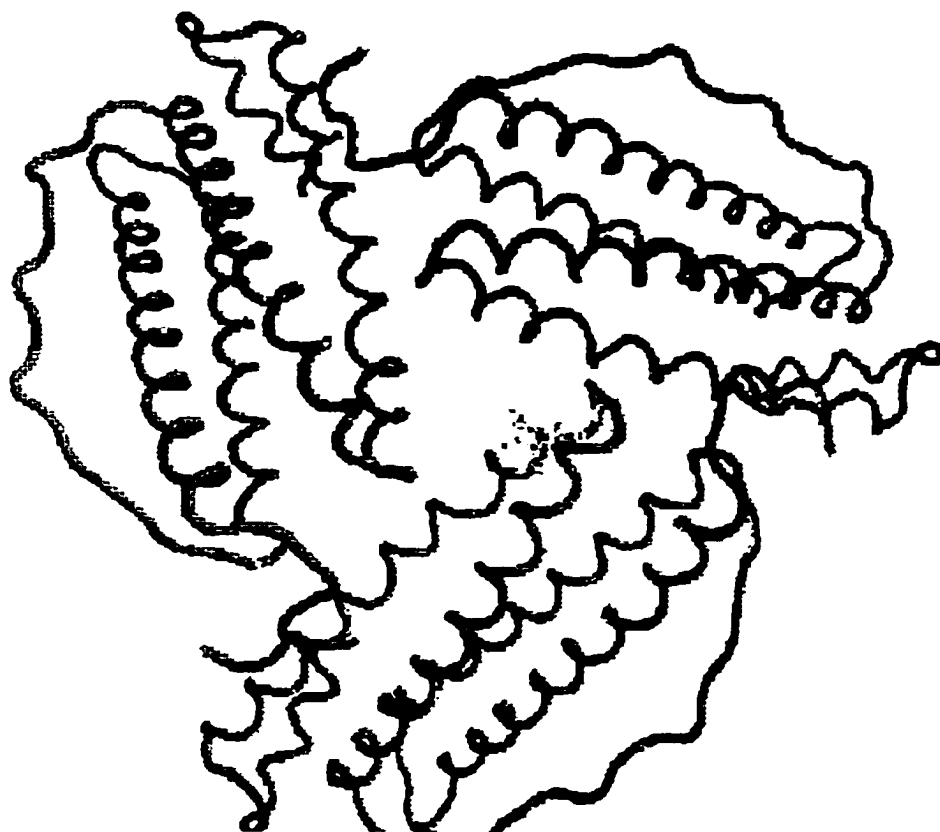


Figure 4.13 The visual local structure of HoSF-Fe-NO in ferritin 3-fold channel generated with Chemsite Molecular Modeling. File name, 4.13.wpd

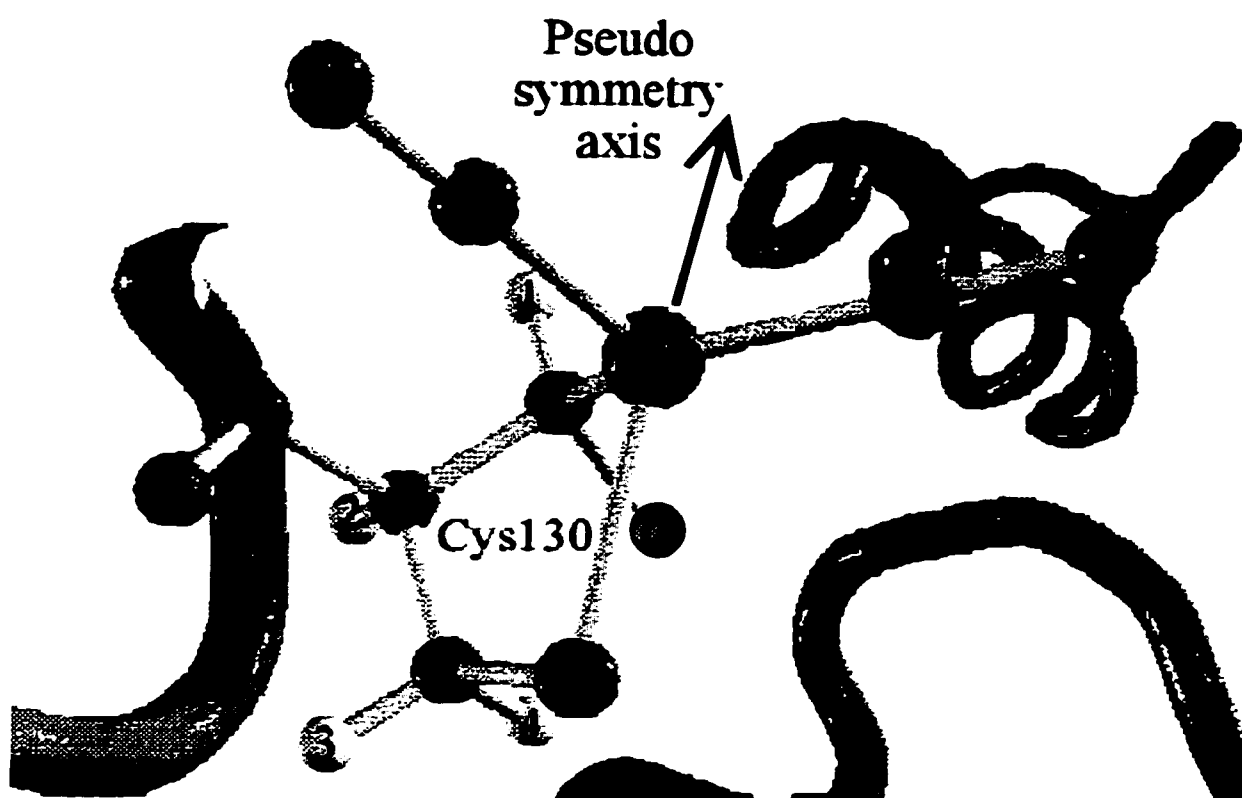


Figure 4.14 The enlarged view of the complex structure of ferritin iron nitrosyl complex.
File name, 4.14.wpd.

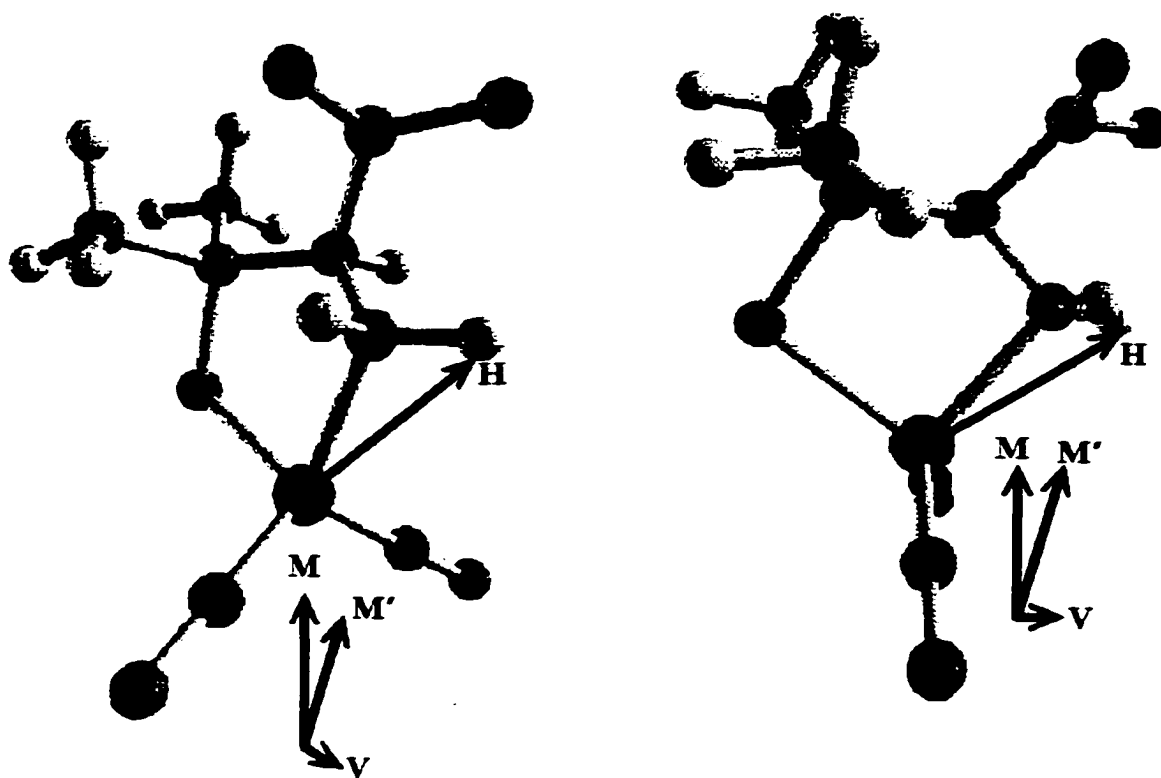


Figure 4.15 The schematic diagram for the vector operation on Penicillamine iron nitrosyl complex. File name, 4.15.wpd.

directly by ChemSite. Thus, vector operation was used to determine the ϕ_0 along with a triangle method as an independent check of the calculation (see Appendix H). The schematic diagram of the vector operation on the cysteine iron nitrosyl complex is shown in Figure 4.15, where the **M** vector represents the pseudo-symmetry axis. The coordinates of the atoms in complexes are arbitrarily generated in ChemSite. The system origin is first moved to the iron center by $A_i(x_i-x_{Fe}, y_i-y_{Fe}, z_i-z_{Fe})$, where A_i represents any atom in the complex. Then the coordinates of the midpoint between the two nitrosyl nitrogens are obtained with $M((x_{N1}+x_{N2})/2, (y_{N1}+y_{N2})/2, (z_{N1}+z_{N2})/2)$. The vector from the iron origin to any proton and the vector from the midpoint **M** to the iron can then be expressed by $H_i(x_{hi}, y_{hi}, z_{hi})$ and $M(-x_m, -y_m, -z_m)$. From the vector dot product $M \cdot H = |M| |H| \cos(\phi_0)$, we obtain

$$\phi_0 = \cos^{-1}\left(\frac{M \cdot H}{|M| |H|}\right) \quad 4.1$$

Here, $M \cdot H = x_mx_h + y_my_h + z_mz_h$ and $|M| = (x_m^2 + y_m^2 + z_m^2)^{1/2}$ and $|H| = (x_h^2 + y_h^2 + z_h^2)^{1/2}$.

In order to tilt the g-tensor axis toward the normal of the N1-Fe-N2 plane where the vector **M** of the pseudo symmetry axis lies, a unit vector **V** is generated by the vector cross product

$$V = \frac{N1 \times N2}{|N1| |N2|} \quad 4.2$$

where,

$$N1 \times N2 = \begin{vmatrix} y_{N1} & z_{N1} \\ y_{N2} & z_{N2} \end{vmatrix} \mathbf{i} + \begin{vmatrix} z_{N1} & x_{N1} \\ z_{N2} & x_{N2} \end{vmatrix} \mathbf{j} + \begin{vmatrix} x_{N1} & y_{N1} \\ x_{N2} & y_{N2} \end{vmatrix} \mathbf{k} \quad 4.3$$

Here, **i**, **j** and **k** are the unit vectors of the arbitrary axis system. The sum of the two vectors **M** and **kV** (where **k** is a scalar constant) gives a new vector **M'** corresponding to the principle axis of the **g** tensor.

$$\mathbf{M}' = \mathbf{M} + k\mathbf{V} = (x_M + kx_V)\mathbf{x} + (y_M + ky_V)\mathbf{y} + (z_M + kz_V)\mathbf{z} \quad 4.4$$

Equation 4.1 is used to calculate the angle ϕ_0 between **M'** and **H**. The tilt angle can be obtained by adjusting the scalar **k**. When **k** = 0, **M'** = **M** and the pseudo symmetry axis and the principle axis of the **g**-tensor coincide.

By changing the tilt angle and calculating the hyperfine couplings with Equation 4.6 (see next section), we were able to match the calculated couplings with the experimental ones rather well for the protein complex but less so for the model complexes (see Figures 4.3, 4.5, 4.7 - 4.10). The tilt angle of the **g**-tensor axis out of the N-Fe-N plane and the corresponding hyperfine couplings are presented in Table 4.4. The calculated stick bar spectra are presented at the bottom of the experimental spectra in Figures 4.3, 4.5 and 4.7 - 4.10. The calculated couplings also enable us to assign the sign for the experimental couplings. The bond lengths and angles for the first coordination sphere ligand atoms are listed in Table 4.4a.

The model calculation for HoSF-Fe-NO gives four separate couplings at the parallel field position and eight partially mixed couplings at the perpendicular position (symmetrically placed pairs of bars at the bottom of Figures 4.3 and 4.5). The exchangeable proton gave the smallest splitting (0.74 MHz) at the parallel position but the largest ones (3.41 and 4.15 MHz) at the perpendicular position. Three adjacent peaks with coupling **b'** in the perpendicular spectrum near 1.4 MHz (i.e. -1.27, -1.41 and -1.56

MHz) arise from each of the three different non-exchangeable protons (one α proton and two methylene protons). The smallest splitting of 0.22 MHz at the perpendicular position from methylene proton 3 (see Figure 4.14) could not be distinguished in the spectra. Thus, four peaks at the parallel position and five at the perpendicular position were observed in the proton ENDOR spectra. A tilt angle of 10.5° off the pseudo symmetry axis out of the N-Fe-N plane toward the amide nitrogen was required to fit the spectra. Such a large tilt is most likely due to the restriction imposed by the protein shell on the ligand coordination.

In Pen-Fe-NO, there are a total of nine protons, including six methyl protons, two amine protons and one α carbon proton. A tilt angle of -9° off the pseudo symmetry axis out of the N-Fe-N plane was made to fit the ENDOR spectra (Figure 4.7). At the parallel position, there are nine splittings (Table 4.4). The two exchangeable protons generate two experimental splittings, one is the smallest splitting (0.35 MHz, similar to that in HoSF-Fe-NO) and another is the largest coupling (2.83 MHz) (see Tables 4.2 and 4.4). The calculated values are 0.25 and 2.44 MHz (Table 4.4). The experimental coupling of 1.69 MHz is from the α carbon proton. Five splittings are crowded around 1.2 MHz, which are from five methyl protons. The sixth methyl proton gives a coupling of 1.87 MHz, distinct from the other five protons. Consequently, five splittings are resolved from the ENDOR spectra.

The total number of possible splittings is eighteen from the nine protons at the perpendicular position (Figure 4.8). The methyl proton couplings are crowded around the center peak, which is not exchangeable.

The modeling calculations of bidentate ligation of cysteine with iron do not give stick spectra that match with the ENDOR spectra. Thus, monodentate cysteine ligated complexes were sought with water molecule H-bonded with NO or S in the complexes. It is found that, with a water molecule H-bonded between the two sulfur atoms, the stick spectra basically fit the ENDOR spectra at both parallel and perpendicular positions. Better resolved ENDOR spectra (measured by Wang^[47]) along with the stick spectra for both Pen-Fe-NO and Cys-Fe-NO are presented in Appendix I.

The methylene protons in Cys-Fe-NO give large couplings (6.21, 5.39, 4.49 and 3.62 MHz) at the parallel position. The two α protons have couplings of -0.66 and -0.27 MHz. The exchangeable protons are crowded around the center peak and revealed by the fact that the spectra for Cys-Fe-NO prepared in D₂O has a narrower center peak than does Cys-Fe-NO in H₂O. At the field perpendicular position, there are too many couplings spreading ± 1 MHz around the Larmor frequency. So couplings are barely resolved couplings in the ENDOR spectra.

There are several pairs of A_{\parallel} and $A_{\perp}^{90-\phi_0}$. (exclude A_{\perp}^{90}) in Table 4.4 (underlined) which are both positive. This is true for a proton located at a certain geometric position relevant to the iron center. Figure 4.16 shows the angle dependence of the hyperfine couplings on the proton spherical positions. Figure 4.16 shows that the hyperfine couplings at both parallel and perpendicular positions are positive when ϕ_0 of a proton is between 35 and 55 degrees (Tables 4.4 and 4.5).

E. Distances of Fe Ion to the Surrounding Protons

The measured hyperfine couplings of the iron nitrosyl complexes can be used to calculate the distances from the center iron to the surrounding protons. Since the EPR spectra have g-values near 2.0, a single $S = 1/2$ unpaired electron is responsible for the spectrum. The electron-nuclear dipole-dipole interactions dominate the electron nuclear hyperfine coupling. In addition, according to our previous work,^[47] it is likely that these iron nitrosyl complexes have tetrahedral structures. As a result, little unpaired electron density is expected on the ligand nuclei. So the isotropic hyperfine coupling (which arises from Fermi contact) can be ignored and the point dipole approximation used.

Equation 4.5 is a general formula for the hyperfine interactions under the condition of the point dipole approximation.^[51]

$$A_{\text{obs}} = \beta_e \beta_n g_e g_n (3 \cos^2 \phi - 1) / hr^3 + A_{\text{iso}} \quad 4.5$$

Figure (4.17) is the schematic diagram of the coordination system for the hyperfine interaction. In Equation 4.5, r is the distance between the proton and the unpaired electron. A_{obs} is the experimentally observed hyperfine splitting. A_{iso} is the isotropic hyperfine coupling. β_e and β_n are electron magneton and nuclear magneton, respectively. g_n is the nuclear g-value. g_e is the effective g-value given by $g = (g_{\parallel}^2 \cos^2 \theta + g_{\perp}^2 \sin^2 \theta)^{1/2}$, where θ is the angle between B_0 and the pseudo symmetry axis of the complex, i.e. the principle axis of the g-tensor (see Figure 4.17). ϕ is the angle between the magnetic field and the r vector connecting the unpaired electron and the interacting hydrogen nucleus.

By neglecting the isotropic component and keeping only the dipolar term, Equation 4.5 can be rewritten as Equation 4.6.

Table 4.4 The calculated ϕ_0 and proton hyperfine couplings with a tilted pseudo symmetry axis.

Ferritin-Fe-NO							
Protons ^a	no tilt	tilt 10.5° ^b	ϕ_0 change	$A_{//}$ ^c	$A_{\perp}(90^\circ-\phi_0)$ ^f	A_{\perp}^{90}	$r(\text{\AA})$ ^d
1	61.1	51.2	-9.9	0.74	3.41	-4.15	2.75
4	7.9	18.4	10.5	3.09	-1.27	-1.81	2.62
3	30.9	38.4	7.5	1.19	0.22	-1.41	3.81
2	32.5	27.9	-4.6	2.09	-0.53	-1.56	3.93
Pen-Fe-NO							
Protons ^a	no tilt	tilt - 9° ^b	ϕ_0 change	$A_{//}$ ^c	$A_{\perp}(90^\circ-\phi_0)$	A_{\perp}^{90}	$r(\text{\AA})$ ^d
2	62.0	53.6	-8.4	0.25	4.14	-4.38	2.70
3	51.8	44.2	-7.6	2.44	2.06	-4.51	2.67
14	32.4	-113.0	-145.4	-1.43	4.06	-2.64	3.20
16	22.1	24.4	2.3	1.18	-0.39	-0.79	4.77
17	38.3	38.7	0.4	1.63	0.34	-1.97	3.52
18	36.6	42.3	5.7	0.74	0.41	-1.15	4.22
20	8.3	15.7	7.4	1.11	-0.48	-0.62	5.18
21	25.0	33.7	8.7	0.75	-0.05	-0.70	4.98
22	27.2	33.3	6.1	1.02	-0.09	-0.93	4.53
Cys-Fe-NO ^e							
Protons ^a	no tilt	tilt 0° ^b	ϕ_0 change	$A_{//}$ ^c	$A_{\perp}(90^\circ-\phi_0)$	A_{\perp}^{90}	$r(\text{\AA})$ ^d
11	81.6	81.6	0.0	-0.66	1.37	-0.70	4.91
12	62.3	62.3	0.0	4.49	3.52	1.89	4.43
13	79.0	79.0	0.0	5.39	2.77	1.74	3.53
15	98.0	98.0	0.0	-0.34	0.70	-0.36	6.16
16	97.3	97.3	0.0	-0.51	1.03	-0.53	5.39
23	71.4	71.4	0.0	-0.27	1.03	-0.76	4.26
24	46.8	46.8	0.0	3.62	7.49	-1.21	4.58
25	28.5	28.5	0.0	6.21	3.02	0.66	4.00
27	46.0	46.0	0.0	0.43	-0.03	-0.40	6.00
28	61.6	61.6	0.0	0.10	0.21	-0.31	6.19
29	56.2	56.2	0.0	0.18	0.15	-0.33	6.20
30	84.2	84.2	0.0	-0.35	0.72	-0.36	6.11
31	28.6	28.6	0.0	4.57	-1.79	-2.79	3.11
33	27.3	27.3	0.0	4.29	-1.52	-2.77	3.12

- The proton numbers are the same as in Figure 4.11, 4.12 and 4.14.
- A positive sign means the pseudo symmetry axis is tilted out of the N-Fe-N plane toward the normal in the general direction of the amine protons.
- The hyperfine couplings are in units of MHz.
- Fe-H distance from molecular modeling program.

- e. The hyperfine couplings presented include the isotropic couplings.
 f. The underlined couplings of the complexes are from the same proton, and are both positive at the parallel and the perpendicular field positions.

$$A_{\text{obs}}^D = \beta_e \beta_n g_e g_n (3 \cos^2 \phi - 1) / h r^3 \quad 4.6$$

As the EPR spectra of the ferritin iron nitrosyl complex and the model complexes have an axial feature, it is reasonable to assume that the pseudo symmetry axis is the axis corresponding to $g_{//}$.

Also, if we assume $\phi = \phi_0$ when the magnetic field is set at parallel position, then, at perpendicular position, $\phi = 90^\circ - \phi_0$. We therefore have

$$A_{//}^D = \beta_e \beta_n g_{//} g_n (3 \cos^2 \phi_0 - 1) / h r^3 \quad 4.7$$

$$\begin{aligned} A_{\perp}^D &= \beta_e \beta_n g_{\perp} g_n (3 \cos^2 (90^\circ - \phi_0) - 1) / h r^3 \\ &= \beta_e \beta_n g_{\perp} g_n (3 \sin^2 \phi_0 - 1) / h r^3 \end{aligned} \quad 4.8$$

When $g_{//}$ is close to g_{\perp} , such as in the iron nitrosyl complexes, we can replace $g_{//}$ and g_{\perp} by g . By setting $C = \beta_e \beta_n g_e g_n / h$, we have

$$A_{//}^D = C(3 \cos^2 \phi_0 - 1) / r^3 \quad 4.9$$

$$A_{\perp}^D = C(3 \sin^2 \phi_0 - 1) / r^3 \quad 4.10$$

Addition of 4.9 and 4.10 gives

$$\begin{aligned} A_{//}^D + A_{\perp}^D &= C[(3(\cos^2 \phi_0 + \sin^2 \phi_0) - 2) / r^3] \\ &= C / r^3 \end{aligned} \quad 4.11$$

$$r = \sqrt[3]{\frac{C}{A_{//}^D + A_{\perp}^D}} \quad 4.12$$

Substituting Equation 4.11 into Equation 4.9, we obtain

Table 4.4a The bond lengths and angles for the first coordination sphere ligand atoms of the iron nitrosyl complexes.

Cys-Fe-NO angle (°)			
N8-Fe0-N6	S4-Fe0-N6	S4-Fe0-N8	S4-Fe0-N1
114.0	113.7	111.9	89.7
Cys-Fe-NO bond length (Å)			
Fe0-N8	Fe0-N6	Fe0-S4	Fe0-N1
1.68	1.68	2.34	2.18
Pen-Fe-NO angle (°)			
N8-Fe0-N6	S4-Fe0-N6	S4-Fe0-N8	S4-Fe0-N1
114.3	113.6	111.9	89.1
Pen-Fe-NO bond length (Å)			
Fe0-N8	Fe0-N6	Fe0-S4	Fe0-N1
1.68	1.68	2.34	2.18
HoSF-Fe-NO angle (°)			
N8-Fe0-N6	S4-Fe0-N6	S4-Fe0-N8	S4-Fe0-N1
113.6	110.3	112.1	88.8
HoSF-Fe-NO bond length (Å)			
Fe0-N8	Fe0-N6	Fe0-S4	Fe0-N1
1.68	1.68	2.34	2.18

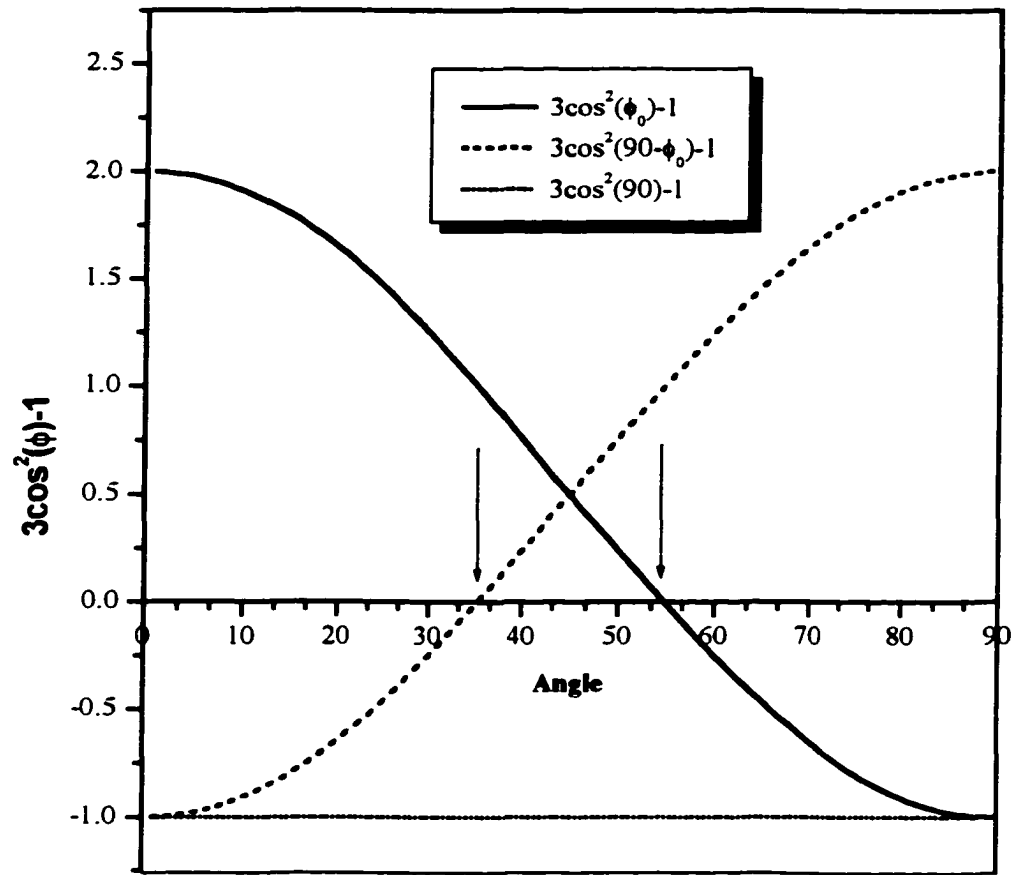


Figure 4.16 The graph of the angle function of $3\cos^2\phi-1$.

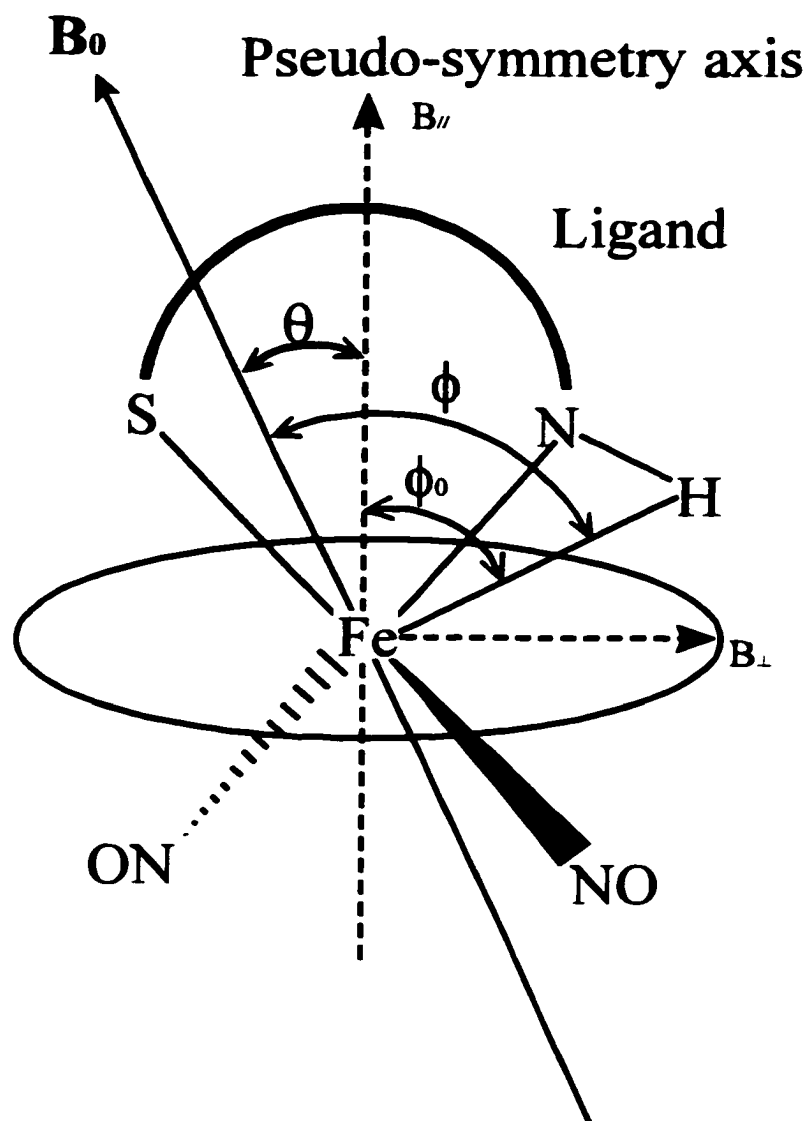


Figure 4.17 The schematic diagram of the iron nitrosyl complex. The iron, sulphur and nitrogen atoms are in the paper plane. The two nitrosyl radicals stick forward and backward outside the paper. B_0 is the applied magnetic field.

$$\frac{A_{//}^D}{C} \cdot \frac{C}{A_{//}^D + A_{\perp}^D} = 3 \cos^2 \phi_0 - 1 \quad 4.13$$

Equation 4.13 can be reduced to

$$\phi_0 = \cos^{-1} \left(\sqrt{\frac{2A_{//}^D + A_{\perp}^D}{3(A_{//}^D + A_{\perp}^D)}} \right) \quad 4.14$$

At the perpendicular position, the measured hyperfine couplings are the integration of all the complexes over 360° in the plane normal to the symmetry axis. However, only at the turning points of $\phi = 90^\circ - \phi_0$, $90^\circ + \phi_0$, 90° and 270° are ENDOR peaks expected. Angles $90^\circ - \phi_0$ and $90^\circ + \phi_0$ give the same resonance. For those protons with $\phi = 90^\circ$, A_{\perp}^{90} can be used to calculate r,

$$r = -3 \sqrt{\frac{g\beta g_n \beta_n}{h A_{\perp}^{90}}} \quad 4.15$$

Thus, ϕ_0 can be determined by the following equation,

$$\phi_0 = \cos^{-1} \left(\sqrt{\frac{A_{//} + A_{\perp}^{90}}{3A_{\perp}^{90}}} \right) \quad 4.16$$

From the hyperfine couplings in Table 4.2 and assignments of the sign for each peak according to the modeling results, we calculate values for r and ϕ_0 using Equations 4.12, 4.14 and 4.15, 4.16. In Equation 4.12, A_{\perp}^D is given by $A_{\perp}^{90 \pm \phi_0}$. The calculated results are presented in Table 4.5 along with the results from the molecular modeling calculations.

Discussion

The ferritin iron nitrosyl complex has been a difficult system to investigate. As the EPR spectrum of the complex reveals no hyperfine splittings from ligand nuclei, and the protons do not coordinate with the iron atom directly, all the information from EPR and ^1H ENDOR collected to date provide only indirect evidence for structure of the complex. ^{14}N ENDOR studies of the iron nitrosyl complexes could possibly determine the number of nitrogen atoms coordinated with the iron ion, and thus prove the bidentate binding of the ligand to the iron. Although nitrogen ENDOR spectroscopy was previously attempted for both ferritin iron nitrosyl complex and the model complexes on both cw and pulsed ENDOR spectrometers and was also sought in this research, no nitrogen spectra were obtained. Relaxation properties of the ligand nuclei may be a key factor for the failure to obtain the nitrogen ENDOR spectra. However, the ^1H ENDOR spectrum of HoSF is readily obtained and its analysis presented here provides strong evidence for the structure of its iron nitrosyl complex as shown in Figure 4.14.

A. EPR Studies of the Model Complexes

In our previous EPR studies on the ferritin iron nitrosyl complex of site-directed mutants of ferritin, three possible docking positions for this complex were His118, His128 and Cys130.^[28] These residues are all near the ferritin three-fold channels. The Cys130 residue is in the vicinity of the outer opening of the three-fold channels. The complex coordinated at Cys130 was produced in the first minutes of passing NO gas over the top of the ferritin solution (see Section 4.2 Experimental). After five minutes, a new species

Table 4.5 The calculated distance for the protons to the iron center from ENDOR data.

Ligand	Assignment of the protons	//, \perp ^a	r (Å) ^b	ϕ_0 (°)	Equations
HoSF	exchangeable proton	(a,d')	2.75 (2.75)	50.8	4.15 and 4.17
	exchangeable proton	(a,e')	2.72 (2.75)	58.7	4.18 and 4.19
	α carbon proton	(d,b')	3.70 (3.62)	15.0	4.15 and 4.17
	methylene proton	(c,a')	3.83 (3.81)	23.7	4.15 and 4.17
Penicillamine	exchangeable proton	(e,c')	2.72 (2.70)	41.0	4.15 and 4.17
	methyl proton	(b,a')	4.84 (4.77)	22.7	4.15 and 4.17
	α carbon proton	(c,d')	3.50 (3.20)	81.2	4.15 and 4.17
Cysteine	exchangeable proton	—	—	—	—

a. $A_{//}$ and A_{\perp} in the parentheses were used to calculate r and ϕ_0 .

b. The distances from the energy minimization calculation using ChemSite are given in parentheses.

accumulated.

The EPR spectrum of ferritin iron nitrosyl complex at 77 K revealed only two broad peaks (parallel and perpendicular), which indicated an axial or pseudo axial structure for the complex. This spectrum is similar to those of the model complexes. Based on the EPR spectra, a reasonable proposal was that the local structure of the ferritin iron nitrosyl complex had a similar structure to the complexes produced with cysteine and its derivative as ligands. Much effort was therefore put into the structural studies of these model complexes.^[47]

The EPR and ¹H ENDOR data of model complexes measured by Wang are listed in Table 4.6. When ethanethiol (ETH, SHCH₂CH₃) was a ligand, there was an isotropic EPR signal at 77 K. When the functional thiol group was replaced by the amino group in

Table 4.6 The g-values and hyperfine couplings for the model complexes from previous work.^[47]

$\begin{array}{c} \text{SH} \\ \\ \text{CH}_2 \\ \\ \text{HO}_2\text{C}-\text{C}-\text{NH}_2 \\ \\ \text{H} \end{array}$		epr peaks	epr g-value	epr hyperfine splitting	endor //	endor ⊥
l-Cysteine	room	13	2.030	$a_N=2.2$ $a_H=1.15$		
	77 K	2	$g_i=2.035$		0.2 1.03 1.44 2.0 3.0	0.22 0.9 4.0
$\begin{array}{c} \text{SH} \\ \\ \text{H}_3\text{C}-\text{C}-\text{CH}_3 \\ \\ \text{HO}_2\text{C}-\text{C}-\text{NH}_2 \\ \\ \text{H} \end{array}$		epr peaks	epr g-value	epr hyperfine splitting	endor //	endor ⊥
l-Penicillamine	room	5	2.028	$a_N=2.5$		
	77 K	2	$g_i=2.034$ $g_r=2.015$		0.22 1.16 1.71 3.09	0.22 1.07 2.39
$\begin{array}{c} \text{SH} \\ \\ \text{CH}_2 \\ \\ \text{HO}-\text{CH}_2 \end{array}$		epr peaks	epr g-value	epr hyperfine splitting	endor	
Mercaptoethanol	room	13	2.029	$a_N=2.1$ $a_H=1.1$		
	77 K	>2	2.003		0.22	2.66
$\begin{array}{c} \text{SH} \\ \\ \text{CH}_2 \\ \\ \text{COOH} \end{array}$		epr peaks	epr g-value	epr hyperfine splitting	endor //	endor ⊥
Thioglycolic Acid	room	1	2.030			
	77 K	2	$g_i=2.033$ $g_r=2.014$		0.22 1.07 2.73 3.5	0.22 1.01 2.07 2.72
$\begin{array}{c} \text{SH} \\ \\ \text{CH}_2 \\ \\ \text{CH}_3 \end{array}$		epr peaks	epr g-value	epr hyperfine splitting	endor	
Ethanethiol	room					
	77 K	>2	2.003			
$\begin{array}{c} \text{SH} \\ \\ \text{CH}_2 \\ \\ \text{H}_2\text{N}-\text{CH}_2 \end{array}$		epr peaks	epr g-value	epr hyperfine splitting	endor //	endor ⊥
Aminoethanethiol	room	13	2.030	$a_N=2.2$ $a_H=1.15$		
	77 K	2	$g_i=2.035$ $g_r=2.016$		0.22 1.16 2.03 3.07	0.22 1.12 1.55

ethylamine ($\text{NH}_2\text{CH}_2\text{CH}_3$), there was no EPR signal. This result indicated that the thiol group was essential in forming a stable iron nitrosyl complex.

When one of the protons in the ETH methyl group is replaced by an amino group or a hydroxyl group, we have aminoethanethiol (AET, $\text{SHCH}_2\text{CH}_2\text{NH}_2$) and mercaptoethanol (MER, $\text{SHCH}_2\text{CH}_2\text{OH}$), respectively. At 77K, both ETH and MER iron nitrosyl complexes had an isotropic EPR spectrum with the same g-value of 2.003. Whereas, the AET complex had an axial spectrum with $g_{\parallel} = 2.0016$ and $g_{\perp} = 2.035$. The room temperature EPR spectra of both MER and AET complexes had the isotropic g values of 2.030 and 2.029, which was consistent with a similar configuration for both complexes in room temperature solution.

Replacement of the second proton in the AET ethylene group adjacent to the amino group with a carboxylate group produces a cysteine (Cys, $\text{SHCH}_2\text{CH}(\text{CO}_2\text{H})\text{NH}_2$). As all the g values and hyperfine couplings were the same for Cys-Fe-NO and AET-Fe-NO at both room temperature and 77 K, the configurations of the two complexes should be the same. The proton EPR spectrum was obtained for ethyl ester of cysteine as a ligand and an axial EPR spectrum was seen. This result precludes carboxylate coordination.

In pencillamine (Pen, $\text{SHC}(\text{CH}_3)\text{CH}(\text{CO}_2\text{H})\text{NH}_2$), the two protons on the same Cys methylene group were replaced by two methyl groups. The g-values of $g_0 = 2.028$, $g_{\parallel} = 2.015$ and $g_{\perp} = 2.034$ were obtained.

The further ^{15}NO isotopic studies on Cys-Fe-NO,^[52] Pen-Fe-NO^[47] and Mer-Fe-NO^[47] complexes gave more information about the configurations of the complexes.

Both Cys-Fe-NO and Mer-Fe-NO complexes have thirteen lines in the room temperature EPR spectrum fitting the assumption of two nitrogen and four hydrogen hyperfine couplings with $a_N = 2.2$, $a_H = 1.15$ for the former and $a_N = 2.1$, $a_H = 1.1$ for the latter complexes, respectively. Normally, two identical nitrogen atoms give five peaks with the peak intensity pattern of 1:2:3:2:1, and four identical hydrogen atoms have five peaks with the 1:4:6:4:1 intensity pattern. The maximum number of hyperfine splittings should be twenty-five. As the proton hyperfine coupling is about half of the nitrogen hyperfine coupling, the twelve proton splitting peaks overlapped with the five nitrogen splitting peaks and were not observed. Thus, thirteen peaks appeared in the EPR spectra. Upon the isotopic substitution of ^{14}N by ^{15}N in NO, only nine peaks are present in the EPR spectra of both complexes. The hyperfine couplings from nitrogen and hydrogen atoms still fit the assumption of two nitrogen and four hydrogen atoms. In the ^{15}N isotopic complex, the two identical nitrogen atoms ($I = \frac{1}{2}$) have three peaks with 1:2:1 intensity pattern. As the A_H is still about half of the A_N , only the two hydrogen splittings in the field range of the nitrogen peaks and the four hydrogen splittings outside the field range of the nitrogen splittings are observed. These results unambiguously indicate that there are two nitric oxide molecules coordinating to the iron atom. In addition, the Pen-Fe-NO complex has five peaks in the room temperature EPR spectrum of Pen-Fe- ^{14}NO , but three peaks for Pen-Fe- ^{15}NO . Once again, the experimental results reinforces our conclusion that two nitrosyl molecules bind to the iron.

Wang's proton ENDOR spectra for model complexes are better resolved (Appendix I) and are not identical to the present ones. The spectral change is most likely

due to the different conditions of the sample preparations, perhaps from inadequate pH control in either her samples or mine.

B. Molecular Modeling Calculations

Molecular modeling calculations on the iron nitrosyl complexes reveal rich information in proton ENDOR spectra. First, the possible hyperfine couplings and signs can be determined. Second, as a rule of thumb, the angle ϕ_0 between the g principal axis and the metal-to-proton vector is crucial in obtaining the correct hyperfine couplings, especially when the angle ϕ_0 is close to the magic angle of 54.7° at the parallel and 35.3° at the perpendicular positions. Thus, a slight tilt of the g principle axis out of the N-Fe-N plane gives pronounced changes in the couplings for the protons 1, 2 and 3 in HoSF-Fe-NO and for the protons 2, 3, 14, 17 and 18 in Pen-Fe-NO. Finally, unlike conventional proton ENDOR studies, where the couplings have opposite signs at the parallel and perpendicular field positions, the results presented here show that certain protons have a positive sign at both the parallel and perpendicular positions (Table 4.4). The modeling calculation and the angular term $3\cos^2\phi-1$ analysis (Figure 4.16) show that if a proton has a ϕ_0 value between 35.3° and 54.7° , its hyperfine couplings are positive at both the parallel and perpendicular positions.

Generally, the stick spectra from the modeling calculations for horse spleen ferritin match the observed proton ENDOR spectra quite well, and enable us to assign the hyperfine couplings to specific protons and to determine the sign of the couplings, thus confirming the structure of the protein complex.

C. Proton ENDOR Results

The metal-to-proton distances determined with the above equations ($\leq 0.1 \text{ \AA}$) are in substantial agreement with our molecular modeling calculations for most of the protons (see Table 4.5). For those protons having large deviations ($\geq 0.1 \text{ \AA}$) between modeling and experimental results, the mismatch arises mainly from the fact that the ENDOR spectra are only partially resolved.

The angles of ϕ_0 in the experimental results are also in good agreement with those in the modeling results for most protons (compare ϕ_0 in Table 4.4 and 4.5). Better resolved proton ENDOR spectra and perhaps lateral tilt of the g-axis are both needed to obtain a better agreement between the two results. The deviation of the angle ϕ_0 (50.8° from 58.7°) for the same exchangeable proton in HoSF-Fe-NO (proton 1 in Figure 4.14) from the Equation 4.12, 4.14 and 4.15, 4.16 indicates that better resolved spectra are needed to accurately determine ϕ_0 .

The structure of the complexes slightly changes in solution, which leads to a small alternation of the angle ϕ_0 . Thus, a spread of hyperfine couplings from the same proton in a complex is expected to give rise to ENDOR peak broadening as seen in our proton ENDOR spectra.

In order to get completely resolved proton ENDOR spectra for the iron nitrosyl complexes in the future, protons in the ligand should be selectively substituted with deuterium. A smaller frequency modulation amplitude is also suggested to help further resolve the narrowly distributed peaks.

D. Comparison of Our Proton Couplings with Those in Literature

The small isotropic hyperfine coupling from Fermi contact in the iron nitrosyl complexes are similar to those of vanadyl complexes. However, the general structure of vanadyl complexes is square pyramid where protons are either located on the symmetry axis of the complex or in the equatorial plane.^[53] For pure dipole-dipole interaction, these positions have large hyperfine couplings with opposite signs (refer to Equation 4.2). For example, an equatorial proton 2.5 Å from the metal ion has a pure dipolar hyperfine coupling of 11 MHz at the perpendicular field position. Similarly, an axial proton 2.9 Å from the metal ion generates 6 MHz hyperfine splitting at the parallel field position.^[51] The protons of a water molecule in the second coordination sphere ~ 5 Å from the metal ion have hyperfine couplings of only ~ 1 MHz or less.^[51] On the contrary, for a tetrahedral complex, such as iron nitrosyl complexes, ligands are neither along the symmetry axis or on the equatorial plane. Thus, smaller hyperfine couplings are expected. For a proton at a certain geometric position where the ϕ_0 is between 35.3° and 54.7°, the hyperfine couplings have positive signs at both the parallel and the perpendicular position.

The proton spectra for all the complexes studied here have hyperfine couplings between 0.35 and 5.72 MHz (Table 4.2, 4.4 and 4.5). All the exchangeable protons in the samples studied were assigned to the protons in the amine group. Although the exchangeable protons observed in aqueous myoglobin and the [4Fe-4S]⁺ cluster of aconitase have hyperfine couplings as large as 4 - 6 MHz covering the exchangeable proton couplings in our experiments,^[54,55] since no distinct changes in the hyperfine pattern or line width for the model complexes prepared in D₂O, indicating no water in the first

coordination sphere,^[47] it is unlikely that a water molecule might coordinate with the iron at 77 K. On the other hand, if the water molecules were not bound to the iron center, such as in uteroferrin-molybdate complex, then the hyperfine coupling should be around 1 MHz.^[56] Although our exchangeable proton hyperfine couplings are from 0.35 to 5.72 MHz within the range of the couplings of both coordinated proton and the remote protons, the model calculations with only the amino acid ligand coordination match with the ENDOR spectra. However, models with a H₂O coordination do not match the ENDOR spectra, thus precluding either a coordinated water molecule or remote water molecules. Our results here are consistent with the tetrahedral structure for iron dinitrosyl complexes described by McDonald and collaborators.^[52] The experimentally measured iron-exchangeable proton distances are 2.75, 2.73 and 2.72 Å for HoSF-Fe-NO, Pen-Fe-NO and Cys-Fe-NO, respectively. Other nonexchangeable protons are in the reasonable range of 3.70 - 4.84 Å away from the iron center. All these distances are in good agreement with our molecular modeling calculations.

The EPR spectra for HoSF-Fe-NO are identical to those of Cys-Fe-NO, Pen-Fe-NO and AET-Fe-NO. The $g_{\parallel} = 2.015$ and $g_{\perp} = 2.035$ of HoSF-Fe-NO are the same as those for these model complexes. However, the ¹H ENDOR data and the molecular modeling calculations show that both HoSF and Pen bound with the iron center through bidentate coordination. Thus, an identical local structure of HoSF-Fe-NO to that of the model complex of Pen-Fe-NO is inferred. In accordance with this idea, the mutant studies of HoSF-Fe-NO support that the iron ion is coordinated to the sulphur atom of the cysteine residue Cys130. The recent proton ENDOR studies obtained on ferritin (this

work) indicate that the largest hyperfine splittings at the perpendicular position are from the exchangeable protons. This result is consistent with the iron being bound with the nitrogen in an amino group.

In summary, the local structure of HoSF-Fe-NO involved the iron atom coordinating with the sulphur atom in Cys130, the nitrogen atom in the peptide backbone and two nitrosyl molecules.

Conclusions

The HoSF-Fe-NO and model complexes had similar EPR features and g-values. The local structure of the ferritin iron nitrosyl complex is very likely identical to that of the Pen-Fe-NO complex with the iron atom coordinating with thiol, amino groups and two nitrosyl molecules, but not so for the Cys-Fe-NO complex which has monodentate ligation from two cysteines. All the complexes have near axial symmetry with a structure close to tetrahedral. Since the proton hyperfine couplings are sensitive to their geometric positions, and the complexes studied here have different numbers of protons, the proton ENDOR spectra are expected to be different. More sophisticated molecular modeling calculations and selectively deuterated ligands are required to clarify the ^1H ENDOR spectra of the model complexes.

CHAPTER 5

EPR AND ENDOR STUDIES OF COPPER TACH CHLORIDE COMPLEXES

Introduction

Copper tach chloride complexes, like other macrocyclic copper complexes, are potential synthetic metalloproteinases which hydrolytically cleave nucleic acids.^[59-66] Hydrolysis of DNA is an important enzymatic reaction. However, it is extremely difficult to achieve in the laboratory due to the stability of DNA toward hydrolysis.^[67] Study of DNA cleavage by small molecules has focused on either hydrolysis of activated substrates or oxidative degradation of the sugar backbone of DNA. Oxidative cleavage agents require activation by a stoichiometric co-oxidant or by light.

One advantage of hydrolytic cleavage agents is that they do not require coreactants and therefore are potentially more useful in drug design. Compared to oxidative cleavage agents which tend to produce diffusable free radicals, hydrolytic agents do not suffer from these shortcomings. In addition, the hydrolysis of phosphodiester bonds activated by metals in enzymes is not well-understood. Small metal complexes promoting the hydrolysis of DNA therefore could be useful in elucidating the precise role of metal ions in enzyme catalysis.^[68-70]

Burstyn and coworkers reported that $[\text{Cu}([9]\text{aneN}_3)\text{Cl}_2]$ promotes the hydrolytic cleavage of plasmid DNA with a low hydrolytic rate constant of $0.04\text{--}0.09\text{ h}^{-1}$.^[62] More effective hydrolytic agents, namely copper tach chloride complexes, (tach \equiv *cis,cis-*

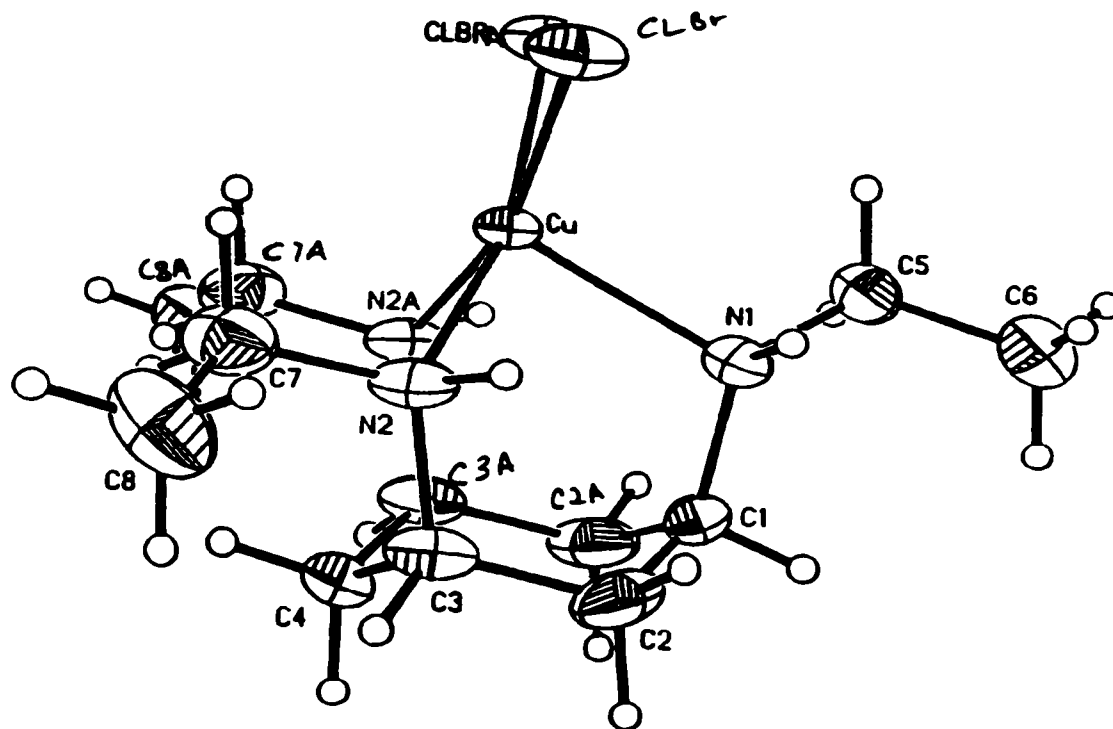


Figure 5.1 The X-ray structure of $[\text{Cu}(\text{N-Et})_3\text{tach}(\text{Cl})_x(\text{Br})_{2-x}]$ complex.^[71] (5.1.wpd)

1,3,5-triaminocyclohexane), have been studied and exhibit a hydrolytic rate constant of 4.3 h^{-1} .^[59]

The structure of copper N-ethyl tach chloride, $[\text{Cu}(\text{N-Et})_3\text{tachCl}_2]$, has been determined by X-ray crystallography (Figure 5.1).^[71] The structure is close to a square pyramid with the two nitrogen and the two chloride atoms displaced a slightly off the plane, and the two chloride atoms having a longer distance to the copper ion than the two nitrogen atoms, 2.3948(6) vs. 2.053(2) Å, due to the larger radius of coordinated chloride over coordinated amino nitrogen. The apical nitrogen atom tilts 6.1° towards the other two basal nitrogen atoms and has a Jahn-Teller-lengthened Cu-N distance of 2.218(5) Å. A schematic diagram of the d orbital energy levels of the copper ion under a series of symmetric crystal fields is shown in Figure 5.2.^[72]

The collaborative research described herein focuses on the bonding properties of the tach derivatives as the ligands for the preparation of the catalytically active copper complexes. X-band and Q-band EPR spectroscopies, in conjunction with visible-near IR ligand-field spectra, have been used to study the structure around the copper ion. Optical and EPR spectra of these copper tach complexes have been used to determine orbital bonding coefficients. The ultimate goal is to understand the function of these complexes in terms of their structures.

Experimental

All the copper tach complexes were prepared as 5 mM of copper ion in HEPES buffer (50 mM HEPES, pH = 7.0) and in methanol by G. Park of Professor Planalp's

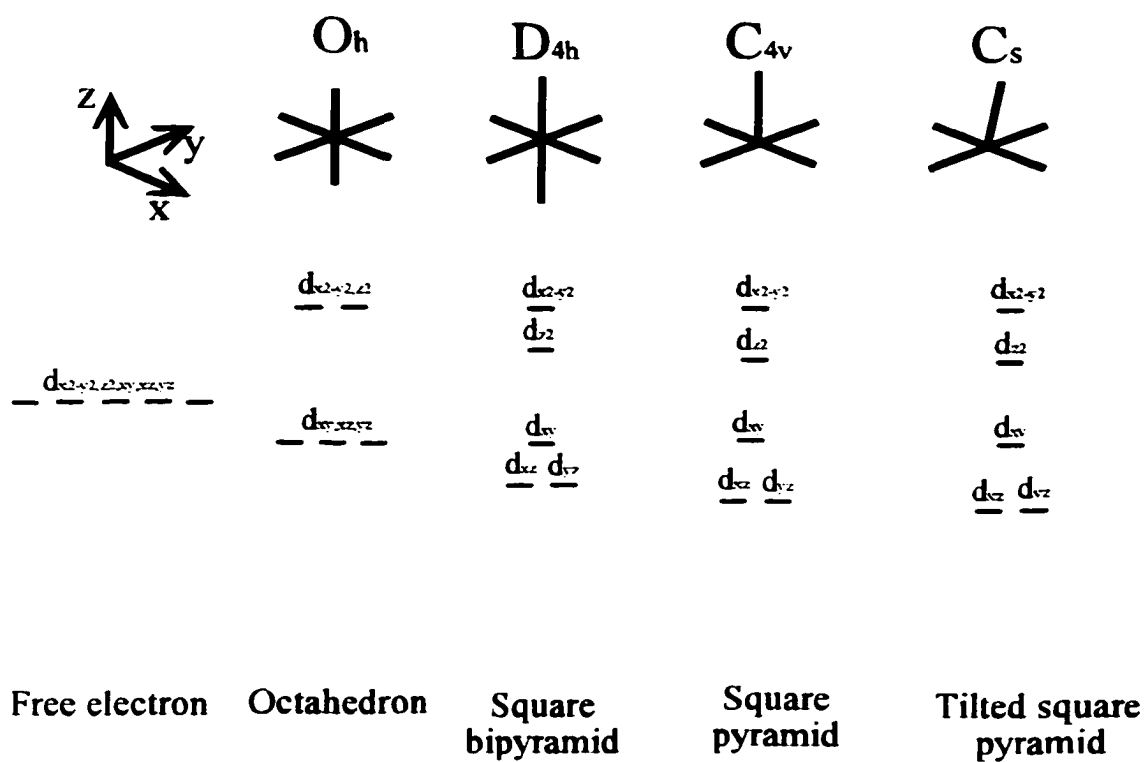


Figure 5.2 The schematic diagram of the d orbital energy levels under a series of symmetric crystal fields.

group. Powder samples of the copper tach complexes were obtained by grinding crystalline samples. The EPR spectra were obtained at either X-band or Q-band frequency. The Q-band spectrometer was equipped with an improved Varian E-110 microwave bridge, an E-line console and a home-made cylindrical TE_{011} cavity operating at 100 K with nitrogen gas flow cooling system (see Chapter 2). The X-band EPR spectrometer was equipped with a Bruker ER 041 XK-H microwave bridge and a Varian TE_{102} cavity as described elsewhere.^[50] X-band EPR spectra were obtained at either 77 K using a finger dewar filled with liquid nitrogen or at room temperature. At room temperature, a sensitive quartz flat cell for lossy solutions was used. In order to position the cell in the cavity for all the measurements, a Philips PM 3050 oscilloscope was connected to the spectrometer display module and placed near the cavity for the flat cell adjustments. Five individual flat cell adjustments were made and the EPR spectra for 1 mM $[Cu(N-Me)_3tachCl_2]$ complex in pH 7.0 HEPES buffer were scanned. A reproducibility in EPR intensity of $\pm 2\%$ was obtained for the room temperature EPR spectra.

Both X-band and Q-band spectrometers were field calibrated with Mn^{2+}/CaO mixed with coal as standard samples ($g_{Mn^{2+}/CaO} = 2.0011$, $g_{coal} = 2.0035$ and field span ($M_I = \pm 5/2$ lines) = 43.573 mT for Mn^{2+}/CaO).^[73] The HP 5350A microwave frequency counter was used for the X-band spectrometer and an EIP model 548A microwave frequency counter was used for the Q-band spectrometer.

The EPR spectra of powder and solution samples were collected at both X-band and Q-band frequencies. All of the optical spectra were measured using a Cary 5 UV-Vis

spectrometer with a 1 ml quartz cuvette most by G. Park of Dr. Planalp's group to obtain the absorption bands for all copper complexes. The bonding parameters for $[\text{Cu}(\text{N-Et})_3\text{tachCl}_2]$ has been calculated and is reported here.

Results

Table 5.1 lists all of the measurements made for the copper tach chloride complexes. Complete EPR studies were carried out on the powder samples and solution samples in HEPES buffer. $[\text{Cu}(\text{N-Et})_3\text{tachCl}_2]$ complex prepared in a series of solutions was studied thoroughly by EPR and optical spectroscopies.

A. g- and A-values of the Copper Tach Complexes

The low temperature (100 K) Q-band EPR spectra of powder samples of copper tach halide complexes are presented in Figure 5.3. Only $[\text{Cu}(\text{N-Et})_3\text{tachCl}_2]$ has an EPR spectrum attributed to a single species. Other samples have complicated EPR spectra indicating the presence of more than one species, due to chemical or crystallographic inequivalence of the copper centers. The g-values for powdered $[\text{Cu}(\text{N-Et})_3\text{tachCl}_2]$ are listed in Table 5.2 along with the g-values of the complex prepared in HEPES buffer and CAPS buffer.

At 100 K, the Q-band EPR spectrum of $[\text{Cu}(\text{N-Et})_3\text{tachCl}_2]$ complex shows a parallel peak and an unresolved perpendicular peak (Figure 5.3). The spectrum does not provide good evidence of rhombicity in the complex. The poor resolution of the spectrum was caused by the microwave power saturation at 100 K. As the tune mode of the Q-

Table 5.1 The complete list of the experiments carried out on the copper tach chloride complexes.

	EPR spectroscopy						Optical spectroscopy			
	Powder	Complex in Hepes buffer			Complex in methanol	Complex in Caps buffer	Powder	Complex in Hepes buffer ^a	Complex in methanol ^b	Complex in Caps buffer ^c
	Q-band 100K	X-band 298 K	X-band 77 K	Q-band 100 K	Q-band 100 K	Q-band 100 K				
Cu(N-Me) ₃ tach Cl ₂	✓	✓	✓	✓					✓	
Cu(N-Et) ₃ tach Cl ₂	✓	✓	✓	✓	✓	✓	✓	✓	✓	✓
Cu(N-Pr) ₃ tach Cl ₂	✓	✓	✓	✓					✓	
Cu(Thioph) ₃ tach Cl ₂	✓	✓	✓	✓					✓	
Cu(Furan) ₃ tach Cl ₂		✓		✓					✓	

a. Complex concentration was 5 mM, HEPES buffer 50 mM and pH 7.0.

b. Complex concentration was 5 mM. Methanol was analytical grade.

c. Complex concentration was 2.5 mM, CAPS buffer 50 mM and pH 10.1.

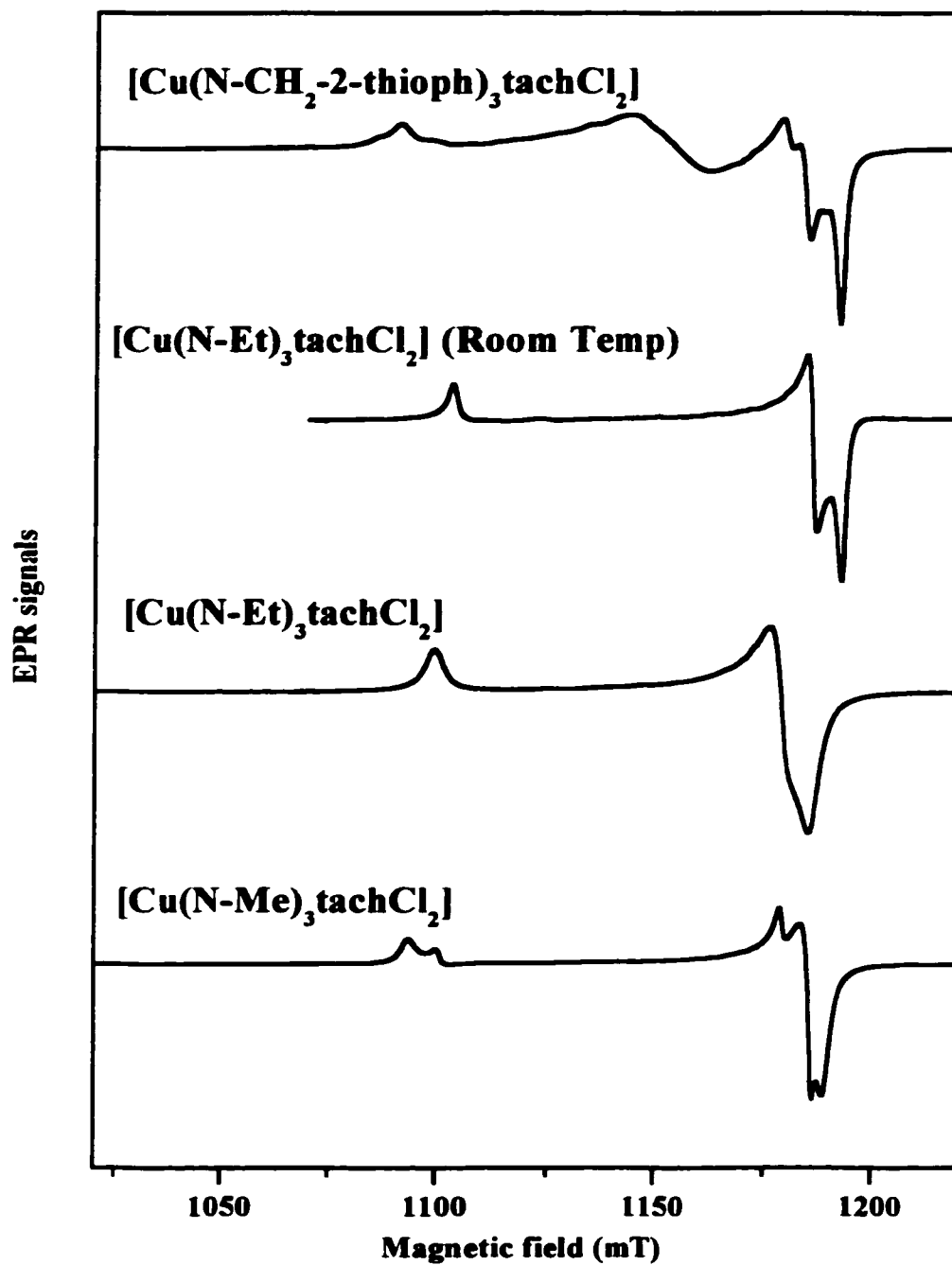


Figure 5.3 The Q-band powder EPR spectra of copper tach chloride complexes.

(continued)

Common Experimental Conditions: Field Set, 1120 mT; Scan Range, 200 mT; Microwave power, 0.01 mW, 37 dB; Modulation Frequency, 100 kHz; Time Constant, 0 s; Scan Time, 30 minutes; Temperature, 100 K; Spectrometer, Q-band EPR/ENDOR; Individual Experimental Conditions: [Cu(N-Me)₃tachCl₂], Modulation Amplitude, 0.05 mT; Receiver Gain, 4; Microwave Frequency, 35.0377 GHz; File Name, 98052002.flr; [Cu(N-Et)₃tachCl₂], Modulation Amplitude, 0.1 mT; Receiver Gain, 20; Microwave Frequency, 35.0482 GHz; File Name, 98052003.flr; [Cu(N-CH₂-2-thioph)₃tachCl₂], Modulation Amplitude, 0.1 mT; Receiver Gain, 20; Microwave Frequency, 35.0447 GHz; File Name, 98052004.flr; [Cu(N-Et)₃tachCl₂] (room temp), Field Set, 1170 mT; Scan Range, 200 mT; Microwave power, 0.1 mW, 27 dB; Modulation Frequency, 100 kHz; Time Constant, 0 s; Scan Time, 30 minutes; Modulation Amplitude, 0.02 mT; Receiver Gain, 6.3; Microwave Frequency, 34.7262 GHz; File Name, 99100502.flr; (5.3.opj)

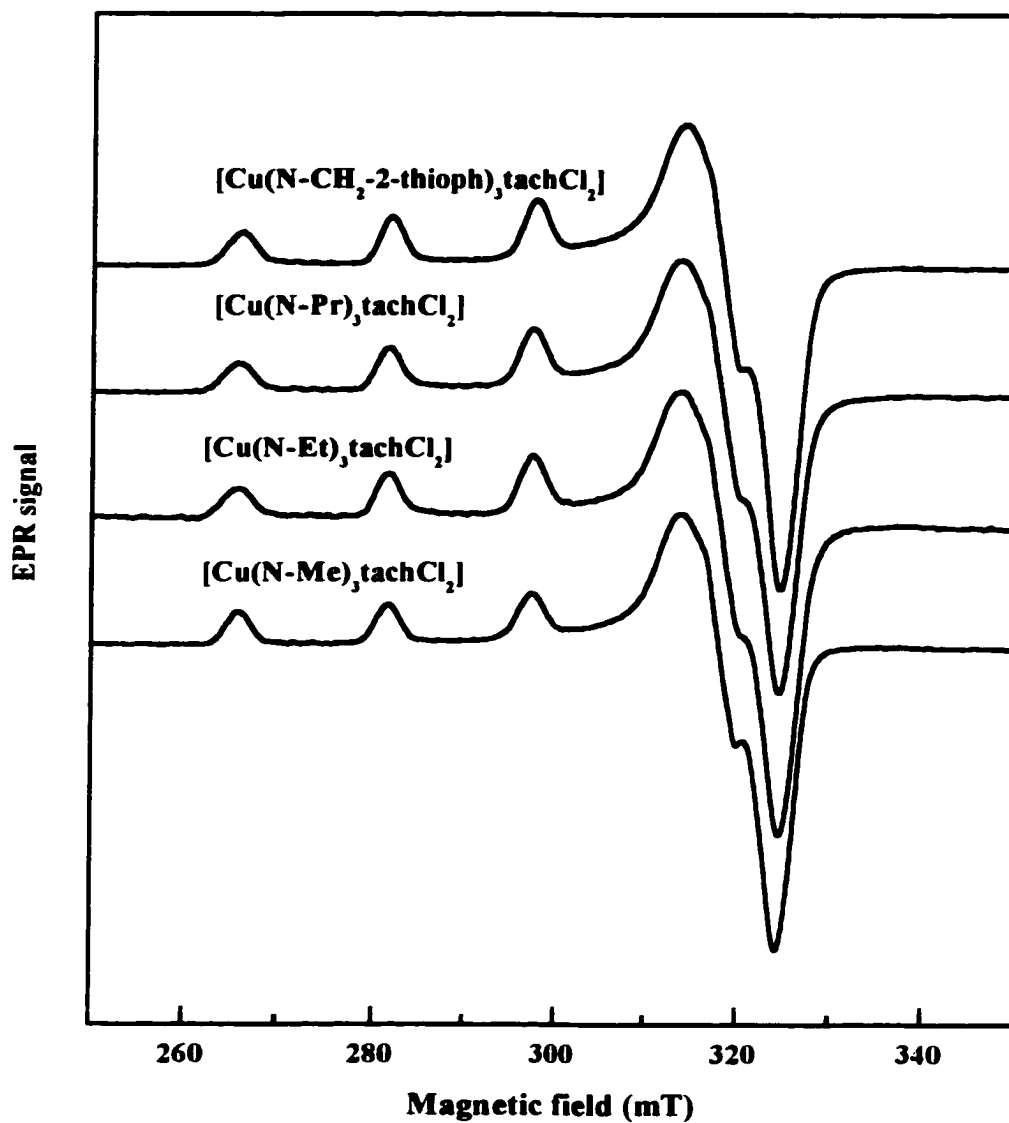


Figure 5.4 The X-band EPR spectra of copper tach chloride complexes at 77 K.
Common experimental conditions: Field set, 300 mT; Scan range, 100 mT; Microwave

(continued)

power, 5 mW; Receiver gain, 0.1 V; Modulation frequency, 100 kHz; Time constant, 0.3 s; Scan time, 1000 s; Temperature, 77 K; Spectrometer, Bruker; Individual experimental conditions: [Cu(N-Me)₃tachCl₂], Modulation amplitude, 0.1 mT; Microwave frequency, 9.1548 GHz; File name, 98061501.fls; [Cu(N-Et)₃tachCl₂], Modulation amplitude, 0.2 mT; Microwave frequency, 9.1523 GHz; File name, 98061502.fls; [Cu(N-Pr)₃tachCl₂], Modulation amplitude, 0.1 mT; Microwave frequency, 9.1523 GHz; File name, 98061503.fls; [Cu(N-CH₂-2-thioph)₃tachCl₂], Modulation amplitude, 0.1 mT; Microwave frequency, 9.1548 GHz; File name, 98061504.fls; (5.4.opj)

band spectrometer is shallow at lower nonsaturating microwave power (≥ 45 db), the AFC (auto frequency control) in the bridge did not function properly when scanning through the EPR absorption region, so higher power saturating microwave levels were required for the spectrometer to function properly. At room temperature, the spectrum of this same complex showed a clear rhombic feature of three peaks with $g_x = 2.061 \pm 0.001$, $g_y = 2.071 \pm 0.001$, $g_z = 2.262 \pm 0.001$.

Figure 5.4 shows the frozen (77 K) X-band EPR spectra of four of the copper complexes in 50 mM HEPES pH 7.0 buffer (HEPES: glycerol = 2:1). The copper concentrations were 5 mM in all cases. In Figure 5.4, all four complexes have similar spectra. The parallel peaks are not completely separated from the perpendicular peaks. Although accurate parallel and perpendicular g-values can be measured from these spectra through simulations, they are more easily obtained from Q-band spectra. Unlike the spectra for powder samples in Figure 5.3, there is no evidence of any rhombicity in the X-band spectra of these complexes (Figure 5.4). Moreover, the width of the parallel peaks increases slightly with the ligand size. The axial spectra for all the copper complexes in solution are also seen in the Q-band EPR spectra, presented below.

Isotopic ^{63}Cu was used to narrow the EPR lines in order to distinguish the hyperfine couplings from the coordinated nitrogen atoms. (Naturally abundant Cu is a mixture of ^{63}Cu and ^{65}Cu with similar nuclear moments.) Unfortunately, the line width was not sufficiently narrowed by isotopic replacement to reveal the hyperfine couplings. Thus, an S-band spectrometer is needed to resolve these parallel peaks.^[74-77] In order to obtain g-values and hyperfine couplings for these complexes, Q-band EPR spectra were

measured.

Figure 5.5 shows the Q-band EPR spectra of frozen copper tach chloride complexes in solution at 100 K. All the aqueous copper complex samples were prepared with 5 mM of copper concentration in 50 mM HEPES buffer, pH = 7.0 (HEPES:glycerol = 2:1). Glycerol was added to form a glass upon freezing the solution. The parallel and perpendicular peaks were separated completely. The $g_{//}$ and $A_{//}$ were calculated from the four parallel peaks (Table 5.2). The perpendicular peaks do not show any hyperfine splittings. Only a g_{\perp} value was measured for each of the spectra (Table 5.2). The six small peaks in the high field range are from Mn^{2+} contamination, which was introduced into the samples from syringe needles used with acidic solutions during the neutralization of the samples. All the complexes of tach ligands have similar values of $g_{//}$, g_{\perp} , and $A_{//}$ values (Table 5.2).

The Q-band EPR spectrum of ethyl copper tach complex prepared wet methanol is also shown in Figure 5.5. The broad and unresolved peaks at the perpendicular field indicate that more than one species exist in the solution. The g-values and hyperfine couplings were $g_x = 1.987$, $g_y = 2.108$, $g_z = 2.260$ and $A_{//} = 157.3 \times 10^{-4} \text{ cm}^{-1}$.

In order to obtain the perpendicular hyperfine couplings for all the aqueous copper complexes, X-band room temperature EPR spectra were measured with a flat cell (see Figure 5.6). Because of the averaging effect of the tumbling of the complexes in the solution, only the isotropic hyperfine couplings were observed. The single sharp peak at high magnetic field was DPPH ($g = 2.0036$) used as a reference mark. The decrease in amplitude of the low field peaks relative to the high field peaks for the large complexes

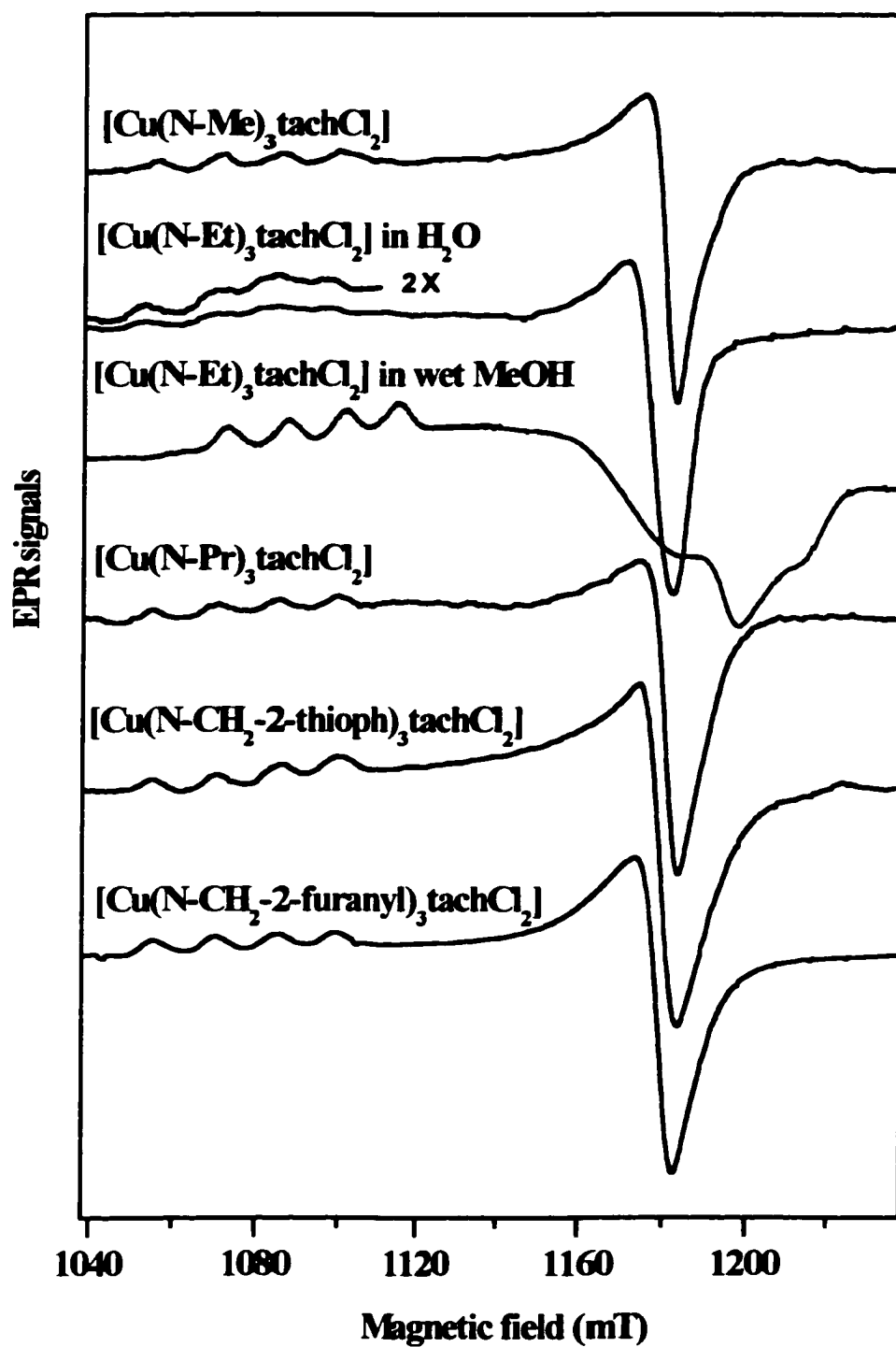


Figure 5.5 The Q-band EPR spectra of copper tach chloride complexes at 100 K.

(continued)

Common Experimental Conditions: Field set, 1138 mT; Scan range, 200 mT; Modulation frequency, 100 kHz; Modulation amplitude, 0.2 mT; Time constant, 1 s; Scan time, 16 minutes; Temperature, 100 K; Spectrometer, Q-band EPR/ENDOR; Individual experimental conditions: [Cu(N-Me)₃tachCl₂], Receiver gain, 200; Microwave frequency, 34.8516 GHz; Microwave power, 0.06 mW; File name, 98061501.flc; [Cu(N-Et)₃tachCl₂], Receiver gain, 32; Microwave frequency, 34.8190 GHz; Microwave power, 0.6 mW; File name, 9807220.flc; [Cu(N-Pr)₃tachCl₂], Receiver gain, 200; Microwave frequency, 34.8453 GHz; Microwave power, 0.06 mW; File name, 98061503.flc; [Cu(N-CH₂-2-thioph)₃tachCl₂], Receiver gain, 100; Microwave frequency, 34.8058 GHz; Microwave power, 0.19 mW; File name, 98072203.flc; [Cu(N-CH₂-2-furanyl)₃tachCl₂], Receiver gain, 40; Microwave frequency, 34.8070 GHz; Microwave power, 0.19 mW; File name, 98072205.flc; (5.5.opj)

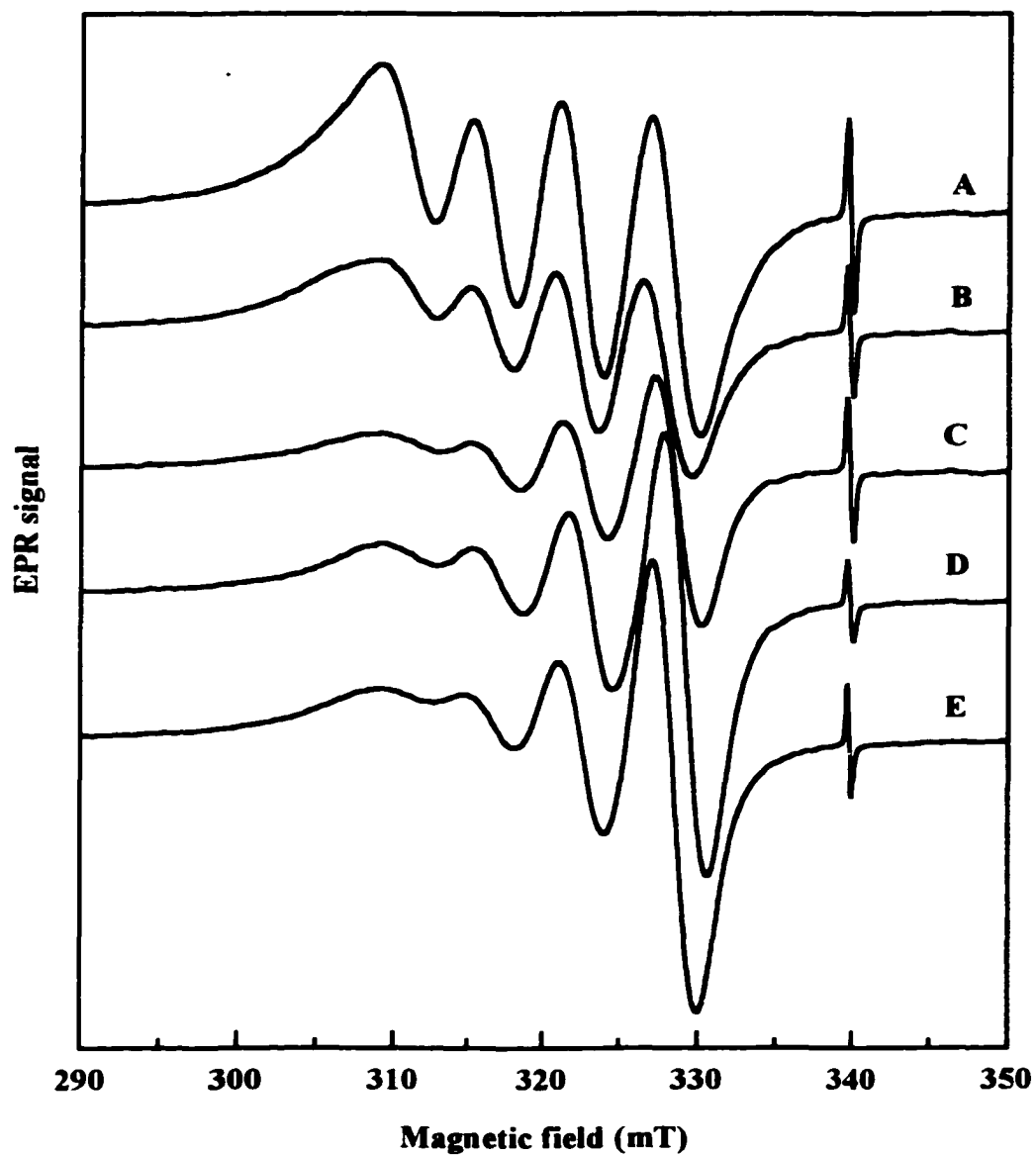


Figure 5.6 The room temperature X-band EPR spectra of copper tach chloride complexes. Common Experimental Conditions: Field Set, 326 mT; Scan Range, 60 mT; Microwave power, 10 mW; Receiver Gain, 0.1 V; Modulation Frequency, 100 kHz; Time

(continued)

Constant, 0.3 s; Scan Time, 500 s; Temperature, 297 K; Spectrometer, Bruker; Individual Experimental Conditions: A, $[\text{Cu}(\text{N-Me})_3\text{tachCl}_2]$, Modulation Amplitude, 0.5 mT; Microwave Frequency, 9.5290 GHz; File Name, 98111802.flr; B, $[\text{Cu}(\text{N-Et})_3\text{tachCl}_2]$, Modulation Amplitude, 0.5 mT; Microwave Frequency, 9.5290 GHz; File Name, 98111803.flr; C, $[\text{Cu}(\text{N-Pr})_3\text{tachCl}_2]$, Modulation Amplitude, 0.5 mT; Microwave Frequency, 9.5291 GHz; File Name, 98111804.flr; D, $[\text{Cu}(\text{N-CH}_2\text{-2-thioph})_3\text{tachCl}_2]$, Modulation Amplitude, 0.5 mT; Microwave Frequency, 9.5292 GHz; File Name, 98111805.flr; E, $[\text{Cu}(\text{N-CH}_2\text{-2-Furanyl})_3\text{tachCl}_2]$, Modulation Amplitude, 0.5 mT; Microwave Frequency, 9.5287 GHz; File Name, 98111806.flr; The high field peak is from DPPH used as a reference (5.6.opj).

Table 5.2 The g-values and hyperfine couplings for the copper tach chloride complexes

Measured at 100 K by Q-band EPR and at room temperature by X-band EPR ^a						
Copper complexes	g_0	$g_{//}$	g_{\perp}	A_0 (10^{-4} cm ⁻¹)	$A_{//}$ (10^{-4} cm ⁻¹)	A_{\perp} (10^{-4} cm ⁻¹) ^c
5mM [Cu(N-Me) ₃ tachCl ₂] in Hepes buffer ^d	2.127	2.264	2.066	58.0	166.9	3.5
5mM [⁶³ Cu(N-Me) ₃ tachCl ₂] in Hepes buffer ^d		2.265	2.066		164.2	
5mM [Cu(N-Et) ₃ tachCl ₂] in Hepes buffer ^d	2.128	2.266	2.066	55.5	164.3	1.2
5mM [Cu(N-Et) ₃ tachCl ₂] in Caps buffer ^c		2.263	2.061		165.0	
[Cu(N-Et) ₃ tachCl ₂] powder ^b		$g_x = 2.262$	$g_x = 2.061$ $g_y = 2.071$			
5mM [Cu(N-Pr) ₃ tachCl ₂] in Hepes buffer ^d	2.127	2.266	2.065	59.3	164.6	6.7
5mM [Cu(N-CH ₂ -2-furanyl) ₃ tachCl ₂] in Hepes buffer ^d	2.127	2.261	2.064	58.8	164.0	6.2
5mM [Cu(N-CH ₂ -2-thioph) ₃ tachCl ₂] in Hepes buffer ^d	2.124	2.261	2.063	60.5	165.7	8.0

- a. All the g-values presented in the table have errors of ± 0.001 . All the hyperfine couplings listed here have errors of $\pm 0.2 \times 10^{-4}$.
b. [Cu(N-Et)₃tachCl₂] powder sample was rhombic symmetry in its g-values.
c. All the A_{\perp} listed here are calculated by $A_0 = 1/3 A_{//} + 2/3 A_{\perp}$.
d. The complexes prepared in HEPES buffer have 5 mM complex, 50 mM HEPES buffer and pH = 7.0.
e. The complex concentration was 2.5 mM, CAPS buffer 50 mM and pH = 10.1.

(such as $[\text{Cu}(\text{N-CH}_2\text{-2-furanyl})_3\text{tachCl}_2]$) arises from the slower tumbling rate for the large complexes.^[78] The isotropic g-value and isotropic hyperfine splitting corrected to second order were calculated by a software written in the C/C++ language (see Appendix E). All the isotropic g-values and hyperfine splittings are listed in Table 5.2.

The $[\text{Cu}(\text{N-Et})_3\text{tachCl}_2]$ complex (5 mM) in CAPS buffer (50 mM, pH = 10.1) was measured on the Q-band spectrometer at 100 K as well. The features of the spectrum were similar to those in Figure 5.5, but are not displayed here. The g-values and hyperfine couplings are listed in Table 5.2.

B. Optical Transitions of Copper Tach Complexes

All the copper complexes were also investigated by optical spectroscopy. Figure 5.7 displays the optical spectra for copper tach chloride complex samples in methanol. Two peaks are observed, one around 700 nm which is not symmetric, and the other near 1100 nm. The unsymmetric peak at ~ 700 nm is assigned to a superimposition of the two electronic transitions of $d_{xz,yz} \rightarrow d_{x^2-y^2}$ and $d_{xy} \rightarrow d_{x^2-y^2}$ for the $\text{Cu}^{2+} d^9$ system (Figure 5.2)^[79-82]. The transition around 1100 nm is assigned to $d_{z^2} \rightarrow d_{x^2-y^2}$. The unsymmetric transition peaks are also present when the spectra are plotted against wavenumber (see Figure 5.8).

Therefore, a Gaussian function was used to simulate the optical spectra. Three Gaussian terms ($A_i \cdot e^{-\ln 2 \left(\frac{\nu - \nu_i}{B_i} \right)^2}$) were summed.^[83] By manually adjusting the height A_i , width B_i and wavenumber ν_i for each peak in the spectrum, the simulated spectrum was obtained, which exactly matched the experimental spectrum (Figure 5.9). A standard

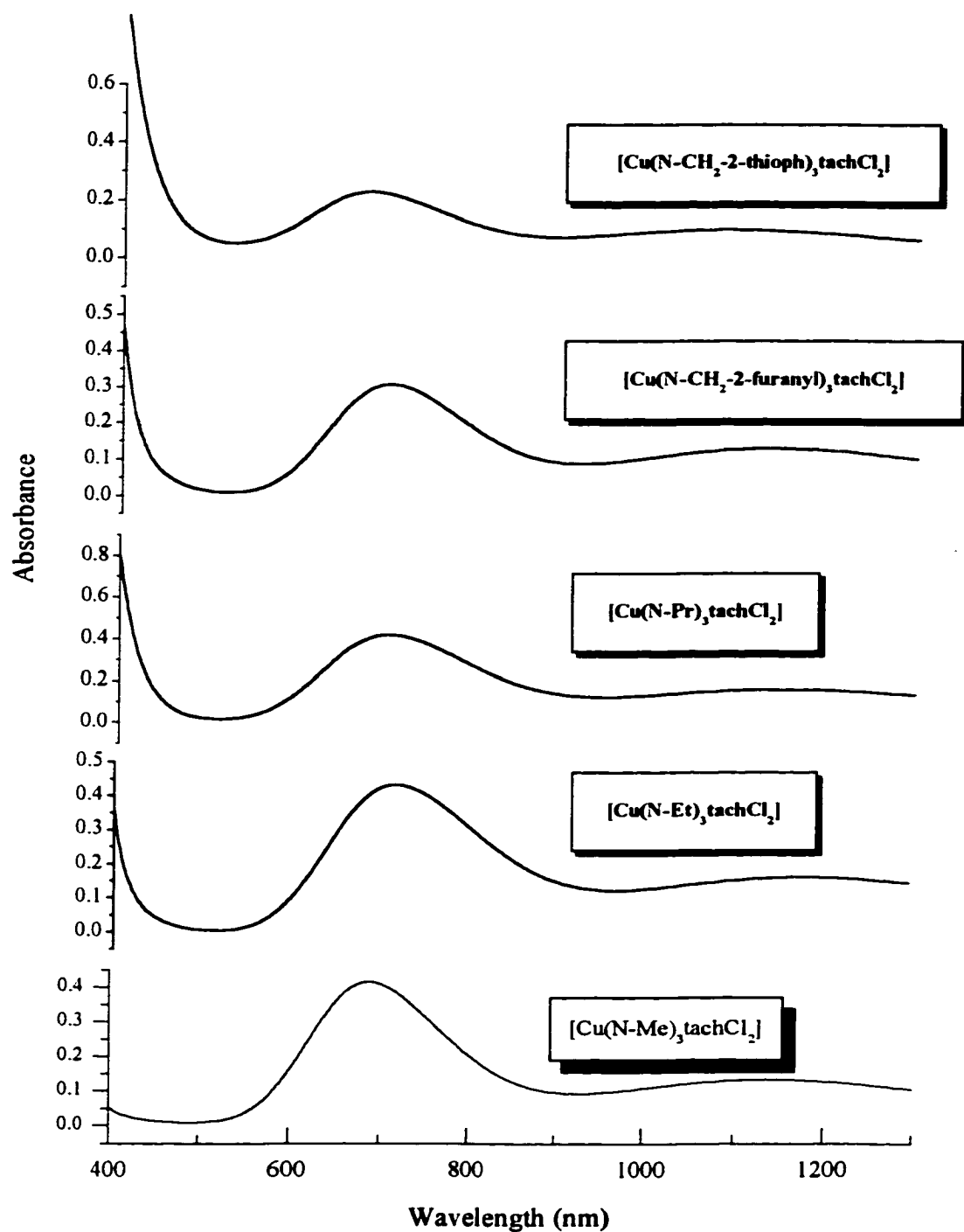


Figure 5.7 The optical spectra of copper tach chloride complexes prepared in methanol. The complex concentrations are 5 mM in analytical grade methanol (5.7.opj).

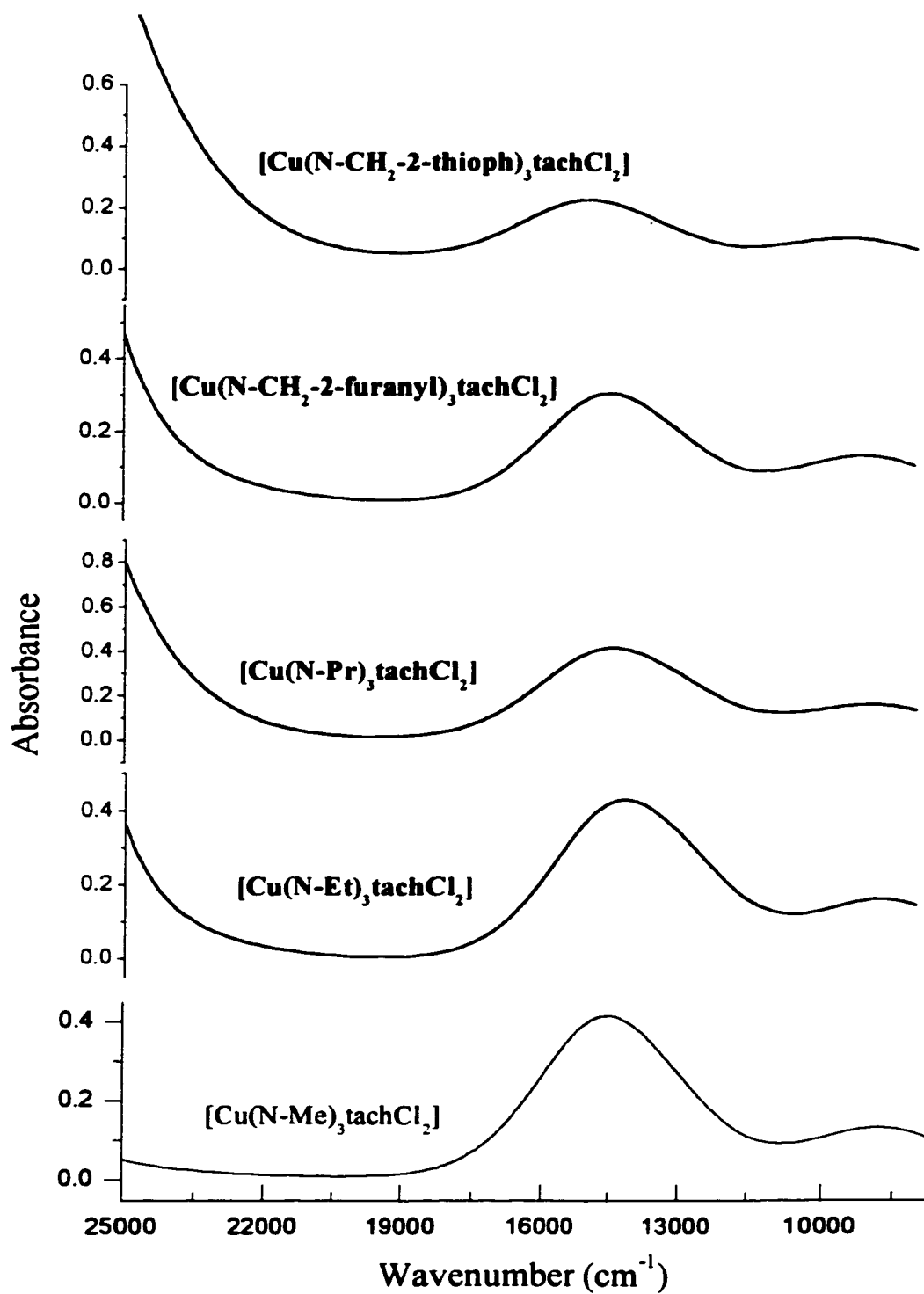


Figure 5.8 The optical spectra of copper tach chloride complexes prepared in methanol. The complex concentrations are 5 mM in analytical grade methanol (5.8.opj).

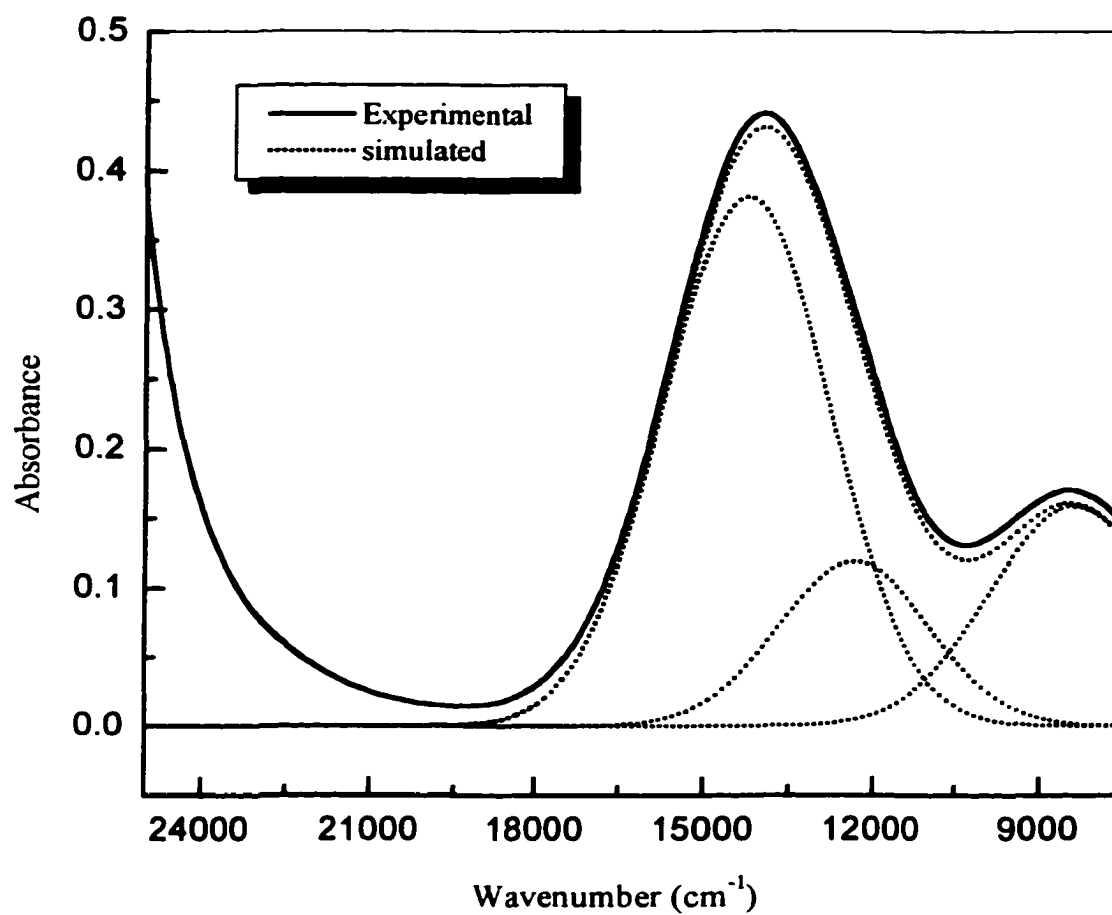


Figure 5.9 The experimental and simulated optical spectrum of [Cu(N-Et)₃tachCl₂] prepared in methanol. (5.9.opj). Note: The experimental curve (solid) was offset by 0.01 to show the match with the simulated curve (dot).

deviation of ≤ 0.01 in the absorbance was obtained for each simulated spectrum. The program, Origin.exe, has a multiple-peak Gaussian curve fitting function under the analysis menu bar. However, the fitting results were not good for all the spectra since the long wavelength peaks in the optical spectra were partially cut off. Figure 5.9 displays the experimental spectrum of the $[\text{Cu}(\text{N-Et})_3\text{tachCl}_2]$ complex and the simulated spectrum. The three individual peaks correspond to the three transitions mentioned above, and the final simulated spectrum was from the summation of these three peaks. The transition wavenumber for each peak was taken from the Gaussian function used in the simulation, and is listed in Table 5.3. The oscillator strengths of these complexes were calculated and are listed in Table 5.3a.

The $[\text{Cu}(\text{N-Et})_3\text{tachCl}_2]$ complex in HEPES buffer and CAPS buffer were also investigated by optical spectroscopy. As was the complex in a powder sample, the optical spectra of these samples were similar to those in Figure 5.7 and are not presented here. The three transitions for each samples were measured and their maximum wavelengths and molar absorptivities are listed in the Table 5.3.

C. Orbital Bonding Coefficients of Copper Tach Complexes

The orbital bonding coefficients of metal complexes can be calculated provided that EPR and optical data are available.^[84-87, 94] As copper tach complexes have a square pyramidal structure, Neiman's method was used in calculating the bonding parameters.^[85] Neiman's notation is used in the following equations. The antibonding molecular orbitals for the "hole" configuration of the copper tach complex can be formed from the central

Table 5.3 The transition assignments for the optical spectra of the copper tach chloride complexes with errors of $\pm 10 \text{ cm}^{-1}$. ^a

Complexes	$\Delta E_{xz,yz}^b$	ΔE_{xy}^b	$\Delta E_{z^2}^b$
[Cu(N-Me) ₃ tachCl ₂] in MeOH	14252 (76.2)	12316 (24.4)	8388 (31.8)
[Cu(N-Et) ₃ tachCl ₂] in Hepes buffer	15075 (54.4)	14214 (17.8)	8670 (22.0)
[Cu(N-Et) ₃ tachCl ₂] in MeOH	14252 (76.2)	12321 (23.8)	8398 (31.8)
[Cu(N-Et) ₃ tachCl ₂] Powder	14496	12544	8223
[Cu(N-Pr) ₃ tachCl ₂] in MeOH	14482 (75.0)	12491 (19.4)	8588 (31.8)
[Cu(N-CH ₂ -2-furanyl) ₃ tachCl ₂] in MeOH	14472 (56.2)	12481 (11.8)	8698 (26.2)
[Cu(N-CH ₂ -2-thioph) ₃ tachCl ₂] in MeOH	14892 (43.0)	12656 (4.4)	9128 (19.2)

a. Molar absorptivities, $\text{M}^{-1}\text{cm}^{-1}$, in parentheses.

b. $\Delta E_{xz,yz} = E_{x^2-y^2} - E_{xz,yz}$; $\Delta E_{xy} = E_{x^2-y^2} - E_{xy}$; $\Delta E_{z^2} = E_{x^2-y^2} - E_{z^2}$

Table 5.3a The oscillator strength for the copper tach complexes

Complex	ν_i (cm ⁻¹)	A_i	$2B_i$ (cm ⁻¹)	$f \times 10^6$
[Cu(N-Me) ₃ tachCl ₂]	14252	0.381	1731	6.07
	12316	0.122	1593	1.79
	8388	0.159	1755	2.57
[Cu(N-Et) ₃ tachCl ₂]	14252	0.381	1731	6.07
	12321	0.119	1603	1.75
	8398	0.159	1755	2.57
[Cu(N-Pr) ₃ tachCl ₂]	14482	0.375	1862	6.42
	12491	0.097	1703	1.52
	8588	0.159	1765	2.58
[Cu(N-CH ₂ -2-furanyl) ₃ tachCl ₂]	14472	0.281	1732	4.48
	12481	0.059	1703	0.92
	8698	0.131	1755	0.21
[Cu(N-CH ₂ -2-thioph) ₃ tachCl ₂]	14892	0.215	2001	3.96
	12656	0.022	2103	0.43
	9128	0.096	1825	1.61

atom 3d and the ligand 2s and 2p orbitals. These anti-bonding molecular orbitals are labeled according to symmetry species and are presented below.

$$B_{lg} = \alpha d_{x^2-y^2} - \alpha'(-\sigma_x^{(1)} + \sigma_y^{(2)} + \sigma_x^{(3)} - \sigma_y^{(4)})/2 \quad 5.1$$

$$B_{2g} = \beta_1 d_{xy} - \beta_1' (p_v^{(1)} + p_x^{(2)} - p_v^{(3)} - p_x^{(4)})/2 \quad 5.2$$

$$A_{1g} = \alpha_1 d_{3z^2-r^2} - \alpha_1' (\sigma_x^{(1)} + \sigma_y^{(2)} - \sigma_x^{(3)} - \sigma_y^{(4)})/2 \quad 5.3$$

$$E_g = \begin{cases} \beta d_{xz} - \beta'(p_z^{(1)} - p_z^{(3)})/2^{1/2} & 5.4 \\ \beta d_{yz} - \beta'(p_z^{(2)} - p_z^{(4)})/2^{1/2} & 5.5 \end{cases}$$

$$\{\beta_{d_{vz}} - \beta'(p_z^{(2)} - p_z^{(4)})/2^{1/2} \quad 5.5$$

Where $\sigma^{(i)} = np^{(i)} \pm (1-n^2)^{1/2}s^{(i)}$, $0 \leq n \leq 1$. n reflects the hybridization of the ligand's sigma orbitals.

$$\alpha^2 + \alpha'^2 - 2\alpha\alpha'S = 1 \quad 5.6$$

The wave functions of Eq. 5.1-5.5 can be used to solve the total Hamiltonian to second order.^[84]

Assuming B_{1g} is the ground state, the resulting spin Hamiltonian is

$$H = \beta_0 [g_{//} H_z S_z + g_{\perp} (H_x S_x + H_y S_y)] + A I_z S_z + B (I_x S_x + I_y S_y) \quad 5.7$$

Thus, we have

$$g_{//} - 2.0023 = -8\rho[\alpha\beta_1 - \alpha'\beta_1S - \alpha'(1-\beta_1^2)^{1/2}T(n)/2] \quad 5.8$$

$$g_{\perp} - 2.0023 = -2\mu[\alpha\beta - \alpha'\beta S - \alpha'(1-\beta^2)^{1/2}T(n)/2^{1/2}] \quad 5.9$$

$$A_{//} = P[-\alpha^2(4/7 + \kappa_0) + (g_{//} - 2.0023) + 3/7(g_{\perp} - 2.0023) - 8\rho\{\alpha'\beta_1 S + \alpha'(1 - \beta_1^2)^{1/2}T(n)/2 - 6/7\mu\{\alpha'\beta S + \alpha'(1 - \beta^2)^{1/2}T(n)/2^{1/2}\}] \quad 5.10$$

As well as,

$$\rho = \frac{\lambda_0 \alpha \beta_1}{\Delta E_{xz}} \quad 5.11$$

$$\mu = \frac{\lambda_0 \alpha \beta}{\Delta E_{xy}} \quad 5.12$$

where, λ_0 is the spin-orbit coupling constant which is chosen to be -828 cm^{-1} .^[85] κ_0 is the Fermi-contact term which is taken as $\kappa_0 = 0.43$ for the free ion.^[85] ΔE_{xy} and ΔE_{xz} are $E_{xy} - E_{x^2-y^2}$ and $E_{xz} - E_{x^2-y^2}$, respectively. S is the overlap integral of the copper ion and ligand B_{1g} orbitals. The values of $S_{\text{nitrogen}} = 0.093$ and $S_{\text{oxygen}} = 0.076$.^[85] $T(n) = n + 1/2(1-n^2)^{1/2} R\Omega$, is a function of the metal-ligand internuclear distance (R), the effective nuclear charge (Ω) and the s-p hybridization of the ligand orbitals (n), and takes the values of $T(n)_{\text{nitrogen}} = 0.333$ and $T(n)_{\text{oxygen}} = 0.220$.

Microcal's Origin was used to calculate all the bonding parameters (see Appendix F). The protocol file named Bondingpara.org was set up with the script language to do the calculation. Given the g_{\parallel} , g_{\perp} and A_{\parallel} from the EPR measurements and the ΔE_{xy} and ΔE_{xz} from the optical spectra, the bonding parameters α^2 , β^2 and β_1^2 were calculated and are tabulated in Table 5.4.

D. ENDOR Studies of the $[\text{Cu}(\text{N-Me})_3\text{tachCl}_2]$ Complex

As the EPR spectra of the copper tach chloride complexes did not resolve the hyperfine couplings from the apical and basal coordinated nitrogen atoms, ENDOR

Table 5.4 The calculated bonding parameters of the Cu(N-Et)₃ tach Cl₂ complex in HEPES buffer and in methanol

Copper complexes	$g_{//}$ -2.0023	g_{\perp} -2.0023	$A_{//}$ (cm ⁻¹)	ΔE_{xzyz} (cm ⁻¹)	ΔE_{xy} (cm ⁻¹)	α^2	β^2	β_1^2
in Hepes buffer	0.2636	0.0633	0.0164	15075	14214	0.78	0.92	0.88

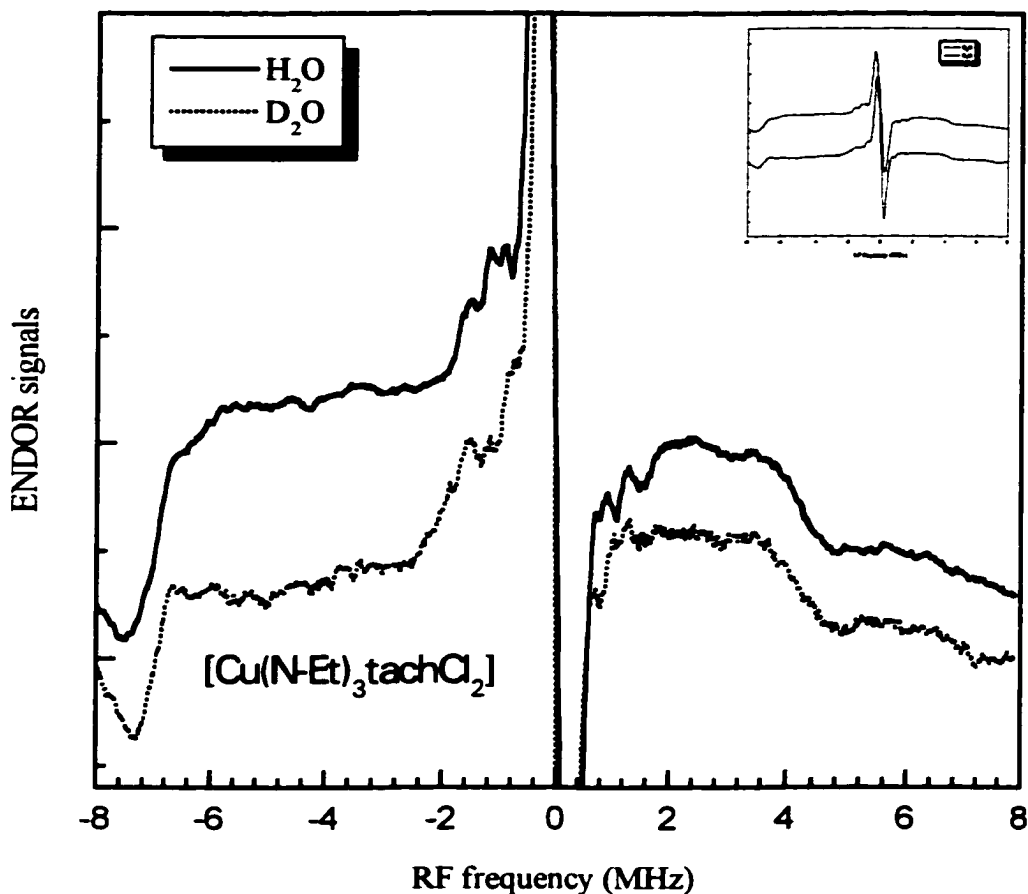


Figure 5.10 The ^1H ENDOR spectra at the parallel field position of $M_I = -1/2$ for the copper complex in H_2O and D_2O . Common experimental conditions: Microwave power, 2 mW; Radio frequency power, 100 W; Modulation depth, 1.75 V, 180 kHz; Time constant, 0.1 s; Scan rate, 0.8 MHz/s; Temperature, 2.4 K; Scan range, 16 MHz; Number of scans, 150; Individual experimental conditions: in H_2O , Receiver gain, 25,000; File name, 99041508.flis; in D_2O , Receiver gain, 50,000; File name, 99041516.flis; The inset are the full scale ^1H ENDOR spectra at the parallel field position. (5.10.opj)

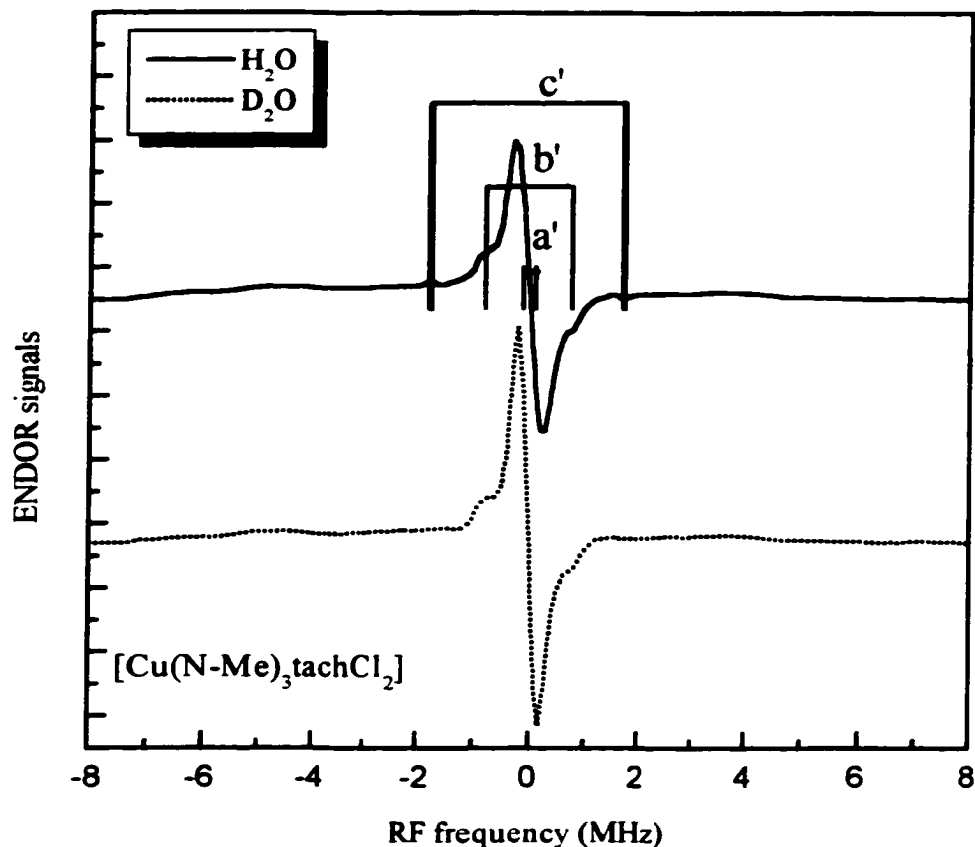


Figure 5.11 The ^1H ENDOR spectra at perpendicular position for the copper complex in H_2O and D_2O . These spectra were obtained from the subtraction of the ENDOR signals by the background (off EPR lines). Common experimental conditions: Microwave power, 2 mW; Radio frequency power, 100 W; Modulation depth, 1.75 V, 180 kHz; Time constant, 0.1 s; Scan rate, 0.8 MHz/s; Temperature, 2.4 K; Scan range, 16 MHz; Scan times, 150; Individual experimental conditions: in H_2O , Receiver gain, 2,500; File name, 99041523.flis; in D_2O , Receiver gain, 3,200; File name, 99041512.flis; (5.11.opj)

Table 5.5 The ^1H hyperfine couplings (MHz) and ^{14}N peak positions of aqueous $[\text{Cu}(\text{N-Me})_3\text{tachCl}_2]$ sample. ^a ^b The measurement error was ± 0.02 MHz.

	Parallel position, //					Perpendicular position, \perp		
Proton ENDOR hyperfine couplings (MHz)	a	b	c	d	e	a'	b'	c'
	0.22	1.70	2.27	3.07	6.47	0.22	1.54	3.48
Nitrogen ENDOR peak positions (MHz)	a	b	c	d				
	0.78	1.54	2.64	3.40				

- a. The complex concentration was 5 mM, HEPES buffer 50 mM and pH 7.0.
b. The bold numbers are the hyperfine couplings from the exchangeable protons.

spectroscopy was applied to obtain more information about the structure of these complexes.

Figure 5.10 shows the proton ENDOR spectra of $[\text{Cu}(\text{N-MeEt})_3\text{tachCl}_2]$ samples (in H_2O and D_2O) at the parallel field position of $M_I = -1/2$. The measured hyperfine couplings are presented in Table 5.5. There are four hyperfine splittings, 6.47, 3.07, 2.27 and 1.70 MHz. The 2.27 MHz coupling decreased in amplitude in the D_2O sample, which indicated that the coupling was from an exchangeable proton.

The proton ENDOR spectra at perpendicular position for both samples in H_2O and D_2O are presented in Figure 5.11. The two hyperfine couplings of 3.48 and 1.54 MHz are also listed in Table 5.5. The 3.48 MHz coupling disappeared upon deuteration. As there is more than one exchangeable proton in the complex, we are not able to assign the exchangeable protons at present.

The nitrogen ENDOR spectrum was scanned as well (see Figure 5.12). A tentative

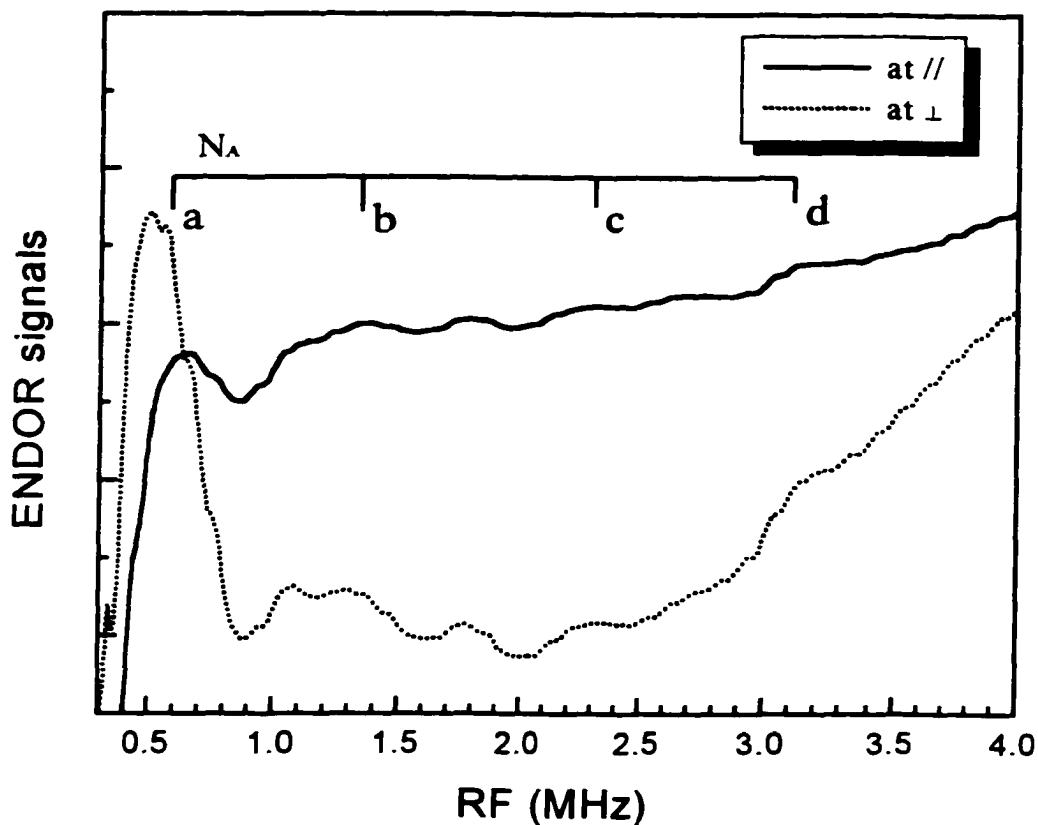


Figure 5.12 The ^{14}N ENDOR spectra of $[\text{Cu}(\text{N-Et})_3\text{tachCl}_2]$ complex in H_2O . Common experimental conditions: Microwave power, 1 mW; Radio frequency power, 100 W; Modulation depth, 1.75 V, 180 kHz; Time constant, 0.1 s; Scan rate, 0.25MHz/s; Temperature, 2.3 K; Scan range, 5 MHz; Scan times, 10; Individual experimental conditions: At Parallel position, Receiver gain, 8,000; File name, 99041521.flis; At Perpendicular position, Receiver gain, 63,000; File name, 99041522.flis; (Cu_Nitrogen_H2O.ORG)

assignment of the peaks for one of the two kinds of nitrogen atoms was made with the 0.78, 1.54, 2.64 and 3.40 MHz for the four peaks which are listed in Table 5.5. Thus, we have the following four equations^[4]

$$0.78 = A_{N_A}/2 - \nu_N - Q_N/2 \quad 5.13$$

$$1.54 = A_{N_A}/2 - \nu_N + Q_N/2 \quad 5.14$$

$$2.64 = A_{N_A}/2 + \nu_N - Q_N/2 \quad 5.15$$

$$3.40 = A_{N_A}/2 + \nu_N + Q_N/2 \quad 5.16$$

Here ν_N is the nitrogen nuclear Larmor frequency taken as 1.077 MHz at 350 mT.^[4]

Solving Equations 5.13 - 5.16 gives $A_{N_A} = 4.18$ MHz and $Q_N = 0.76$ MHz. The spectrum was not good enough for the assignment of the second type of nitrogen atom.

Discussion

A. The Structure of Copper Tach Complexes

The $[\text{Cu}(\text{N-Et})_3\text{tachCl}_2]$ complex has a distorted square-pyramidal solid-state structure. The two nitrogen and two chloride atoms are displaced from the basal plane slightly. The apical nitrogen-copper bond is not perpendicular to the basal plane, but is tilted 6.1° towards the other two nitrogen atoms. EPR spectroscopy is sensitive to the structure of the complex. The powder EPR spectrum of $[\text{Cu}(\text{N-Et})_3\text{tachCl}_2]$ is rhombic, which is consistent with the X-ray structure.^[71] Thus, the small difference between $g_x = 2.061$ and $g_y = 2.071$ may reflect the slight tilt of the apical nitrogen atom as well as the inequivalence of the chloride vs. amine nitrogens in the basal plane.

When the complex is in aqueous solution, its EPR spectrum loses the rhombic

feature. An axial spectrum exists in both X-band and Q-band spectra (Figures 5.4 and 5.5). Thus, EPR spectra support a structure which is more symmetric for the complexes in aqueous solution. The complex does not have true axial symmetry, however. The cause of the slight structural change might arise from the flexible environment around the complex in solution.

Generally, copper(II) complexes with nitrogen or oxygen atoms bound to the metal ion in a square or square pyramidal structure give $g_{\parallel} \approx 2.230$ and $g_{\perp} \approx 2.060$,^[88] similar to the values reported here (Table 5.2). The optical spectra for these copper complexes have three transitions, but the two peaks in the higher energy band superimpose with each other in some complexes.^[80] The other reasonable alternative is a trigonal bipyramidal structure.^[83, 84] However, the positions and intensities of two high-energy optical absorbances of $[\text{Cu}(\text{N-Et})_3\text{tachCl}_2]$ in MeOH (Figure 5.9 and Table 5.3) are not consistent with a trigonal-bipyramidal structure.

The similar EPR and optical spectra for all the copper tach chloride complexes (see Figures 5.4 to 5.7) suggests an identical structure for all these complexes. However, the Q-band EPR spectrum of the ethyl copper tach complex in wet methanol shows three peaks at the perpendicular field position, which indicates that more than one species exist in the solution. A reasonable explanation is that water molecules replace one or two of the coordinating chloride ions in the aqueous sample. Since H_2O is a stronger field ligand than Cl^- ion in the spectrochemical series,^[89] smaller g_{\parallel} and A_{\parallel} are expected in water. Similarly, when the complex was prepared in CAPS buffer with $\text{pH} = 10.1$, OH^- may replace H_2O as a ligand. The titration of a mixture of $(\text{N-Et})_3\text{tach}$ and CuCl_2 in water is

consistent with the presence of one coordinated hydroxide ligand at pH 10.1.^[85a] The optical spectra are consistent with the above explanation as well. In aqueous samples, water molecules replace the chloride atoms as ligands. Since water is a stronger field ligand than chloride, the energy of the $d_{x^2-y^2}$ level is expected to be higher for the aqueous complex (see Figure 5.2). Thus, higher energy transitions are expected for the samples in aqueous solution. The optical spectra clearly reflect the ligand exchange (see Table 5.3).

Copper(II) complexes with nitrogen atoms bound to the copper ion in square or square pyramidal structures have been widely studied by ENDOR spectroscopy.^[90-93] As the unpaired electron resides in the copper $d_{x^2-y^2}$ orbital, the ligand atoms (hydrogen and nitrogen) have large Fermi contact with the electron spin. Thus, large nitrogen and hydrogen hyperfine splittings with large isotropic couplings may be observed. Comparatively, an axial nitrogen or hydrogen has much smaller isotropic couplings, thus small hyperfine couplings. The typical basal nitrogen and hydrogen hyperfine couplings are 40.0 and 10.0 MHz, respectively.^[92, 93] An apical proton has a typical hyperfine coupling of 7 MHz.^[90]

The $A_N = 4.18$ MHz at parallel field position seen for $[\text{Cu}(\text{N-Me})_3\text{tachCl}_2]$ is most likely from the apical nitrogen, since the value is much smaller than 40.0 MHz. Ignoring the isotropic component, the distance from the apical nitrogen atom to the copper ion is estimated as 2.74 Å from Equation 4.6. This value is larger than 2.218(5) Å distance determined from the X-ray data.^[71] The deviation of the nitrogen ENDOR result from the X-ray result could arise from ignoring the isotropic coupling for the nitrogen atom and the slight structural change in solvent for the complex. Further nitrogen ENDOR experiments

need to be done in order to determine the distance between the basal nitrogen and the copper ion.

It is difficult to assign the proton hyperfine couplings, since the angle effect reduces the basal proton hyperfine coupling to half of its maximum value (5.0 MHz). There are two types of basal exchangeable protons and one apical exchangeable proton. The experimental hyperfine couplings could not be unambiguously assigned to any exchangeable protons. The nonexchangeable protons also could not be assigned without selective deuteration of the ligand.

B. The Orbital Bonding Coefficients of $[\text{Cu}(\text{N-Et})_3\text{tachCl}_2]$

The bonding parameters of the aqueous $[\text{Cu}(\text{N-Et})_3\text{tachCl}_2]$ complex is presented in Table 5.4. A bonding parameter of 0.5 corresponds to a "pure" covalent bond and a parameter of 1.0 to a "pure" ionic bond. The in-plane σ bond (expressed by α^2) is less sensitive to the ligand change, whereas the in-plane π bond (depicted by β_1^2) is more sensitive to the ligand change. The out-plane π bonds (expressed by β^2) are in between. For the aqueous complex, the in-plane and out-plane π bonds are rather ionic (Table 5.4). However, its in-plane σ bond is more covalent in character.

Nieman and collaborators found that β_1^2 is a better indicator of covalent character than is α^2 .^[85] Their finding is consistent with the results presented here. Most complexes with nitrogen or oxygen coordinated with a metal ion have an in-plane sigma bonding α^2 close to 0.8.^[85] The results derived here are also in the same range.

Conclusions

The $[\text{Cu}(\text{N-Et})_3\text{tachCl}_2]$ complex has a crystal structure which is close to a square pyramid with the apical nitrogen tilted 6.1° towards the other two basal nitrogen atoms. EPR spectroscopy supports this structure by showing a slightly rhombic spectrum for the powder. Contrary to the crystal structure, the complex in solution has an axial EPR spectrum which suggests a more symmetric, pseudo- C_{4v} structure. In pure methanol, there is no ligand exchange in the complex. However, the chloride atoms are replaced by water molecules in aqueous solution, as indicated by optical spectroscopy and EPR spectroscopy. The in-plane σ bonds are covalent, but the out-plane π bonds are ionic for the complex in aqueous solution. The in-plane π bond is ionic for the aqueous sample.

CHAPTER 6

THE APPLICATION OF Q-BAND EPR TO THE FOSSIL TOOTH DATING

Introduction

EPR tooth dating is one of the successful applications of EPR in the earth sciences and archaeology.^[95] Tooth enamel is a desirable material for dating by EPR due to its characteristics which satisfy the criteria for crystalline substance dating.^[96] Like other crystalline insulating materials, tooth enamel has two energy bands which electrons may occupy (see Figure 6.1). One band is called the valence band (ground state), and the other one is the conductance band (excited state). All electrons exist in the ground state when the mineral is formed. Afterwards, successive natural irradiation (such as α , β , or γ particles) over time excites electrons into the conduction band. Most of the electrons relax to the ground state, but a few diffuse through the crystal and are trapped in charge defect sites, forming paramagnetic centers. The trapped electrons can be detected by EPR spectroscopy. The intensity of the EPR signal is proportional to the strength of the radioactive field (dose rate) and the time (age) of the irradiation.

The EPR age is determined by the following equation:^[97]

$$A_{\Sigma} = A_{\text{int}} + A_{\text{ext}} = \int_0^t D_{\Sigma}(t) dt = \int_0^t (D_{\text{int}}(t) + D_{\text{ext}}(t)) dt \quad 6.1$$

where $A_{\Sigma} \equiv$ the total accumulated dose in the sample,

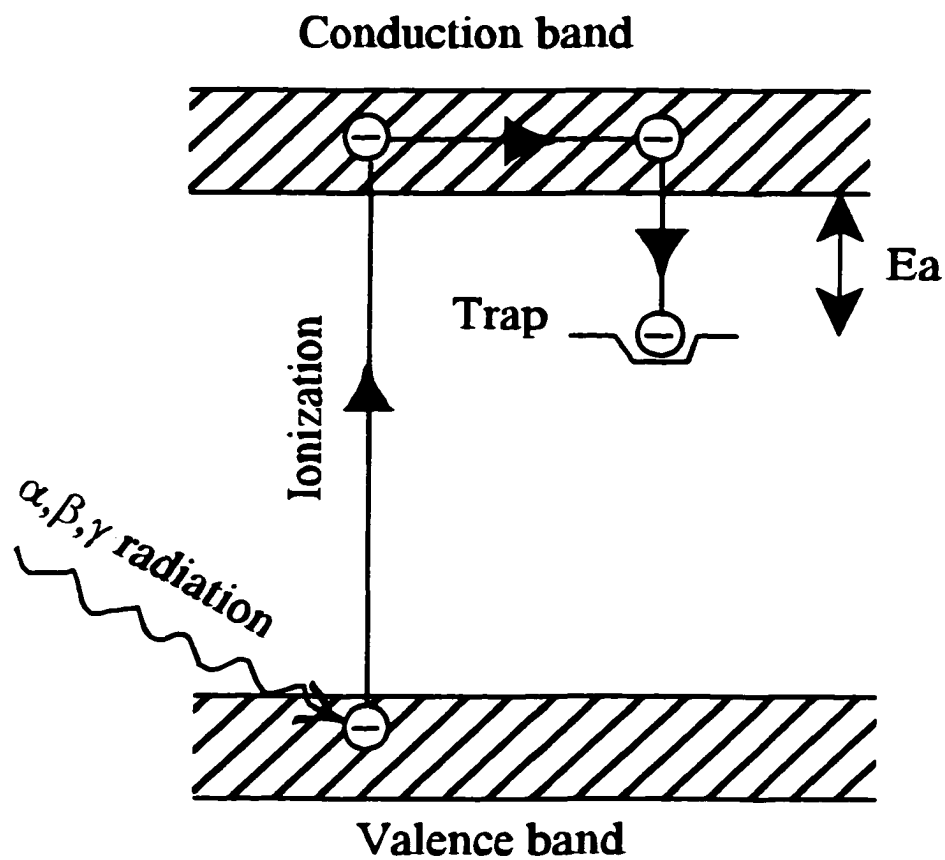


Figure 6.1 The trapping scheme of electrons in minerals.

A_{int} \equiv the internally derived accumulated dose component due to internal radiation sources (such as uranium impurities) within the sample,

A_{ext} \equiv the externally derived accumulated dose component from naturally occurring radiation external to the sample,

$D_{\Sigma}(t)$ \equiv the total dose rate,

$D_{\text{int}}(t)$ \equiv the total dose rate from within the sample,

$D_{\text{ext}}(t)$ \equiv the total dose rate from the external environment,

t \equiv the sample's age.

The total accumulated dose (A_{Σ}) is usually determined by the additive dose method, in which more than eight sample aliquots are irradiated with successive doses of increasing γ or β radiation. The EPR signal amplitudes grow larger accordingly. By extrapolating the curve to zero amplitude, A_{Σ} can be derived. The total dose rate $D_{\Sigma}(t)$ is usually determined empirically. If the dose rate, $D_{\Sigma}(t)$, is a constant, then Equation 6.1 reduces to

$$t = \frac{A_{\Sigma}}{D_{\Sigma}} = \frac{A_{\Sigma}}{D_{\text{int}} + D_{\text{ext}}} \quad 6.2$$

X-band EPR spectra of fossil tooth powder show an axial structure.^[98] However, for some tooth enamel samples, the dating peak is not well resolved at X-band. In order to completely resolve these peaks, Q-band EPR spectroscopy is needed. The Q-band study described below is a collaborative project with Dr. Anne R. Skinner of Williams College. These Q-band spectra were obtained to determine the suitability of X-band EPR spectroscopy for routine fossil tooth dating.

Experimental

The Q-band spectrometer is the assembly of a modified Varian Q-band E-110 microwave bridge, a Varian E-9 console and a home made cylindrical TE 011 cavity as described in Chapter 2. The EPR spectra were obtained at room temperature. One sample was scanned at 100 K to study the microwave power saturation characteristics of an artificially irradiated sample.

Results and Discussion

Figure 6.2 shows the X-band EPR spectrum of the fossil tooth sample artificially irradiated for 200 Grays (the SI unit, 1 Gray = 1 joule deposited per kilogram of silicon). The g_{\perp} and g_{\parallel} peaks arise from radical centers in hydroxyapatite.^[98] The dating peak is the g_{\perp} peak at 2.0018, and the g_{\parallel} is 1.9996. However, at the perpendicular position, there exists another peak which overlaps with the dating peak. The interfering peak potentially limits the application of X-band EPR spectroscopy for fossil tooth dating. In order to solve this problem, we need to know the source and characteristics of the interfering peak. Therefore, Q-band EPR spectroscopy was applied to fully separate the dating peaks from the interfering peak.

Figure 6.3 displays the Q-band EPR spectrum of the sample in Figure 6.2. Here, four peaks were resolved with the dating peak having $g_{\perp} = 2.0016 \pm 0.0002$ and $g_{\parallel} = 1.9970 \pm 0.0002$. The Q-band g_{\perp} value is in agreement with the X-band g -value of 2.0018, but the Q-band g_{\parallel} value is not. The two extra peaks seen in Figure 6.3 having $g_A = 2.0050 \pm 0.0002$ and $g_B = 2.0002 \pm 0.0002$ were not resolved at X-band from the g_{\perp}

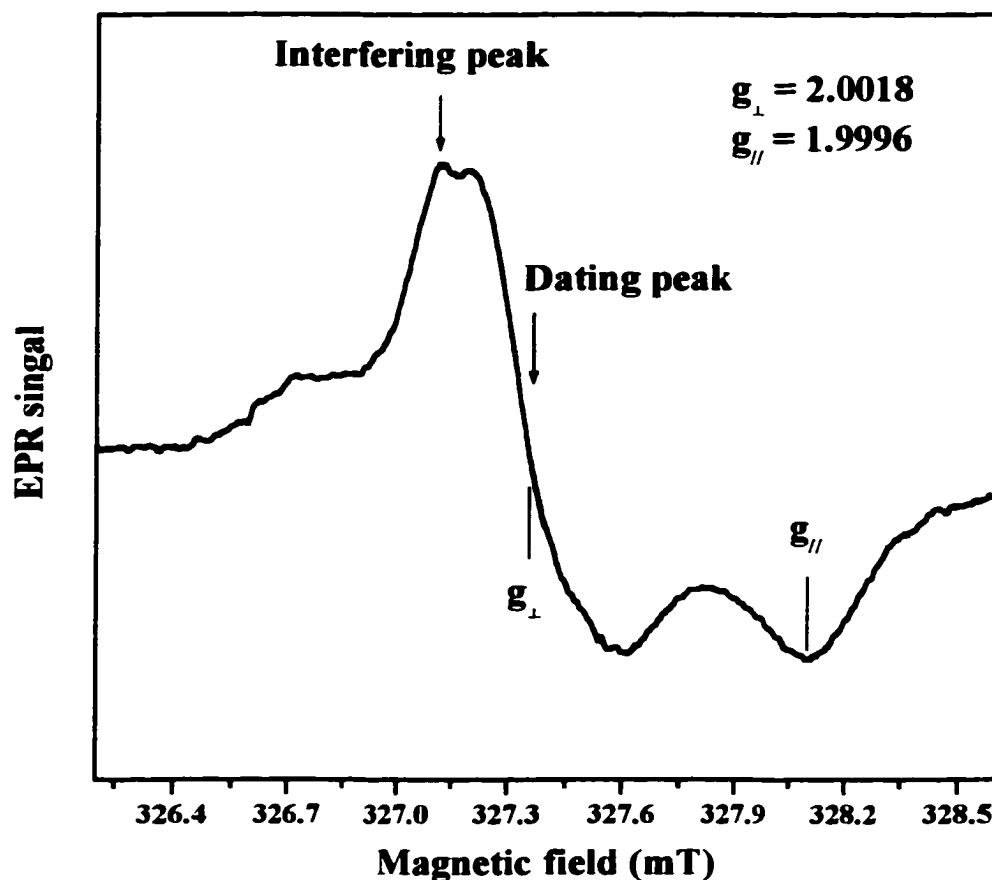


Figure 6.2 The X-band EPR spectrum of a fossil tooth enamel sample (59-200).
 Experimental Conditions: Microwave power, 0.2 mW; Modulation Amplitude, 0.03 mT;
 Field Set, 327.4 mT; Scan Range, 2.4 mT; Receiver Gain, 0.003 V; Modulation
 Frequency, 100 kHz; Time Constant, 1 s; Scan Time, 500 s; Temperature, 298 K;
 Spectrometer, Bruker; Microwave Frequency, 9.1639 GHz; File Name, 99112501.flr; (X-
 band fossil.opj)

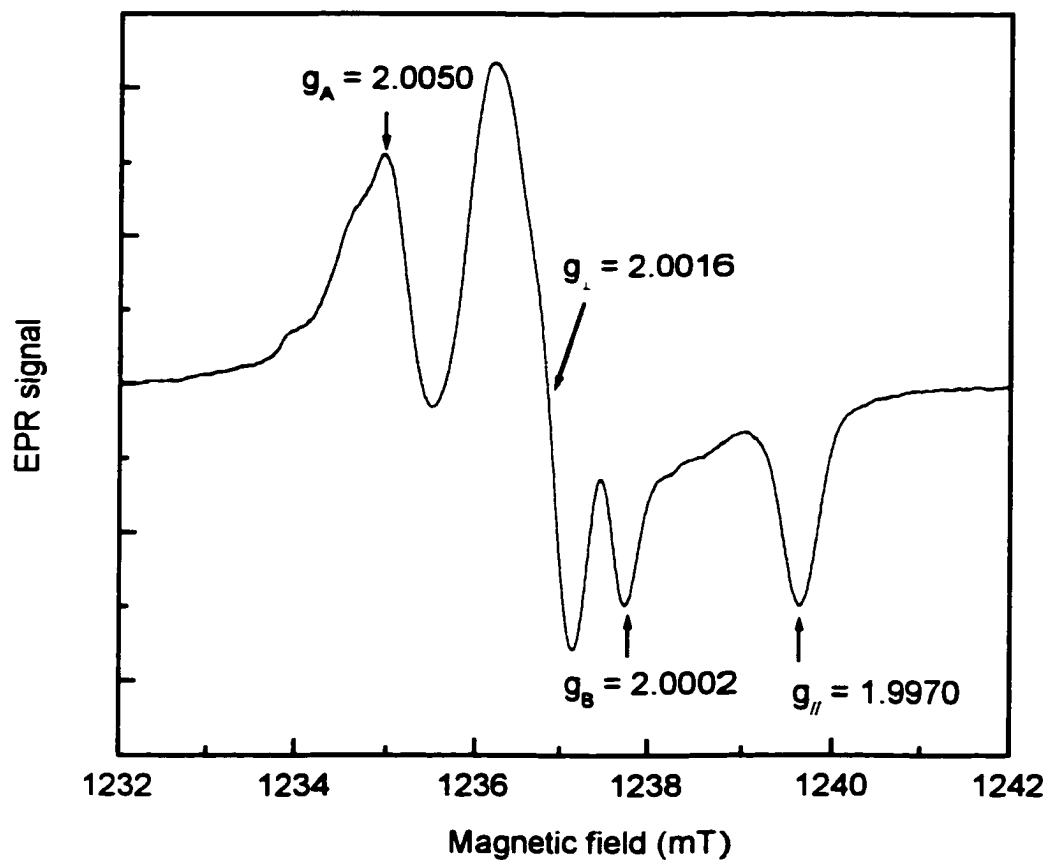


Figure 6.3 The Q-band EPR spectrum of the fossil tooth enamel sample of Figure 6.2. Experimental Conditions: Microwave power, 0.06 mW; Modulation Amplitude, 0.1 mT; Field Set, 1237 mT; Scan Range, 10 mT; Receiver Gain, 32; Modulation Frequency, 100 kHz; Time Constant, 1 s; Scan Time, 8 minutes; Temperature, 297 K; Spectrometer, Varian Q-band; Microwave Frequency, 34.6995 GHz; File Name, 5910200.flis; (FOSSIL-59-200.OPJ)

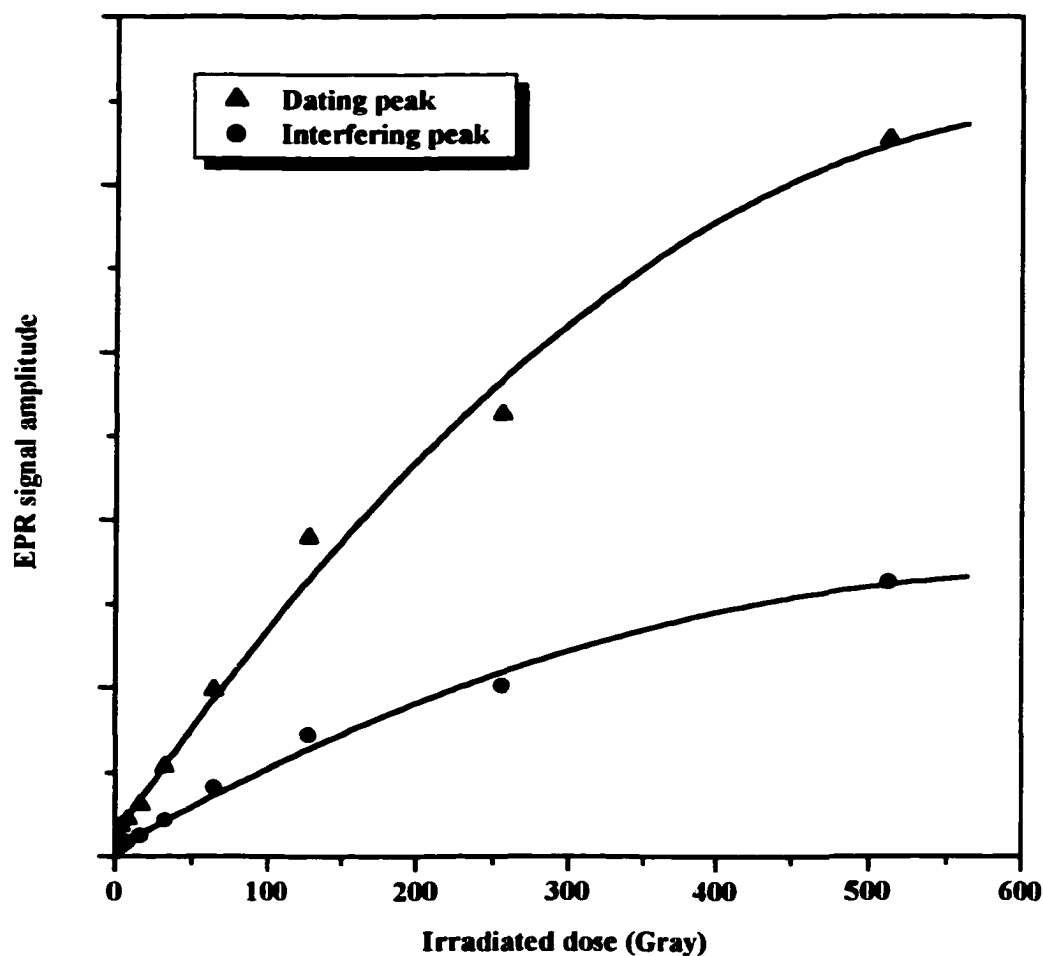


Figure 6.4 The EPR amplitudes of the dating ($g_1 = 2.0016$) peak and the interfering ($g_A = 2.0050$) peak versus the irradiation dose. Experimental Conditions: Microwave power, 0.06 mW; Modulation Amplitude, 0.1 mT; Field Set, 1237 mT; Scan Range, 10 mT; Receiver Gain, 20~400; Modulation Frequency, 100 kHz; Time Constant, 1 s; Scan Time, 16 minutes; Temperature, 100 K; Spectrometer, Varian Q-band; Microwave Frequency, 34.7057 GHz; File Name, 59100.fl, 59101.fl, 59104.fl, 59108.fl, 591016.fl, 591032.fl, 591064.fl, 5910128.fl, 5910256.fl, 5910512.fl; (fossil.opj)

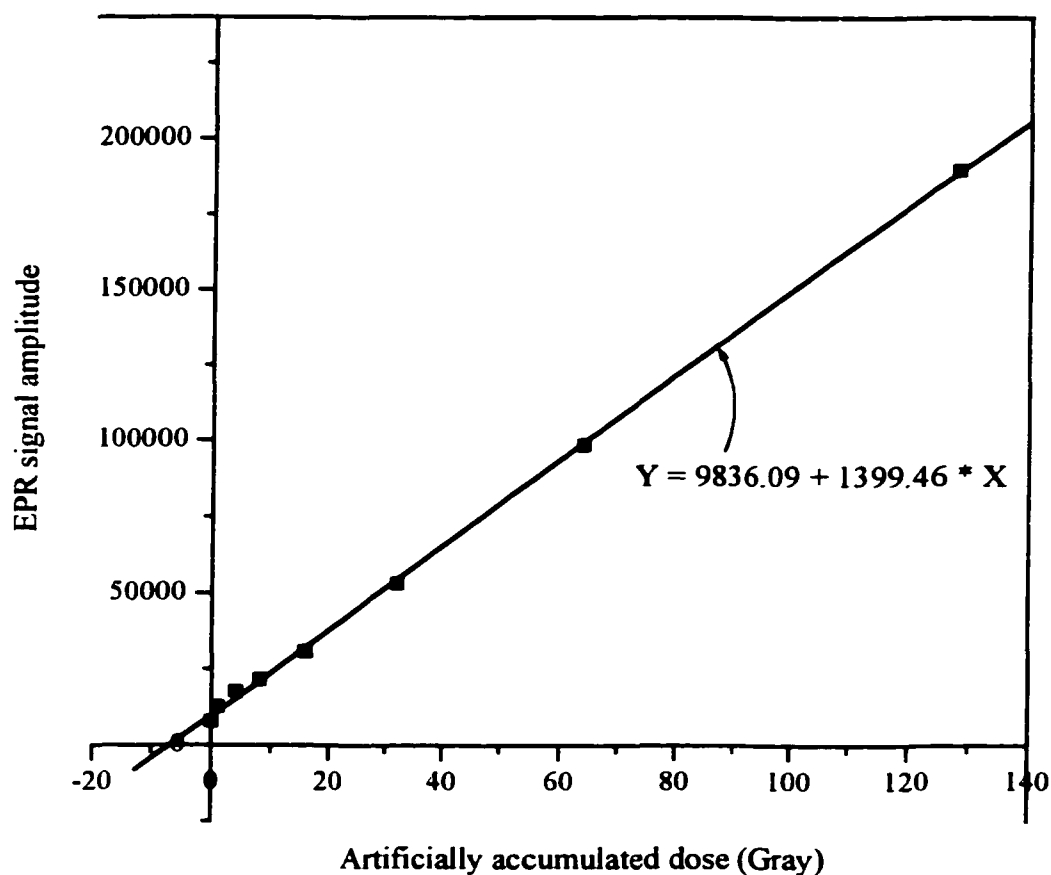


Figure 6.5 The EPR signal amplitude versus the artificially irradiated dose for the fossil teeth samples (59-0 ~ 59-512). Experimental conditions: Microwave power, 0.06 mW; Modulation Amplitude, 0.1 mT; Field Set, 1237 mT; Scan range, 10 mT; Receiver gain, 20~400; Modulation frequency, 100 kHz; Time constant, 1 s; Scan time, 16 minutes; Temperature, 100 K; Spectrometer, Varian Q-band; Microwave frequency, 34.7057 GHz; File Name, 59100.fl, 59101.fl, 59104.fl, 59108.fl, 591016.fl, 591032.fl, 591064.fl, 5910128.fl, 5910256.fl, 5910512.fl; (fossil.opj)

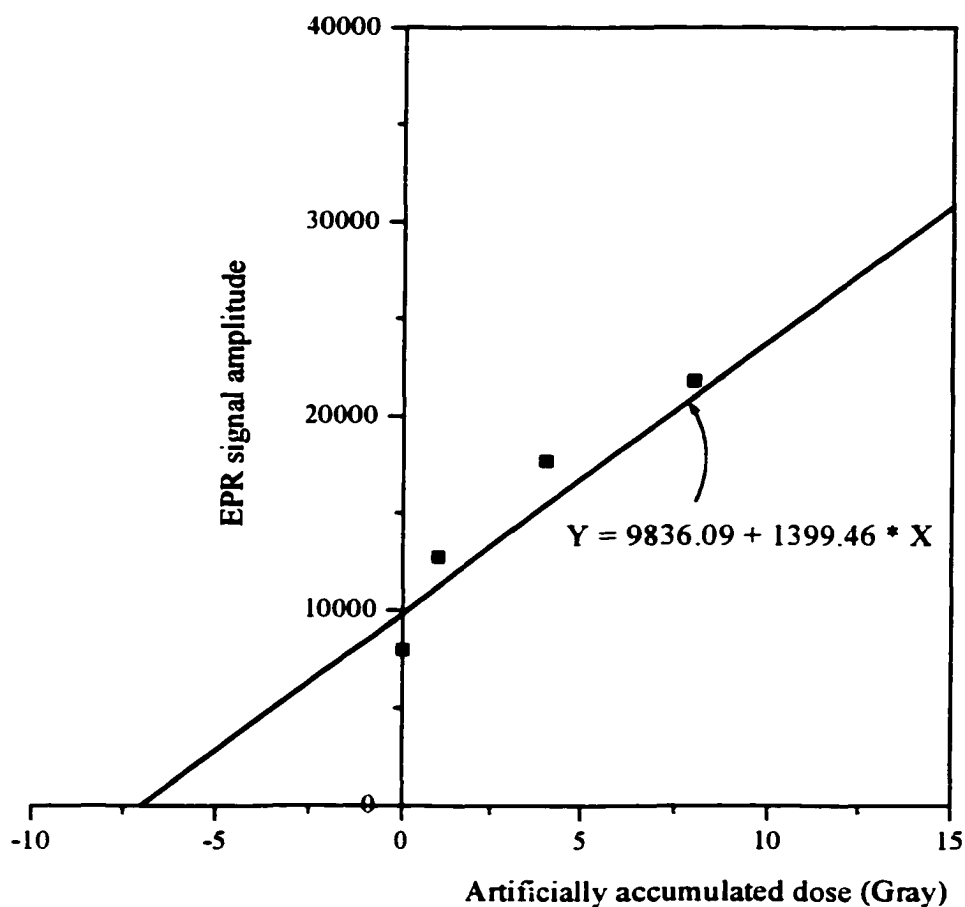


Figure 6.6 The EPR signal amplitude versus the artificially accumulated dose for the fossil teeth samples (59-0 ~ 59-512). Experimental conditions: Microwave power, 0.06 mW; Modulation Amplitude, 0.1 mT; Field Set, 1237 mT; Scan range, 10 mT; Receiver gain, 20~400; Modulation frequency, 100 kHz; Time constant, 1 s; Scan time, 16 minutes; Temperature, 100 K; Spectrometer, Varian Q-band; Microwave frequency, 34.7057 GHz; File Name, 59100.fl, 59101.fl, 59104.fl, 59108.fl, 591016.fl, 591032.fl, 591064.fl, 5910128.fl, 5910256.fl, 5910512.fl; (fossil.opj)

peak.

Q-band EPR spectra were measured for a series of fossil tooth samples from a mastadon exposed to various doses of artificial irradiation. The peak intensities of g_A and the dating peak at g_1 were measured for each sample and are plotted as a function of irradiation dose in Figure 6.4. Except for artificial doses above ~ 300 Grays, both the interfering peak and the dating peak intensities are linear functions of the artificial dose. So, both the dating peak and the interfering peak are proportional to the irradiation dose. Ignoring the saturated points at 256 and 512 Grays and fitting the rest of the data points for the dating peak in Figure 6.4 gives a straight line which is presented in Figure 6.5 for the lower doses. The accumulated dose A_Σ before artificial irradiation of the fossil teeth was determined from the fitted line in Figure 6.6 to be 7.0 Grays. Assuming that a typical natural dose rate, D_Σ , is about 5 mGray/year,^[95] the age of the fossil teeth is about 1400 years old.

The dating peak and the interfering peak were also tested for microwave power saturation at low temperature. At 100 K, the sample having 200 Grays irradiation was measured under various microwave powers. The intensities of the dating and interfering peak intensities were measured and are plotted in Figure 6.7. Both peaks became saturated above 3 μ W power as indicated by the deviation from linearity in the intensity vs. square-root of power. The maximum power of the microwave bridge is 60 mW. On the other hand, no power saturation was observed for both the dating peak and the interfering peak at room temperature.

Based on the above Q-band EPR study of the fossil tooth samples, we found that

the dating peak and the interfering peak have the same sensitivity to radiation dose and microwave power. These similarities suggest that the sources of the interfering peaks is also a hydroxyapatite defect. Multiple potential sites that vary slightly from each other are probably present in the mineral. Because of the linear correlation between the dating and interfering peak intensities, X-band spectroscopy can be used in fossil tooth dating even though the two signals overlap. However, higher field modulation amplitude is used to smooth the interfering and dating peaks.^[99]

Conclusions

The interfering peak which overlays the dating peak probably arises from a hydroxapatite defect site in the fossil tooth enamel. By smoothing the composite dating peak with a high modulation, X-band spectroscopy can be reliably used in routine fossil tooth dating. It is also possible to eliminate the effect of the interfering peak by determining the height of the peak at $g_{\parallel} = 1.9996 \pm 0.0002$ relative to the spectral baseline in the X-band spectrum, a measurement which is unaffected by this particular interference. Since the g_{\parallel} peak is much smaller than the primary one at $g_{\perp} = 2.0018 \pm 0.0002$, the uncertainties of measurement increase considerably. Finally, the age of the measured fossil teeth is estimated to be about 1400 years old.

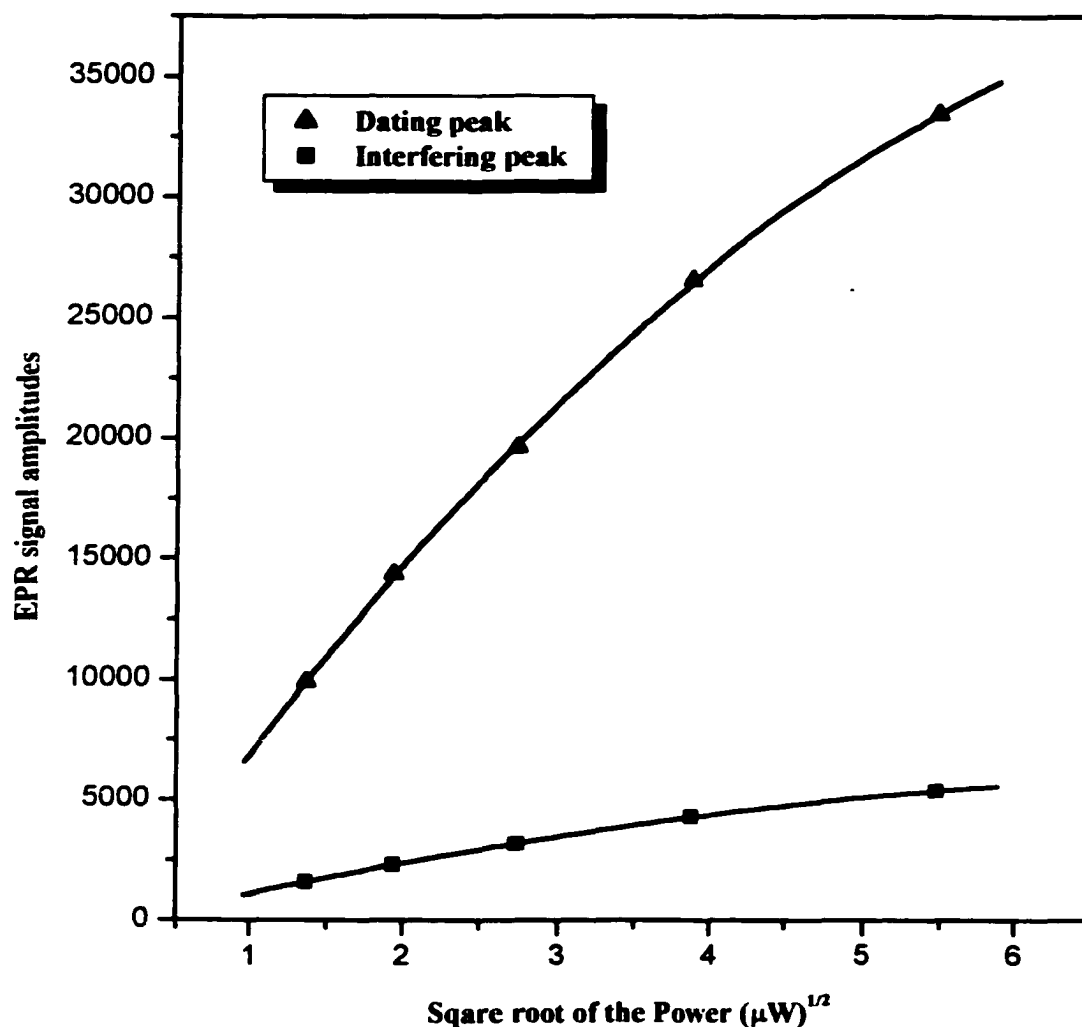


Figure 6.7 The microwave power saturation characteristics of the fossil tooth enamel sample. Experimental Conditions: Modulation Amplitude, 0.1 mT; Field Set, 1241 mT; Scan Range, 10 mT; Receiver Gain, 630; Modulation Frequency, 100 kHz; Time Constant, 1 s; Scan Time, 16 minutes; Temperature, 100 K; Spectrometer, Varian Q-band; Microwave Frequency, 34.8244 GHz; File Name, 98070603~98070607.flx; (fossil.opj)

REFERENCES

1. G. V. Buxton and Q. G. Mulazzani, *Metal Ions in Biological Systems*, 36, (1999), 103.
2. G. S. Timmins and M. J. Davies, *Biological Free Radicals*, in *Electron Paramagnetic Resonance*, 16, (1998), p. 1.
3. J. E. Wertz and J. R. Bolton, "Electron Spin Resonance", McGraw-Hill Book Co., N. Y., 1972, p. 368.
4. N. D. Chasteen and P. A. Snetsinger, *ESEEM and ENDOR Spectroscopy*, in *Physical Methods in Inorganic and Bioinorganic Chemistry*, L. Que ed., University Science Books, Mill Valley, California, 2000, in Press.
5. L. Keven and L. D. Kispert, "Electron Spin Double Resonance Spectroscopy", John Wiley & sons, New York, 1976, p. 28.
6. E-4 EPR Spectrometer System, Technical Manual, p. 4-2.
7. C. P. Poole, Jr., *Electron Spin Resonance*, 2nd Ed., John Wiley & Sons, N. Y., 1983. p. 125.
8. M. W. Makinen and G. B. Wells, in *Metal Ions in Biological Systems*. Vol. 22, *ENDOR, EPR and Electron Spin Echo for Probing Coordination Spheres*, H. Sigel, Ed., (Marcel Dekker, Inc., New York, 1987), p. 129.
9. S. A. Dzuba, Y. A. Golovina and Y. D. Tsvetkov, *J. Magn. Reson. Ser. B*, 101, (1993), 217.
10. G. R. Eaton, *Biophys. J.*, 64, (1993), 1373.
11. E. Bill, *Hyperfine Interactions*, 90, (1994), 1.
12. M. W. Makinen and D. Mustafi, in *Metal Ions in Biological Systems*. 31, (1995), 89.
13. J. S. Hyde, M. E. Newton, R. A. Strangeway, T. G. Camenisch and W. Froncisz, *Rev. Sci. Instrum.* 62, 1991, 2969.
14. R. R. Ernst, in *Advances in Magnetic Resonance*, ed. J. S. Waugh (Academic, New York, 1966), 2, p. 122.

15. P. Horowitz and W. Hill, *The Art of Electronics*, Cambridge University Press, 1980, p. 94.
16. W. Wang and N. D. Chasteen, *J. Magn. Reson., Ser. A*, 116, (1995), 237.
17. J. Shao and N. D. Chasteen, *EPR Newsletter*, 9, 1998, 10.
18. J. Hüttermann and R. Kappl, ENDOR: Probing the Coordination Environment in Metalloproteins, in *Metal Ions in Biological Systems, Volume 22., Endor, EPR, and Electron Spin Echo for Probing Coordination Spheres*, H. Sigel, Ed., (Marcel Dekker, Inc., New York, 1987), p. 1.
19. P. Curry-Proulx, *Dissertation, Construction of an X-band Electron Nuclear Double Resonance Spectrometer and Partial Characterization of an Iron Nitrosyl Complex of Transferrin*, University of New Hampshire, 1998.
20. W. Zweggart, R. Thanner and W. Lubitz, *J. Magn. Reson., Ser. A*, 109, (1994), 172.
21. P. M. Curry-Proulx and N. D. Chasteen, *Coord. Chem. Rev.*, 144, (1995), 347.
22. P. M. Harrison, S. C. Andrews, P. J. Artymiuk, G. C. Ford, J. R. Guest, J. Hirzmann, D. M. Lawson, J. C. Livingstone, J. M. A. Smith, A. Treffry and S. J. Yewdall, *Adv. Inorg. Chem.*, 36, (1991), 449.
23. T. Jones, R. Spencer and C. Walsh, *Biochemistry*, 17, (1978), 4011.
24. P. M. Harrison, *J. Mol. Biol.*, 1, (1959), 69.
25. S. H. Banyard, D. K. Stammers and P. M. Harrison, *Nature*, 271, (1978), 282.
26. G. A. Clegg, R. F. D. Stansfield, P. E. Bourne, and P. M. Harrison, *Nature*, 288, (1980), 298.
27. G. D. Watt, R. B. Frankel and G. C. Papaethymiou, *Proc. Natl. Acad. Sci. USA*, 82, (1985), 3640.
28. M. Lee, P. Arosio, A. Cozzi and N. D. Chasteen, *Biochemistry*, 33, (1994), 3679.
29. J. M. Nocek, D. M. Kartz, Jr., J. T. Sage, P. G. Debrunner, M. J. Maroney and L. Que, Jr., *J. Am. Chem. Soc.*, 107, (1985), 3382.
30. M. J. Nelson, *J. Biol. Chem.*, 262, (1987), 12137.

31. S. H. Snyder, *Science*, 257, (1992), 494.
32. J. M. Fukuto and D. A. Wink, *Metal Ions in Biological Systems*, 36, (1999), 547.
33. D. W. Reif and R. D. Simmons, *Arch. Biochem. Biophys.*, 283, (1990), 537.
34. J. C. Drapier, C. Pellat and Y. Henry, *J. Biol. Chem.*, 266, (1991), 10162.
35. E. Culotta and D. E. Koshland, Jr., *Science*, 258, (1992), 1862.
36. J. C. Drapier, H. Hirling, J. Wietzerbin, P. Kaldy and L. C. Kuhn, *EMBO J.*, 12, (1993), 3643.
37. Y. Henry, C. Ducrocq, J. C. Drapier, D. Servent, C. Pellat and A. Guissani, *Eur. Biophys.*, 20, (1991), 1.
38. J. S. Stamler, D. J. Singel and J. Loscalzo, *Science*, 258, (1992), 1898.
39. T. G. Traylor and V. S. Sharma, *Biochemistry*, 31, (1992), 2847.
40. D. R. Richardson and P. Ponka, *Methods in Neurosciences*, 31, (1996), 329.
41. J. R. Lancaster, Jr. and J. B. Hibbs, Jr., *Proc. Natl. Acad. Sci. U. S. A.*, 87, (1990), 1223.
42. C. Pellat, Y. Henry and J. C. Drapier, *Biochem. Biophys. Res. Commun.*, 166, (1990), 119.
43. Y. Henry, M. Lepoivre, J. C. Drapier, C. Ducrocq, J. L. Boucher and A. Guissani, *FASEB J.*, 7, (1993), 1124.
44. J. Stadler, H. A. Bergonia, M. D. Silvio, M. A. Sweetland, T. R. Billiar, R. L. Simmons and J. R. Lancaster, Jr., *Arch. Biochem. Biophys.*, 302, (1993), 4.
- 45 C. C. McDonald, W. D. Phillips and H. F. Mower, *J. Am. Chem. Soc.*, 87, (1965), 3319.
- 45a. M. Boese, P. I. Mordvintcev, A. F. Vanin, R. Busse and A. Mulsch, *J. Bio. Chem.*, 270, (1995), 29244.
46. A. F. Vanin, P. I. Mordnvintcev, S. Hauschildt and A. Muelsch, *Biochim. Biophys. Acta*, 1177, (1993), 37.

47. W. Wang, Dissertation, Development of Q-band EPR/ENDOR Spectrometer and EPR/ENDOR Studies of Dinitrosyl Iron Model Complexes, University of New Hampshire, 1996.
48. Y. C. Barrett, Dissertation, Characterization of Radical Formation and Iron Oxidation/Hydrolysis during Iron Deposition in Ferritin, University of New Hampshire, 1994. p136.
49. M. Heusterpreute and R. R. Crichton, *FEBS Lett.*, 129, (1981), 322.
50. X. Yang and N. D. Chasteen, *J. Biophys.*, 71, (1996), 1587.
51. D. Mustafi and M. W. Makinen, *Inorg. Chem.* 27, (1991), 3360.
- 51a. G. C. Hurst, T. A. Henderson and R. W. Kreilick, *J. Am. Chem. Soc.*, 107, (1985), 7294.
- 51b. T. A. Henderson, G. C. Hurst and R. W. Kreilick, *J. Am. Chem. Soc.*, 107, (1985), 7299.
52. C. C. McDonald, E. Tiezzi and B. Commoner, *Biochim. Biophys. Acta*, 160, (1968), 311.
53. N. M. Atherton and J. F. Shackleton, *Mol. Phys.*, 39, (1980), 1471.
54. C. F. Mulks, C. P. Scholes, L. C. Dickinson and A. Lapidot, *J. Am. Chem. Soc.*, 101, (1979), 1645.
55. M. M. Werst, M. C. Kennedy, H. Beinert and B. M. Hoffman, 29, (1990), 10526.
56. K. Doi, J. McCracken, J. Peisach and P. Aisen, 263, (1988), 5757.
57. R. C. Scarrow, B. S. Strickler, J. J. Ellison, S. C. Shoner, J. A. Kovacs, J. G. Cummings and M. J. Nelson, *J. Am. Chem. Soc.*, 120, (1998), 9237.
58. T. G. Hoy, P. M. Harrison and R. J. Hoare, *J. Mol. Biol.*, 86, (1974), 301.
59. T. Itoh, H. Hisada, T. Sumiya, M. Hosono, Y. Usui and Y. Fujii, *Chem. Commun.*, (1997), 677.
60. E. L. Hegg and J. N. Burstyn, *J. Am. Chem. Soc.*, 117, (1995), 7015.
61. K. A. Deal and J. N. Burstyn, *Inorg. Chem.*, 35, (1996), 2792.

62. E. L. Hegg and J. N. Burstyn, *Inorg. Chem.*, 35, (1996), 7474.
63. E. L. Hegg, K. A. Deal, L. L. Kiessling and J. N. Burstyn, *Inorg. Chem.*, 36, (1997), 1715.
64. E. L. Hegg, S. H. Mortimore, C. L. Cheung, J. E. Huyett, D. R. Powell and J. N. Burstyn, 38, (1999), 2961.
65. J. N. Burstyn and K. A. Deal, *Inorg. Chem.*, 35, (1993), 3585.
66. K. A. Deal, A. C. Hengge and J. N. Burstyn, *J. Am. Chem. Soc.*, 118, (1996), 1713.
67. A. Radzicka and R. Wolfenden, *Science*, 235, (1995), 90.
68. R. D. Bereman and R. S. Giordano, *J. am. Chem. Soc.*, 96, (1974), 1019.
69. R. D. Bereman, S. N. Choi and J. R. Wasson, *J. Inorg. Nucl. Chem.*, 87, (1975), 2087.
70. R. D. Bereman, F. T. Wang, J. Najdzionek and D. M. Braitsch, *J. Am. Chem. Soc.*, 98, (1976), 7266.
71. G. Park, F. H. Lu, R. D. Rogers, J. Shao, N. D. Chasteen, M. W. Brechbiel and R. P. Planalp, *Inorg. Chem.*, in preparation.
72. B. J. Hathaway and D. E. Billing, *Coordin. Chem. Rev.*, 5, (1970), 143.
73. N. D. Chasteen, J. Grady and J. Shao, *EPR Newsletter*, 10, in press.
74. W. Froncisz and J. S. Hyde, *J. Chem. Phys.*, 73, (1980), 3123.
75. J. S. Hyde and W. Froncisz, *Ann. Rev. Biophys. Bioeng.*, 11, (1982), 391.
76. W. E. Blumberg and J. Peisach, *Life Chem. Rep.*, 5, (1987), 5.
77. R. Basosi, W. E. Antholine and J. S. Hyde, *EMR of Paramagnetic Molecules in Biological Magnetic Resonance*, 13, (1993), p. 103.
78. Y. Yang, R. Pogni and R. Basosi, *J. Chem. Soc., Faraday Trans. 1*, 85, (1989), 3995.
79. M. Duggan, N. Ray, B. Hathaway, G. Tomlinson, P. Brint and K. Pelin, *J. C. S. Dalton*, (1980), 1342.
80. K. D. Karlin, J. C. Hayes, S. Juen, J. P. Hutchinson and J. Zubieta, *Inorg. Chem.*, 21,

(1982), 4108.

81. A. M. Ramadan, *J. Inorg. Biochem.*, 63, (1996), 183.

82. A. L. Abuhijleh, *J. Inorg. Biochem.*, 55, (1994), 255.

83. D. C. Harris and M. D. Bertolucci, *Symmetry and Spectroscopy*, Oxford University Press Inc., 1978, p. 336.

84. A. H. Maki and B. R. McGarvey, *J. Chem. Phys.*, 29, (1958), 31.

85. D. Kivelson and R. Neiman, 35, (1961), 149.

85a. G. Park and R. Planalp, Personal communications.

86. M. Fujimoto and J. Janecka, *J. Chem. Phys.*, 55, (1971), 1152.

87. R. K. Ray and G. B. Kauffman, *Inorg. Chim. Acta*, 174, (1990), 257.

88. B. J. Hathaway and A. A. G. Tomlinson, *Coord. Chem. Rev.*, 5, (1970), 1.

89. W. L. Jolly, *Modern Inorganic Chemistry*, McGraw-Hill Inc., 1976. p409.

90. N. M. Atherton and A. J. Horsewill, *Mol. Phys.*, 37, (1979), 1349.

91. N. M. Atherton and A. J. Horsewill, *Mol. Phys.*, 42, (1981), 985.

92. N. M. Atherton and A. J. Horsewill, *J. C. S. Fara. II*, 76, (1980), 660.

93. H. L. Van Camp, R. H. Sands and J. A. Fee, *J. Chem. Phys.*, 75, (1981), 2098.

94. T. R. Reddy and R. Srinivasan, *J. Chem. Phys.*, 43, (1965), 1404.

95. R. Grün, *Quaternary International*, 1, (1989), 65.

96. H. P. Schwarcz, *Nucl. Tracks*, 10, (1985), 865.

97. B. A. Blackwell, *Electron Spin Resonance*. In: *Dating Methods for Quaternary Deposits*, (eds. N. W. Rutter and N. R. Catto), 1995, 209.

98. M. Ikeya, *Naturwissenschaften*, 68, (1981), 474.

99. A. R. Skinner, B. A. B. Blackwell, N. D. Chasteen, J. Shao, and S. S. Min, *Applied Radiation & Isotopes*, 2000, accepted.

APPENDIX A

OPERATION OF THE Q-BAND EPR/ENDOR SPECTROMETER

Console control is converted from X-band to Q-band by the procedures described in the Appendix E in Wang's dissertation.^[47] The spectrometer operations are also the same as before except that the phase adjustment is less sensitive than before. The detector current is still set at 50 μ A.

Setup of the low temperature nitrogen flowing system

Figure A. 1 is the schematic diagram of the low temperature nitrogen flowing system used in the Q-band EPR/ENDOR spectrometer. Nitrogen gas flows out of the gas cylinder being regulated by the regulator (output pressure is usually set at 10 psi), passes a flow rate gauge (controlled at 25 SCFH), then runs through a piece of ~ 5 meters long rubber tubing or a large liquid nitrogen container (41 liter) to minimize any fluctuations in flow. The stabilized nitrogen gas goes through a circular wound copper tube immersed in liquid nitrogen, a piece of transfer line, the Dewar containing the cavity and finally through a piece of insulating foam tubing. The cavity temperature can be adjusted by controlling the nitrogen gas flow, and is monitored by a copper-constantan thermocouple. The reference junction temperature is kept at 0 °C by immersing it in a beaker containing ice water. A DC millivolts meter (Univac Inc., Remington Rand, NJ) is used to measure the voltage.

After the completion of low temperature operation and no liquid nitrogen remains in the liquid nitrogen dewar, nitrogen gas is then passed through the whole system for at least two hours to keep moisture away from the cavity.

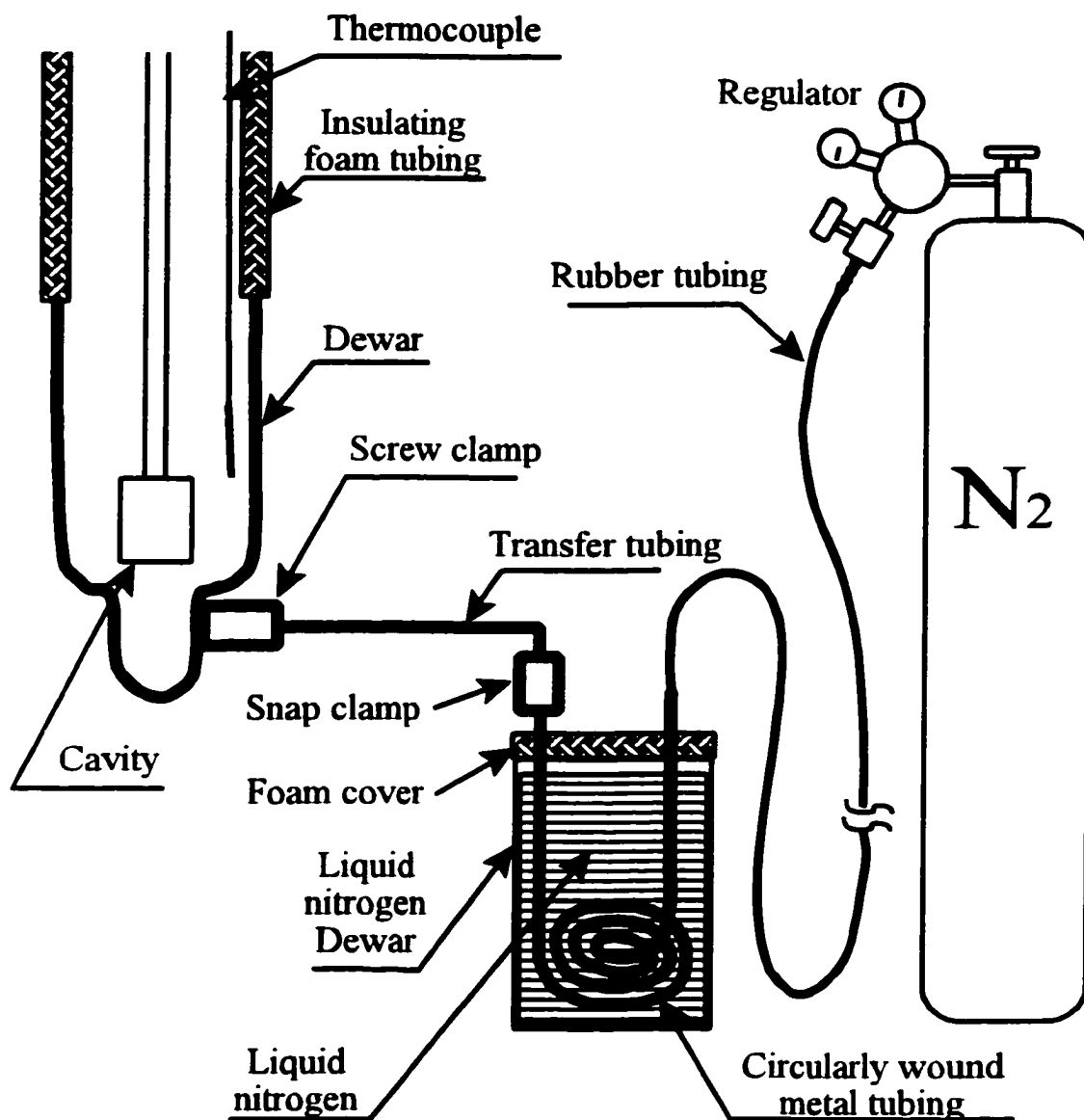


Figure A.1 The schematic diagram of the Q-band liquid nitrogen flow system. (A.1.wpd)

APPENDIX B

OPERATION OF LIQUID HELIUM COOLING SYSTEM IN THE X-BAND EPR/ENDOR SPECTROMETER

The schematic diagram of the helium flow cryostat system is displayed in Figure B.1. The temperature is monitored by the model 330 autotuning temperature controller (Lake Shore Cryotronics, Inc., Westerville, OH). The low temperature sensor is a GaAlAs Diode with TG-120P Package, serial number 10017 (Lake Shore Cryotronics, Inc., Westerville, OH). The working curve used in the temperature controller is number 12. The liquid helium level in the reservoir is measured by the Liquid Helium Level meter model 1200 S/H (Cryomagnetics, Inc., Oak Ridge, TN). The high vacuum (1×10^{-6} torr) is achieved with a Varian SD-200 pump system (Varian, Inc., Walnut Creek, CA).

High Vacuum Pump

Usually, before carrying out ENDOR experiment at liquid helium temperature, the transfer line and the cryostat should be pumped by the diffusion pump system for 48 hours to 1×10^{-6} torr. The connection between the high vacuum system, the transfer line and the cryostat system is presented in Figure B.1. The pumping steps are described in the following:

1. Check the status of all the values according to Table B.1.
2. Power on the Mechanical Pump A (Varian SD-200) and pump the bellowed steel

vacuum tubing for 1/2 hour.

3. Open Valve A, Valve B and Valve E, respectively.

4. Pump the whole system with only the Mechanical Pump A for about another 1/2 hour.

Check the system vacuum by the thermocouple Vacuum Gauge (operation range, 1×10^{-3} torr - 760 torr).

5. When the system vacuum is about 1×10^{-3} torr, power on the Diffusion Pump.

Table B.1 The status of all the valves in Figure B.1 at the beginning and the end of an ENDOR experiment.

Valves	A	B	C	D	E	F	G	H	P	R	T
Beginning	closed	closed	closed	opened	closed	opened	closed	closed	closed	opened	closed
End	closed	closed	opened	opened	closed	opened	closed	closed	closed	opened	closed

6. Pump the whole system for 48 hours. Check the system vacuum with the Cold Cathode Vacuum Gauge (operation range, 1×10^{-3} - 1×10^{-7} torr). The system vacuum should be around 1×10^{-6} torr.

7. Close Valve E on the transfer line, Valve A, Valve B and Valve D, respectively.

8. Open Valve C, disconnect the transfer line from the Adaptor A and Close Adaptor A with a stopper.

9. Connect the Mechanical Pump B (Varian SD-450) to the connector A and power on the Mechanical Pump B for 15 minutes.

10. Close Valve C, shut down the power for the Mechanical Pump B and disconnect the Mechanical Pump B.

11. Open Valve D slowly, until it is wide open, then open Valve A and Valve B again.

The high vacuum system is left on for the entire period of the cryostat temperature experiment.

Flushing the Whole Cooling System with Helium Gas

Just before cooling down the cryostat system, the flow route is flushed with helium gas from a cylinder for 15 minutes. An empty sample tube should be put in the cavity and tightened up. Valve H is opened, but Valve P is closed. A rubber tubing is used to connect the helium gas cylinder to Vent I above the reservoir. The helium gas goes through Vent I, the Reservoir, the Pancake, the Dewar inside the cavity, the top cover, and out from Valve H. Valve R can be set at large opening, say 10 turns (clockwise) to facilitate the gas flow.

Close the valve of the helium gas cylinder, set Valve R at 2 turns, close Valve H, then disconnect the rubber tubing from Vent I, and connect the rubber tubing from the helium cylinder to the transfer line Tip I. Open Valve T widely (5 turns clockwise) and open the helium gas cylinder. Flush the transfer line for 2 minutes. Then set valve T at 2 turns. Turn off the helium gas, and disconnect the rubber tubing from the transfer line Tip I. Immediately proceed to the next step before air is allowed to enter the transfer line.

Cooling down the System

The following steps should be followed when cooling down the cryostat system.

A. Two people are needed to put the transfer line into the liquid helium tank and

the cryostat system. First, the helium tank pressure should be released through a vent valve at the top of the storage dewar, then the tank vent valve should be closed. One person should hold the transfer line and put the Tip I slowly into the liquid helium tank. The second person at the rear of the magnet holds the transfer line above the Tip II and tries to insert the Tip II into the transfer line inlet above the reservoir. When the Tip II is in the inlet completely, a clamp is used to tighten the connection.

B. Now the helium gas flows out of Vent I. The pressure in the storage dewar is high (about 10 psi) due to evaporation of liquid helium when the transfer line is put in. It will drop gradually afterwards. When it is below 3 psi, a helium cylinder regulated at 3 psi should be connected to the storage dewar through the storage dewar vent. Then, turn on the temperature and liquid level monitors.

C. It takes about 40 minutes to cool down the reservoir and accumulate liquid helium in the reservoir.

D. When the liquid helium accumulates to about 1.5 inches, turn on the Pump C, turn the Valve P half way open and begin to pump helium through the cryostat system.

E. Adjust the transfer line Valve T and reservoir capillary Valve R to reach the lowest temperature (about 2.3 K). The transfer line should be about one and half turns open, and the reservoir valve should be about a half turn clockwise open. If a temperature higher than 2.3 K is wanted, partially close Valve R and Valve P.

Changing Samples

When changing samples, Valve P is closed. The temperature in the cavity

increases quickly. When the temperature rises to about 77 K, take off the nitrogen defrosting case cover and swiftly screw off the sample cap and take out the sample. Meanwhile, insert the new sample tube in and screw the sample cap tightly as quickly as possible. Put the defrosting case cover back again. Then open the Valve P half way again. The temperature should drop to 2.3 K.

Shutting down the Cooling System

When the helium in the tank is used up, the helium level in the reservoir begins to drop. When the temperature in the cavity cannot hold at ~ 2.3 K, the helium is empty. Now is the time to raise the temperature in the cryostat system back to room temperature.

- A. Close the transfer line valve T and shut down Pump C.
- B. Connect a rubber tubing from the helium gas cylinder to Vent I, close Valve P, open Valve H, open the helium gas cylinder with the regulator set at 3 psi and blow helium gas through the cryostat system for one hour.
- C. When the temperature rises to 100 K, the helium gas is replaced by cheaper nitrogen gas and the gas is left to flow overnight.
- D. Take the transfer line Tip II out of the Transfer Line Inlet, clamp a cover on Inlet, and take the transfer line Tip I out of the liquid helium tank.
- E. After the temperature rises to 100 K, close Valve A and Valve B, unplug the Diffusion pump cord, wait for an hour, then Shut down the Mechanical pump A.

At the end, the status of all the valves in Figure B.1 should be kept as in Table B.1.

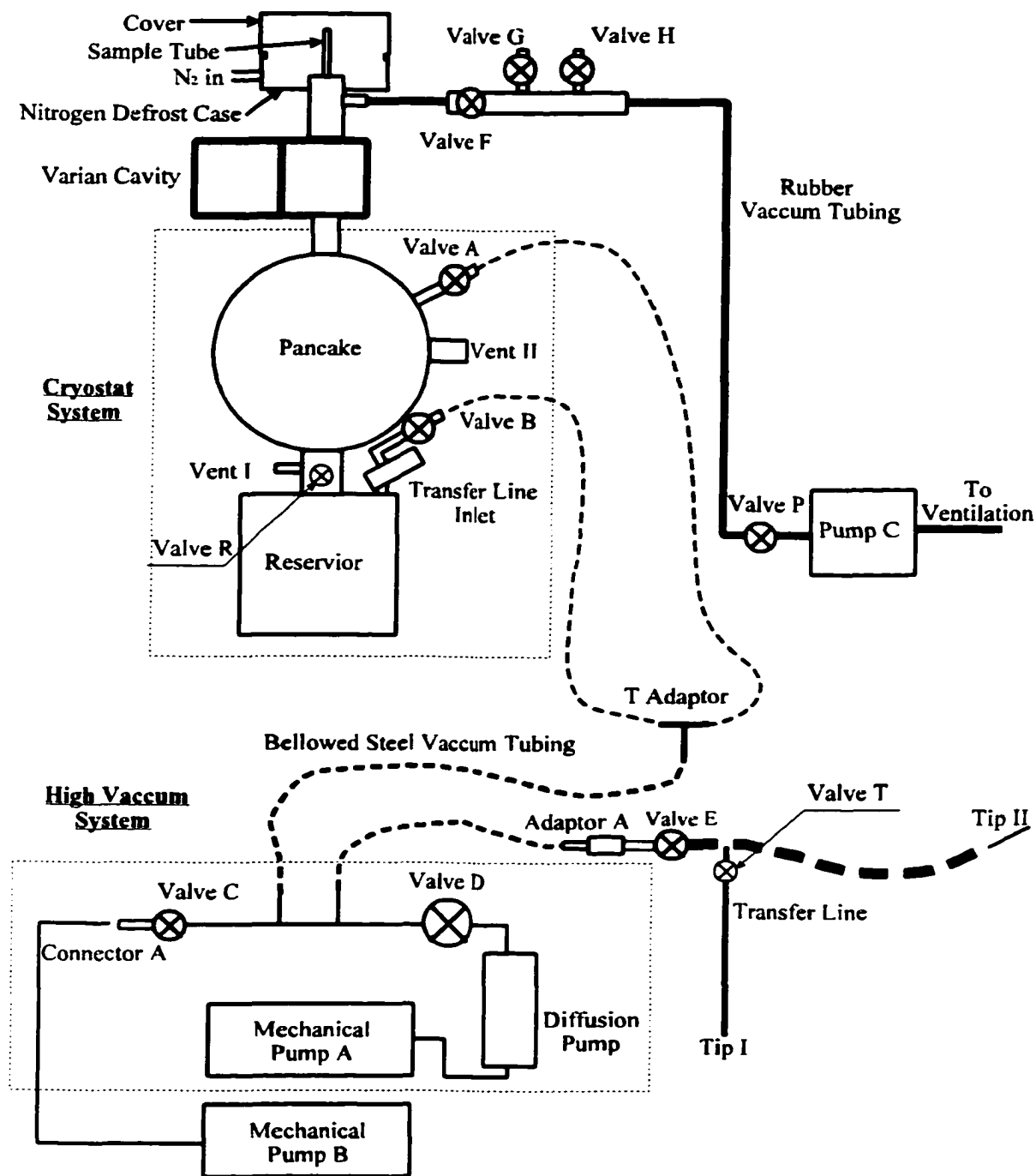


Figure B.1 The complete liquid helium cooling system in the X-band EPR/ENDOR spectrometer. (B.1.wpd)

APPENDIX C

OPERATION OF THE X-BAND EPR/ENDOR SPECTROMETER

The E-9 EPR System Manual is completely followed in obtaining EPR spectrum on the improved X-band EPR/ENDOR spectrometer. A home-made channel selector is put at the rear of the console for switching between high frequency of 100 kHz and low frequency of ≤ 10 kHz modulation channels. The channel selector is set at high for collecting EPR signal (see Figure C.1). Figure C.2 is the wiring of the radio frequency circuit. The procedures for collecting ENDOR spectrum are presented below.

- a. The software used for running ENDOR is called `endor.bat`. First, simply type `endor` followed by your name, then return. Refer to the instruction menus for all the functions of the program.
- b. After scanning the EPR spectrum, the recorder is stopped. The plotting pen is moved to the specific field position where ENDOR spectrum will be scanned. Then, the recorder is turned off, and the time constant, the 100 kHz modulation amplitude and the receiver gain on the 100 kHz module are set to zero.
- c. Switch the channel selector to low.
- d. Switch both the Oscilloscope Monitor and the Recorder Input on the System Function Selector module to LOW FREQ.
- e. On the Low Frequency module, set the time constant to 0.1 s, modulation amplitude to 5 G, Frequency to 1×10^4 Hz, phase to Mark ENDOR, and the receiver gain to a value

where the current needle is at or below the center of the current meter receiver. If the ENDOR signal is strong, the receiver gain is adjusted until the full scale ENDOR signal is not off of the computer screen.

- f. Set RF power to desired value (typically 100 to 120 W), set RF power by turning the signal synthesizer level knob so that the ENI amplifier output is 100 W at 9 MHz (for scanning from 9 to 19 MHz). Set modulation to 2.0 V (220 kHz modulation depth, or the value you choose referring to the chart in front of the modulator, see Appendix G).
- g. As the detector current in the microwave bridge increases with the RF power, the cavity iris needs be adjusted to bring back the current to 200 μ A. The flow rate of nitrogen gas blowing through the cavity should be increased if too much heat is generated in the cavity from the ENDOR coil.
- h. The typical sweep rate is 1 MHz/s. The time constant is 0.1 s.
- i. The RF power is usually set at 100 W (0.24 V on PTS) for proton ENDOR starting from 9 MHz.

Now, the spectrometer is ready to collect ENDOR data.

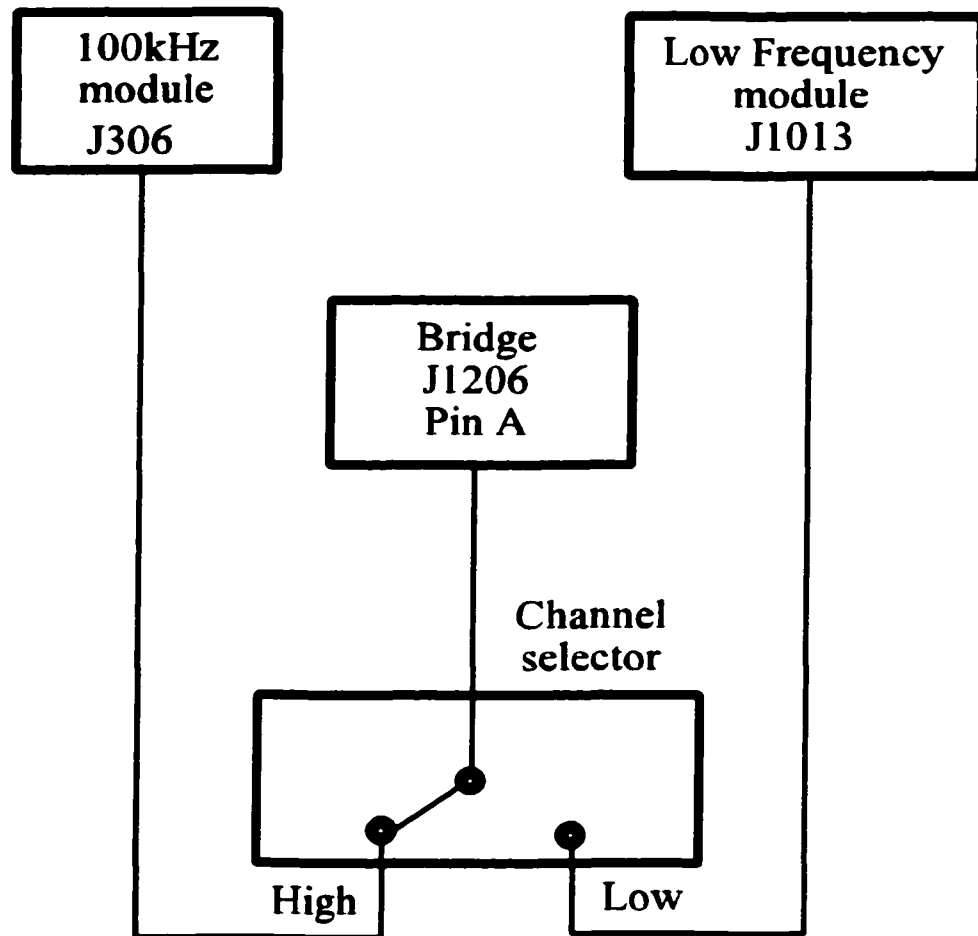


Figure C.1 The schematic diagram of the channel selector wiring. (C.1.wpd)

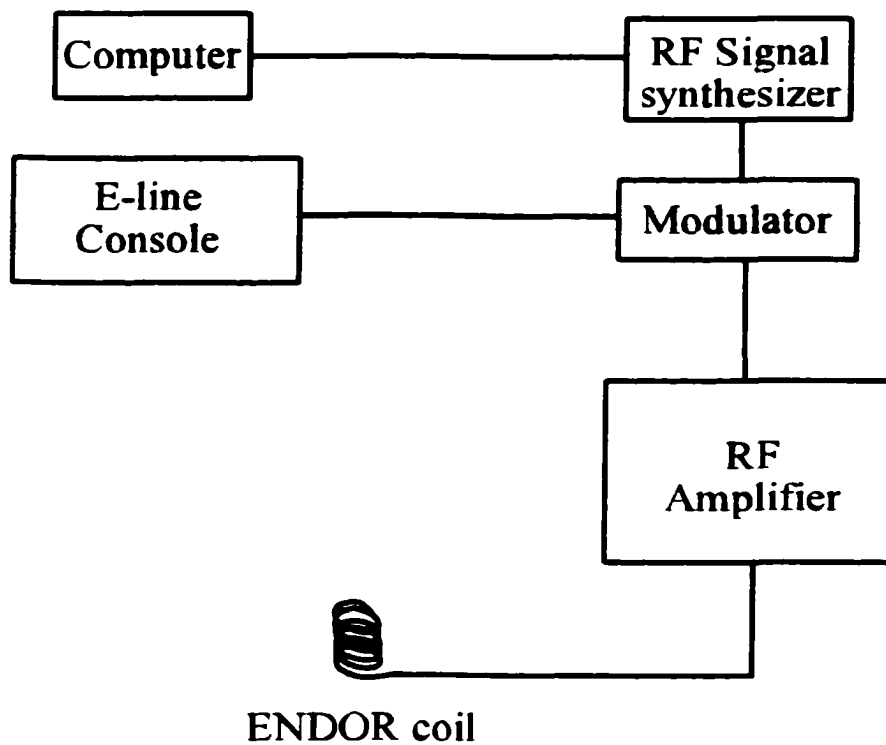


Figure C.2 The wiring of the RF circuit in the X-band ENDOR spectrometer. (C.2.wpd)

APPENDIX D

PROCEDURES FOR MAKING THE ENDOR COILS

A standard photo fabrication method was used in making printed ENDOR coil. Each copper coil was cut into pieces of 130 mm x 35 mm (see Figure D.1). One corner of the foil piece was cut off for the side identification in the dark room. Two alignment holes were drilled with the plate mold.

Pieces of the copper foil (FQ40649, DuPont Electronics Inc., Waltham, MA) were coated Naval Jelly Rust Dissolver (Loctite Corporation, Cleveland, OH) with a brush and left for about ten minutes to dissolve any corrosion followed by rinsing with water afterwards. Then the pieces of copper foil were immersed in acetone for a few minutes to remove any grease from the copper surface. Finally, they were dried under the hood for five minutes and then put in a 80° oven for 1/2 hour.

The photo resist coating of the copper foil was carried out in the dark room in the hood. Each piece of the foil was clamped with a clipper and was dipped into a petri dish half filled with KPR-3 photo resist (Kepro Circuit Systems, Inc., St. Louis, MO). Then the foils were hung in the hood for curing overnight. Then, they were put in a brown bottle (covered and wrapped with aluminum foil) and were baked in the 80° oven for half an hour. If the photo resist was not dry, the absorption of ultraviolet radiation by the material was low and no adequate exposure could be done.

The exposure of the coil circuit onto the copper foil was processed in the dark

room. Figure D.2 is the schematic diagram of the exposure process. The Photo ECT (500 W, 120 V, 3200 K) bulb (Osram Sylvania Inc., St. Marys, PA) was hung about 300 mm above the desk top. Under the red light of the dark room, the negative film (see Chapter 3) was put on the copper foil and was orientated so that the two alignment holes exactly matched the holes in the foil. Several pieces of heavy metal blocks were put on the edges of the negative film to flatten the film. Then the bulb was lit and the timer was started. The exposure time was 30 minutes for each side. The same steps were taken for the exposure of the other side. Then, the exposed foil was put into the petri dish half filled with developing solution KD-1QT (Kepro Circuit Systems, Inc., St. Louis, MO) for two minutes. The foil was then flushed with warm water to remove any trace of photo resist. If the foil was not developed enough, it was dried first and then developed for a second or a third two-minute time period. The foil was then rinsed completely, dried up and examined under a magnifying glass. If over developed spots were found, a Resist Ink pen (Radio Shack Inc., Ft. Worth, TX) was used to redraw the wire. In case of underdeveloping, the residuals were scratched off with a razor.

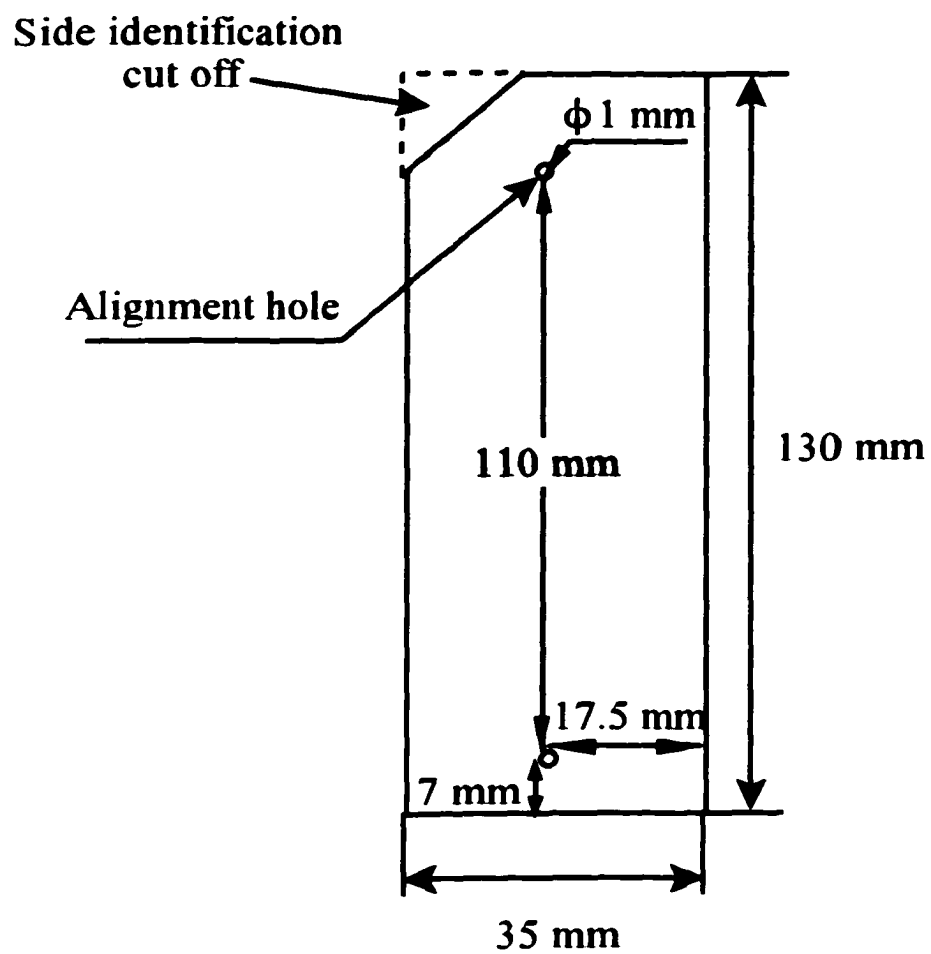


Figure D.1 The schematic diagram of one piece of the copper foil. (D.1.wpd)

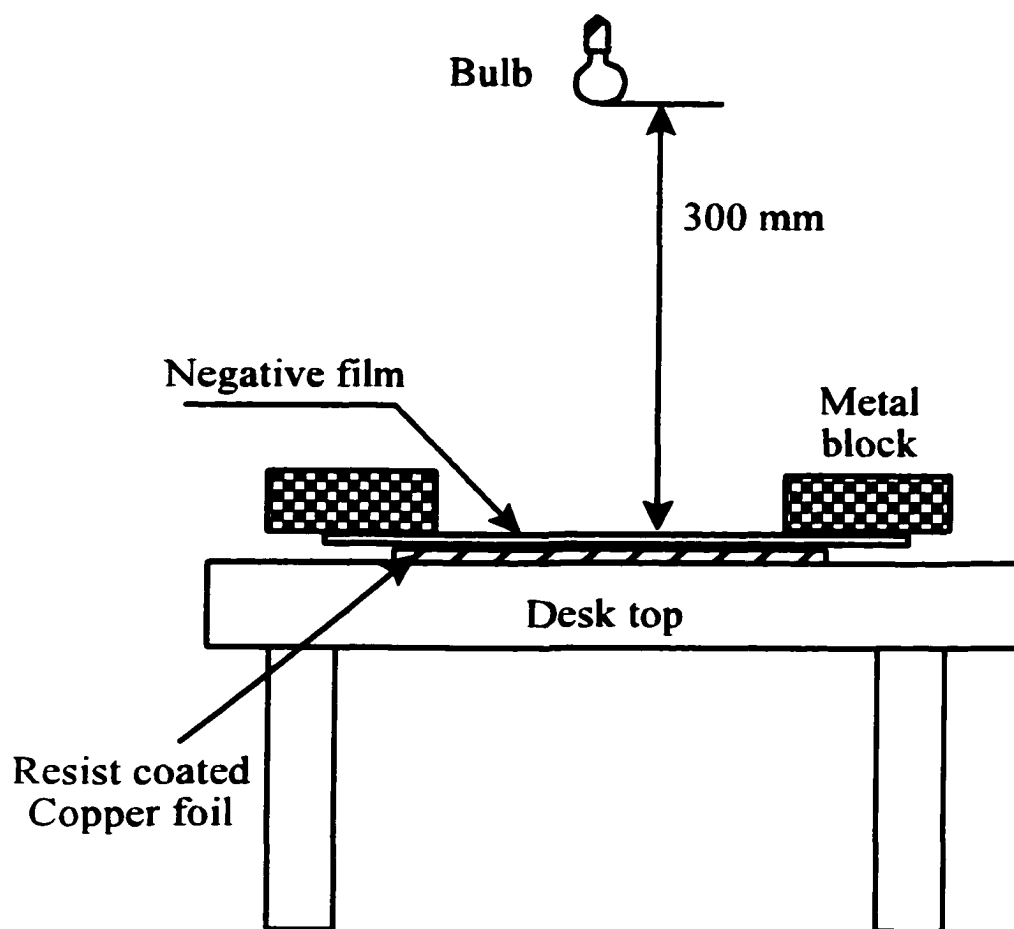


Figure D.2 The schematic diagram of the exposure process. (D.2.wpd)

APPENDIX E

CALCULATION OF ISOTROPIC g -VALUES AND ISOTROPIC HYPERFINE COUPLINGS

At X-band, the positions of all the lines in a spectrum can be expressed in the following equation to second order,

$$\begin{aligned} B &= B^{(0)} + B^{(1)} + B^{(2)} \\ &= B^{(0)} - \sum_i a_i M_i - \sum_i \frac{hA_{i0}^2}{2g\beta\nu_{i0}} [I(I+1) - M_i^2] \end{aligned} \quad \text{E.1}$$

If there is only one kind of hyperfine coupling, then we have,

$$B = B^{(0)} - aM - \frac{hA_0^2}{2g_0\beta\nu_0} [I(I+1) - M^2] \quad \text{E.2}$$

Also we have,

$$h\nu_0 = g_0\beta B^{(0)} \quad \text{E.3}$$

$$hA_0 = g_0\beta a_0 \quad \text{E.4}$$

Equations E.2 ~ E.4 are used for the calculation of g_0 and A_0 .

The following are the steps for the g_0 and A_0 calculation.

- a. Take the experimental line positions to estimate values for $B^{(0)}$, a_0 and g_0 .

$$B^{(0)} \approx \frac{\sum_{i=1}^n B_i}{n} \quad \text{E.5}$$

$$a_0 \approx \frac{B_{\max} - B_{\min}}{n - 1} \quad \text{E.6}$$

$$g_0 = \frac{h\nu_0}{\beta B^{(0)}} \quad \text{E.7}$$

$$A_0 = \frac{g_0 \beta a}{h} \quad \text{E.8}$$

where n is the number of lines observed.

b. Calculate the second order term with E.7 and E.8.

c. Calculate $B^{(0)}$ again with Equation E.2. rather than E.5, and g_0 with the more accurate $B^{(0)}$.

Repeat the steps b and c until the calculated g_0 and A_0 no longer change.

The calculation is achieved by a program in Dell-ITC named g_a_2ndorder.exe written in C/C++. The flow chart of the calculation is presented in Figure E.1. The experimental lines and the calculated line positions from Equation E.1 will be displayed on the screen, so are the values of g_0 , a_0 , A_0 .

```
#include <stdio.h>
#include <graph.h>
```

```

#define len 20
#define scale 1

struct col{
    short x;
    short y;
    float value;
    char explanin[len];
};
struct collect{
    short x;
    short y;
    double value;
    char explain[len];
};
struct inform{
    struct col pkno;
    struct collect fc;
    struct collect range;
    struct collect freq;
    struct collect crtratio;
    struct collect stdfield;
    struct collect stdg;
    struct collect peaks[8];
    struct collect crtpeak[8];
    struct collect firstodpk[8];
    struct collect deltah;
    struct collect g0;
    struct collect a0;
    struct collect A0;
};

main()
{
    int x,xx;
    static struct inform data;
    x=121;
    xx=121;
    while(xx==121||xx==89||xx==10){
        initstruct(&data);
        init();
        noofpeak(&data);
        peaksite(&data);
    }
}

```

```

inputdata(&data);
peakvalue(&data);
crtpeak(&data);
firstodpk(&data);
raw_peaks(&data);
crt_peaks(&data);
x=10;
while(x==121||x==89||x==10){
    posta0g0(&data);
    firstodpk(&data);
    fstod_peaks(&data);
    _moveto(50,300);
    _setcolor(12);
    _outtext("Do you want to iterate the calculation?");
    x=_getch();
    _moveto(50,300);
    _setcolor(0);
    _outtext("Do you want to iterate the calculation?");
}
    _moveto(50,300);
    _setcolor(12);
    _outtext("Do you want to analyze another sample?");
    xx=_getch();
    _moveto(50,300);
    _setcolor(0);
    _outtext("Do you want to analyze another sample?");
}
_setvideomode(_TEXT80);
}

initstruct(data)
struct inform *data;
{
    data->pkno.x=30;
    data->pkno.y=95;
    data->fc.x=10;
    data->fc.y=145;
    data->range.x=195;
    data->range.y=145;
    data->freq.x=400;
    data->freq.y=145;
    data->crtratio.x=10;
    data->crtratio.y=195;
}

```

```

    data->stdfield.x=260;
    data->stdfield.y=195;
    data->stdg.x=400;
    data->stdg.y=195;

}

init()
{
/* the following paragraph is to initialize the monitor */

    _setvideomoderows(_VRES16COLOR,20);
    _setviewport(0,0,639,479);
    _setcolor(14);
    _rectangle(_GBORDER,1,1,638,318);
    _rectangle(_GBORDER,1,319,638,479);
    _moveto(20,380);
    _lineto(619,380);
    _moveto(20,381);
    _lineto(619,381);
}

/* ***** writing the labels ***** */
noofpeak(data)
    struct inform *data;
    {
        char x[3];
        int i;
        _registerfonts("c:\\windows\\system\\*.fon");
        _setfont("h30t'roman'w24p");
        _moveto(70,30);
        _setcolor(12);
        _outtext("g0 and A0 Calculation");
        _setfont("h16t'roman'w12p");
        i=0;
        while(i<=1||i>=9){
            _moveto((*data).pkno.x,(*data).pkno.y);
            _outtext("How many peaks do you see: ");
            _settextposition(7,45);
            _settextcolor(0);
            printf("          ");
            _settextposition(7,45);
            scanf("%f",&data->pkno.value);

```



```

        i=(int)data->pkno.value;
    }

}

/* ***** read in all the data needed ***** */
inputdata(data)
struct inform *data;
{
    float x;
    _setfont("h14t'roman'w1lp");
    _moveto((*data).fc.x,(*data).fc.y);
    _setcolor(3);
    _outtext("Field Center: ");
    _settextposition(10,19);
    scanf("%f",&x);
    data->fc.value=x;
    _moveto((*data).fc.x,(*data).fc.y);

    _moveto((*data).range.x,(*data).range.y);
    _outtext("Scan Range: ");
    _settextposition(10,41);
    scanf("%f",&x);
    data->range.value=x;

    _moveto((*data).freq.x,(*data).freq.y);
    _outtext("Frequency (GHz): ");
    _settextposition(10,73);
    scanf("%f",&x);
    data->freq.value=x;

    _moveto((*data).crtratio.x,(*data).crtratio.y);
    _outtext("Correction ratio: ");
    _settextposition(13,23);
    scanf("%f",&x);
    data->crtratio.value=x;

    _moveto((*data).stdfield.x,(*data).stdfield.y);
    _outtext("Std Field: ");
    _settextposition(13,46);
    scanf("%f",&x);
    data->stdfield.value=x;
}

```

```

    _moveto((*data).stdg.x,(*data).stdg.y);
    _outtext("Standard g value: ");
    _settextposition(13,74);
    scanf("%f",&x);
    data->stdg.value=x;

    _setcolor(2);
    _moveto(20,225);
    _outtext("Low Field");
    _moveto(512,225);
    _outtext("High Field");
}

/* ***** calculate the position of the peaks ***** */
peaksite(data)
struct inform *data;
{
    int i,peakno;
    peakno=(int)data->pkno.value;
    for(i=1;i<=peakno;i++){
        data->peaks[i-1].x=17;
        data->peaks[i-1].y=(i-1)*68/(peakno-1)+4;
    }
}

/* ***** read in the magnetic fields of the peaks ***** */
peakvalue(data)
struct inform *data;
{
    int i,peakno;
    float x;
    char num[2];
    peakno=(int)data->pkno.value;
    for(i=1;i<=peakno;i++){
        _settextposition((*data).peaks[i-1].x,(*data).peaks[i-1].y);
        _settextcolor(2);
        _outtext("Peak");
        _itoa(i,num,10);
        /*printf("%i",i);*/
        _outtext(num);
        _settextposition((*data).peaks[i-1].x+1,(*data).peaks[i-1].y-1);
    }
}

```

```

scanf("%f",&x);
data->peaks[i-1].value=x;
    }
}

/* ***** calculate the calibrated peak positions ***** */
crtpeak(data)
struct inform *data;
{
    int i,peakno;
    float pkno;
    double pn;

    peakno=(int)data->pkno.value;
    pkno=data->pkno.value;
    data->deltah.value=714.4844*data->freq.value/data->stdg.value-data->stdfield.value;
    for(i=1;i<=peakno;i++){

data->crtpeak[i-1].value=data->crtratio.value*(data->peaks[i-1].value-data->fc.value)+da
ta->fc.value+data->deltah.value;
    }
    data->a0.value=(data->crtpeak[peakno-1].value-data->crtpeak[0].value)/(pn-1);

data->g0.value=1428.9688*data->freq.value/(data->crtpeak[0].value+data->crtpeak[peak
no-1].value);
}

/***** calculate the 2nd-order terms and the 1st-order peaks *****/
firstodpk(data)
struct inform *data;
{
    int i,peakno;
    float x;
    double sndodpeak,pkno,sum,y;
    sum=0.0;

    pkno=data->pkno.value;
    peakno=(int)data->pkno.value;
    for(i=1;i<=peakno;i++){

sndodpeak=data->a0.value*data->a0.value*data->g0.value*(0.25*(pkno+1.)*(pkno-1.)-((
pkno-1.)/2.-i+1.)*((pkno-1.)/2.-i+1.))/(1428.9688*data->freq.value);
    data->firstodpk[i-1].value=data->crtpeak[i-1].value+sndodpeak;

```

```

y=data->firstodpk[i-1].value;
sum=sum+y;
    }
    data->a0.value=(data->firstodpk[peakno-1].value-data->firstodpk[0].value)/(pkno-1.);
    data->g0.value=4.*714.4844*data->freq.value/sum;
    data->A0.value=data->g0.value*data->a0.value/21539.65937;
}

/***** draw the raw peaks *****/
raw_peaks(data)
struct inform *data;
{
    int peakno,i;
    double peakfield[8];
    float pf[8];
    peakno=(int)data->pkno.value;
    _setcolor(13);
    _moveto(320,379);
    _lineto(320,329);
    for(i=1;i<=peakno;i++){

peakfield[i-1]=320+600*scale*(data->peaks[i-1].value-data->fc.value)/data->range.value;
        pf[i-1]=peakfield[i-1];
        _setcolor(5);
        _moveto((int)pf[i-1],379);
        _lineto((int)pf[i-1],349);
    }
}

/***** draw the calibrated peaks *****/
crt_peaks(data)
struct inform *data;
{
    int peakno,i;
    double peakfield[8],fc;
    float fcc;
    peakno=(int)data->pkno.value;
    fc=320+600*scale*data->deltah.value/data->range.value;
    fcc=fcc;
    _setcolor(10);
    _moveto((int)fcc,382);
    _lineto((int)fcc,400);
}

```

```

    for(i=1;i<=peakno;i++){

peakfield[i-1]=320+600*scale*(data->crtpeak[i-1].value-data->fc.value)/data->range.valu
e;

        _setcolor(2);
        _moveto((int)peakfield[i-1],382);
        _lineto((int)peakfield[i-1],412);
    }

}

/***** draw the 1st-order peaks *****/
fstod_peaks(data)
struct inform *data;
{
    int peakno,i;
    double peakfield[8],fcc;
    float fc;
    peakno=(int)data->pkno.value;
    for(i=1;i<=peakno;i++){

peakfield[i-1]=320+600*scale*(data->firstodpk[i-1].value-data->fc.value)/data->range.val
ue;

        _setcolor(4);
        _moveto((int)peakfield[i-1],382);
        _lineto((int)peakfield[i-1],432);
    }

    fcc=(peakfield[0]+peakfield[peakno-1])/2;
    fc=fcc;
    _setcolor(12);
    _moveto((int)fc,382);
    _lineto((int)fc,440);

}

/***** post the a0 and g0 *****/
posta0g0(data)
struct inform *data;
{
    float x;
    x=data->a0.value;
    _setcolor(14);
    _settextposition(28,20);
    printf("a0=%7.4f G",x);
}

```

```

    _settextposition(29,36);
    x=data->g0.value;
    printf("g0=%6.4f",x);
    _settextposition(28,3);
    x=data->A0.value;
    printf("A0=%6.4f/cm",x);
    _setcolor(13);
    _moveto(570,350);
    _lineto(610,350);
    _moveto(470,342);
    _setcolor(13);
    _outgtext("Raw lines");
    _setcolor(10);
    _moveto(570,430);
    _lineto(610,430);
    _moveto(410,422);
    _setcolor(10);
    _outgtext("Corrected lines");
    _setcolor(12);
    _moveto(570,460);
    _lineto(610,460);
    _moveto(394,452);
    _setcolor(12);
    _outgtext("First-order lines");

```

```

}

```

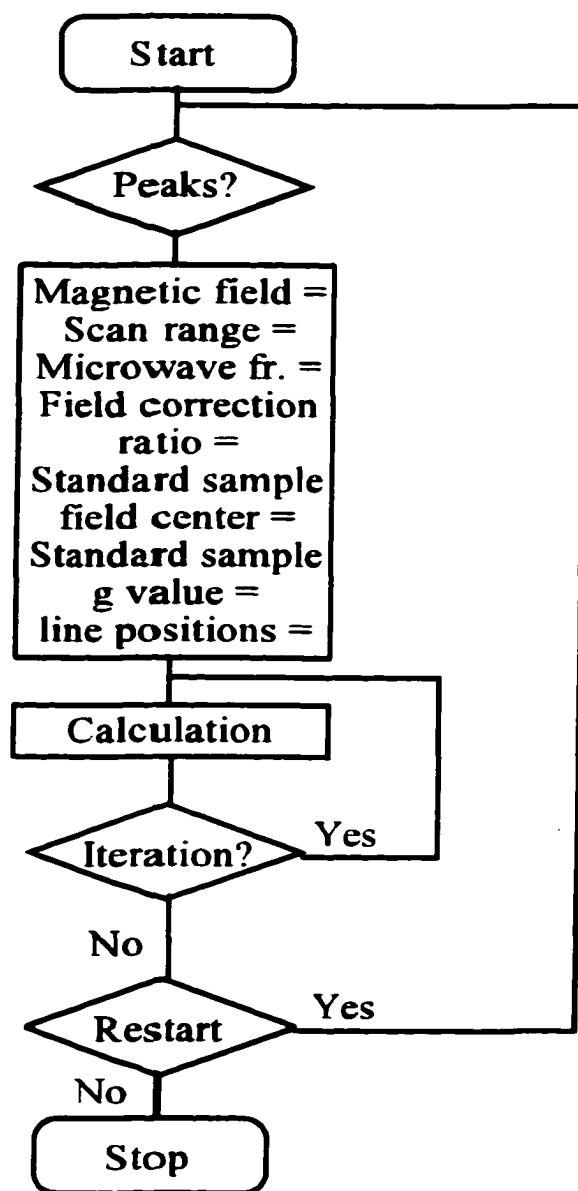


Figure E.1 The flow chart for the second-order calculation of isotropic g_0 and isotropic A_0 . (E.1.wpd)

APPENDIX F

CALCULATION OF BONDING PARAMETERS

Numeric calculation is used to derive the bonding parameters. For convenience, the Equations 5.6 ~ 5.12 are also listed here.

$$\alpha^2 + \alpha'^2 - 2\alpha\alpha'S = 1 \quad \text{F.1}$$

$$g_{//} - 2.0023 = -8\rho[\alpha\beta_1 - \alpha'\beta_1S - \alpha'(1-\beta_1^2)^{1/2}T(n)/2] \quad \text{F.2}$$

$$g_{\perp} - 2.0023 = -2\mu[\alpha\beta - \alpha'\beta S - \alpha'(1-\beta^2)^{1/2}T(n)/2^{1/2}] \quad \text{F.3}$$

$$A_{//} = P[-\alpha^2(4/7 + \kappa_0) + (g_{//} - 2.0023) + 3/7(g_{\perp} - 2.0023) - 8\rho\{\alpha'\beta_1S + \alpha'(1-\beta_1^2)^{1/2}T(n)/2 - 6/7\mu\{\alpha'\beta S + \alpha'(1-\beta^2)^{1/2}T(n)/2^{1/2}\} \quad \text{F.4}$$

$$\rho = \frac{\lambda_0 \alpha \beta_1}{\Delta E_{xz, yz}} \quad \text{F.5}$$

$$\mu = \frac{\lambda_0 \alpha \beta}{\Delta E_{xy}} \quad \text{F.6}$$

From Equation F.1, we can solve for α' ,

$$\alpha' = (2\alpha S \pm (4\alpha^2 S^2 - 4\alpha^2 + 4)^{1/2})/2$$

As $\alpha^2 \leq 1$, thus, $4\alpha^2 S^2 - 4\alpha^2 + 4 \geq 4\alpha^2 S^2$. In order to get a positive α' , we have

$$\alpha' = (2\alpha S + (4\alpha^2 S^2 - 4\alpha^2 + 4)^{1/2})/2 \quad \text{F.7}$$

Substituting Equation F.5 into F.2, we obtain,

$$-\frac{(g_{//} - 2.0023)\Delta E_{xy}}{8\lambda_0} = \alpha^2 \beta_1^2 - \alpha\alpha' S \beta_1^2 - \frac{T(n)}{2} \alpha\alpha' \sqrt{\beta_1^2 - \beta_1^4} \quad \text{F.8}$$

If we set, $A_1 = \frac{-(g_{//} - 2.0023)\Delta E_{xy}}{8\lambda_0}$; $A_2 = \alpha^2 - \alpha\alpha' S$ and $A_3 = T(n)\alpha\alpha'/2$, then,

we obtain a simplified equation,

$$A_1 = A_2 \beta_1^2 - A_3 (\beta_1^2 - \beta_1^4)^{1/2} \quad \text{F.9}$$

Equation F.9 is solved in the following way,

$$-A_1 + A_2 \beta_1^2 = A_3 (\beta_1^2 - \beta_1^4)^{1/2}$$

$$A_2^2 \beta_1^4 - 2 A_1 A_2 \beta_1^2 + A_1^2 = A_3^2 \beta_1^2 - A_3^2 \beta_1^4$$

$$(A_2^2 + A_3^2) \beta_1^4 - (2 A_1 A_2 + A_3^2) \beta_1^2 + A_1^2 = 0$$

$$\begin{aligned} \beta_1^2 &= \frac{2 A_1 A_2 + A_3^2 \pm \sqrt{(2 A_1 A_2 + A_3^2)^2 - 4 A_1^2 (A_2^2 + A_3^2)}}{2(A_2^2 + A_3^2)} \\ &= \frac{2 A_1 A_2 + A_3^2 \pm A_3 \sqrt{A_3^2 + 4 A_1 A_2 - 4 A_1^2}}{2(A_2^2 + A_3^2)} \end{aligned}$$

Considering the physical meaning, β_1^2 should be close to 1. So, we take,

$$\beta_1^2 = \frac{2 A_1 A_2 + A_3^2 + A_3 \sqrt{A_3^2 + 4 A_1 A_2 - 4 A_1^2}}{2(A_2^2 + A_3^2)} \quad \text{F.10}$$

In the same way, we can derive β^2 . Substituting Equation F.6 into F.3, We have,

$$-\frac{(g_{\perp} - 2.0023)\Delta E_{x,yz}}{2\lambda_0} = \alpha^2 \beta^2 - \alpha\alpha' S \beta^2 - \frac{T(n)}{\sqrt{2}} \alpha\alpha' \sqrt{\beta^2 - \beta^4} \quad \text{F.11}$$

If we define, $B_1 = \frac{-(g_{\perp} - 2.0023)\Delta E_{x,yz}}{2\lambda_0}$; $B_2 = \alpha^2 - \alpha\alpha'S$ and $B_3 = T(n)\alpha\alpha'/2^{1/2}$ (here

$B_2 = A_2$ and $B_3 = A_3$ are redefined for the clarity in writing program),
we obtain a simplified equation,

$$B_1 = B_2\beta^2 - B_3(\beta^2 - \beta^4)^{1/2} \quad \text{F.12}$$

The solution for Equation F.12 is,

$$\beta^2 = \frac{2B_1B_2 + B_3^2 + B_3\sqrt{B_3^2 + 4B_1B_2 - 4B_1^2}}{2(B_2^2 + B_3^2)} \quad \text{F.13}$$

Now we have all the equations needed to calculate the bonding parameters. The procedures in the calculation is described below. The protocol program is called Bondingpara.org.

1. The initial α^2 is calculated by the following Equation F.14.^[85]

$$\alpha^2 = -(A/P) + (g_{\perp} - 2.0023) + (3/7)(g_{\perp} - 2.0023) + 0.04 \quad \text{F.14}$$

2. Calculate α' with Equation F.7.

3. Calculate A_1 , A_2 , A_3 , B_1 , B_2 and B_3 , respectively.

4. Calculate β_1^2 by Equation F.10.

5. Calculate β^2 by Equation F.13.

6. Calculate κ by $\kappa = 0.43 \alpha^2$.^[85]

The following are the iteration steps.

7. Calculate ρ by Equation F.5.

8. Calculate μ by Equation F.6.

9. Calculate C_1 by $C_1 = \alpha' \beta_1 S + \frac{\sqrt{1 - \beta^2} T(n)}{2}$.

10. Calculate C_2 by $C_2 = \alpha' \beta S + \frac{\sqrt{1 - \beta^2} T(n)}{\sqrt{2}}$.

11. Calculate α^2 by Equation F.4.

12. Calculate α' by Equation F.7.

13. Calculate A_1 , A_2 , A_3 , B_1 , B_2 and B_3 , respectively.

14. Calculate β_1^2 by Equation F.10.

15. Calculate β^2 by Equation F.13.

16. Calculate κ by $\kappa = 0.43 \alpha^2$.

Step 1 to 6 is arranged in INITIATION button, and Iteration is put in the ITERATION button. The Origin LabTalk script language was used to write the program. The program of Bondingpara.org is in Dell-ITC. Table F.1 is the arrangement of all the data used and parameters in the bonding parameter calculations. Column A is the input data. The program is presented below.

Table F.1 The arrangement of all the data used and resolved in the bonding parameter calculations.

	Col A	Col B	Col C
1	$g_{//}$	κ	κ
2	g_{\perp}	α^2	α^2
3	$A_{//}$	β^2	β^2
4	A_{\perp}	β^2	β^2
5	λ		
6	P	α'	α'
7	ΔE_{xyz}	A_1	A_1
8	ΔE_{xy}	A_2	A_2
9	S	A_3	A_3
10	$T(n)$	B_1	B_1
11		B_2	B_2
12		B_3	B_3
13			
14			ρ
15			μ
16			C_1
17			C_2

data2_b[2]=-data2_a[3]/data2_a[6]+data2_a[1]-2.0023+(data2_a[2]-2.0023)*3/7+0.04;

data2_b[6]=sqrt(data2_b[2])*data2_a[9]+sqrt(data2_b[2]*(data2_a[9]^2-1)+1);

data2_b[7]=-(data2_a[1]-2.0023)*data2_a[8]/(8*data2_a[5]);

data2_b[8]=data2_b[2]-sqrt(data2_b[2])*data2_b[6]*data2_a[9];

data2_b[9]=sqrt(data2_b[2])*data2_b[6]*data2_a[10]/2;

```

data2_b[10]=-(data2_a[2]-2.0023)*data2_a[7]/(2*data2_a[5]);
data2_b[11]=data2_b[2]-sqrt(data2_b[2])*data2_b[6]*data2_a[9];
data2_b[12]=sqrt(data2_b[2])*data2_b[6]*data2_a[10]/sqrt(2);
data2_b[4]=2*data2_b[7]*data2_b[8]+data2_b[9]^2+data2_b[9]*sqrt(data2_b[9]^2+4*data2_b[7]*data2_b[8]-4*data2_b[7]^2)/(2*(data2_b[8]^2+data2_b[9]^2));
data2_b[3]=2*data2_b[10]*data2_b[11]+data2_b[12]^2+data2_b[12]*sqrt(data2_b[12]^2+4*data2_b[10]*data2_b[11]-4*data2_b[10]^2)/(2*(data2_b[11]^2+data2_b[12]^2));
data2_b[1]=0.43*data2_b[2];

data2_c[14]=data2_a[5]*sqrt(data2_b[2])*sqrt(data2_b[4])/data2_a[8];
data2_c[15]=data2_a[5]*sqrt(data2_b[2])*sqrt(data2_b[3])/data2_a[7];
data2_c[16]=data2_b[6]*(sqrt(data2_b[4])*data2_a[9]+sqrt(1-data2_b[4]))*data2_a[10]/2;
data2_c[17]=data2_b[6]*(sqrt(data2_b[3])*data2_a[9]+sqrt(1-data2_b[3]))*data2_a[10]/sqrt(2);
data2_c[2]=-data2_a[3]/data2_a[6]+data2_a[1]-2.0023+(data2_a[2]-2.0023)*3/7-8*data2_c[14]*data2_c[16]-data2_c[15]*data2_c[17]*6/7;
data2_c[6]=sqrt(data2_c[2])*data2_a[9]+sqrt(data2_c[2]*(data2_a[9]^2-1)+1);
data2_c[7]=-(data2_a[1]-2.0023)*data2_a[8]/(8*data2_a[5]);
data2_c[8]=data2_c[2]-sqrt(data2_c[2])*data2_c[6]*data2_a[9];
data2_c[9]=sqrt(data2_c[2])*data2_c[6]*data2_a[10]/2;
data2_c[10]=-(data2_a[2]-2.0023)*data2_a[7]/(2*data2_a[5]);

```

```

data2_c[11]=data2_c[2]-sqrt(data2_c[2])*data2_c[6]*data2_a[9];
data2_c[12]=sqrt(data2_c[2])*data2_c[6]*data2_a[10]/sqrt(2);
data2_c[4]=2*data2_c[7]*data2_c[8]+data2_c[9]^2+data2_c[9]*sqrt(data2_c[9]^2+4*data2_c[7]*data2_c[8]-4*data2_c[7]^2)/(2*(data2_c[8]^2+data2_c[9]^2));
data2_c[3]=2*data2_c[10]*data2_c[11]+data2_c[12]^2+data2_c[12]*sqrt(data2_c[12]^2+4*data2_c[10]*data2_c[11]-4*data2_c[10]^2)/(2*(data2_c[11]^2+data2_c[12]^2));
data2_c[1]=0.43*data2_c[2];
data2_b[2]=data2_c[2];
data2_b[3]=data2_c[3];
data2_b[4]=data2_c[4];
data2_b[6]=data2_c[6];

```

All the data are listed in data sheet 2 named data2. Column b in data2 is labeled data2_b and the cell in the nth row of data2_b is data2_b[n]. For instance, the $g_{//}$ is in data2_a[1] and α^2 is in data2_c[2].

APPENDIX G

MEASUREMENT OF FREQUENCY MODULATION DEPTH

The wiring of the modulation depth measurement is in Figure G.1. The signal from the synthesizer is modulated by the modulator with the modulating signal from the console. Ten cycles of the sine signal are displayed on the oscilloscope. The tenth sine signal is spread out. The width of the spread signal at the tenth circle is then measured with the unit of time (see Figure G.2). A series of Δt were measured for the modulation amplitude changing in steps. As we have

$$\frac{t}{10} = \frac{1}{\nu}$$

G.1

$$\frac{\Delta t}{10} = \frac{\Delta \nu}{\nu^2}$$

Then,

$$\Delta \nu = \frac{\Delta t}{10} \cdot \nu^2$$

G.2

All the $\Delta \nu$ are calculated with the Equation G.2. The data in Table G.1 are plotted in Figure G.3.

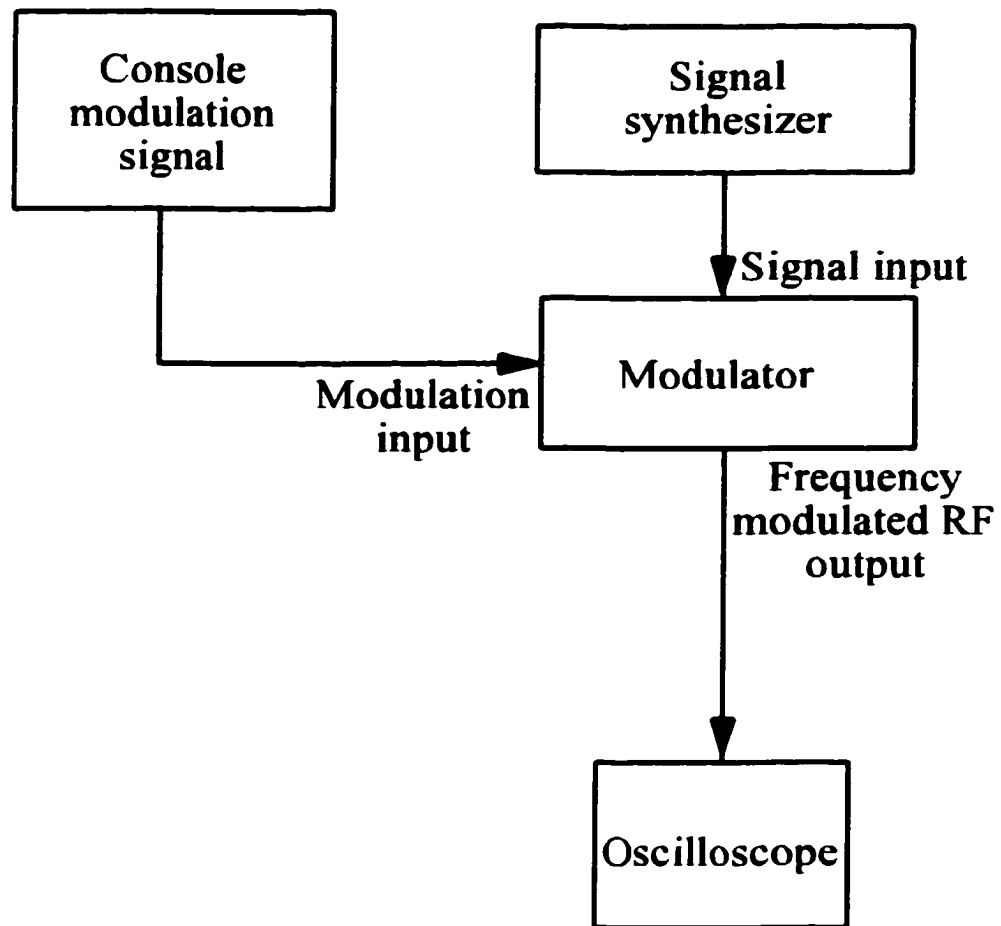


Figure G.1 The wiring for the modulation depth measurement. (G.1.wpd)

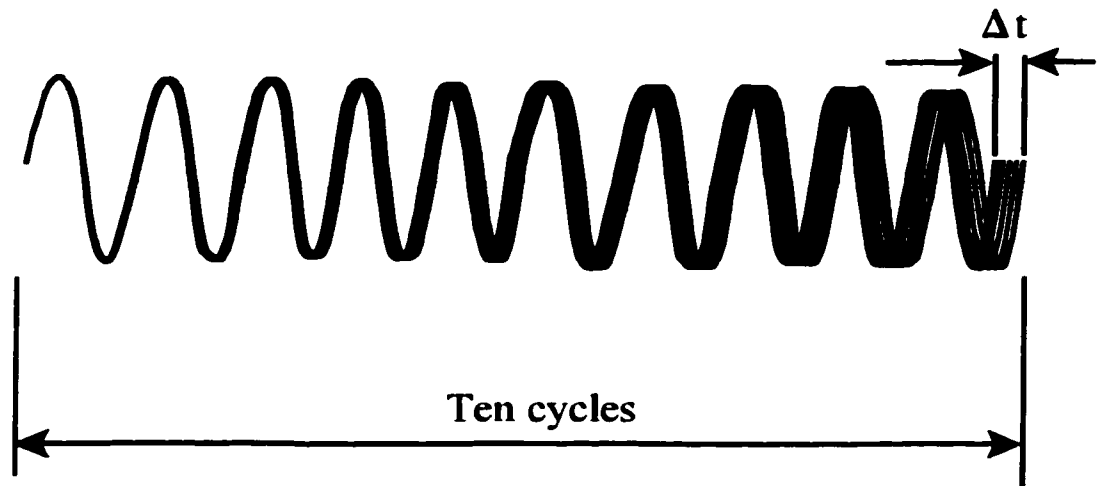


Figure G.2 The diagram of the modulated signal displayed on the oscilloscope. (G.2.wpd)

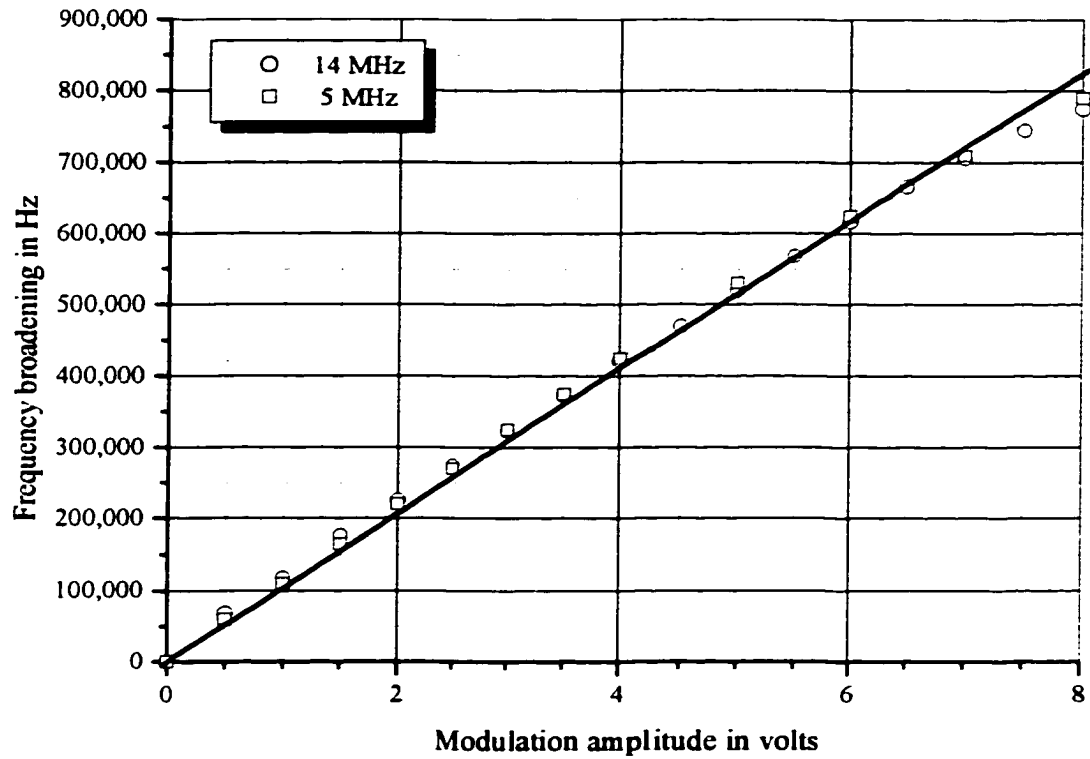


Figure G.3 The measured modulated frequency depth versus the modulation signal amplitude. The least-square fitting line is $y = 103022.2 \cdot x$. (G.3.wpd)

Table G.1 The frequency modulation depth at (14 MHz) versus the modulation voltage for 10 kHz modulation on Varian console set at 5 G.

Voltage (V)	Broadening in 10 cycles (ns)	Broadening in 1 cycle (ns)	Frequency broadening (kHz)
0	0	0	0
0.5	3.50	0.35	68.6
1.0	6.00	0.60	117.6
1.5	9.00	0.90	176.4
2.0	11.50	1.15	225.4
2.5	14.00	1.40	274.4
3.0	16.50	1.65	323.4
3.5	19.00	1.90	372.4
4.0	21.50	2.15	421.4
4.5	24.00	2.40	470.4
5.0	26.50	2.65	519.4
5.5	29.00	2.90	568.4
6.0	31.50	3.15	617.4
6.5	34.00	3.40	666.4
7.0	36.00	3.60	705.6
7.5	38.00	3.80	744.8
8.0	39.50	3.95	774.2

APPENDIX H

DETERMINATION OF THE ANGLES BETWEEN THE PSEUDO SYMMETRIC AXIS AND THE VECTOR OF THE CENTRAL METAL ION TO THE SURROUNDING PROTONS

Figure H.1 is the schematic diagram of the geometric position of one proton atom relevant to the iron center. The pseudo symmetric axis is assumed to be in the O1-Fe-O2 plane and bisect the angle $\angle O1-Fe-O2$. It crosses the line O1-O2 at the midpoint M. Two lines normal to the symmetric axis and the line O1-O2 cross at V and W, respectively. For convenience in deriving following formula deduction, we assign the lengths $a \equiv \underline{O1-Fe}$, $b \equiv \underline{(O1-O2)/2}$, $c \equiv \underline{Fe-M}$, $x \equiv \underline{Fe-V}$, $y \equiv \underline{HV}$, $z \equiv \underline{MW}$, $l \equiv \underline{Fe-H}$, $m \equiv \underline{H-O1}$ and $n \equiv \underline{H-O2}$ (distance between two points are underlined here). From the triangle H-Fe-V, we have

$$l^2 = x^2 + y^2 \quad \text{H.1}$$

$$\cos(\phi_0) = \frac{x}{l} \quad \text{H.2}$$

From triangles H-W-O1 and H-W-O2, we have

$$m^2 - (b + z)^2 = n^2 - (b - z)^2 \quad \text{H.3}$$

Equation H.3 can be rearranged and deduced to

$$z = \frac{m^2 - n^2}{4b} \quad \text{H.4}$$

From triangle H-W-M, H-W-O1 and H-M-V, we obtain

$$m^2 - (b + z)^2 + z^2 = (x + c)^2 + y^2 \quad \text{H.5}$$

Substituting y of Equation H.1 into Equation H.5, we obtain

$$\begin{aligned} x &= \frac{m^2 + n^2 - 2l^2 - 2b^2 - 2c^2}{4c} \\ &= \frac{m^2 + n^2 - 2l^2 - 2a^2}{4c} \end{aligned} \quad \text{H.6}$$

Substituting x of Equation H.6 into Equation H.2, we finally obtain

$$\phi_0 = \cos^{-1} \frac{(m^2 + n^2 - 2a^2 - 2l^2)}{4cl} \quad \text{H.7}$$

By measuring l, m, n, a, b and c, we can calculate ϕ_0 with Equation H.7.

The distances from each proton to the Fe, O1 and O2 in the two model complexes were measured and are presented in Table H.1. Using $l \equiv r$ and ϕ_0 in this table and Equation 4.2 (see Chapter 4), we calculated the hyperfine couplings for each protons at both parallel and perpendicular field positions and present the results in Table H.1 as well.

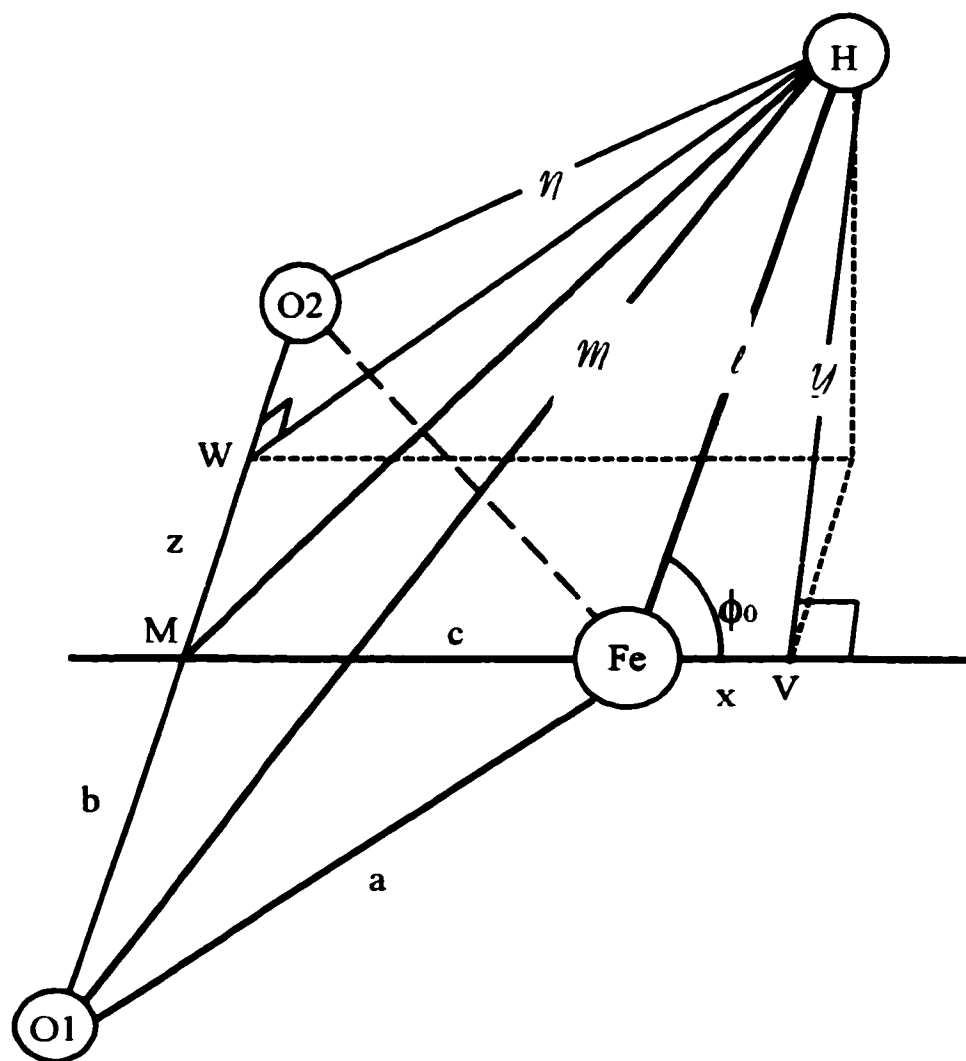


Figure H.1 The schematic diagram for the determination of ϕ_0 . (H.1.wpd)

Table H.1 The measured bond lengths and the calculated ϕ_0 and proton hyperfine couplings.

Cys-Fe-NO							
proton	l (Å)	m (Å)	n (Å)	ϕ_0 (°)	$A_{//}^b$	$A_{\perp} (90^\circ - \phi_0)$	A_{\perp}^{90}
2	2.71	4.68	4.05	62.8	-1.61	5.93	-4.33
3	2.67	3.95	4.99	51.3	0.78	3.74	-4.53
14	3.21	5.85	4.34	33.3	2.85	-0.25	-2.60
15	4.06	6.21	5.89	12.6	2.39	-1.10	-1.29
16	3.51	5.00	6.00	18.9	3.36	-1.37	-1.99
Pen-Fe-NO							
2	2.7	4.69	4.03	62.5	-1.57	5.95	-4.38
3	2.67	3.94	4.98	52.1	0.60	3.93	-4.53
14	3.2	5.82	4.36	33.3	2.88	-0.25	-2.63
17	3.51	4.29	6.26	38.0	1.72	0.28	-1.99
18	4.21	5.15	6.76	36.4	1.09	0.07	-1.15
16	4.77	5.99	7.27	21.4	1.27	-0.48	-0.79
20	5.18	7.28	6.93	8.9	1.19	-0.57	-0.62
21	4.97	6.89	6.76	24.3	1.05	-0.35	-0.70
22	4.53	6.97	5.76	27.1	1.28	-0.35	-0.93
Ferritin-Fe-NO							
1	2.75	4.84	4	60.5	-1.14	5.28	-4.14
2	3.81	6.39	4.91	31.5	1.84	-0.28	-1.56
3	3.94	6.42	5.14	31.5	1.66	-0.25	-1.41
4	3.63	5.68	5.67	7.6	3.51	-1.71	-1.80

- a. The proton numbers are the same as in Figure 4.11, 4.12 and 4.14.
b. The hyperfine couplings are in unit of MHz.

APPENDIX I

MOLECULAR MODELING CALCULATIONS FOR THE PREVIOUS PROTON ENDOR SPECTRA OF CYSTEINE AND PENICILLAMINE IRON NITROSYL COMPLEXES

The analysis on the previous ^1H ENDOR spectra was also carried out with molecular modeling calculations. The calculation procedures are demonstrated below.

- a. Build complexes with ChemSite. Give each atom correct properties, such as charge, hybridization, number of bonds and bond lengths. Then, do energy minimization on the complex. Finally, save the complex in a file.
- b. Use word reading program (such as WordPad) to read in the complex file. Delete all useless information in the complex file and copy the coordinates of all the atoms in the complex.
- c. Open Excel and paste the copied coordinates into the ANGLEII worksheet. The calculated hyperfine couplings are then copied and rearranged in a spare worksheet. Copy the rearranged proton hyperfine couplings.
- d. Open Origin and paste the calculated hyperfine couplings in a worksheet and plot them as stick spectrum with the proton ENDOR spectrum in separated layers.

The modeling calculations usually do not give a matched stick spectra with ENDOR spectra. The tilt of the pseudo symmetry axis, the type of ligation by ligands (monodentate or bidentate) and the consideration of H-bonded water molecule are taken into account to obtain the well matched stick spectra with ENDOR spectra.

Figure I.1 - I.4 are the ENDOR spectra (obtained by Wang^[47]) treated with the modeling calculations. It turned out that the bidentate ligation with the pseudo axis tilt of -9° fits proton ENDOR spectra of the Pen-Fe-NO complex. But a monodentate ligation and the insertion of a water molecule H-bonded with the two sulfur atoms generate stick spectra basically matched with the ENDOR spectra of Cys-Fe-NO complex.

In order to obtain exact matched stick spectra and ENDOR spectra of the model complexes, more sophisticated modeling calculations^[51a, 51b] and selectively deuterated ligands are required.

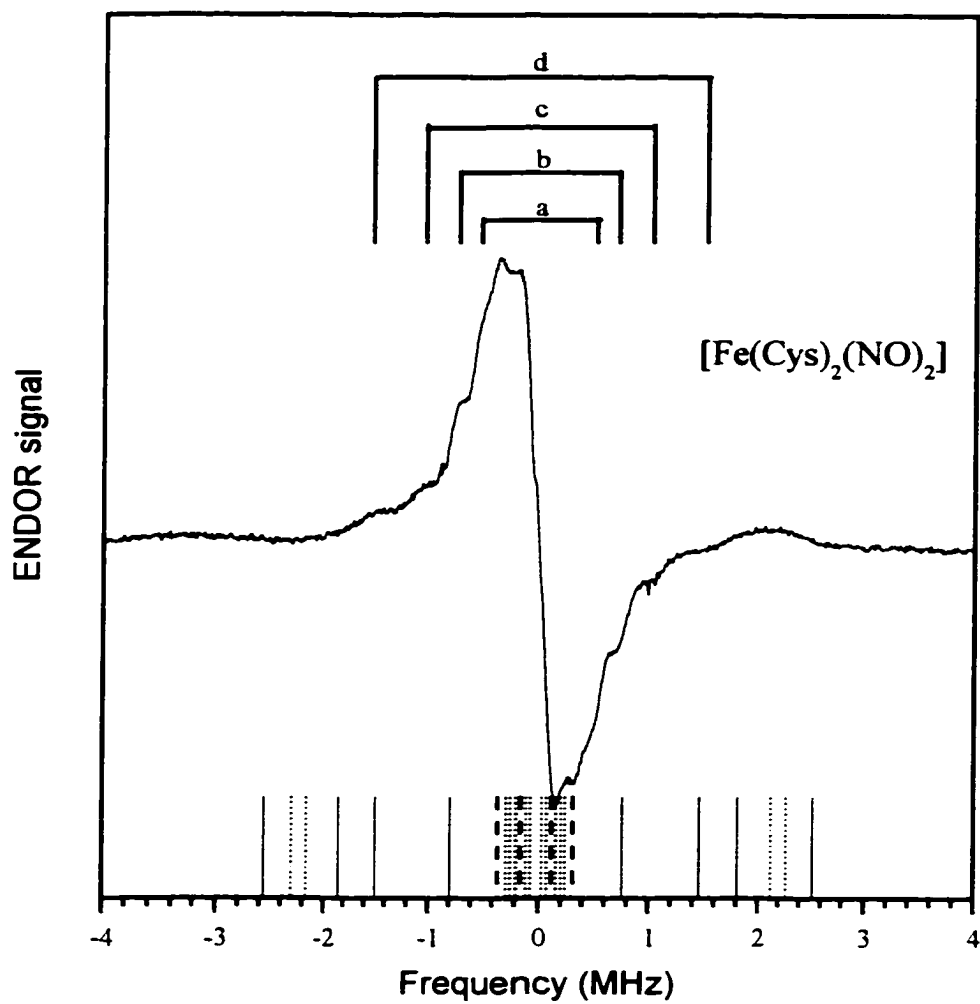


Figure I.1 The proton ENDOR spectrum of Cys-Fe-NO along with the modeling calculation results at the field parallel position. The dot lines represent the couplings from the exchangeable protons, dashed line from α protons, solid line from methylene protons.

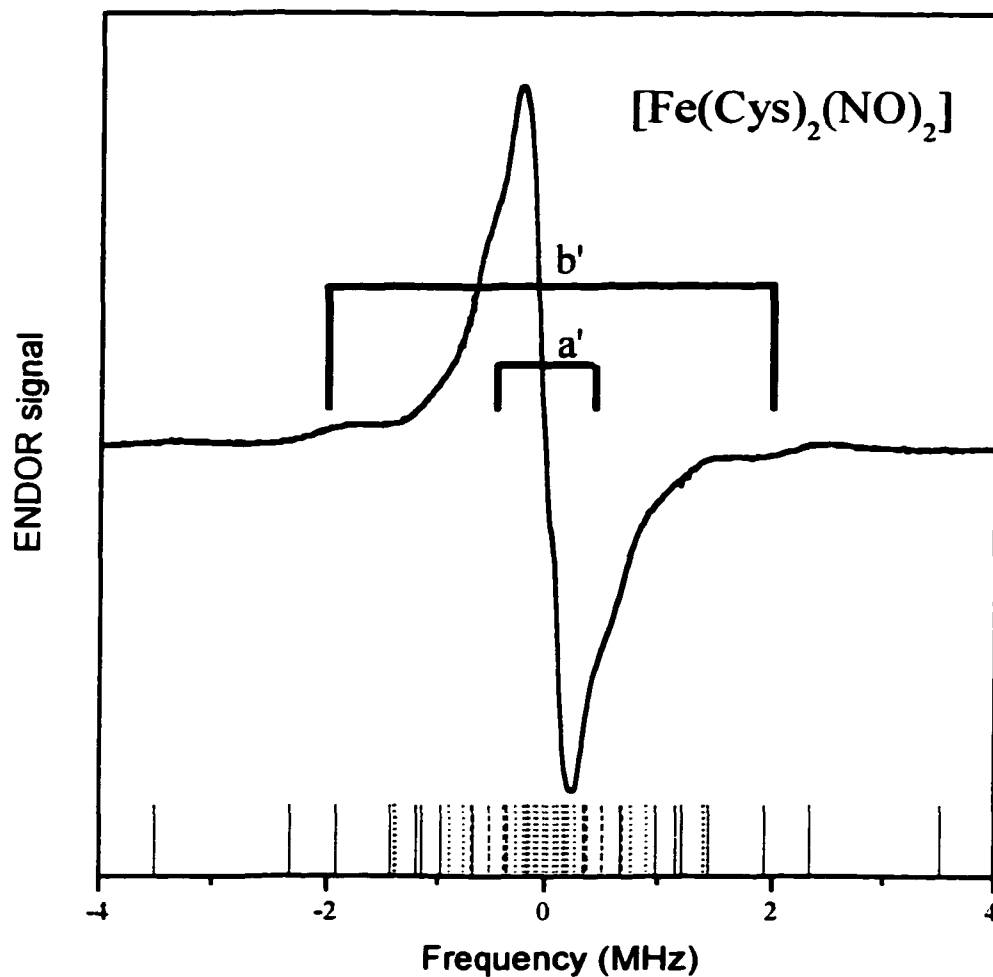


Figure I.2 The proton ENDOR spectrum of Cys-Fe-NO along with the modeling calculation results at the field perpendicular position. The line types are the same as in Figure I.1.

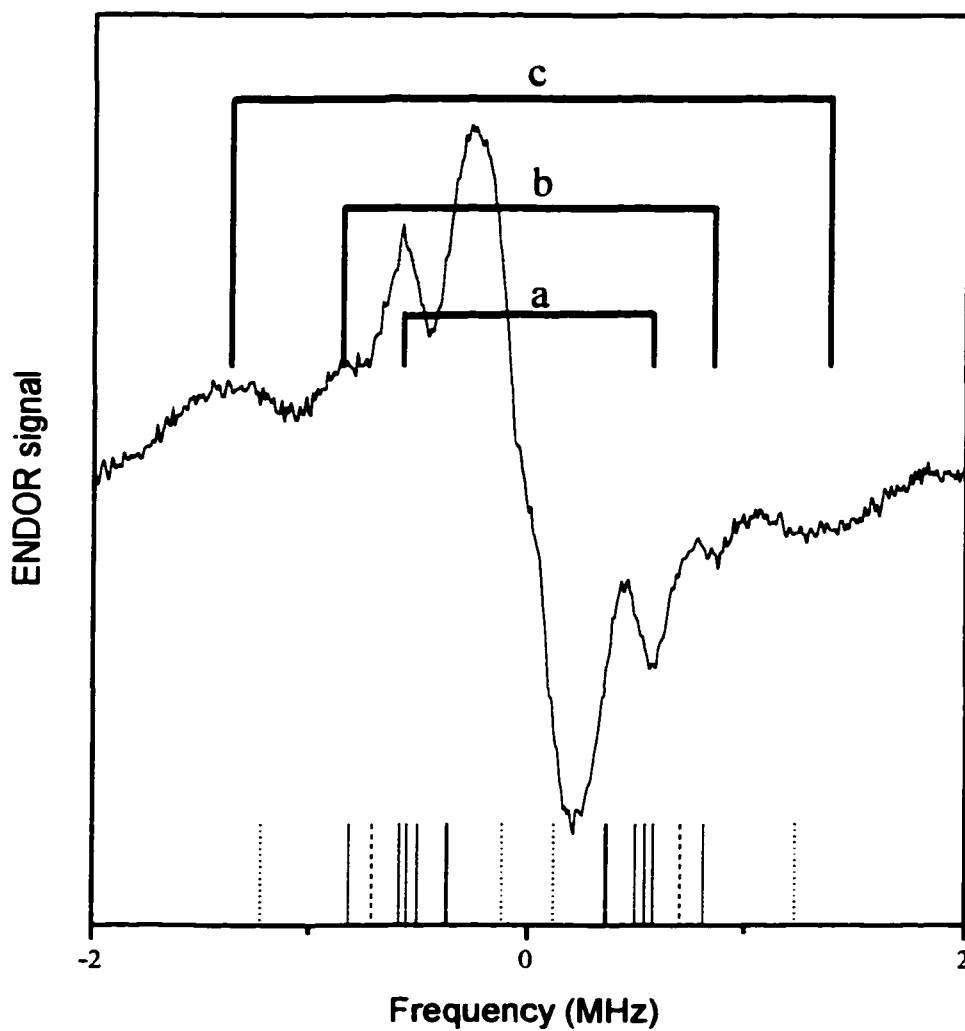


Figure I.3 The proton ENDOR spectrum of Pen-Fe-NO along with the modeling calculation results at the field parallel position. The dot lines represent the couplings from the exchangeable protons, dashed line from α protons, solid line from methyl protons.

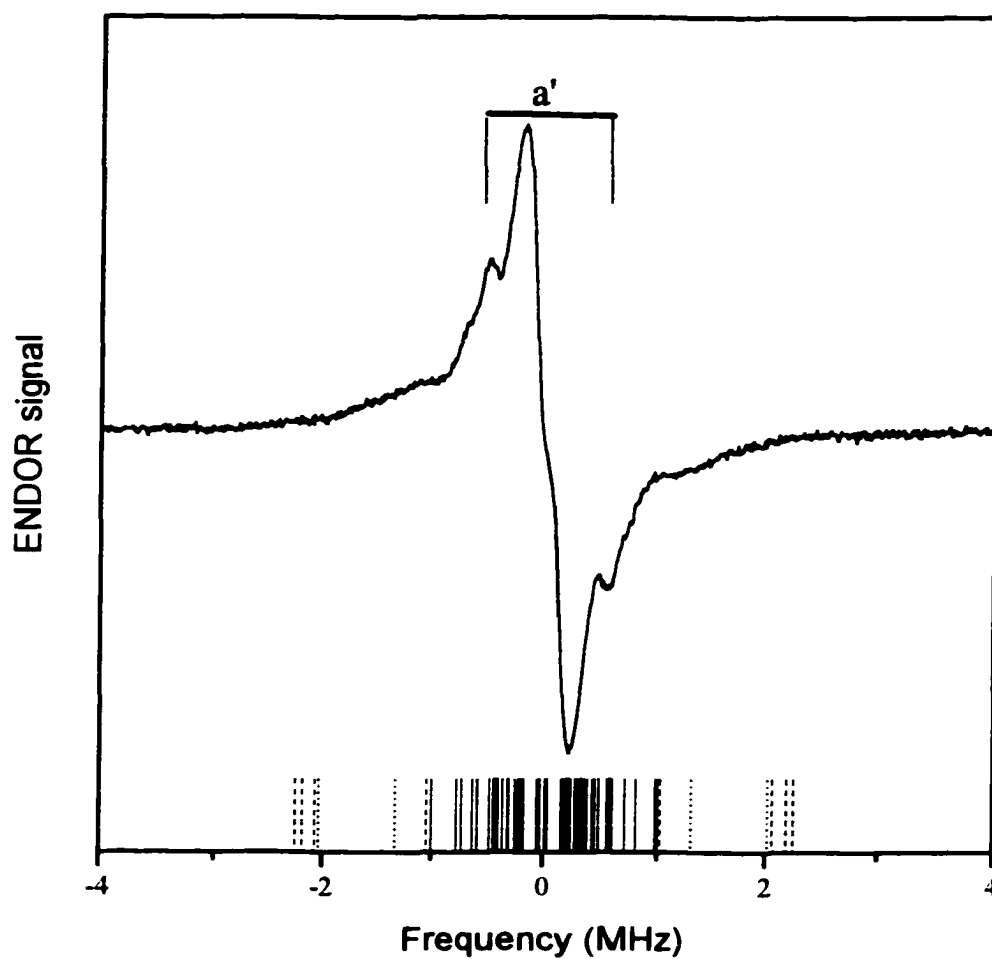


Figure I.4 The proton ENDOR spectrum of Pen-Fe-NO along with the modeling calculation results at the field perpendicular position. The line types are the same as in Figure I.3.